



Modelling and simulation of ventilation devices in nuclear waste geological repositories

Yumeng Zhang

► To cite this version:

Yumeng Zhang. Modelling and simulation of ventilation devices in nuclear waste geological repositories. Other. Université Nice Sophia Antipolis, 2015. English. NNT : 2015NICE4132 . tel-01293676

HAL Id: tel-01293676

<https://theses.hal.science/tel-01293676>

Submitted on 25 Mar 2016

HAL is a multi-disciplinary open access archive for the deposit and dissemination of scientific research documents, whether they are published or not. The documents may come from teaching and research institutions in France or abroad, or from public or private research centers.

L'archive ouverte pluridisciplinaire **HAL**, est destinée au dépôt et à la diffusion de documents scientifiques de niveau recherche, publiés ou non, émanant des établissements d'enseignement et de recherche français ou étrangers, des laboratoires publics ou privés.

UNIVERSITE NICE SOPHIA ANTIPOLIS - UFR Sciences
Ecole Doctorale en Sciences Fondamentales et Appliquées EDSFA

T H E S E

pour obtenir le titre de
Docteur en Sciences
de l'UNIVERSITE Nice Sophia Antipolis

Discipline : Mathématiques

présentée et soutenue par

Yumeng ZHANG

Modélisation et simulation des dispositifs de
ventilation dans les stockages de déchets
radioactifs

Thèse dirigée par Thierry GOUDON et Roland MASSON
soutenue le 17 décembre 2015

Jury :

Mme	CHAINAIS Claire	Rapporteur
M.	ERN Alexandre	Rapporteur
M.	GALLOUËT Thierry	Examineur
M.	GOUDON Thierry	Directeur de thèse
M.	MASSON Roland	Co-directeur de thèse
M.	TRENTY Laurent	Examineur

Modélisation et simulation des dispositifs de ventilation dans les stockages de déchets radioactifs

Résumé: l'objectif de cette thèse est de fournir des modèles et des outils de simulation pour décrire les échanges de masse entre les circuits de ventilation (galeries) et les milieux poreux des ouvrages souterrains d'enfouissement des déchets nucléaires. La modélisation prend en compte le couplage à l'interface poreux-galerie entre les écoulements liquide gaz compositionnels dans le milieu poreux constituant le stockage et les écoulements gazeux compositionnels dans le milieu galerie libre.

Dans le chapitre 1 on étudie trois différentes formulations de l'écoulement gaz liquide compositionnel dans le milieu poreux dont on montre l'équivalence du point de vue des transitions de phases. Ces formulations sont comparées numériquement sur des cas tests 1D puis 3D discrétisés en espace par le schéma Vertex Approximate Gradient (VAG).

Le Chapitre 2 se concentre sur un modèle réduit couplant les écoulements diphasiques compositionnels 3D en milieu poreux et l'écoulement monophasique compositionnel 1D dans la galerie. Il suppose que l'extension longitudinale de la galerie est grande par rapport à son diamètre. Le modèle poreux prend aussi en compte les échanges entre un réseau de fractures discrètes de co-dimension 1 et le milieu matriciel environnant. Le schéma VAG est étendu afin de prendre en compte le couplage entre les écoulements 3D dans la matrice, 2D dans le réseau de fractures discrètes et 1D dans la galerie. La convergence de cette discrétisation est étudiée dans le cas du modèle linéaire monophasique stationnaire ainsi que dans le cas d'un modèle non linéaire couplant l'équation de Richards à l'écoulement 1D monophasique ou de type traceur dans la galerie. Différents cas tests correspondant au jeu de données Andra sont présentés.

Le chapitre 3 développe un algorithme de point fixe pour résoudre le couplage entre les écoulements gaz liquide dans le milieu poreux et l'écoulement gazeux libre dans la galerie. Cet algorithme repose sur la compréhension des couplages forts et faibles dans le système. Il consiste à résoudre, dans une première étape, l'écoulement dans le milieu poreux couplé aux équations de convection diffusion sur les fractions molaires dans la galerie à vitesse fixée. Dans une deuxième étape, connaissant le flux total à l'interface, il résout les équations de Navier Stokes pour déterminer la vitesse et la pression dans la galerie. Cet algorithme est étudié sur différents cas tests posés par l'Andra et les solutions obtenues sont comparées à celles du modèle réduit du chapitre précédent. Pour cela, l'épaisseur de la couche limite visqueuse en concentration d'eau dans la galerie est approchée par une approximation diagonale basse fréquence de l'opérateur de Steklov Poincaré associé à l'équation de convection diffusion à vitesse fixée dans la galerie.

Mots-clés: séchage convectif, stockage des déchets radioactifs, écoulement diphasique compositionnel en milieu poreux, écoulement monophasique compositionnel libre, couplage des écoulements en milieux poreux et libre, schémas volume fini, schémas gradients, analyse numérique.

Modelling and simulation of ventilation devices in nuclear waste geological repositories

Abstract: the objective of this thesis is to develop models and algorithms to simulate efficiently the mass exchanges occurring at the interface between the nuclear waste deep geological repositories and the ventilation excavated galleries. To model such physical processes, one needs to account in the porous medium for the flow of the liquid and gas phases including the vaporization of the water component in the gas phase and the dissolution of the gaseous components in the liquid phase. In the free flow region, a single phase gas free flow is considered assuming that the liquid phase is instantaneously vaporized at the interface. This gas free flow has to be compositional to account for the change of the relative humidity in the free flow region which has a strong feedback on the liquid flow rate at the interface.

In chapter 1, three formulations of the gas liquid compositional Darcy flow are studied. Their equivalence from the point of phase transitions is shown and they are compared numerically on 1D and 3D test cases including gas appearance and liquid disappearance. The 3D discretization is based on the Vertex Approximate Gradient (VAG) scheme and takes into account discontinuous capillary pressures.

In chapter 2, a reduced model coupling a 3D gas liquid compositional Darcy flow in a fractured porous medium, and a 1D compositional free gas flow is introduced. The VAG discretization is extended to such models taking into account the coupling between the 3D matrix, the 2D network of fractures and the 1D gallery. Its convergence is studied both for the linear single phase stationary model and for a non linear model coupling the Richards equation to a single phase 1D flow or a 1D tracer equation in the gallery. Different test cases with Andra data sets are presented.

In Chapter 3, a splitting algorithm to solve the coupling between the gas liquid compositional Darcy flow in the porous medium and the gas compositional free flow in the gallery is developed. The idea is to solve, in a first step, the porous medium equations coupled to the convection diffusion equations for the gas molar fractions in the gallery at fixed velocity and pressure in the gallery. Then, the total molar normal flux at the interface is computed and used in the second step of the algorithm to compute the velocity and pressure in the gallery solving the Navier Stokes equations. This algorithm is tested on several 2D test cases and the solutions obtained are compared with the ones obtained by the previous reduced model. To that end, the gas molar fraction boundary layer thickness used as a parameter in the reduced model is computed based on a low frequency diagonal approximation of a Steklov Poincaré type operator for the stationary convection diffusion equation at fixed velocity.

Keywords: convective drying, nuclear waste geological repository, gas liquid compositional Darcy flow, gas compositional free flow, coupling Darcy and free flow, finite volume scheme, gradient scheme, numerical analysis.

Remerciements

La thèse s'est effectuée au Laboratoire J.A. Dieudonné, sous la supervision de Thierry Goudon et Roland Masson. Je souhaite tout d'abord vivement les remercier. Ils m'ont épaulé pendant toute la période de ma thèse et ont rendu possible l'aboutissement de mon travail de thèse. Ils m'ont permis aussi de découvrir mon intérêt pour la recherche dans le domaine de la simulation numérique. De plus, je voudrais remercier spécialement Roland pour tout le temps que nous avons passé à travailler ensemble.

Je tiens également à remercier Konstantin Brenner pour son aide pendant mes travaux de thèse. Ses compétences en analyse de convergence des schémas numériques m'ont été très précieuses.

Je remercie aussi l'Andra pour le financement de ma thèse et en particulier Laurent Trenty qui m'a suivi pendant ses trois années de recherches. Sans son aide sur la définition des jeux de données expérimentales je n'aurais pu valider les modèles développés pendant ma thèse.

Je remercie beaucoup Claire Chainais et Alexandre Ern qui ont bien voulu rapporter sur ma thèse. J'en suis très honorée et je les remercie pour leurs remarques qui ont contribué à l'amélioration du manuscrit.

Je remercie chaleureusement Thierry Gallouët, je lui suis très reconnaissante d'avoir accepté de participer à mon jury.

Je voudrais aussi remercier tous les membres du LJAD. Ils m'ont accompagné et ont enrichi ma vie de recherche durant ces trois années.

Je remercie finalement mes parents, pour leur support constant dès le début de mes études en France.

A mes parents

Contents

Introduction	3
1 Formulations of liquid gas compositional Darcy flows with phase transitions	13
1.1 Introduction	13
1.2 Formulations of compositional liquid gas Darcy flows	15
1.2.1 Natural variable formulation (PSC)	16
1.2.2 Pressures, saturations and fugacities formulation (PSF)	20
1.2.3 Pressures, and fugacities formulation (PPF)	21
1.3 Numerical comparison of the three formulations	25
1.3.1 One dimensional test cases	25
1.3.2 Three dimensional test cases	36
1.3.3 Vertex Approximate Gradient discretization	36
1.3.4 Drying by suction	39
1.3.5 Migration of gas in a basin with capillary barriers	42
1.4 Conclusion	50
2 Coupling of a liquid gas compositional 3D Darcy flow with a 1D compositional free gas flow	51
2.1 Introduction	51
2.2 Model problem	53
2.2.1 Geometry and functional setting	53
2.2.2 Gradient scheme discretization of the model problem	58
2.2.3 VAG Discretization of the model problem	61
2.2.4 Convergence analysis of the VAG discretization of the model problem	66
2.2.5 Numerical examples	71
2.3 Extension to the Compositional Model	77
2.3.1 Compositional Model	77
2.3.2 VAG discretization of the compositional model	80
2.4 Numerical experiments without fractures	82
2.4.1 Comparison with an approximate stationary solution	84
2.4.2 Heterogeneous anisotropic test case	89
2.4.3 Model with gas molar fraction and diffusion at the interface	92

2.5	Numerical experiments with fractures	96
2.5.1	Test case with 1 fracture	96
2.5.2	Test case with 4 fractures	99
2.6	Convergence analysis of a simplified model	100
2.6.1	Vertex Approximate Gradient Discretization	102
2.6.2	Convergence analysis	103
2.7	Conclusion	114
3	Coupling of a liquid gas compositional 2D Darcy flow with a 2D compositional free gas flow	116
3.1	Introduction	116
3.2	Formulation of the coupled model and fixed point algorithm	118
3.2.1	Formulation of the coupled model	119
3.2.2	Fixed point algorithm	121
3.3	Reduced model	123
3.3.1	Reduced 1D model in the free flow domain	123
3.3.2	Molar fraction boundary layer thickness model	124
3.4	Numerical tests	125
3.4.1	Finite Volume Discretization on a Cartesian mesh	127
3.4.2	Andra test case with an horizontal gallery	132
3.4.3	Andra test case with a vertical gallery	145
3.4.4	Drying test case	153
3.5	Conclusions	161
	Conclusions et perspectives	162

Introduction

Contexte de l'étude et état de l'art

L'objectif de ce travail est de fournir des modèles et des outils de simulation pour décrire les échanges de masse et d'énergie entre les circuits de ventilation et les milieux poreux des ouvrages souterrains d'enfouissement des déchets nucléaires. Ce travail vise à contribuer, par l'expérimentation numérique, à l'amélioration de la connaissance du comportement des gaz dans les phases d'exploitation, élément constitutif du Dossier d'Autorisation de Construction du Stockage (DAC).

La figure 1 montre une représentation de l'évolution de la température et de l'humidité relative de l'air au sein d'un quartier du stockage sur la période d'exploitation de 100 ans. Le réseau de ventilation qui s'étend sur une longueur cumulée d'une centaine de kilomètres, respecte les grands principes de fractionnement et de modularité qui lui confèrent une indépendance de la ventilation vis-à-vis (i) des activités de travaux et d'exploitation nucléaire et (ii) des différentes zones de stockage.

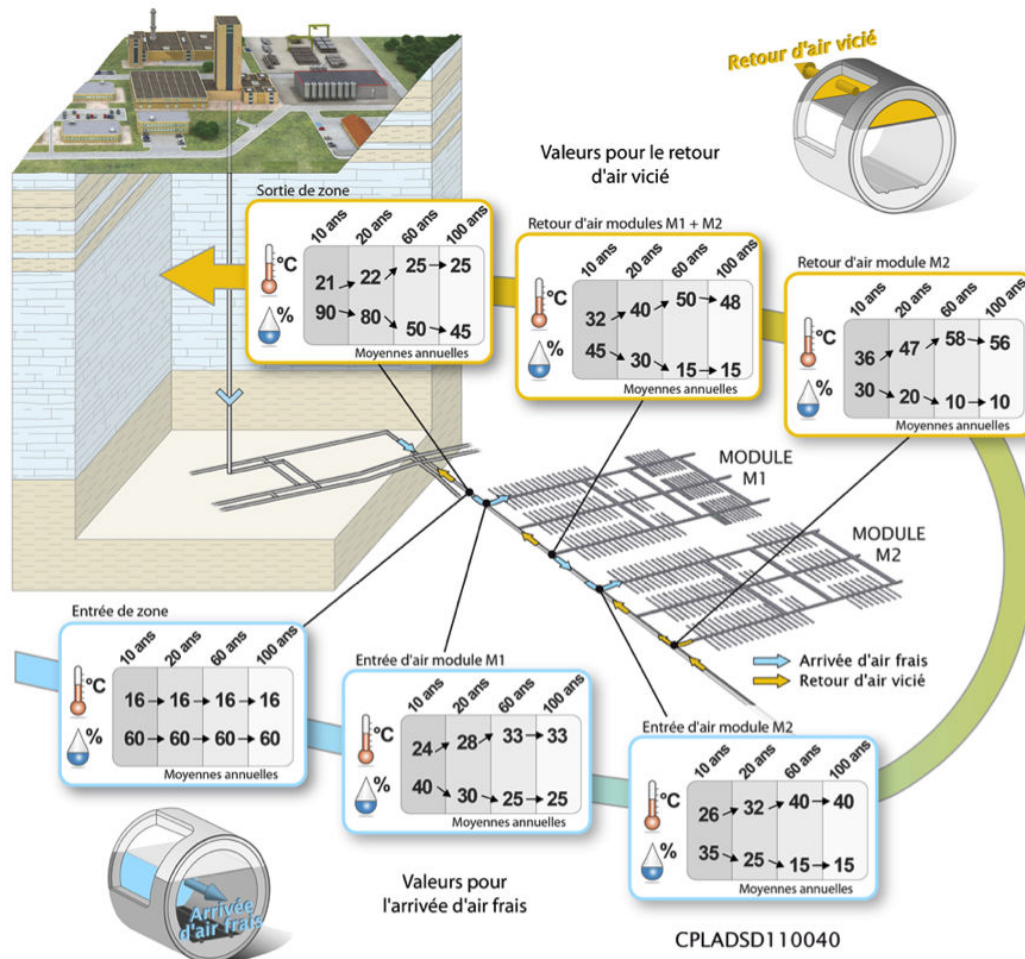


Figure 1: Evolution des conditions d'environnement en amont/aval de quartiers de stockage à 10 ans, 20 ans, 60 ans et 100 ans (hypothèse de quartiers maintenus ouverts et ventilés).

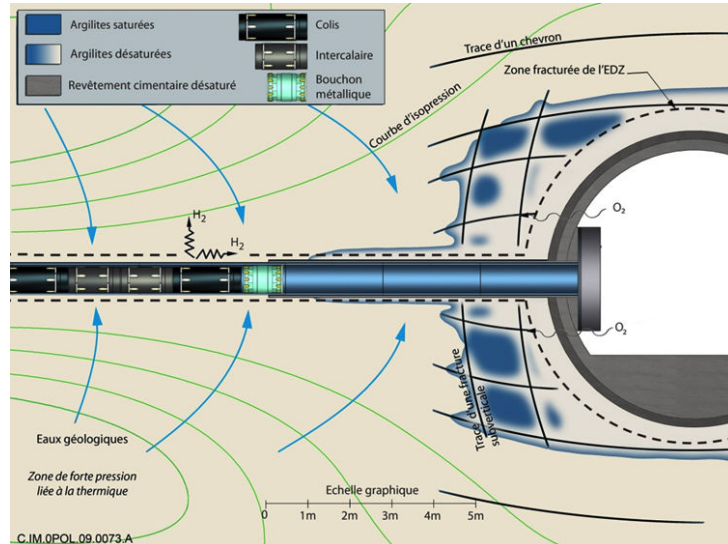


Figure 2: Illustration des interactions hydraulique et hydrique entre l'alvéole et la galerie d'accès localisées au niveau de la tête d'alvéole.

Un premier objectif est de prédire sur une telle durée l'évolution de la température et de l'humidité relative (liée à la fraction molaire d'eau (H_2O)) dans le réseau de galeries et d'alvéoles de stockage et de contrôler la qualité de l'air afin de protéger l'homme et l'environnement de tout risque opérationnel pendant la phase d'exploitation. Un autre objectif est de prédire la désaturation (et le cas échéant la resaturation) des argilites mais aussi des composants cimentaires induite par la ventilation au voisinage de l'interface entre le stockage et les galeries (cf. Figure 2).

Les phénomènes physiques mis en jeu font partie de la problématique plus générale du séchage ou de l'évaporation à l'interface entre un milieu poreux et un milieu libre. Ils font intervenir principalement

- les écoulements diphasiques liquide gaz dans le milieu poreux avec prise en compte de la composition des phases, de la diffusion dispersion des composants dans les phases liquide et gazeuse, et de la gestion de l'apparition et de la disparition des phases (typiquement apparition de la phase gaz et disparition de la phase eau).
- l'écoulement de la phase gazeuse dans le milieu libre (galeries de ventilation dans notre cas) avec prise en compte de la composition avec diffusion moléculaire ou turbulente des composants dans la phase gaz. La phase liquide n'est pas prise en compte car l'on suppose qu'elle se vaporise instantanément à l'interface entre le milieu poreux et le milieu libre. On verra que la diffusion en général turbulente joue un rôle essentiel sur le taux d'évaporation du liquide à l'interface.
- La thermique à la fois dans le milieu poreux et dans le milieu libre.
- La mécanique dans le milieu poreux liée aux effets thermiques et à la désaturation.

La modélisation du séchage intervient dans de nombreuses autres applications comme par exemple la fabrication de matériaux de construction (béton, briques), les procédés de fabrication alimentaire, l'entretien des surfaces extérieures des bâtiments historiques, l'interaction sol atmosphère ... On revoit à [25] pour une liste exhaustive. Une particularité liée à l'application aux dispositifs de ventilation dans les stockages de déchets nucléaires est que l'on s'intéresse à l'effet du couplage sur l'évolution du milieu libre, notamment le suivi des fractions molaires dans les galeries, alors qu'en général dans les problèmes de séchage la modélisation est exclusivement focalisée sur l'évolution du milieu poreux. Notamment, les cas accidentels d'une ventilation faible ou nulle qui vont a priori accroître l'effet du couplage sur le milieu libre ne sont pas pris en compte dans les modèles de séchage habituels.

Dans cette thèse, on se concentre sur les seuls échanges de masse en supposant dans une première étape les écoulements isothermes à température constante T_e identique dans le milieu poreux et dans le réseau de galeries.

Une représentation schématique 2D du problème couplé est donnée Figure 3 qui représente le milieu poreux Ω^p , la galerie Ω^g , l'interface poreux galerie Γ . Y figurent également les inconnues principales du modèle d'écoulement en milieu poreux (p^l, s^l, c^l) qui décrivent la phase liquide et (p^g, s^g, c^g) qui décrivent la phase gazeuse, où p^α est la pression de la phase $\alpha = l, g$, s^α est sa fraction volumique ou saturation et c^α sa composition molaire (avec typiquement les deux composants eau et air potentiellement présents dans les deux phases). Les variables de l'écoulement de gaz libre sont notées (\mathbf{u}, p, c) avec la vitesse \mathbf{u} du gaz, sa pression p et sa fraction molaire c (avec typiquement les mêmes composants eau et air que dans le milieu poreux).

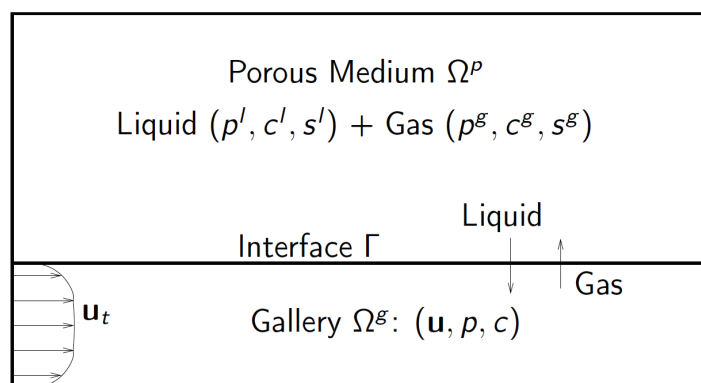


Figure 3: Géométrie schématique 2D du problème couplé avec le milieu poreux Ω^p , la galerie Ω^g , l'interface Γ , ainsi que les inconnues principales du modèle d'écoulement gaz liquide poreux et du modèle d'écoulement gazeux libre.

Si il existe de nombreux travaux sur le couplage à l'interface entre un écoulement de Darcy et un écoulement libre dans le cas d'un seul fluide, on trouve peu de références

sur la modélisation du couplage d'un modèle diphasique en milieu poreux avec un modèle monophasique en milieu libre. Or la physique qui gouverne ce dernier type de couplage est très différente du cas monophasique. Typiquement, dans le cas du couplage diphasique - monophasique les variations de la pression p dans la galerie sont en général faibles et ont peu d'effet sur le milieu poreux. On verra que le comportement physique du système est plutôt piloté au premier ordre par le couplage entre grosso modo l'équation de Richards dans le milieu poreux (qui ne simule pas directement la phase gazeuse) et les équations de convection diffusion des composants gazeux dans le milieu libre.

Le modèle qui nous servira de référence dans le cadre de cette thèse est celui proposé par [48, 49]. Quelques simplifications seront faites pour tenir compte de la faible perméabilité du milieu poreux dans les stockages.

Les phases gazeuse et liquide dans le milieu poreux et gazeuse dans le milieu libre sont supposées constituées d'un ensemble unique de composants noté \mathcal{C} . Typiquement il s'agira du composant eau présent sous forme liquide et sous forme vapeur, et de composants gazeux pouvant se dissoudre dans la phase liquide comme l'air, le CO_2 , le N_2 .

Les modèles considérées dans cette thèse prennent en compte les lois suivantes:

- Modèle poreux: loi de Darcy généralisée pour les écoulements des phases gaz et liquide, loi de diffusion des composants dans les phases liquide et gazeuse, prise en compte des changements de phase modélisés par les lois d'équilibre thermodynamique.
- Modèle gaz libre: équations de Navier Stokes compositionnelles, on supposera pour simplifier l'écoulement incompressible, la turbulence sera prise en compte par un modèle RANS (Reynolds Averaged Navier Stokes) avec un modèle simple de turbulence algébrique pour le calcul de la viscosité et de la diffusion turbulentes, diffusion moléculaire et turbulente des composants dans le gaz [9, 19].
- Conditions de couplage à l'interface: elles expriment selon [48, 49] la continuité des flux de chaque composant en tenant compte de l'hypothèse de vaporisation instantanée de la phase liquide à l'interface, la continuité des fractions molaires de la phase gaz et l'équilibre thermodynamique liquide gaz. Dans notre cas, la loi de Beavers Joseph [7] sera remplacée par un glissement nul du fait de la faible perméabilité du milieu poreux. On négligera aussi en pratique le saut de pression de gaz qui dérive de la continuité de la composante normale de la contrainte normale.

La plupart des modèles numériques de séchage simulent exclusivement le domaine poreux, la prise en compte de l'écoulement (et de la thermique) dans le domaine libre étant réduite à des coefficients de transfert convectif de masse (et de chaleur) déterminés par des corrélations en fonction des caractéristiques de l'écoulement. Comme indiqué dans le récent article de synthèse [25], ces approches donnent une bonne approximation du taux d'évaporation dans le cas d'écoulements et de géométries simples mais elles sont dans de nombreux cas insuffisantes car elles ne prennent pas en compte les variations spatiale et temporelle des coefficients de transfert convectif. Dans notre cas où on cherche

à modéliser les variations de compositions (et de température) dans le réseau de galerie, on ne pourra pas a priori s'en contenter.

Depuis une dizaine d'années, on voit dans la littérature du séchage émerger des modèles simulant véritablement les deux écoulements et leur couplage. Deux types d'approches ressortent de l'article [25]. La première repose sur un couplage séquentiel de type Dirichlet Neumann entre les écoulements diphasique poreux et gaz libre le plus souvent simulés par deux codes distincts. Comme indiqué dans [26, 24] ce type de couplage conduit à l'utilisation de pas de temps à l'échelle de l'écoulement du gaz libre, très petits par rapport à l'échelle de temps du milieu poreux. Cette instabilité est due au fort couplage non linéaire entre la fraction molaire d'eau à l'interface et la pression de liquide (donc le flux de liquide) à l'interface par la relation d'équilibre thermodynamique. En pratique, il est par exemple indiqué dans [26, 24], où un algorithme séquentiel est utilisé, un pas de temps de l'ordre de 0.1 s et 100 h de temps CPU pour quelques jours de simulations. Ce type d'approche n'est bien sûr pas viable dans notre cas. Afin de pouvoir simuler une période de 100 ans, il faut un algorithme capable de traiter des pas de temps à l'échelle du milieu poreux avec un écoulement quasi stationnaire dans la galerie.

Alternativement de nombreux travaux utilisent un algorithme complètement implicite qui résout l'ensemble du système couplé par un algorithme de Newton global après une discrétisation en temps implicite. Le plus souvent un solveur linéaire direct creux est utilisé pour résoudre le système linéaire couplant toutes les inconnues du système. C'est par exemple le cas de [6, 41, 48] et a priori des simulations réalisées dans ComSol (voir l'article de synthèse [25] qui présente une liste de codes pour la simulation du séchage avec mention du type de couplage). Cette approche monolithique est coûteuse en temps calcul et n'exploite pas les différents niveaux de couplage dans le modèle.

Plan de la thèse

Formulation des modèles gaz liquide compositionnels en milieux poreux: Dans ce chapitre 1 on se concentre sur l'étude comparative de formulations de l'écoulement gaz liquide compositionnel dans le milieu poreux. Ces modèles sont utilisés dans de nombreuses applications notamment en géosciences comme le stockage du CO_2 dans des aquifères salins, la production pétrolière et gazière, le stockage de gaz dans des réservoirs géologiques ou encore le stockage géologique profond des déchets nucléaires.

Leur simulation repose sur une formulation adaptée au couplage non linéaire entre la conservation molaire des composants, la conservation du volume et les lois de fermetures hydrodynamique et thermodynamique. Une difficulté majeure est la prise en compte des changements de phase induits par les lois d'équilibre thermodynamique. Plusieurs formulations ont été proposées dans l'industrie pétrolière (voir [18] et les références associées), et plus récemment dans le domaine de la modélisation de la migration de gaz dans les stockages géologiques profonds de déchets nucléaires (voir par exemple [1], [4], [11]).

Le principal objectif du chapitre 1 est de comparer trois formulations des écoulements gaz liquide compositionnels en milieu poreux prenant en compte les changements de phase.

La première formulation dite à variables naturelles est couramment utilisée dans la communauté de la simulation des réservoirs pétroliers depuis les années 80 [20], [21]. Elle est aussi connue sous le nom de formulation avec changement de système d’inconnues car elle utilise un jeu de variables du système non linéaire défini par les pressions p^l , p^g , les saturations s^l , s^g et les fractions molaires $c^\alpha = (c_i^\alpha)_{i \in \mathcal{C}}$ des phases $\alpha \in Q$ où Q représente l’ensemble des phases présentes en chaque point du domaine espace temps. L’ensemble Q qui prend en compte les changements de phase est typiquement déterminé par un flash négatif [59].

La seconde formulation a été introduite dans [45]. Son avantage principal par rapport à la formulation précédente est d’utiliser un jeu d’inconnues unique pour le système non linéaire défini par les pressions p^l , p^g , les saturations s^l , s^g , et les fugacités des composants $f = (f_i)_{i \in \mathcal{C}}$. Dans cette formulation les fractions molaires des composants dans chacune des phases c^α , $\alpha = g, l$ sont exprimées comme des fonctions du vecteur des fugacités f et des pressions p^g , p^l . Les fractions molaires d’une phase absente sont ainsi étendues par celles à l’équilibre avec la phase présente conduisant à un jeu unique d’inconnues. Un autre avantage a priori est lié à la formulation des changements de phase par le biais de conditions de complémentarité évitant ainsi le recours à un flash négatif.

La dernière formulation étudiée est une extension au cas compositionnel de la formulation en pressions des phases introduite dans [4] dans le cas de deux composants. Cette extension repose sur l’utilisation du vecteur des fugacités f dans l’esprit de la formulation précédente. En plus de l’extension précédente des fractions molaires pour une phase absente, la pression d’une phase absente est également étendue par la pression faisant apparaître la phase à vecteur des fugacités fixé f . L’apparition ou la disparition d’une phase est alors déterminée par le graphe monotone inverse de la pression capillaire et n’implique aucune contrainte inégalité.

On commence par détailler dans ce chapitre 1 les trois formulations en montrant leur équivalence du point de vue des changements de phase sous certaines hypothèses sur le système thermodynamique qui correspondent à l’application de la thèse. Les avantages et inconvénients de chacune des formulations sont aussi discutés.

Ensuite, les trois formulations sont comparées numériquement du point de vue de la convergence non linéaire sur des cas tests 1D et 3D et pour des familles de maillages de tailles croissantes. La discrétisation en espace des cas tests 3D repose sur le schéma Vertex Approximate Gradient (VAG) introduit dans [32] pour les équations de diffusion en milieu hétérogène anisotrope sur des maillages polyédriques. Ce schéma a été étendu au cas des écoulements de Darcy multiphasiques compositionnels dans [33] puis dans [35] pour la prise en compte des pressions capillaires discontinues aux interfaces entre différents types de roches.

Le premier cas test considéré est issu du benchmark Couplex proposé par l’Andra [50], [11] simulant la désaturation par succion de la barrière géologique à l’interface avec la galerie de ventilation. Ce cas test est simulé à la fois en géométries 1D et 3D avec différents types de roches et prise en compte de l’anisotropie du milieu Callovo Oxfordien.

Le second cas test simule en 1D l’assèchement d’un milieu poreux saturé de liquide par injection d’un gaz sec qui peut par exemple subvenir au voisinage des puits d’injection

dans les stockages de CO_2 . Le troisième cas test simule la migration du gaz dans un bassin en géométrie 3D en présence de deux barrières capillaires de façon à comparer les formulations sur des cas avec forts contrastes de capillarités.

Etude d'un modèle réduit 3D poreux - 1D galerie

Dans ce chapitre 2 on étudie un modèle réduit couplant les écoulements gaz liquide compositionnels en milieu poreux avec un écoulement 1D de gaz compositionnel dans la galerie. On suppose pour cela que l'extension longitudinale de la galerie est grande par rapport à son diamètre. On supposera dans ce chapitre pour simplifier la présentation que les phases sont constituées de deux composants, l'eau sous forme liquide et gazeuse et l'air pouvant se dissoudre dans la phase liquide. L'extension à un modèle à $N > 2$ composants est immédiate en suivant la formulation en pressions des phases et fugacités des composants du chapitre 1.

Le modèle poreux prend en compte les échanges entre un réseau de fractures discrètes et le milieu matriciel environnant, selon le modèle asymptotique considéré dans [2, 53, 12, 13] où les fractures sont représentées comme des surfaces de co-dimension 1. Les pressions des deux phases seront considérées continues aux interfaces entre les fractures et la matrice, correspondant à une hypothèse de fractures n'agissant pas comme des barrières.

Le modèle couplé 3D pour la matrice, 2D pour les fractures et 1D pour la galerie est formulé dans un jeu de variables unique correspondant aux pressions des deux phases, selon la 3ème formulation du chapitre 1 où les fugacités des deux composants sont éliminées par la somme à 1 des fractions molaires de chacune des phases. Sa discrétisation repose sur le schéma VAG qui a été étendue aux réseaux de fractures discrètes dans [12, 13]. Le schéma VAG essentiellement nodal a l'avantage par rapport aux schémas nodaux classiques de type Control Volume Finite Element (CVFE) [6] d'éviter le mélange des différents types de roches dans les volumes de contrôle situés aux interfaces, notamment matrice fractures. Ce concept est ici étendu au couplage entre le milieu poreux et le milieu libre 1D avec une discrétisation à l'interface poreux galerie non nécessairement conforme de façon à pouvoir mailler des réseaux de fractures généraux.

Afin d'introduire le modèle réduit et son cadre fonctionnel, on considère tout d'abord un problème modèle monophasique et stationnaire couplant les écoulements 3D matrice, 2D fractures et 1D galerie. On décrit ensuite sa discrétisation par le schéma VAG dont la convergence est analysée dans le cadre des schémas gradients introduit dans [32], [29] et ici étendu à notre problème modèle.

On étend ensuite dans la section 2.3 le modèle réduit et sa discrétisation au cas compositionnel. Le modèle compositionnel est aussi complété sur le plan physique au paragraphe 2.4.3 par l'introduction d'une fraction molaire du gaz à l'interface poreux galerie et d'un terme de diffusion entre l'interface et la galerie modélisant la couche limite de convection diffusion. L'ordre de grandeur de cette diffusion à l'interface, lié aux propriétés de l'écoulement dans la galerie, joue un rôle essentiel sur le taux d'évaporation du liquide à l'interface. Notons aussi que le modèle réduit de la section 2.3 correspond au cas d'un

coefficient de diffusion à l'interface infini.

Le chapitre 2 est articulé comme suit: la section 2.2 étudie le problème monophasique stationnaire avec la description du modèle et de son cadre géométrique et fonctionnel au paragraphe 2.2.1, puis de sa discrétisation par le schéma VAG au paragraphe 2.2.3. L'analyse de la convergence du schéma VAG est effectuée au paragraphe 2.2.4 selon le cadre des schémas gradients étendu à notre modèle au paragraphe 2.2.2.

La section 2.3 étend le modèle précédent et sa discrétisation au cas des écoulements compositionnels en utilisant un jeu d'inconnue unique défini par les pressions des phases. Son comportement numérique est étudié dans la section 2.4 pour 3 cas tests avec notamment une comparaison avec une solution stationnaire approchée et l'étude de l'influence de la diffusion à l'interface. La section 2.5 donne deux exemples de cas tests incluant respectivement 1 et 4 fractures.

Finalement la section 2.6 étudie la convergence par compacité du schéma VAG vers une solution faible sur un modèle simplifié couplant l'équation de Richards dans le milieu poreux avec un écoulement monocomposant de type Poiseuille dans la galerie. La même analyse s'applique au couplage de l'équation de Richards avec l'équation 1D de convection diffusion sur la fraction molaire d'eau dans la galerie. Ce dernier modèle est une assez bonne approximation du modèle complet.

Etude du modèle 2D-2D et comparaison avec le modèle réduit

L'étude du modèle réduit 3D poreux - 1D libre précédent nous a permis de bien identifier le couplage fortement non linéaire entre la fraction molaire d'eau convectée dans la galerie de ventilation et la pression et le flux de liquide à l'interface poreux galerie. Ce couplage est lié à l'équilibre thermodynamique liquide gaz à l'interface.

Le chapitre 3 développe un algorithme de point fixe préservant ce couplage fort et relaxant le couplage de la vitesse et de la pression dans la galerie avec les inconnues du milieux poreux et les compositions du gaz dans la galerie. Cet algorithme consiste à résoudre à la première étape du point fixe les équations du modèle poreux couplées avec les équations de traceur sur les compositions à vitesse et pression fixées dans la galerie. Le flux total à l'interface calculé lors de cette première étape sert dans une deuxième étape à résoudre les équations de Navier Stokes pour déterminer la vitesse et la pression dans la galerie.

Afin de tester cet algorithme nous utilisons la configuration géométrique simplifiée 2D de la figure 3. Dans le domaine poreux Ω^p , on considère un écoulement de Darcy gaz liquide compositionnel formulé dans le jeu d'inconnues pressions des phases et fugacités des composants du chapitre 1. Dans le domaine galerie Ω^g , de façon à prendre en compte la nature turbulente de l'écoulement, on commence par calculer un profil de vitesse turbulent en utilisant un modèle de turbulence algébrique. Ce profil est solution stationnaire unidirectionnelle du modèle RANS incompressible sans couplage avec le milieu poreux. Une condition de type contrainte normale est imposée en sortie de la galerie qui permet de donner la référence de pression dans la galerie. Ce profil \mathbf{u}_t est ensuite imposé à l'entrée de

la galerie et fournit la viscosité et la diffusion turbulente du modèle RANS incompressible qui calcule la perturbation de la vitesse $\mathbf{u} - \mathbf{u}_t$ et la perturbation de pression liées au couplage avec le milieu poreux. Les conditions de couplage à l'interface sont issues de [48, 49]. Elles expriment la continuité des flux de chaque composant en tenant compte de l'hypothèse de vaporisation instantanée de la phase liquide à l'interface, la continuité des fractions molaires de la phase gaz et l'équilibre thermodynamique liquide gaz. La loi de Beavers Joseph est remplacée par un glissement nul du fait de la faible perméabilité du milieu poreux et on peut en pratique négliger le saut sur la pression de gaz qui dérive de la continuité de la composante normale de la contrainte normale.

Le domaine est maillé par une grille Cartésienne conforme et raffinée fortement à l'interface Γ de façon à prendre en compte la couche limite laminaire coté galerie et le fort gradient de pression capillaire coté poreux. La discrétisation en espace est un schéma MAC pour les équations de Navier Stokes à viscosité variable et un schéma volume fini centré aux mailles à la fois pour le modèle Darcy diphasique dans le domaine poreux et pour les équations de convection diffusion sur les fractions molaires du gaz dans la galerie. Dans les deux cas, les flux de type diffusion sont approchés par un schéma deux points et la partie convective utilise un schéma amont d'ordre 1. La discrétisation en temps est de type Euler implicite.

Afin de comparer le modèle couplé 2D-2D au modèle réduit (ici 2D-1D) développé au chapitre 2 il nous faut déterminer l'épaisseur de la couche limite introduite comme paramètre du modèle réduit au paragraphe 2.4.3. Cette épaisseur joue en effet un rôle essentiel sur l'ordre de grandeur du taux d'évaporation du liquide à l'interface. Le modèle proposé repose sur une approximation diagonale basse fréquence d'un opérateur de type Steklov Poincaré pour l'équation de convection diffusion stationnaire sur la fraction molaire d'eau dans la galerie. La vitesse de convection est fixée par le profil turbulent \mathbf{u}_t indépendant du temps. Ce calcul conduit à une épaisseur de couche limite indépendante du temps et fonction de la coordonnée x le long de la galerie.

Afin d'évaluer la performance de l'algorithme de point fixe et de comparer le modèle 2D-2D au modèle réduit 2D-1D trois cas tests sont considérés. Le premier reprend grosso modo les paramètres du cas test du paragraphe 2.4.2 avec différentes longueurs de galerie et trois vitesses de ventilation (5, 0.5, 0.05 m s⁻¹). Le deuxième cas test considère une galerie verticale avec deux types de roches et le troisième cas test correspond à une configuration de type séchage avec un milieu poreux de perméabilité environ 1 Darcy et des dimensions de l'ordre du mètre.

Chapter 1

Formulations of liquid gas compositional Darcy flows with phase transitions

Abstract: In this Chapter, three formulations of two phase compositional Darcy flows taking into account phase transitions are compared. The first formulation is the so called natural variable formulation commonly used in reservoir simulation, the second has been introduced in [45] and uses the phase pressures, saturations and component fugacities as main unknowns, and the third is an extension to general compositional two phase flows of the pressure pressure formulation introduced in [4] in the case of two components. The three formulations are shown to lead to equivalent definitions of the phase transitions for our gas liquid thermodynamical model. Then, they are compared numerically in terms of solution and convergence of the Newton type non linear solver on several 1D and 3D test cases including gas appearance and liquid disappearance. The 3D discretization is based on the Vertex Approximate Gradient (VAG) scheme [32] and takes into account discontinuous capillary pressures.

1.1 Introduction

The simulation of two phase gas liquid compositional Darcy flows is used in many applications such as the storage of carbon dioxide in saline aquifers, the gas recovery in petroleum reservoirs, the storage of gas in geological reservoirs, or also the safety assessment of geological radioactive waste disposals.

The numerical simulation of such models relies on a proper formulation coupling the mole balance of each component belonging to the set of components \mathcal{C} , the pore volume balance, and the hydrodynamical and thermodynamical laws. A major difficulty is to account for the phase transitions induced by the change of phase reactions assumed to be at thermodynamical equilibrium. Many formulations have been proposed in the oil industry (see [18] and the numerous references therein), and more recently for the mod-

elling of liquid gas migration in deep geological formation waste disposal (see for example [1, 4, 11, 37]).

The main objective of this Chapter is to compare three different formulations for two phase gas (g) liquid (l) compositional Darcy flows taking into account the phase transitions.

The first formulation is the so called natural variable formulation commonly used in the reservoir simulation community and which has been introduced in [20], [21]. It is also known as the switch of variable formulation since it uses a set of unknowns defined by the phase pressures p^l , p^g , the phase saturations s^l , s^g , and the molar fractions of the components $c^\alpha = (c_i^\alpha)_{i \in \mathcal{C}}$ in each phase $\alpha \in Q$ where Q is the set of present phases at each point of the time space domain. The set Q , accounting for the phase transitions, is typically obtained by a negative flash computation [59]. This formulation will be denoted by PSC in the following.

The second formulation has been introduced in [45]. Its main advantage compared with the previous one is to use a fixed set of equations and a fixed set of unknowns defined by the phase pressures p^l , p^g , the phase saturations s^l , s^g , and the component fugacities f_i , $i \in \mathcal{C}$. In this formulation the component molar fractions c^α are expressed as functions of the component fugacities f and of the phase pressures. It results that the component molar fractions of an absent phase are naturally extended by the ones at equilibrium with the present phase leading to a fix set of unknowns and equations. Another advantage is that the phase transitions simply take the form of complementary constraints which avoids negative flash calculations. This formulation will be denoted by PSF in the following.

The last formulation is an extension to general compositional two phase flow of the pressure pressure formulation introduced in [4] in the case of two components. This extension is based on the use of fugacities in addition to the phase pressures in the spirit of [45]. In this formulation, thanks to the extension of the phase pressure p^α in the absence of the phase by \tilde{p}^α for $\alpha = l, g$, and to the extension of the capillary function $p_c(s^l)$ by its monotone graph, the phase transitions reduce to $s^l = (p_c)^{-1}(\tilde{p}^g - \tilde{p}^l)$ and no longer involve inequality constraints. This formulation will be denoted by PPF in the following.

In the subsequent section, the three formulations are detailed and their equivalence is shown to hold under some assumptions on the fugacities. Advantages and drawback of each formulation are also further discussed.

Then, in the numerical test section, the three formulations are compared in terms of non linear convergence on several 1D and 3D test cases with families of refined meshes. The 3D spatial discretization is based on the Vertex Approximate Gradient (VAG) scheme which has been introduced in [32] for diffusion problems in heterogeneous anisotropic media. The VAG scheme has been extended to multiphase Darcy flows in [33] and in [35] in order to take into account discontinuous capillary pressures at the interfaces between different rocktypes using a pressure pressure formulation. It is basically a nodal discretization with an improved treatment of the heterogeneities of the media and of the hydrodynamic laws compared with usual Control Volume Finite Element methods for multiphase Darcy flows [42].

The first test case is a Couplex benchmark proposed by Andra [50], [11] simulating

the drying by liquid suction of the geological barrier at the interface with the ventilation gallery. It will be simulated both in 1D and in 3D taking into account two rocktypes and the anisotropy of the media. The second test case is a 1D test case which simulates the drying of a porous media saturated with the liquid phase by gas injection which can arise for instance in the nearwell region of carbon dioxide storage. The third test case simulates the migration of gas in a 3D basin with two capillary barriers in order to compare the compositional formulations with highly contrasted capillary pressures.

1.2 Formulations of compositional liquid gas Darcy flows

The liquid and gas phases denoted respectively by l and g are assumed to be both defined by a mixture of components $i \in \mathcal{C}$ among which the water component denoted by e which can vaporize in the gas phase, and a set of gaseous components $j \in \mathcal{C} \setminus \{e\}$ which can dissolve in the liquid phase. The number of components is assumed to be at least 2.

For the sake of simplicity, the model will be assumed to be isothermal with a fixed temperature T_e , and consequently the dependence of the physical laws on the temperature will not always be specified in the following. We will denote by $c^\alpha = (c_i^\alpha, i \in \mathcal{C})$ the vector of molar fractions of the components in the phase $\alpha = g, l$ with $\sum_{i \in \mathcal{C}} c_i^\alpha = 1$, and by p^g and p^l the two phase pressures. The mass densities of the phases are denoted by $\rho^\alpha(p^\alpha, c^\alpha)$ and the molar densities by $\zeta^\alpha(p^\alpha, c^\alpha)$, $\alpha = g, l$. They are related by

$$\rho^\alpha(p^\alpha, c^\alpha) = \left(\sum_{i \in \mathcal{C}} c_i^\alpha M_i \right) \zeta^\alpha(p^\alpha, c^\alpha),$$

where M_i , $i \in \mathcal{C}$ are the molar masses of the components. The viscosities of the phases are denoted by $\mu^\alpha(p^\alpha, c^\alpha)$, $\alpha = g, l$.

The hydrodynamical Darcy laws are characterized by the relative permeability functions $k_r^\alpha(s^\alpha)$, for both phases $\alpha = g, l$, and by the capillary pressure function $p_c(s^l)$, where $s^\alpha, \alpha = l, g$ denote the saturations of the phases with $s^g + s^l = 1$.

Each component $i \in \mathcal{C}$ will be assumed to be at thermodynamical equilibrium between both phases which is characterized by the equality of its fugacities f_i^α , $\alpha = g, l$ if both phases are present. The fugacities of the components in the gas phase are assumed to be given by Dalton's law for an ideal mixture of perfect gas

$$f_i^g = c_i^g p^g, \quad i \in \mathcal{C}. \quad (1.1)$$

A correction of type $f_i^g = c_i^g p^g \phi(p^g, T_e)$ for more general gas mixtures could also be readily taken into account. The fugacities of the components in the liquid phase are assumed to be given by Henry's law for the dissolution of the gaseous components in the liquid phase

$$f_j^l = c_j^l H_j(T_e), \quad j \in \mathcal{C} \setminus \{e\}, \quad (1.2)$$

and by Raoult-Kelvin's law for the water component in the liquid phase [22]

$$f_e^l = c_e^l p_{sat}(T_e) \exp\left(\frac{-(p^g - p^l)}{\zeta^l(p^l) RT}\right), \quad (1.3)$$

where $p_{sat}(T_e)$ is the vapor pressure of the pure water. It is assumed in the following, in order to prove rigorously the equivalence between the three formulations, that the liquid molar density in f_e^l depends only on the liquid pressure p^l , and possibly on the temperature T_e . It will be denoted by $\zeta^l(p^l)$ in the following.

1.2.1 Natural variable formulation (PSC)

A classical choice coming from the reservoir simulation community [20], [21] is given by the set of unknowns of the hydrodynamical and thermodynamical laws defined by

$$Q, p^l, p^g, s^l, s^g, c^\alpha, \alpha \in Q,$$

where the discrete unknown Q denotes the set of present phases taking the following possible values

$$Q = \{l, g\} \text{ or } \{g\} \text{ or } \{l\}.$$

Then, the model accounts for the mole balance of each component $i \in \mathcal{C}$ with phase velocities given by the Darcy laws and a Fickian diffusion of the components in each phase. It is closed by the pore volume balance $s^g + s^l = 1$, the capillary relation between the two phase pressures, and the thermodynamical equilibrium stating the equality of the fugacities of the present phases. We obtain the following system for the set of unknowns $p^l, p^g, s^l, s^g, c^\alpha, \alpha \in Q$

$$\left\{ \begin{array}{l} \phi \partial_t \sum_{\alpha \in Q} \zeta^\alpha s^\alpha c_i^\alpha + \operatorname{div} \left(\sum_{\alpha \in Q} \zeta^\alpha c_i^\alpha \mathbf{V}^\alpha - \phi s^\alpha \zeta^\alpha D_i^\alpha \nabla c_i^\alpha \right) = 0, \quad i \in \mathcal{C}, \\ p^g - p^l = p_c(s^l), \\ \sum_{\alpha \in Q} s^\alpha = 1, \\ s^\alpha = 0, \quad \alpha \notin Q, \\ \sum_{i \in \mathcal{C}} c_i^\alpha = 1, \quad \alpha \in Q, \\ f_i^l(c^l, p^g, p^l) = f_i^g(c^g, p^g, p^l), \quad i \in \mathcal{C} \text{ if } Q = \{l, g\}, \end{array} \right. \quad (1.4)$$

together with the Darcy laws for the phase velocities

$$\mathbf{V}^\alpha = -\frac{k_r^\alpha(s^\alpha)}{\mu^\alpha} \mathbf{K} \left(\nabla p^\alpha - \rho^\alpha \mathbf{g} \right), \quad \alpha \in Q.$$

The system (1.4) must be closed by an equation for the set of present phases Q which is usually obtained by a negative flash computation [59] at fixed phase pressures p^l, p^g and

fixed component total molar fractions

$$z_i = \frac{\sum_{\alpha \in Q} \zeta^\alpha s^\alpha c_i^\alpha}{\sum_{\alpha \in Q} \zeta^\alpha s^\alpha}, \quad i \in \mathcal{C}.$$

The negative flash computes the gas phase molar fraction $\theta^g \in \mathbb{R}$, possibly negative, and the gas and liquid component molar fractions \bar{c}^g and \bar{c}^l at equilibrium such that

$$\left\{ \begin{array}{l} z_i = \theta^g \bar{c}_i^g + (1 - \theta^g) \bar{c}_i^l, \quad i \in \mathcal{C}, \\ \sum_{i \in \mathcal{C}} \bar{c}_i^\alpha = 1, \quad \alpha = g, l, \\ f_i^l(\bar{c}^l, p^g, p^l) = f_i^g(\bar{c}^g, p^g, p^l), \quad i \in \mathcal{C}, \\ \bar{c}_i^g \geq 0, \quad \bar{c}_i^l \geq 0, \quad i \in \mathcal{C}. \end{array} \right. \quad (1.5)$$

Then, the set of present phases Q is defined by

$$\left\{ \begin{array}{l} Q = \{l, g\} \text{ and } \theta^g \in]0, 1[, \\ \quad \text{or} \\ Q = \{l\} \text{ and } \theta^g \leq 0, \\ \quad \text{or} \\ Q = \{g\} \text{ and } \theta^g \geq 1. \end{array} \right. \quad (1.6)$$

In other words, the negative flash computes the solution \bar{c}^g , \bar{c}^l , θ^g satisfying the thermodynamical equilibrium and the component total mole balance, and the signs of the phase molar fractions θ^g and $\theta^l = 1 - \theta^g$ provide the criteria for the phase appearance or disappearance.

Let us give below a simpler definition of the set Q that will be used to show the equivalence of the natural variable formulation with the two other formulations presented in the next two subsections. For $Q = \{l\}$, let us define the component molar fractions in the gas phase in equilibrium with the component molar fractions in the liquid phase (note that \tilde{c}^g differs in general from \bar{c}^g)

$$\left\{ \begin{array}{l} \tilde{c}_e^g = c_e^l \frac{p_{sat}(T_e)}{p^g} \exp\left(\frac{-(p^g - p^l)}{\zeta^l(p^l)RT}\right), \\ \tilde{c}_j^g = c_j^l \frac{H_j(T_e)}{p^g}, \quad j \in \mathcal{C} \setminus \{e\}, \end{array} \right. \quad (1.7)$$

and, for $Q = \{g\}$, the component molar fractions in the liquid phase in equilibrium with the component molar fractions in the gas phase (note that \tilde{c}^l differs in general from \bar{c}^l)

$$\left\{ \begin{array}{l} \tilde{c}_e^l = c_e^g \frac{p^g}{p_{sat}(T_e)} \exp\left(\frac{(p^g - p^l)}{\zeta^l(p^l)RT}\right), \\ \tilde{c}_j^l = c_j^g \frac{p^g}{H_j(T_e)}, \quad j \in \mathcal{C} \setminus \{e\}. \end{array} \right. \quad (1.8)$$

Then, the coupled system (1.4)-(1.6) is equivalent to the system (1.4) coupled with the

following simpler conditions on the set of present phases Q :

$$\left\{ \begin{array}{l} Q = \{l, g\} \text{ and } s^g > 0, s^l > 0, \\ \text{or} \\ Q = \{l\} \text{ and } \sum_{i \in \mathcal{C}} \bar{c}_i^g \leq 1, \\ \text{or} \\ Q = \{g\} \text{ and } \sum_{i \in \mathcal{C}} \bar{c}_i^l \leq 1. \end{array} \right. \quad (1.9)$$

Proof: Thanks to our assumptions on the fugacities, the negative flash reduces to the following Rachford Rice equation for the molar fraction of the gas phase θ^g (see [59])

$$f^{rc}(\theta^g) = \sum_{i \in \mathcal{C}} (\bar{c}_i^g - \bar{c}_i^l) = \sum_{i \in \mathcal{C}} \frac{(K_i - 1)z_i}{1 + \theta^g(K_i - 1)} = 0,$$

with coefficients

$$K_j = \frac{H_j(T_e)}{p^g}$$

for $j \in \mathcal{C} \setminus \{e\}$ and

$$K_e = \frac{p_{sat}(T_e)}{p^g} \exp\left(\frac{-(p^g - p^l)}{\zeta^l(p^l)RT}\right)$$

depending only on p^l , p^g and T .

Let us define

$$\bar{\mathcal{C}} = \{i \in \mathcal{C} \mid z_i \neq 0, K_i \neq 1\}.$$

If $\bar{\mathcal{C}} = \emptyset$, this is a degenerate case for which both phases cannot be distinguished and hence can be considered as present for both formulations.

If $\bar{\mathcal{C}} \neq \emptyset$, let us define

$$K_{max} = \max_{i \in \bar{\mathcal{C}}} K_i, \quad K_{min} = \min_{i \in \bar{\mathcal{C}}} K_i,$$

and

$$\theta_0 = \frac{1}{1 - K_{max}}, \quad \theta_1 = \frac{1}{1 - K_{min}}.$$

To fix ideas, we will consider the case $\theta_0 < 0$ and $\theta_1 > 1$, the extension to the two other cases $\theta_0 \geq \theta_1 > 1$, or $\theta_1 \leq \theta_0 < 0$ is not difficult. It results that the Rachford Rice function f^{rc} is strictly decreasing and admits a unique solution θ^g such that $\bar{c}_i^\alpha \geq 0$, $i \in \mathcal{C}$, $\alpha = g, l$ on the interval $]\theta_0, \theta_1[$.

In order to prove the equivalence of the system (1.6)-(1.4) with the system (1.9)-(1.4), let us consider the three cases $Q = \{l, g\}$, $Q = \{l\}$, $Q = \{g\}$.

First if $Q = \{l, g\}$, then according to the system (1.4), the equilibrium equations are already satisfied which means that $c^\alpha = \bar{c}^\alpha$ for $\alpha = l, g$ and

$$\theta^g = \frac{\zeta^g s^g}{\sum_{\alpha=l,g} \zeta^\alpha s^\alpha}.$$

It is then clear (assuming a positive total number of moles) that the condition $\theta^g > 0$ and $\theta^l = 1 - \theta^g > 0$ in (1.6) is equivalent to $s^g > 0$ and $s^l > 0$ in (1.9).

Next for $Q = \{l\}$, let us prove that the gas appearance criteria $\theta^g > 0$ in (1.6) is equivalent to the gas appearance criteria $\sum_{i \in \mathcal{C}} \tilde{c}_i^g > 1$ in (1.9). In such a case $z_i = c_i^l$ which implies that

$$f^{rc}(0) = \sum_{i \in \mathcal{C}} \tilde{c}_i^g - 1.$$

Using the monotonicity of f^{rc} and $0 \in]\theta_0, \theta_1[$, it results that the gas appearance criteria $\theta^g > 0$ is equivalent to

$$0 = f^{rc}(\theta^g) < f^{rc}(0) = \sum_{i \in \mathcal{C}} \tilde{c}_i^g - 1.$$

The proof of equivalence for the case $Q = \{g\}$ is similar to the case $Q = \{l\}$.

The system (1.4)-(1.9)-(1.7)-(1.8) is discretized using a fully implicit Euler integration in time and a finite volume discretization in space (see subsection 1.3.3 for the detailed example of the Vertex Approximate Gradient discretization). The mobility terms are upwinded with respect to the sign of the phase Darcy flux, and an harmonic averaging is chosen for the Fick flux terms $\phi s^\alpha \zeta^\alpha$ (see [5],[20],[21]).

The non linear system arising from this discretization is solved at each time step by a Newton Raphson algorithm coupled with a fixed point update of the set of present phases Q in each cell using (1.9)-(1.7)-(1.8). In order to reduce the size of the linear system to $\#\mathcal{C}$ equations and unknowns in each cell, the set of unknowns is splitted into $\#\mathcal{C}$ primary unknowns and remaining secondary unknowns. This splitting is done cell by cell depending on the set of present phases in the cell in such a way that the Schur complement is well defined (see [20],[21],[33]). For our thermodynamical system, to fix ideas let j_1 denote the component with the largest Henry constant H_{j_1} , then our set of primary unknowns is defined by

$$\begin{cases} p^g, s^l, c_i^g, i \in \mathcal{C} \setminus \{j_1, e\} & \text{for } Q = \{l, g\}, \\ p^g, c_i^l, i \in \mathcal{C} \setminus \{e\} & \text{for } Q = \{l\}, \\ p^g, c_i^g, i \in \mathcal{C} \setminus \{e\} & \text{for } Q = \{g\}, \end{cases} \quad (1.10)$$

which guarantees the invertibility of the closure laws w.r.t. the secondary unknowns provided that

$$H_{j_1} \neq p_{sat}(T_e) \exp\left(\frac{-(p^g - p^l)}{\zeta^l(p^l)RT}\right) \quad (\text{for } Q = \{l, g\})$$

which should not physically arise.

The main advantage of this formulation is to use the natural set of unknowns for the hydrodynamical and thermodynamical laws and to extend to a large class of compositional Darcy flow models ranging from immiscibility to full miscibility (see [33]). On the other hand, its main drawbacks are an additional complexity to deal with sets of unknowns and equations depending on the set Q , and the use of a fixed point algorithm to compute

the set of present phases \mathcal{Q} at each point of the space time domain. The efficiency of this formulation has mainly been shown for reservoir simulation test cases with complex thermodynamics, two and tri phase Darcy flows, but with usually small capillary effects and the use of a reference pressure in the thermodynamical state laws rather than the phase pressures. In the next section it will be assessed and compared with the two other formulations on test cases with both strong or weak capillary effects.

1.2.2 Pressures, saturations and fugacities formulation (PSF)

We recall in this subsection the formulation introduced in [45] using a fix set of unknowns defined by the phase pressures p^l , p^g , the phase saturations s^l , s^g , and the component fugacities $f = (f_i, i \in \mathcal{C})$. The component molar fractions c^α of each phase $\alpha = l, g$ are assumed to be defined as the unique solution denoted by $\tilde{c}^\alpha(p^g, p^l, f)$ of the system

$$f_i^\alpha(c^\alpha, p^g, p^l) = f_i, i \in \mathcal{C}. \quad (1.11)$$

If the phase α is present, ie $s^\alpha > 0$, the function $\tilde{c}^\alpha(p^g, p^l, f)$ will match with the component molar fractions c^α . If the phase is absent, the function $\tilde{c}^\alpha(p^g, p^l, f)$ will match with the extension of the component molar fractions by those in equilibrium with the component molar fractions in the present phase as in (1.7) and (1.8). This extension is clearly arbitrary for the conservation equations since the component molar fractions are always in factor of the saturation or the relative permeability of the phase both vanishing for an absent phase. On the other hand, the choice of this extension will affect the convergence of the non linear solver to the solution. In our case, thanks to our assumptions on the fugacities, we simply have the following expressions of the extended component molar fractions:

$$\begin{cases} \tilde{c}_e^l(p^g, p^l, f) = \frac{f_e}{p_{sat}(T_e)} \exp\left(\frac{(p^g - p^l)}{\zeta^l(p^l)RT}\right), \\ \tilde{c}_j^l(p^g, p^l, f) = \frac{f_j}{H_j(T_e)}, j \in \mathcal{C} \setminus \{e\}, \\ \tilde{c}_e^g(p^g, p^l, f) = \frac{f_e}{p^g}, \\ \tilde{c}_j^g(p^g, p^l, f) = \frac{f_j}{p^g}, j \in \mathcal{C} \setminus \{e\}. \end{cases} \quad (1.12)$$

Note that the PSF formulation can be defined for more general fugacity models provided that the equations $f = f^\alpha(c^\alpha, p^g, p^l)$ can be inverted for both phases $\alpha = g, l$. Finally, the

set of equations obtained in [45] for the set of unknowns p^l, p^g, s^l, s^g, f is defined by

$$\left\{ \begin{array}{l} \phi \partial_t \sum_{\alpha=g,l} \zeta^\alpha s^\alpha \tilde{c}_i^\alpha + \text{div} \left(\sum_{\alpha=g,l} \zeta^\alpha \tilde{c}_i^\alpha \mathbf{V}^\alpha - \phi s^\alpha \zeta^\alpha D_i^\alpha \nabla \tilde{c}_i^\alpha \right) = 0, i \in \mathcal{C}, \\ s^g + s^l = 1, \\ p^g - p^l = p_c(s^l), \\ \left(1 - \sum_{i \in \mathcal{C}} \tilde{c}_i^l \right) s^l = 0, 1 - \sum_{i \in \mathcal{C}} \tilde{c}_i^l \geq 0, s^l \geq 0, \\ \left(1 - \sum_{i \in \mathcal{C}} \tilde{c}_i^g \right) s^g = 0, 1 - \sum_{i \in \mathcal{C}} \tilde{c}_i^g \geq 0, s^g \geq 0, \end{array} \right. \quad (1.13)$$

with the Darcy phase velocities

$$\mathbf{V}^\alpha = - \frac{k_r^\alpha(s^\alpha)}{\mu^\alpha} \mathbf{K} \left(\nabla p^\alpha - \rho^\alpha \mathbf{g} \right), \alpha = g, l.$$

Its equivalence with the previous formulation is readily obtained in view of (1.7), (1.8) and (1.9), and setting $c^\alpha = \tilde{c}^\alpha$ if $s^\alpha > 0$, $\alpha = g, l$.

The space and time discretization is the same as for the previous formulation, and the non linear system arising at each time step is solved by a semi-smooth Newton algorithm (Newton-Min) adapted to complementary constraints (see [44], [38]). This is one advantage of this formulation to fit into the semi-smooth Newton framework. The other advantage is to lead to a fix set of unknowns and equations. Nevertheless, the choice of the secondary unknowns to be eliminated from the linearized system using the closure laws is also as above dependent on the set of present phases. For our thermodynamical system, as for the PSC formulation, let j_1 denote the component with the largest Henry constant H_{j_1} , then our set of primary unknowns is defined by

$$\left\{ \begin{array}{ll} p^g, s^l, f_i, i \in \mathcal{C} \setminus \{j_1, e\} & \text{if } s^l > 0 \text{ and } s^g > 0, \\ p^g, f_i, i \in \mathcal{C} \setminus \{e\} & \text{if } s^l = 0 \text{ or } s^g = 0, \end{array} \right. \quad (1.14)$$

which again guarantees the invertibility of the closure laws w.r.t. the secondary unknowns provided that

$$H_{j_1} \neq p_{sat}(T_e) \exp \left(\frac{-(p^g - p^l)}{\zeta^l(p^l) RT} \right)$$

The next formulation goes a step further since it eliminates all the inequality constraints, and leads to a fix choice of the secondary unknowns in the linear systems.

1.2.3 Pressures, and fugacities formulation (PPF)

The aim of the following formulation is to avoid any inequalities in the set of equations while taking into account phase transitions. This has been achieved in [4] for a liquid gas two components model taking into account the dissolution of the gaseous components in the liquid phase. We propose below an extension of this formulation to compositional two phase flows with an arbitrary number of components.

The starting point is the formulation (1.13) of the previous section based on the definition of the extended component molar fractions $\tilde{c}^\alpha(p^g, p^l, f)$, $\alpha = l, g$ (1.12). The next step is to extend the definition of the phase pressures denoted by \tilde{p}^α in the absence of the phase writing that

$$\sum_{i \in \mathcal{C}} \tilde{c}_i^\alpha(\tilde{p}^g, \tilde{p}^l, f) = 1, \alpha = g, l.$$

This definition clearly matches with the phase pressure p^α if the phase α is present and defines an extension of the phase pressure if the phase is absent.

To deal with phase appearance and disappearance, one extends the graph of the capillary pressure curve by its monotone graph ie by

$$s^l = 1, p_c \in [p_c(1), -\infty[$$

to deal with the single phase liquid - two phase gas liquid transition, and by

$$s^l = 0, p_c \in [p_c(0), +\infty[$$

to deal with the single phase gas - two phase gas liquid transition. We will denote by \tilde{p}_c the resulting monotone graph and its inverse by \mathcal{S}^l . Then, the equation

$$s^l = \mathcal{S}^l(\tilde{p}^g - \tilde{p}^l), \quad (1.15)$$

together with the definition of the extended pressures suffice to account for the phase transitions. More specifically, we will show that the system

$$\left\{ \begin{array}{l} s^g + s^l = 1, \\ p^g - p^l = p_c(s^l), \\ \left(\sum_{i \in \mathcal{C}} \tilde{c}_i^\alpha(p^g, p^l, f) - 1 \right) s^\alpha = 0, \alpha = l, g, \\ \sum_{i \in \mathcal{C}} \tilde{c}_i^\alpha(p^g, p^l, f) \leq 1, \alpha = l, g, \\ s^\alpha \geq 0, \alpha = l, g, \end{array} \right. \quad (1.16)$$

and the system

$$\left\{ \begin{array}{l} s^g + s^l = 1, \\ s^l = \mathcal{S}^l(\tilde{p}^g - \tilde{p}^l), \\ \sum_{i \in \mathcal{C}} \tilde{c}_i^\alpha(\tilde{p}^g, \tilde{p}^l, \tilde{f}) = 1, \alpha = l, g, \end{array} \right. \quad (1.17)$$

lead to equivalent conditions on the physical unknowns defined by both saturations s^g , s^l , the pressures $p^\alpha = \tilde{p}^\alpha$ and the molar fractions

$$c^\alpha = \tilde{c}^\alpha(\tilde{p}^g, \tilde{p}^l, \tilde{f}) = \tilde{c}^\alpha(p^g, p^l, f)$$

for the present phases $\alpha = l, g$ such that $s^\alpha > 0$. This definition also specifies the correspondance between the component fugacities f and \tilde{f} in the sense that

$$f = f^\alpha(c^\alpha, p^g, p^l)$$

and

$$\tilde{f} = f^\alpha(c^\alpha, \tilde{p}^g, \tilde{p}^l)$$

for all $\alpha = l, g$ such that $s^\alpha > 0$.

Proof: For both systems, the saturations are such that $s^g + s^l = 1$ and $s^g \geq 0, s^l \geq 0$. Hence we will consider the three cases corresponding to (i) $s^l > 0$ and $s^g = 1 - s^l > 0$, to (ii) $s^l = 1$ and $s^g = 0$, and to (iii) $s^l = 0$ and $s^g = 1$.

- (i) if both phases are present ie $s^l > 0$ and $s^g = 1 - s^l > 0$, then $p^l = \tilde{p}^l, p^g = \tilde{p}^g, f = \tilde{f}$, and the equivalence of the conditions on the physical unknowns for both systems is clear.
- (ii) If the gas phase is absent ie $s^l = 1, s^g = 0$, the physical unknowns are defined by the pressure $p^l = \tilde{p}^l$, and the liquid molar fractions $c^l = \tilde{c}^l(\tilde{p}^g, p^l, \tilde{f}) = \tilde{c}^l(p^g, p^l, f)$ such that $\sum_{i \in \mathcal{C}} c_i^l = 1$. In other words, given p^l and c^l such that $\sum_{i \in \mathcal{C}} c_i^l = 1$, we need to prove that the condition on c^l, p^l

$$\sum_{i \in \mathcal{C}} \tilde{c}_i^g(p^g, p^l, f) \leq 1,$$

with $p^g = p^l + p_c(1)$ and $f = f^l(c^l, p^g, p^l)$, is equivalent to the condition

$$\mathcal{S}^l(\tilde{p}^g - p^l) = 1,$$

with \tilde{p}^g and \tilde{f} such that $\sum_{i \in \mathcal{C}} \tilde{c}_i^g(\tilde{p}^g, p^l, \tilde{f}) = 1, \tilde{f} = f^l(c^l, \tilde{p}^g, p^l)$. The inequality $\sum_{i \in \mathcal{C}} \tilde{c}_i^g(p^g, p^l, f) \leq 1$ is equivalent to

$$\sum_{i \in \mathcal{C}} \tilde{c}_i^g(p^g, p^l, f^l(c^l, p^g, p^l)) \leq 1 = \sum_{i \in \mathcal{C}} \tilde{c}_i^g(\tilde{p}^g, p^l, f^l(c^l, \tilde{p}^g, p^l)).$$

It is easy to check in our case that the function

$$g^{gl}(u) = \sum_{i \in \mathcal{C}} \tilde{c}_i^g(u, p^l, f^l(c^l, u, p^l))$$

is non increasing. Hence the latter inequality is equivalent to

$$\tilde{p}^g \leq p^g = p^l + p_c(1),$$

and hence to $1 = \mathcal{S}^l(\tilde{p}^g - p^l)$.

- (iii) If the liquid phase is absent ie $s^l = 0$, $s^g = 1$, the physical unknowns are defined by the pressure $p^g = \tilde{p}^g$, and the gas molar fractions $c^g = \tilde{c}^g(p^g, \tilde{p}^l, \tilde{f}) = \tilde{c}^g(p^g, p^l, f)$ such that $\sum_{i \in \mathcal{C}} c_i^g = 1$. In other words, given p^g and c^g such that $\sum_{i \in \mathcal{C}} c_i^g = 1$, we need to prove that the condition on c^g, p^g

$$\sum_{i \in \mathcal{C}} \tilde{c}_i^l(p^g, p^l, f) \leq 1,$$

with $p^l = p^g - p_c(0)$ and $f = f^g(c^g, p^g, p^l)$, is equivalent to the condition

$$\mathcal{S}^l(p^g - \tilde{p}^l) = 0,$$

with \tilde{p}^l and \tilde{f} such that $\sum_{i \in \mathcal{C}} \tilde{c}_i^l(p^g, \tilde{p}^l, \tilde{f}) = 1$, $\tilde{f} = f^g(c^g, p^g, \tilde{p}^l)$. The inequality $\sum_{i \in \mathcal{C}} \tilde{c}_i^l(p^g, p^l, f) \leq 1$ is equivalent to

$$\sum_{i \in \mathcal{C}} \tilde{c}_i^l(p^g, p^l, f^g(c^g, p^g, p^l)) \leq 1 = \sum_{i \in \mathcal{C}} \tilde{c}_i^l(p^g, \tilde{p}^l, f^g(c^g, p^g, \tilde{p}^l)).$$

It is easy to check in our case that the function

$$g^{lg}(u) = \sum_{i \in \mathcal{C}} \tilde{c}_i^l(p^g, u, f^g(c^g, p^g, u))$$

is non increasing (the molar density of the liquid phase is non decreasing w.r.t. the liquid pressure). Hence the latter inequality is equivalent to

$$p^g - p_c(0) = p^l \geq \tilde{p}^l,$$

ie to $0 = \mathcal{S}^l(p^g - \tilde{p}^l)$.

Finally we obtain the following system of equations for the set of unknowns $\tilde{p}^g, \tilde{p}^l, f$

$$\left\{ \begin{array}{l} \phi \partial_t \sum_{\alpha=g,l} \zeta^\alpha s^\alpha \tilde{c}_i^\alpha + \operatorname{div} \left(\sum_{\alpha=g,l} \zeta^\alpha \tilde{c}_i^\alpha \mathbf{V}^\alpha - \phi s^\alpha \zeta^\alpha D_i^\alpha \nabla \tilde{c}_i^\alpha \right) = 0, \quad i \in \mathcal{C}, \\ \sum_{i \in \mathcal{C}} \tilde{c}_i^g(\tilde{p}^g, \tilde{p}^l, f) = 1, \\ \sum_{i \in \mathcal{C}} \tilde{c}_i^l(\tilde{p}^g, \tilde{p}^l, f) = 1, \end{array} \right. \quad (1.18)$$

where

$$\left\{ \begin{array}{l} \mathbf{V}^\alpha = -\frac{k_r^\alpha(s^\alpha)}{\mu^\alpha} \mathbf{K}(\nabla \tilde{p}^\alpha - \rho^\alpha \mathbf{g}), \quad \alpha = g, l, \\ s^g + s^l = 1, \\ s^l = \mathcal{S}^l(\tilde{p}^g - \tilde{p}^l). \end{array} \right. \quad (1.19)$$

The same discretization will be used for this formulation as for the previous ones. The two main advantages of this formulation are the absence of inequality constraints to express the phase transitions, and the fix set of unknowns and equations. In addition even the choice of the secondary unknowns can be fixed, choosing two fixed fugacities (for instance f_e and f_{j_1} with the largest Henry constant $H_{j_1}(T_e)$ provided that the condition

$$H_{j_1} \neq p_{sat}(T_e) \exp\left(\frac{-(p^g - p^l)}{\zeta^l(p^l)RT}\right)$$

is satisfied). This means that a classical Newton Raphson algorithm can be used with also a simplified computation of the Jacobian. On the other hand this formulation also increases the non linearities due to the composition of functions which might increase the stiffness of the non linear systems.

1.3 Numerical comparison of the three formulations

In this section, the PSC, PSF and PPF formulations are compared in terms of solution and of non linear convergence on 1D and 3D test cases. In all test cases, a sub-relaxation of the Newton type solver is used. The relaxation parameter is computed at each Newton iteration by prescribing a maximum variation of the saturation for the PSF and the PSC formulations while a maximum variation of the capillary pressure is prescribed for the PPF formulation.

Note that the norm of the residual is computed as the sum over all components of the l^1 norm of each component mole balance equation residual. The non linear convergence criteria is prescribed on the relative norm of the residual defined by the ratio of the residual norm by the initial residual norm.

1.3.1 One dimensional test cases

Drying by suction

This test case proposed by Andra [50] models the drying of geological radioactive waste disposal at the interface between the ventilation gallery and the porous media initially saturated with pure water. We consider an horizontal one dimensional domain $(0, L)$, with $L = 10$ m, representing the storage in the neighbourhood of the gallery located at the right end $x = L$. The temperature is fixed at $T_e = 300$ K for the sake of simplicity. The rock is considered to be the Callovo-Oxfordian argillites (COx) of homogeneous porosity $\phi = 0.15$ and permeability $\mathbf{K} = 5 \cdot 10^{-20}$ m². The relative permeabilities of the liquid and gas phases, and the inverse of the capillary pressure are defined by the following Van Genuchten laws

$$k_r^l(s^l) = \begin{cases} 0 & \text{if } s^l < s_r^l, \\ 1 & \text{if } s^l > 1 - s_r^g, \\ \sqrt{s^l} \left(1 - (1 - (s^l)^{1/m})^m\right)^2 & \text{if } s_r^l \leq s^l \leq 1 - s_r^g, \end{cases} \quad (1.20)$$

$$k_r^g(s^g) = \begin{cases} 0 & \text{if } s^g < s_r^g, \\ 1 & \text{if } s^g > 1 - s_r^l, \\ \sqrt{1 - \bar{s}^l} \left(1 - (\bar{s}^l)^{1/m}\right)^{2m} & \text{if } s_r^g \leq s^g \leq 1 - s_r^l, \end{cases} \quad (1.21)$$

and

$$\mathcal{S}^l(p_c) = s_r^l + (1 - s_r^l - s_r^g) \frac{1}{\left(1 + \left(\frac{p_c}{P_r}\right)^n\right)^m}, \quad (1.22)$$

$$p_c(s^l) = P_r \left((\bar{s}^l)^{-\frac{1}{m}} - 1 \right)^{\frac{1}{n}}, \quad (1.23)$$

with

$$\bar{s}^l = \frac{s^l - s_r^l}{1 - s_r^l - s_r^g},$$

and the parameters $n = 1.49$, $m = 1 - \frac{1}{n}$, the residual liquid and gas saturations $s_r^l = 0.40$, $s_r^g = 0$, and $P_r = 15 \cdot 10^6$ Pa (see Figure 1.1).

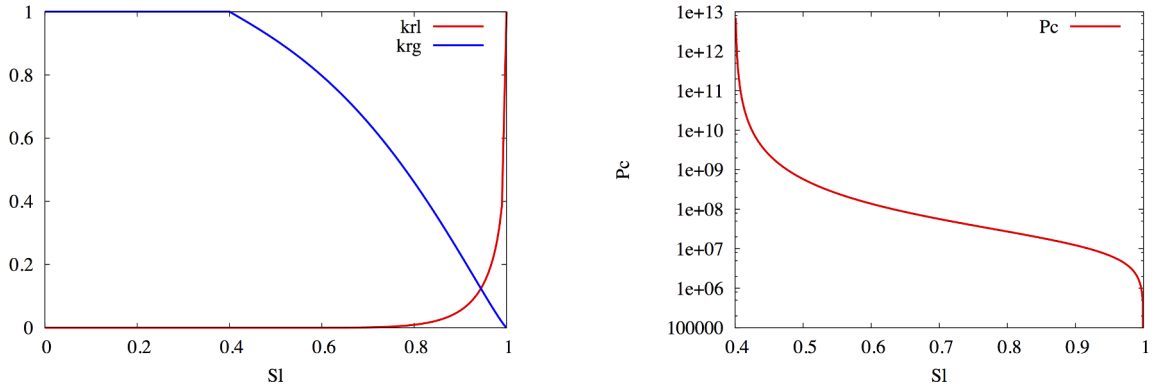


Figure 1.1: Left: relative permeabilities of the gas and liquid phase k_r^α , $\alpha = g, l$ function of the liquid saturation s^l . Right: capillary pressure p_c (in Pa) function of s^l .

The liquid and gas phases are modeled as mixtures of two components water denoted by e and air denoted by a . Their thermodynamical laws are defined by the constant liquid molar density $\zeta^l = 1000/0.018 \text{ mol.m}^{-3}$, the perfect gas molar density $\zeta^g = \frac{p^g}{RT_e}$, with $R = 8.314 \text{ J.K}^{-1}.\text{mol}^{-1}$, and the constant liquid and gas viscosities $\mu^l = 10^{-3} \text{ Pa.s}$, and $\mu^g = 18.51 \cdot 10^{-6} \text{ Pa.s}$. The vapor pressure is defined by the correlation

$$p_{sat}(T_e) = 1.013 \cdot 10^5 e^{\frac{13.7 - 5120}{T_e}} \text{ in Pa}, \quad (1.24)$$

and the Henry constant of the air component is set to $H_a = 6.467 \cdot 10^9 \text{ Pa}$. The Fick diffusion coefficients are fixed to $D_e^g = D_a^g = 10^{-7} \text{ m}^2.\text{s}^{-1}$, and $D_e^l = D_a^l = 3 \cdot 10^{-9} \text{ m}^2.\text{s}^{-1}$.

The initial and left end conditions are defined by a liquid phase $s^l = 1$ composed of pure water $c_e^l = 1$, $c_a^l = 0$ at the pressure $p^l = p_0^l = 40 \cdot 10^5$ Pa.

At the interface with the gallery, the gas is defined by its pressure $p^g = p_L^g = 10^5$ Pa, its temperature T_e , and its relative humidity

$$H_r = \frac{c_e^g p_L^g}{p_{sat}(T_e)} = 0.5.$$

It results that the gas molar composition is given by

$$c_e^g = \frac{H_r p_{sat}(T_e)}{p_L^g}, \quad c_a^g = 1 - c_e^g.$$

Assuming that the liquid phase is present at the interface, we deduce from the thermodynamical equilibrium that

$$p_L^l = p_L^g - \zeta^l R T_e \ln\left(\frac{1 - c_a^g p_L^g / H_a(T_e)}{H_r}\right)$$

and

$$s_L^l = \mathcal{S}^l(p_L^g - p_L^l) > s_r^l.$$

Since the solution exhibits a steep liquid pressure gradient at the right end, the mesh will be locally refined around $x = L$ using the following family of meshes. Let

$$\Delta x_r < L, \quad r > 1, \quad \Delta x_l < \Delta x_r < L$$

be given parameters for the definition of the mesh. Numbering the cells from right to left, the first cell $[x_1, L]$ is of size $\Delta x_1 = \Delta x_r$, with left end $x_1 = L - \Delta x_1$, and we set for the cell $[x_{i+1}, x_i]$,

$$\Delta x_{i+1} = r \Delta x_i, \quad x_{i+1} = x_i - \Delta x_{i+1}.$$

Let N_1 be the last index i such that $\Delta x_i > \Delta x_l$ and $x_i > 0$, we set

$$N_2 = \left\lceil \frac{x_{N_1}}{\Delta x_l} \right\rceil, \quad N = N_1 + N_2,$$

and $\Delta x_i = \frac{L - x_{N_1}}{N_2}$ for $i = N_1 + 1, \dots, N$.

In the following numerical experiments we will consider the 5 following meshes

$$\begin{array}{llll} N = 27 & \text{with} & r = 2, & \Delta x_r = 10^{-3}, \quad \Delta x_l = 0.5, \\ N = 60 & \text{with} & r = 1.4, & \Delta x_r = 10^{-4}, \quad \Delta x_l = 0.5/2, \\ N = 126 & \text{with} & r = 1.2, & \Delta x_r = 10^{-5}, \quad \Delta x_l = 0.5/4, \\ N = 265 & \text{with} & r = 1.1, & \Delta x_r = 10^{-6}, \quad \Delta x_l = 0.5/8, \\ N = 559 & \text{with} & r = 1.05, & \Delta x_r = 10^{-7}, \quad \Delta x_l = 0.5/16. \end{array} \quad (1.25)$$

The simulation is run over the time interval $(0, T)$ with $T = 10$ years, an initial time step of 1 hour, and a maximum time step of 30 days.

Figure 1.2 exhibits the gas saturation, and the extended gas and liquid pressures \tilde{p}^g , \tilde{p}^l at different times obtained with the mesh $N = 559$ and the PPF formulation. A zoom at the right end is exhibited in Figure 1.3 showing the steep gradient of the liquid and gas pressures at a scale of say 0.1 mm which justifies the use of the exponentially refined meshes. Figure 1.4 exhibits the extended air molar fraction in the gas phase \tilde{c}_a^g at final time with and without Fickian diffusion for the liquid and gas phases. In view of the position of the gas front at time $t = 10$ years exhibited Figure 1.2 in blue located at roughly $x = 5.3$ m, and of the position of the air front (pink curve) without diffusion, we clearly deduce that the gas appear by vaporization of the water first. This is confirmed if the diffusion is added in the liquid phase only (blue curve). In that case, the air component diffuses in the liquid phase and the vaporization of the liquid makes it appear in the gas phase. With the diffusion in the gas phase only, the position of the air front (red curve) matches with the position of the gas front showing the dominant diffusion compared with the Darcy convection. The green curve exhibits the case with diffusion in both phases. In that case the air is diffused in the liquid phase and the extended air molar fraction in the gas phase at equilibrium with the liquid phase is non zero.

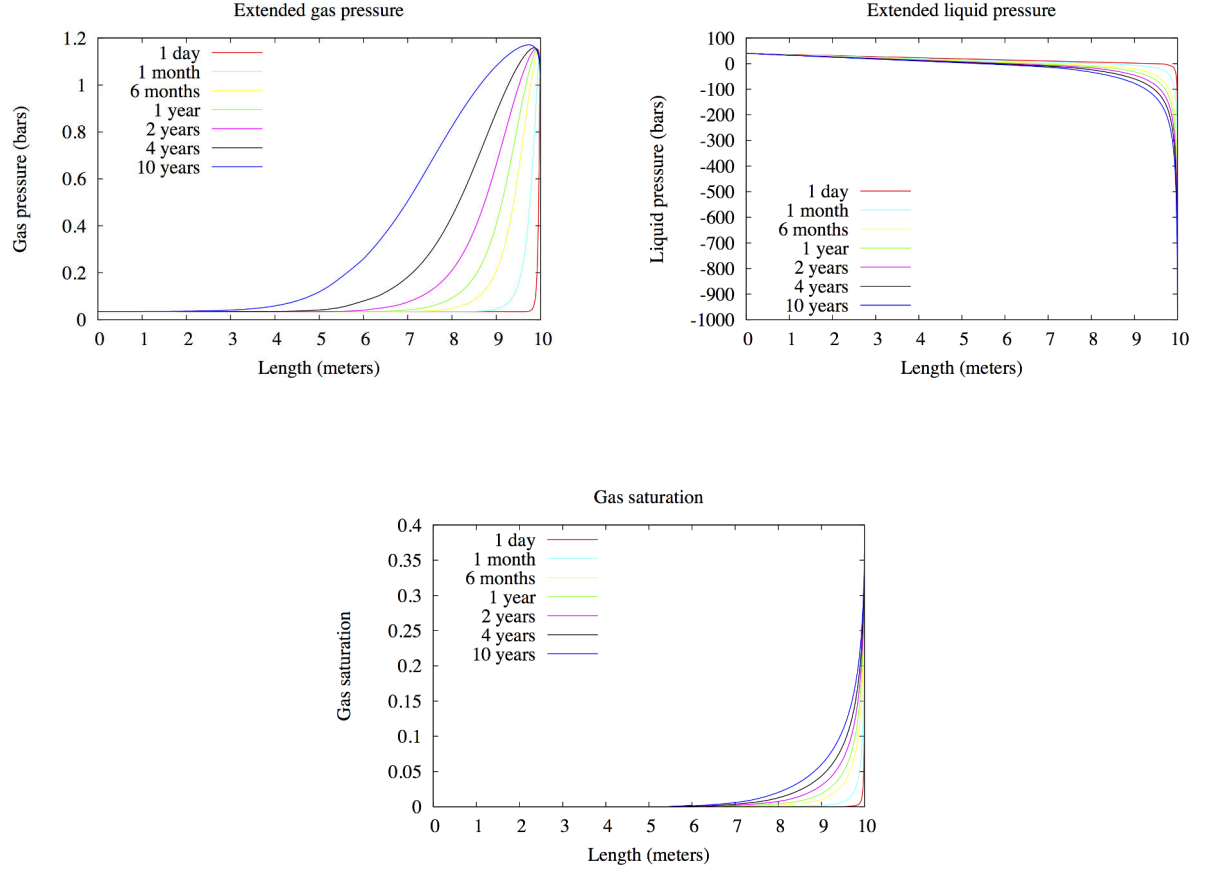


Figure 1.2: Gas saturation, and extended gas and liquid pressures \tilde{p}^g , \tilde{p}^l at times $t = 1$ day, 1 month, 6 months, 1 year, 2 years, 4 years, and 10 years obtained with the mesh $N = 559$ and the PPF formulation.

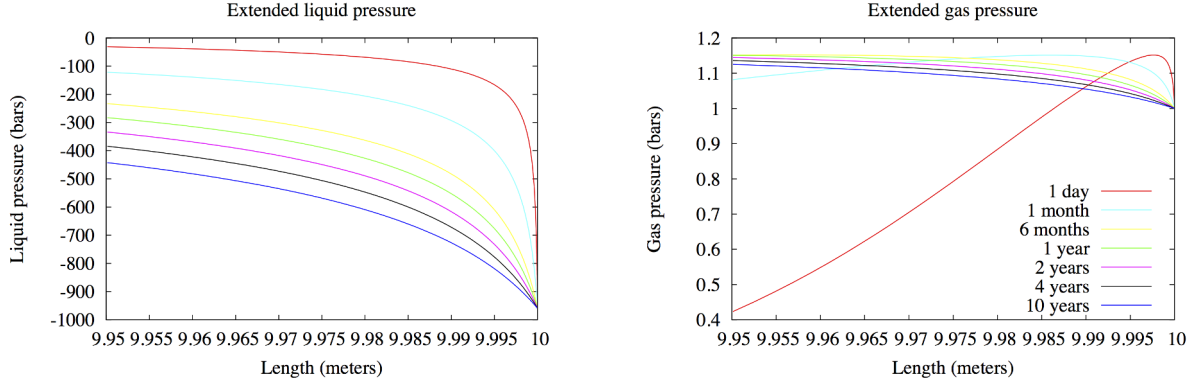


Figure 1.3: Extended gas and liquid pressures \tilde{p}^g , \tilde{p}^l at the gallery boundary at times $t = 1$ day, 1 month, 6 months, 1 year, 2 years, 4 years, and 10 years obtained with the mesh $N = 559$ and the PPF formulation.

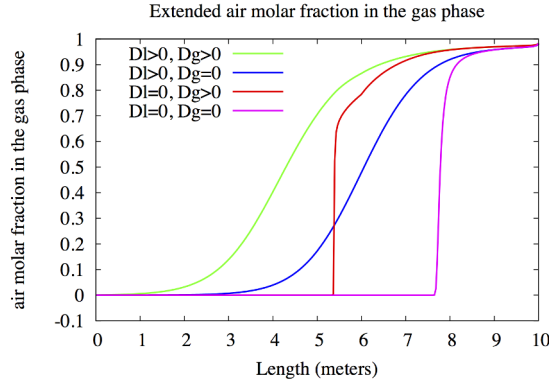


Figure 1.4: Extended air molar fraction in the gas phase \tilde{c}_a^g in the four cases (i) $D^l = D^g = 0 \text{ m}^2.\text{s}^{-1}$; (ii) $D^l = 0 \text{ m}^2.\text{s}^{-1}$, $D^g = 10^{-7} \text{ m}^2.\text{s}^{-1}$; (iii) $D^l = 3 \cdot 10^{-9} \text{ m}^2.\text{s}^{-1}$, $D^g = 10^{-7} \text{ m}^2.\text{s}^{-1}$; (iv) $D^l = 3 \cdot 10^{-9} \text{ m}^2.\text{s}^{-1}$, $D^g = 0 \text{ m}^2.\text{s}^{-1}$ at time $t = 10$ years obtained with the mesh $N = 559$ and the PPF formulation.

At the interfaces between two phase and single phase regions, differences could appear especially on coarse meshes between the discrete solutions of the PPF formulation and of the PSC and PSF formulations due to the extension of the pressure \tilde{p}^α in the absence of the phase α used in the PPF formulation. To check this, the solutions obtained with the three formulations are compared on the coarse mesh $N = 27$ in Figure 1.5. The three

solutions are almost the same, and we have checked that the slight differences are due to the regularization of the Van Genuchten capillary pressure for the formulations PSF and PSC to avoid an infinite derivative at $s^l = 1$. This regularization uses a continuous linear extension for $s^l > 1 - \epsilon$ with $\epsilon = 0.005$. It is not required for the PPF formulation since it only uses the inverse of the capillary pressure function.

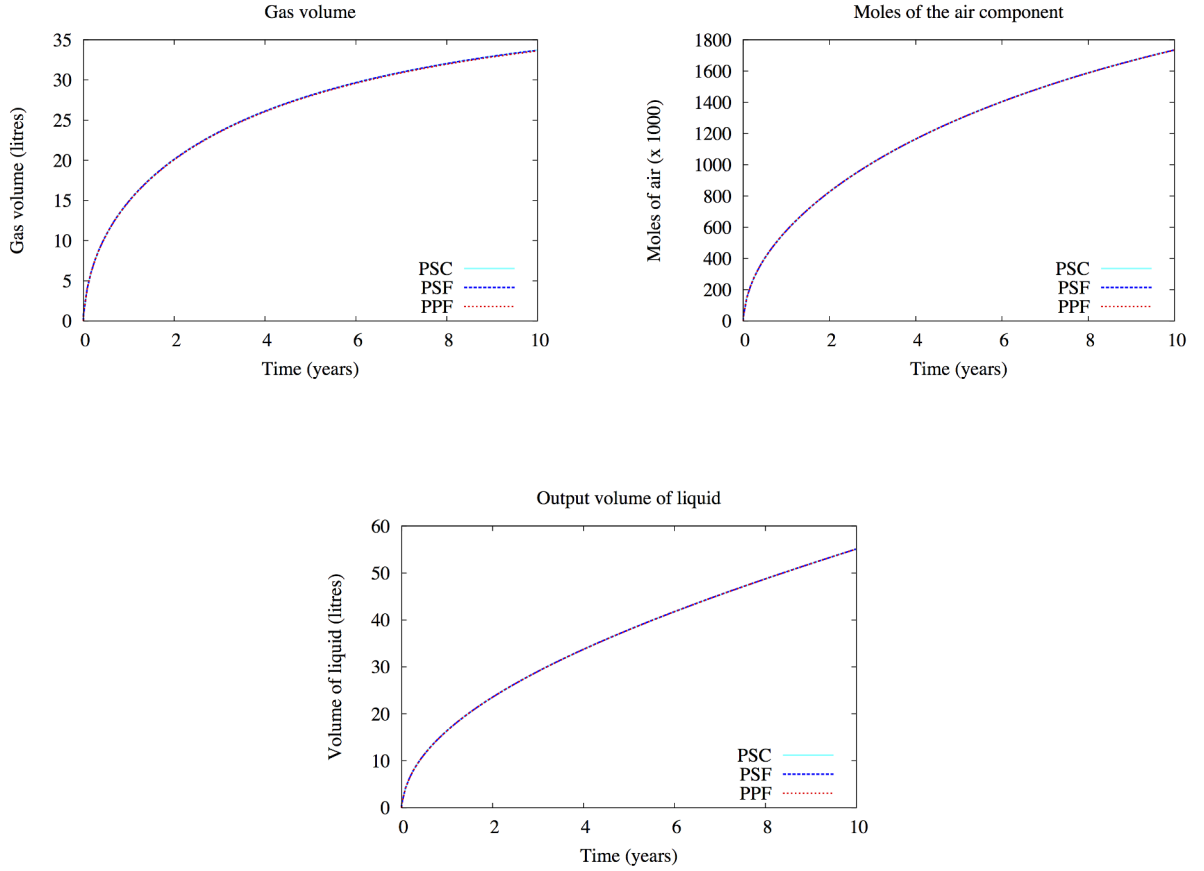


Figure 1.5: Comparison of the gas volume, the number of moles of the air component, and the output volume of liquid at time $t = 10$ years obtained with the mesh $N = 27$ and the three formulations PPF, PSF and PSC.

Convergence to a stationary analytical solution: a stationary solution can be computed for this test case assuming no dissolution of the gaseous component a , and no Fickian diffusion. This solution is defined by

$$p^l(x) = \begin{cases} p_L^g + \frac{x-x_I}{x_I}(p_L^g - p_0^l), & x \in [0, x_I], \\ p_L^g - \psi^{-1}\left(\frac{x_I-x}{x_I}(p_L^g - p_0^l)\right), & x \in]x_I, L], \end{cases}$$

$$\tilde{p}^g(x) = \begin{cases} p^l(x) & x \in [0, x_I], \\ p_L^g, & x \in]x_I, L], \end{cases}$$

and

$$\tilde{c}_e^g(x) = \frac{p_{sat}(T_e)}{\tilde{p}^g(x)} e^{-\frac{\tilde{p}^g(x) - p^l(x)}{\zeta^l R T_e}}, \quad \tilde{c}_a^g(x) = 1 - \tilde{c}_e^g(x),$$

where the position of the stationary gas front is given by

$$x_I = \frac{(p_0^l - p_L^g)L}{p_0^l - p_L^g + \psi(p_{c,L})},$$

with

$$p_{c,L} = -\zeta^l R T_e \log(H_r),$$

and

$$\psi(u) = \int_0^u k_r^l(\mathcal{S}^l(u)) du.$$

This solution has been used to test the numerical convergence of the discrete solutions obtained by the 3 formulations, and no significant differences have been observed between the three formulations. Hence the results are exhibited in Figure 1.6 for the PPF formulation only showing the spatial convergence of the finite volume scheme.

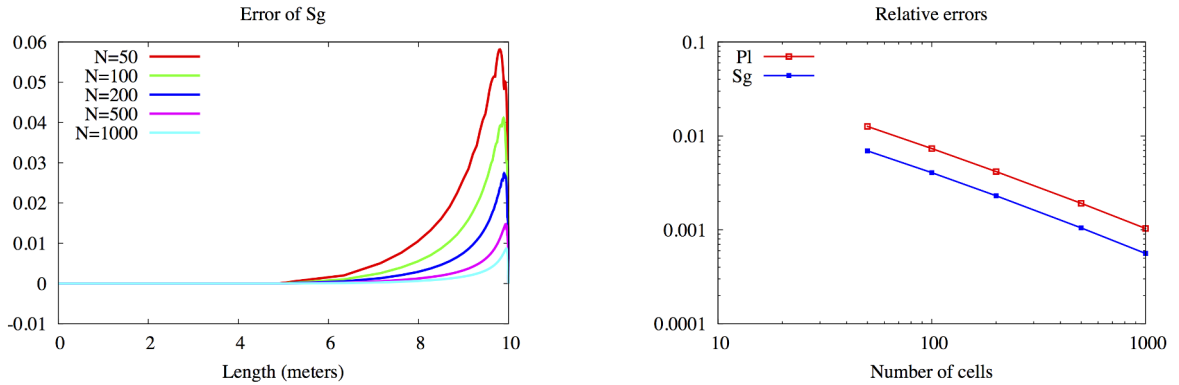


Figure 1.6: Convergence of the discrete gas saturation s^g and liquid pressure p^l obtained at large times to the stationary analytical solutions for the family of uniform meshes $N = 50, 100, 200, 500, 1000$ and the PPF formulation. The results obtained with the two other formulations are the same.

Comparison of Newton convergence: the three formulations are compared in Table 1.1 for all meshes in terms of number of time steps, of time step chops, and total number of Newton iterations. The stopping criteria for the Newton algorithm is chosen as before to be the relative norm of the residual of both mole balance equations to obtain the same

criteria for all formulations, and is set to 10^{-7} . Note that a special treatment of the initial guess for the Newton algorithm at initial time had to be used for all formulations in order to obtain the convergence of the first time step. This is due to the incompressibility of the liquid pressure and to the boundary condition at the porous media gallery interface exhibiting a large negative value of the liquid pressure. Basically the initial guess must anticipate the gas appearance at the right boundary.

N	PPF	PSF	PSC
27	132/0/344	132/0/316	132/0/319
60	132/0/355	132/0/329	132/0/335
126	132/0/361	132/0/354	132/0/371
265	132/0/408	132/0/433	132/0/404
559	132/0/435	132/0/496	132/0/567

Table 1.1: Number of time steps, of time step chops, and total number of Newton iterations for the three formulations PPF, PSF and PSC and for each mesh.

From Table 1.1, it is clear that the three formulations have roughly the same efficiency in terms of Newton convergence except for the finest mesh for which the PPF formulation is clearly better than the PSC formulation, and slightly better than the PSF formulation. Note that the same behaviour has been observed for increased time steps, as well as without Fickian diffusion, as well as for modified values of the n parameter of the Van-Genuchten laws.

Drying by gas injection

In order to further compare the three formulations, we consider a test case including gas appearance and liquid disappearance by injection of a dry gas at the right boundary with an imposed gas pressure $p^g = 50 \cdot 10^5$ Pa.

The porous media is the horizontal one dimensional domain $(0, L)$, with $L = 1000$ m of homogeneous porosity $\phi = 0.15$, and permeability $\mathbf{K} = 10^{-12}$ m². The temperature is fixed to $T_e = 360$ K.

The relative permeabilities and the capillary pressure are again given by the Van Genuchten laws (1.20), (1.21), (1.22) with parameters $n = 4$, $s_r^l = 0.4$, $s_r^g = 0$, and $P_r = 10^5$ Pa. The capillary pressure is extended linearly to $s^l = 0$ between $(s^l, p_c) = (\mathcal{S}^l(p_{c,0}), p_{c,0})$ and $(s^l, p_c) = (0, 2 p_{c,0})$ with $p_{c,0} = 4P_r$ to account for the liquid disappearance.

The liquid and gas phases are still modeled as mixtures of water and air components with the same molar densities, viscosities, and vapor pressure as in the previous test case. The Henry constant for the air component is here fixed to $H_a = 10^8$ Pa, and the Fick diffusion can be neglected compared with the Darcy convection.

The initial and left end conditions are defined by a pure water liquid phase $s^l = 1$ of composition $c_e^l = 1$, $c_a^l = 0$ and pressure $p^l = 40 \cdot 10^5$ Pa. At the right end, the gas

phase $s^g = 1$ is injected with the composition $c_e^g = 5 \cdot 10^{-4}$, $c_a^g = 1 - c_e^g$ and the pressure $p^g = 50 \cdot 10^5$ Pa.

The mesh is uniform with the number of cells denoted by N , and the simulation is run over the time interval $(0, T)$ with $T = 40$ years, an initial time step of 1 hour, a maximum time step of 5 days until the gas reaches the left end, and a maximum time step of 1 year in the remaining of the simulation.

Figure 1.7 exhibits the gas saturation front at different times obtained with the PPF formulation with $N = 100$. The gas hydrodynamic front propagates from right to left at the beginning of the simulation until it reaches the left end, next, the liquid saturation decreases to values close to the residual saturation corresponding to the immobility of the liquid phase, and the liquid begins to disappear at a larger time scale by vaporization of the water and air components in the injected dry gas.

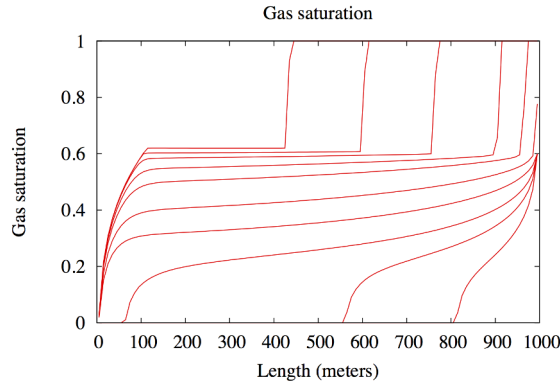


Figure 1.7: Gas saturation at times $t = 1, 3, 6$ months, and $t = 1, 2, 5, 10, 20, 30, 40$ years obtained with the mesh $N = 100$ and the PPF formulation .

The solutions obtained with the three formulations are as in the previous test case compared on the coarse mesh $N = 20$ in Figure 1.8 which exhibits no significant differences.

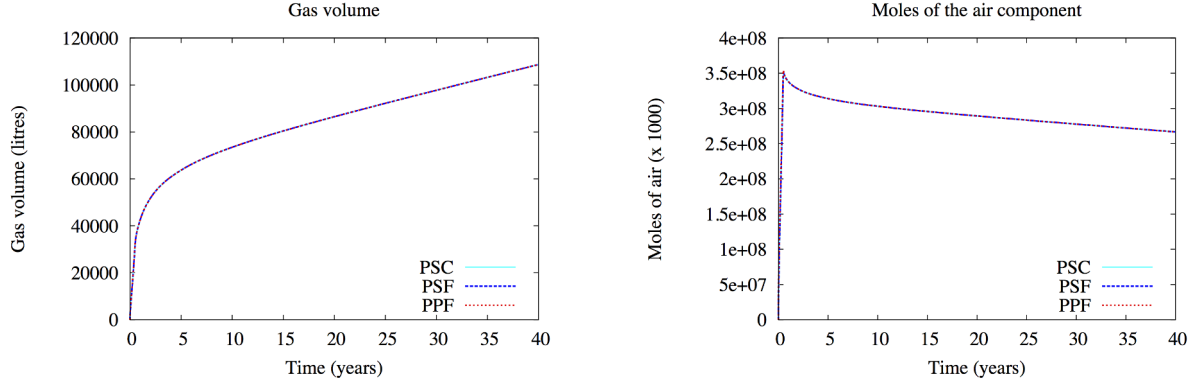


Figure 1.8: Comparison of the gas volume and the number of moles of the air component as a function of time obtained with the mesh $N = 20$ and the three formulations PPF, PSF and PSC.

Comparison of Newton convergence: We compare as in the previous test case the different formulations in Figure 1.2. The non linear stopping criteria is the same as in the previous test case. The pressure pressure formulation PPF_2 includes a modification of the Newton algorithm compared with the previous pressure pressure formulation here denoted by PPF_1 . This modification forces the Newton iterates to pass by the phase transition points

$$\tilde{p}^g - \tilde{p}^l = p_c(1) \text{ or } \tilde{p}^g - \tilde{p}^l = p_c(0)$$

once at each time step and in each cell if a phase transition is observed at this cell at this time step during the Newton algorithm. We observe a considerable improvement of the Newton convergence using this trick although it remains less efficient than the two other formulations.

It seems that the pressure pressure formulation has difficulties in that test case to deal with the gas phase appearance which was not the case for the previous Andra test case. It may be due to the fact that in the previous test case, the gas front is governed by capillary effects (well approximated by Richards equation), while here it appears by transport of the air component.

N	PPF ₁	PPF ₂	PSF	PSC
20	192/12/1500	158/0/686	158/0/527	158/0/519
40	224/18/2324	169/1/943	165/0/677	165/0/678
80	272/31/3562	170/1/1192	166/0/900	166/0/900
160	431/74/6702	197/9/2098	166/0/1339	172/2/1477

Table 1.2: Number of time steps, of time step chops, and total number of Newton iterations for the three formulations PPF, PSF and PSC and for each mesh. The pressure formulation PPF₂ includes a modification of the Newton algorithm compared with the previous PPF₁ pressure pressure formulation.

1.3.2 Three dimensional test cases

In this section, the Vertex Approximate Gradient (VAG) discretization is introduced for the PPF and PSF formulation of our gas liquid compositional model. The discretization takes into account discontinuous capillary pressures in order to capture the saturation jump at different rocktype interfaces. Then, the PSF and PPF formulations combined with the VAG discretization are compared on two 3D heterogeneous test cases.

In both test cases, we consider the gas liquid thermodynamical model described in section 1.2 with the three components carbon dioxide (c), *air* (a) and water (e) with Molar masses $M_c = 44 \text{ g mol}^{-1}$, $M_a = 29 \text{ g mol}^{-1}$, $M_e = 18 \text{ g mol}^{-1}$, a constant temperature $T_e = 300 \text{ K}$, the constant liquid molar density $\zeta^l = 1000/0.018 \text{ mol.m}^{-3}$, the perfect gas molar density $\zeta^g = \frac{p^g}{RT_e}$, with $R = 8.314 \text{ J.K}^{-1}.\text{mol}^{-1}$, and the constant liquid and gas viscosities $\mu^l = 10^{-3} \text{ Pa.s}$, and $\mu^g = 18.51 \cdot 10^{-6} \text{ Pa.s}$. The vapor pressure is defined by the correlation $p_{sat}(T_e) = 1.013 \cdot 10^5 e^{13.7 - 5120/T} \text{ Pa}$, and the Henry constants of the carbon dioxide and *air* components are set to $H_c(T_e) = 10^9 \text{ Pa}$, and $H_a(T_e) = 6.467 \cdot 10^9 \text{ Pa}$. No Fickian diffusion is considered.

Note that the PSC formulation is no longer considered in this section since it is very close to the PSF formulation for our gas liquid thermodynamical model as exhibited by the 1D test cases.

1.3.3 Vertex Approximate Gradient discretization

The Vertex Approximate Gradient (VAG) discretization [32] is a finite volume discretization of diffusion problem adapted to general meshes and heterogenous anisotropic media. It has been extended to multiphase Darcy flows in [33] for compositional models, and to two phase flows with discontinuous capillary pressures in [35] in order to take into account accurately the saturation jump at the interfaces between different rocktypes using a pressure pressure formulation.

Let us consider a polyhedral mesh and denote by \mathcal{M} the set of cells K , by \mathcal{V} the set of vertices \mathbf{s} , by \mathcal{V}_K the set of vertices of each cell $K \in \mathcal{M}$, and by \mathcal{M}_s the set of cells

sharing the node \mathbf{s} . Let

$$X_{\mathcal{D}} = \mathbb{R}^{\mathcal{M}} \oplus \mathbb{R}^{\mathcal{V}}$$

denote the vector space of degrees of freedom of the VAG scheme including nodal and cell unknowns. The VAG discretization builds fluxes $V_{K,\mathbf{s}}$ connecting each cell K to its vertices $\mathbf{s} \in \mathcal{V}_K$ and defined for any $u_{\mathcal{D}} \in X_{\mathcal{D}}$ by

$$V_{K,\mathbf{s}}(u_{\mathcal{D}}) = \sum_{\mathbf{s}' \in \mathcal{V}_K} T_K^{\mathbf{s},\mathbf{s}'}(u_K - u_{\mathbf{s}'}),$$

where

$$T_K = (T_K^{\mathbf{s},\mathbf{s}'})_{\mathbf{s},\mathbf{s}' \in \mathcal{V}_K}$$

is a symmetric positive matrix depending on the geometry of the cell K and on the permeability tensor \mathbf{K} .

The control volumes of the VAG discretization on which the mole balance of each component is written, are defined at each cell $K \in \mathcal{M}$ and at each node $\mathbf{s} \in \mathcal{V} \setminus \mathcal{V}_D$ excluding the nodes with Dirichlet boundary conditions \mathcal{V}_D . The VAG discretization does not use the geometry of these control volumes but only needs to define the fractions $\alpha_{K,\mathbf{s}} \geq 0$ distributing the volume of each cell $K \in \mathcal{M}$ to its nodes $\mathbf{s} \in \mathcal{V}_K \setminus \mathcal{V}_D$, constrained to satisfy the condition

$$1 - \sum_{\mathbf{s} \in \mathcal{V}_K \setminus \mathcal{V}_D} \alpha_{K,\mathbf{s}} \geq 0.$$

In practice, the choice of the fractions $\alpha_{K,\mathbf{s}}$ is done in order to avoid the mixing of different rocktypes at nodal control volumes. This choice of the control volumes improves the discretization of heterogeneous test cases compared with usual Control Volume Finite Element (CVFE) approaches.

Let \mathcal{U} denote the unknowns of the compositional model with

$$\mathcal{U} = (p^g, p^l, f)$$

for the PPF formulation (dropping the tilde for convenience), and

$$\mathcal{U} = (p^g, p^l, s^g, s^l, f)$$

for the PSF formulation. Let us denote by \mathcal{U}_K the cell unknowns, by $\mathcal{U}_{\mathbf{s}}$ the node unknowns, and let us set

$$\mathcal{U}_{\mathcal{D}} = (U_{\nu})_{\nu \in \mathcal{M} \cup \mathcal{V}},$$

and

$$p_{\mathcal{D}}^{\alpha} = (p_{\nu}^{\alpha})_{\nu \in \mathcal{M} \cup \mathcal{V}}.$$

For convenience in the notations, the physical laws in both formulations will be considered as functions of \mathcal{U} and denoted by $c_i^{\alpha}(\mathcal{U})$ (dropping the tilde), $\rho^{\alpha}(\mathcal{U})$, $\zeta^{\alpha}(\mathcal{U})$, and $\mu^{\alpha}(\mathcal{U})$.

The VAG discretization of two phase Darcy flows can be adapted to take into account the jump of the saturations at different rocktype interfaces. The capillary pressures and relative permeabilities are assumed to be cellwise constant and denoted respectively by $p_c(\mathbf{x}, s^l)$ and $k_r^\alpha(\mathbf{x}, s^\alpha)$. The inverse of the monotone graph extension of $p_c(\mathbf{x}, \cdot)$ is denoted by $\mathcal{S}^l(\mathbf{x}, \cdot)$. The PPF formulation has the advantage to work directly with phase pressures as primary unknowns which can be considered continuous at different rocktype interfaces. Then, following [35], it naturally leads to define the discrete saturations as follows:

$$\begin{aligned} s_K^l &= \mathcal{S}^l(\mathbf{x}_K, p_K^g - p_K^l), & s_K^g &= 1 - s_K^l \text{ for all } K \in \mathcal{M}, \\ s_{K,s}^l &= \mathcal{S}^l(\mathbf{x}_K, p_s^g - p_s^l), & s_{K,s}^g &= 1 - s_{K,s}^l \text{ for all } \mathbf{s} \in \mathcal{V}_K, K \in \mathcal{M}. \end{aligned}$$

In the case of the PSF formulation, the saturations s_K^α and s_s^α , $\alpha = g, l$, are primary unknowns and one capillary pressure curve denoted by $p_{c,s}(\cdot)$ must be prescribed at each node $\mathbf{s} \in \mathcal{V}$ among the curve $p_c(\mathbf{x}_K, \cdot)$, $K \in \mathcal{M}_s$. If $p_c(s^l = 1) = 0$ for all rocktypes (no entry pressure), all rocktypes among those in the cells $K \in \mathcal{M}_s$ can be chosen, otherwise, one must choose one rocktype with the lowest entry pressure. Then, in order to account for the saturation jump at different rocktype interfaces, the discretization uses the following saturations at the interfaces

$$s_{K,s}^l = \mathcal{S}^l(\mathbf{x}_K, p_{c,s}(s_s^l)), \quad s_{K,s}^g = 1 - s_{K,s}^l \text{ for all } \mathbf{s} \in \mathcal{V}_K, K \in \mathcal{M}.$$

The discretization of the Darcy fluxes combines the VAG fluxes, the above definition of the saturations, and a phase by phase upwinding of the mobility terms w.r.t. the sign of the flux:

$$V_{K,s}^{\alpha,i}(\mathcal{U}_D) = \left(\frac{\zeta^\alpha c_i^\alpha}{\mu^\alpha} \right) (\mathcal{U}_{K,s}^{\alpha,up}) k_r^\alpha(\mathbf{x}_K, s_{K,s}^{\alpha,up}) \left(V_{K,s}(p_D^\alpha) + g \rho_{K,s}^\alpha V_{K,s}(Z_D) \right),$$

with the upwindings

$$\begin{aligned} \mathcal{U}_{K,s}^{\alpha,up} &= \begin{cases} \mathcal{U}_K & \text{if } V_{K,s}(p_D^\alpha) + g \rho_{K,s}^\alpha V_{K,s}(Z_D) \geq 0, \\ \mathcal{U}_s & \text{else,} \end{cases} \\ s_{K,s}^{\alpha,up} &= \begin{cases} s_K^\alpha & \text{if } V_{K,s}(p_D^\alpha) + g \rho_{K,s}^\alpha V_{K,s}(Z_D) \geq 0, \\ s_{K,s}^\alpha & \text{else,} \end{cases} \end{aligned}$$

with the average density

$$\rho_{K,s}^\alpha = \frac{\rho^\alpha(\mathcal{U}_K) + \rho^\alpha(\mathcal{U}_s)}{2},$$

and the vector of the vertical coordinates at all d.o.f. $Z_D = ((z_\nu)_{\nu \in \mathcal{M} \cup \mathcal{V}})$.

With these notations, the discrete mole balance of each component $i \in \mathcal{C}$ in each control volume writes for both formulations: given $\mathcal{U}^0 = (\mathcal{U}_\nu^0)_{\nu \in \mathcal{M} \cup \mathcal{V}}$ at initial time, find $\mathcal{U}_D^n = (\mathcal{U}_\nu^n)_{\nu \in \mathcal{M} \cup \mathcal{V}}$ for all times t^n , $n = 1, \dots, N$ such that

$$\begin{cases} (1 - \sum_{\mathbf{s} \in \mathcal{V}_K \setminus \mathcal{V}_D} \alpha_{K,s}) \phi_K \frac{n_{i,K}(\mathcal{U}_K^n) - n_{i,K}(\mathcal{U}_K^{n-1})}{t^n - t^{n-1}} + \sum_{\alpha=g,l} \sum_{\mathbf{s} \in \mathcal{V}_K} V_{K,s}^{\alpha,i}(\mathcal{U}_D^n) = 0, & K \in \mathcal{M}, \\ \sum_{K \in \mathcal{M}_s} \alpha_{K,s} \phi_K \frac{n_{i,K,s}(\mathcal{U}_s^n) - n_{i,K,s}(\mathcal{U}_s^{n-1})}{t^n - t^{n-1}} - \sum_{\alpha=g,l} \sum_{K \in \mathcal{M}_s} V_{K,s}^{\alpha,i}(\mathcal{U}_D^n) = 0, & \mathbf{s} \in \mathcal{V} \setminus \mathcal{V}_D, \end{cases}$$

with

$$\begin{aligned} n_{i,K}(\mathcal{U}_K) &= \sum_{\alpha=g,l} \zeta^\alpha(\mathcal{U}_K) s_K^\alpha c_i^\alpha(\mathcal{U}_K), \\ n_{i,K,\mathbf{s}}(\mathcal{U}_{\mathbf{s}}) &= \sum_{\alpha=g,l} \zeta^\alpha(\mathcal{U}_{\mathbf{s}}) s_{K,\mathbf{s}}^\alpha c_i^\alpha(\mathcal{U}_{\mathbf{s}}), \\ \phi_K &= \int_K \phi(\mathbf{x}) d\mathbf{x}, \end{aligned}$$

and specified Dirichlet boundary conditions $\mathcal{U}_{\mathbf{s}}^n$ for all $\mathbf{s} \in \mathcal{V}_D$. The mole balance equations are completed by the following local closure laws in each control volume $\nu \in \mathcal{M} \cup \mathcal{V} \setminus \mathcal{V}_D$ which write

$$\left\{ \begin{array}{l} s_\nu^{g,n} + s_\nu^{l,n} = 1, \\ p_\nu^{g,n} - p_\nu^{l,n} = p_{c,\nu}(s_\nu^{l,n}), \\ s_\nu^{\alpha,n} \left(\sum_{i \in \mathcal{C}} c_i^\alpha(\mathcal{U}_\nu^n) - 1 \right) = 0, \alpha = g, l, \\ s_\nu^{\alpha,n} \geq 0, \sum_{i \in \mathcal{C}} c_i^\alpha(\mathcal{U}_\nu^n) \leq 1, \alpha = g, l, \end{array} \right.$$

for the PSF formulation, and

$$\sum_{i \in \mathcal{C}} c_i^\alpha(\mathcal{U}_\nu^n) = 1, \alpha = g, l,$$

for the PPF formulation.

The non linear system is solved at each time step using a Newton Raphson algorithm. For the PSF formulation, a Newton-Min algorithm adapted to complementary constraints is used [38]. For the PPF formulation, a usual Newton algorithm is used combined with the same trick as in the 1D drying by gas injection test case forcing the Newton iterates to pass through the phase transition points. In both cases, the Jacobian system is reduced to its Schur complement by elimination of the local closure laws which involves the choice of secondary unknowns among \mathcal{U} . This choice depends on the present phases in the case of the PSF formulation and is fixed to two fugacities in the case of the PPF algorithm.

Then, the cell unknowns are eliminated of the linear system without any fill-in using the cell equations and reducing the linear system to the nodal unknowns only.

1.3.4 Drying by suction

The 1D test case is extended to a 3D geometry using a radial mesh of the domain $(0, L) \times (r_G, r_e) \times (0, 2\pi)$ in cylindrical coordinates with $r_G = 2$ m and $r_e = 10$ m, $L = 100$ m. The mesh is exponentially refined at the boundary of the gallery $r = r_G$ to account for the steep gradient of the capillary pressure at the interface. We consider two rocktypes, corresponding to the Excavation Damaged Zone (EDZ) of COx for $r < 3$ m, and to the COx shale for $r > 3$ m (see Figure 1.9). The relative permeabilities and capillary pressures are given by the Van-Genuchten laws (1.20), (1.21), (1.22), with the parameters $n = 1.49$, $s_r^l = 0.4$, $s_r^g = 0$, $P_r = 15 \cdot 10^6$ Pa for COx, and $n = 1.54$, $s_r^l = 0.01$, $s_r^g = 0$, $P_r = 2 \cdot 10^6$ Pa

for EDZ. The porosities are constant for each rocktype and equal to $\phi = 0.15$ for COx, and $\phi = 0.3$ for EDZ. The absolute permeability tensor is heterogeneous and anisotropic

with $\mathbf{K} = \begin{pmatrix} \lambda & 0 & 0 \\ 0 & \lambda & 0 \\ 0 & 0 & \frac{\lambda}{100} \end{pmatrix}$, in the x, y, z Cartesian coordinates where z is the vertical

coordinate and x the direction of the Gallery, $\lambda = 5 \cdot 10^{-20} \text{ m}^2$ for COx and $\lambda = 10^{-18} \text{ m}^2$ for EDZ. Note that the principal directions of \mathbf{K} are not aligned with the radial mesh excluding the use of a Two Point Flux Approximation for this test case.

The initial and external boundary ($r = r_e$) conditions are defined by a liquid phase $s^l = 1$ composed of pure water $c_e^l = 1$, $c_a^l = 0$, $c_c^l = 0$ at the hydrostatic pressure $p^l = p_0 - \rho^l g z$ with $p_0 = 40 \cdot 10^5 \text{ Pa}$. At the interface with the gallery, the gas is defined by its constant pressure $p^g = 10^5 \text{ Pa}$, and its relative humidity function of x along the gallery

$$H_r(x) = \frac{c_e^g p^g}{p_{sat}(T_e)} = 0.3 + \frac{x}{2L}.$$

The gas molar composition is given by

$$c_e^g(x) = \frac{H_r(x) p_{sat}(T_e)}{p^g}, \quad c_a^g(x) = c_c^g(x) = \frac{1 - c_e^g(x)}{2}.$$

We deduce from the thermodynamical equilibrium that

$$p^l(x) = p^g - \zeta^l R T_e \ln\left(\frac{1 - c_a^g(x) p^g / H_a(T_e) - c_c^g(x) p^g / H_c(T_e)}{H_r(x)}\right),$$

and

$$s^l(x) = \mathcal{S}^l(p^g - p^l(x)) > s_r^l.$$

This variation of the relative humidity along the gallery mimics the coupling of the flow in the gallery with the Darcy flow in the surrounding porous media.

The simulation is run over a period of 20 years with an initial time step of 1000 s and a maximum time step of 30 days on the meshes $n_x \times n_r \times n_\theta$ with

$$n_x = n_r = n_\theta = n$$

and $n = 20, 30, 40, 50, 60$. The linear systems are solved using a GMRes iterative solver preconditioned by an ILU0 preconditioner with the stopping criteria 10^{-6} on the relative residual. The Newton stopping criteria is fixed to 10^{-6} on the relative residual.

Figure 1.11 exhibits the convergence of the volume of gas and of the liquid volumic outflow in the gallery as a function of time for the family of meshes. The curves are plotted for the PPF formulation only since no visible difference is observed between both formulations. Figure 1.10 exhibits a transversal cut of the final solutions s^g and $s^g c_e^g$ for both formulations and for the mesh $n = 60$, showing only slight differences in the shape of the fronts between both formulations.

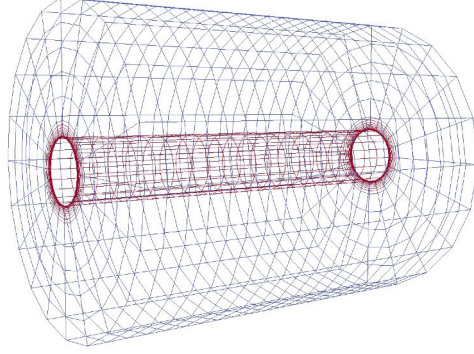


Figure 1.9: Radial mesh for $n = 20$ with the EDZ rocktype in red.

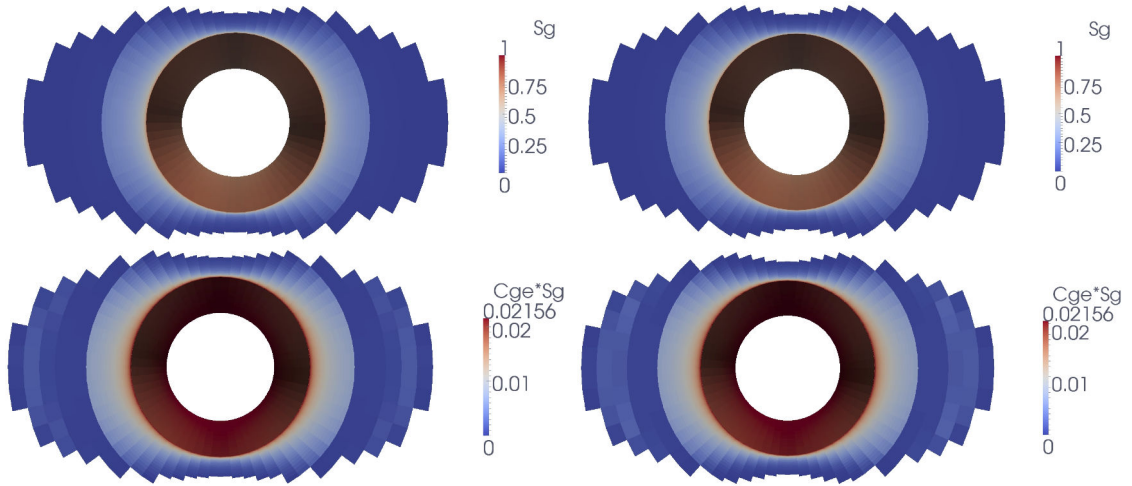


Figure 1.10: Transversal cut of s^g and of $s^g c_e^g$ at final time obtained on the mesh $n = 60$ for the PPF formulation (left) and the PSF formulation (right).

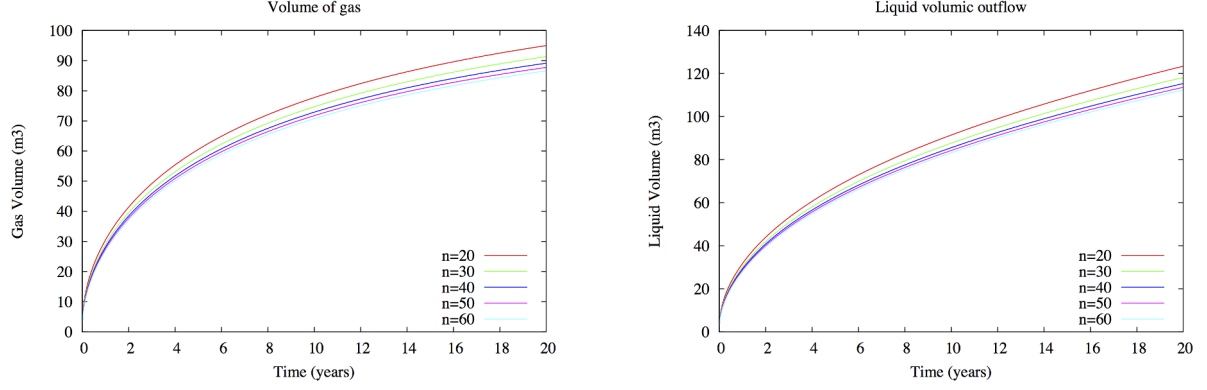


Figure 1.11: For each mesh $n = 20, 30, 40, 50, 60$: volume of gas in the porous media as a function of time, and volumic cumulative outflow of liquid in the gallery function of time.

Table 1.3 exhibits the numerical behavior of the simulations for each mesh and for both the PPF and PSF formulations. It is clear that both formulations are very robust for this test case in terms of Newton convergence with an advantage to the PPF formulation for the finest meshes which confirms the results obtained in 1D.

formulation	mesh	$N_{\Delta t}$	N_{Chop}	N_{Newton}	N_{GMRes}	CPU(s)	α_{CPU}
PPF	$n = 20$	279	0	2.36	16.3	644	
PPF	$n = 30$	279	0	2.38	23.5	2527	1.12
PPF	$n = 40$	279	0	2.41	31.4	6850	1.16
PPF	$n = 50$	279	0	2.42	41.1	14311	1.10
PPF	$n = 60$	279	0	2.47	58.3	29338	1.31
PSF	$n = 20$	279	0	2.33	16.0	690	
PSF	$n = 30$	279	0	2.48	21.9	2807	1.15
PSF	$n = 40$	279	0	2.57	29.3	7493	1.14
PSF	$n = 50$	279	0	2.7	40.9	21304	1.56
PSF	$n = 60$	279	0	2.87	79.7	46985	1.45

Table 1.3: For each mesh and both formulations PPF and PSF: number $N_{\Delta t}$ of successful time steps, number N_{Chop} of time step chops, number N_{Newton} of Newton iterations per successful time step, number N_{GMRes} of GMRes iterations by Newton iteration, CPU time in seconds, and scaling of CPU time (α_{CPU}) by $CPU \sim \text{cells}^{\alpha_{CPU}}$.

1.3.5 Migration of gas in a basin with capillary barriers

The second test case is designed to assess the numerical behavior of the two formulations PPF and PSF with discontinuous capillary pressures. We consider the migration of gas

in a basin $(0, L) \times (0, L) \times (0, H)$ with $L = H = 100$ m, including two capillary barriers. We consider a 2D geometry exhibited in Figure 1.14 which can be discretized using a 2D mesh (3D mesh with only one cell in the y direction), and a 3D geometry exhibited in Figure 1.17 discretized using a 3D mesh. In both figures the barriers are exhibited in red and immersed in a blue drain. The permeabilities are isotropic and equal to $\mathbf{K} = 10^{-12}$ m² in the drain and to $\mathbf{K} = 10^{-14}$ m² in the barriers. The porosity is set to $\phi = 0.1$ on the whole basin.

The initial and top boundary ($z = H$) conditions are defined by a liquid phase $s^l = 1$ composed of pure water $c_e^l = 1$, $c_a^l = 0$, $c_c^l = 0$ at the hydrostatic pressure

$$p^l = p_0^l - \rho^l g z$$

with $p_0^l = 15 \cdot 10^5$ Pa. At the bottom boundary $z = 0$, $x^2 + y^2 \leq 25^2$, the gas is injected at the constant pressure $p^g = 16 \cdot 10^5$ Pa, and with the relative humidity

$$H_r = \frac{c_e^g p^g}{p_{sat}(T_e)} = 0.5.$$

The injected gas molar composition is given by

$$c_e^g = \frac{H_r p_{sat}(T_e)}{p^g}, \quad c_a^g = c_c^g = \frac{1 - c_e^g}{2},$$

and the saturation is fixed to $s^g = 0.8$. All the remaining boundaries are impervious.

The capillary pressures exhibited in Figure 1.12 are given by the Corey laws

$$p_c(s^l) = -10^4 \log(s^l),$$

in the drain, and by

$$p_c(s^l) = \begin{cases} \frac{1-s^l}{1-s_1^l} p_{c,1} & \text{if } s^l > s_1^l, \\ 4 \cdot 10^5 - 10^5 \log(s^l) & \text{if } s^l \leq s_1^l, \end{cases}$$

in the barrier with $p_{c,1} = 4.025 \cdot 10^5$ Pa and $s_1^l = e^{-0.025}$. The entry capillary pressure $p_c = 4 \cdot 10^5$ Pa is chosen to be larger than the gravity load below the first barrier but lower than the gravity load below the second barrier. The relative permeabilities are given by the Corey laws

$$k_r^\alpha(s^\alpha) = (s^\alpha)^2, \quad \alpha = g, l,$$

with zero residual saturations.

In view of Figure 1.13, the reference rocktype for the PSF formulation is chosen to be the barrier rocktype. The reverse choice leads to round off errors in the simulation leading to a wrong solution (at infinite accuracy, both choices should be equivalent since $p_c(s^l = 1) = 0$ for both rocktypes in this test case).

The simulation is run over a period of 40 days with an initial time step of 0.02 days and a maximum time step of 0.1 days on a family of topologically Cartesian meshes of

sizes $n \times 1 \times n$ for the 2D geometry (see Figure 1.14), with $n = 16, 32, 64, 128$, and of sizes for the 3D geometry (see Figure 1.17) with $n = 16, 32, 48$. The linear solver and the non linear and linear stopping criteria are the same as in the previous test case. If the Newton non linear solver does not converge after 25 iterations, the time step is chopped by a factor 2, while the time step is increased of a factor 1.2 after a converged time step until it reaches the maximum time step.

Figure 1.15 (resp. 1.18) shows the gas saturation s^g at final time obtained by the PPF and PSF formulations on the different meshes for the 2D (resp. 3D) basin. Figure 1.16 (resp. 1.19) shows the volume of air dissolved in the liquid phase function of time for both formulations and for the different meshes of the 2D (resp. 3D) basin. The equivalence between both formulations does not hold at the discrete level due to discrete interfaces between single and two phase regions. Indeed, the extension of the pressure of an absent phase depending on the formulation, the fluxes at such interfaces can also depend on the formulation if the upwinding is on the present phase side. One can only expect that the solutions obtained with both formulations will converge to the same solution when the mesh is refined. This convergence can be observed in Figures 1.15, 1.18, 1.16, 1.19 especially on the 2D basin using meshes up to $n = 128$. On the 3D basin, we have not been able to refine the mesh further than $n = 48$ due to too large CPU time with the PPF formulation. Nevertheless, the convergence seems also in good way for the 3D basin.

Tables 1.4 and 1.5 exhibit the numerical behavior of both formulations showing the good behavior of the PSF formulation while the PPF formulation requires much smaller time steps to solve the non linear systems especially when the mesh is refined. This has been obtained with the improvement of the Newton algorithm imposing the Newton iterates to pass through the phase transition points of the graph \mathcal{S}^l . Without this modification, the simulation ends before final time with a time step lower than the minimum time step fixed to 10^{-4} days even on the coarsest meshes.

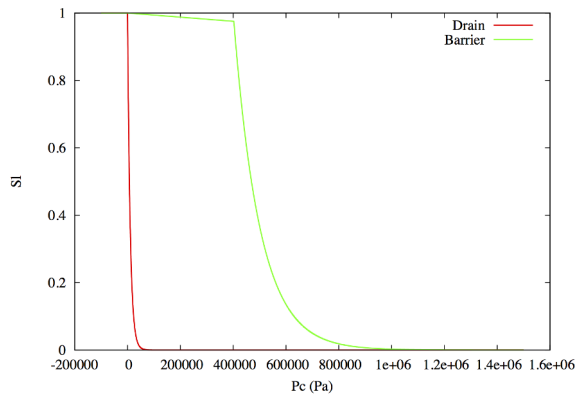


Figure 1.12: Inverses of the monotone graphs of the capillary pressure in the barrier and in the drain.

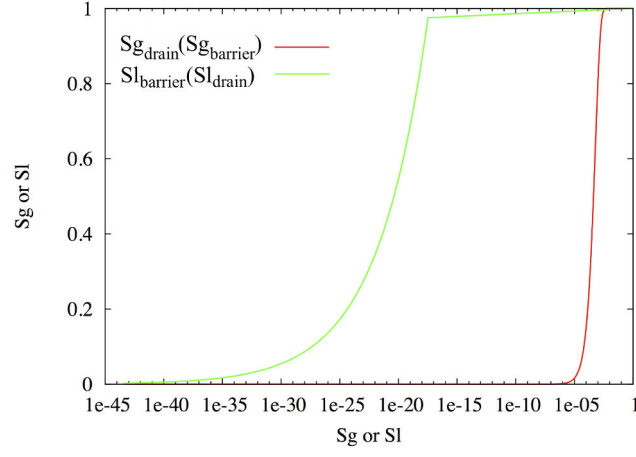


Figure 1.13: $s_{drain}^g = 1 - \mathcal{S}_{drain}^l(p_{c,barrier}(1 - s_{barrier}^g))$ function of $s_{barrier}^g$ and $s_{barrier}^l = \mathcal{S}_{barrier}^l(p_{c,drain}(s_{drain}^l))$ function of s_{drain}^l .

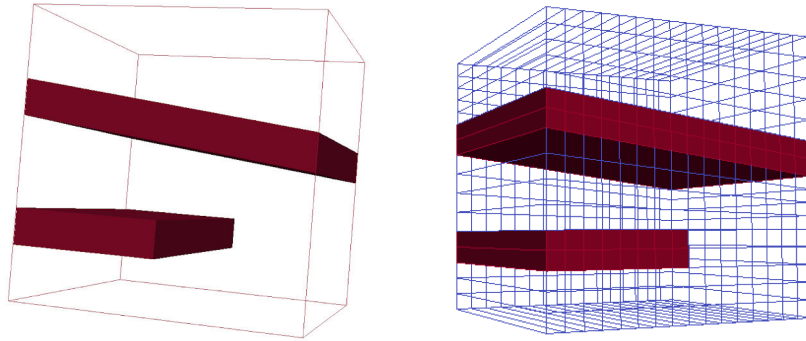


Figure 1.14: 2D geometry of the Basin domain with the two barriers in red and the surrounding drain. Mesh $16 \times 1 \times 16$ of the basin.

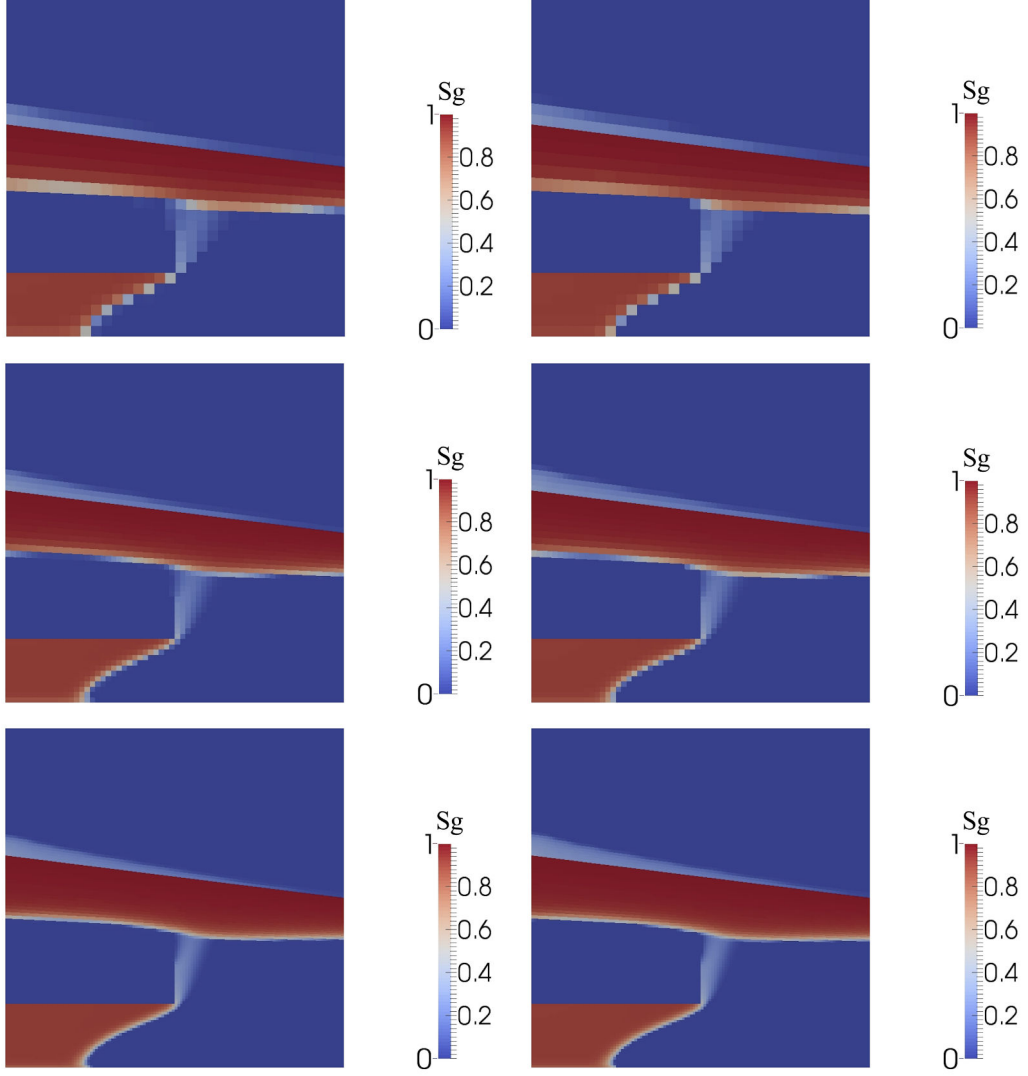


Figure 1.15: Gas saturation s^g above the threshold 10^{-6} at final time for the PPF (left) and PSF (right) formulations on the meshes $32 \times 1 \times 32$, $64 \times 1 \times 64$, $128 \times 1 \times 128$ of the 2D basin.

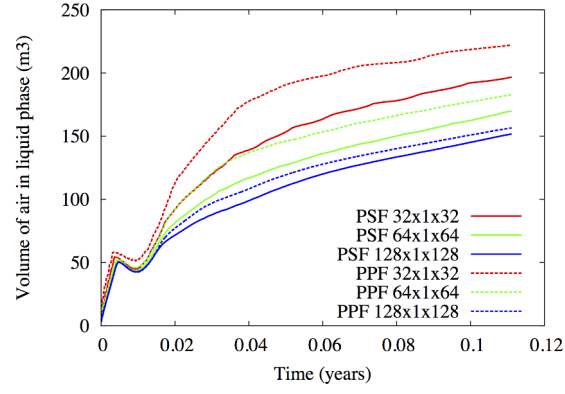


Figure 1.16: Volume of air dissolved in the liquid phase in the 2D basin function of time for both formulations PSF and PPF and for the family of meshes.

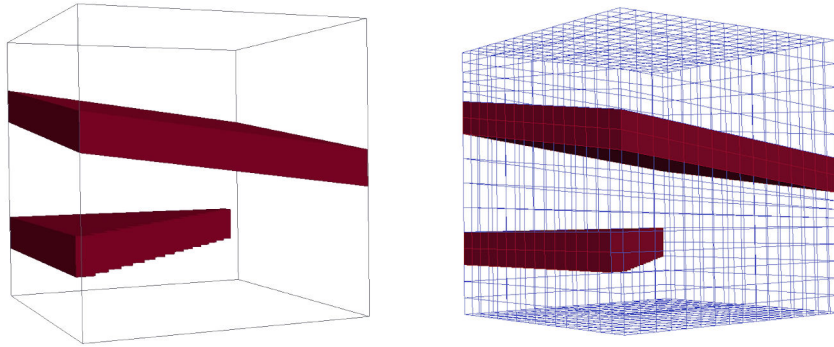


Figure 1.17: 3D geometry of the Basin domain with the two barriers in red and the surrounding drain. Mesh $16 \times 16 \times 16$ of the basin.

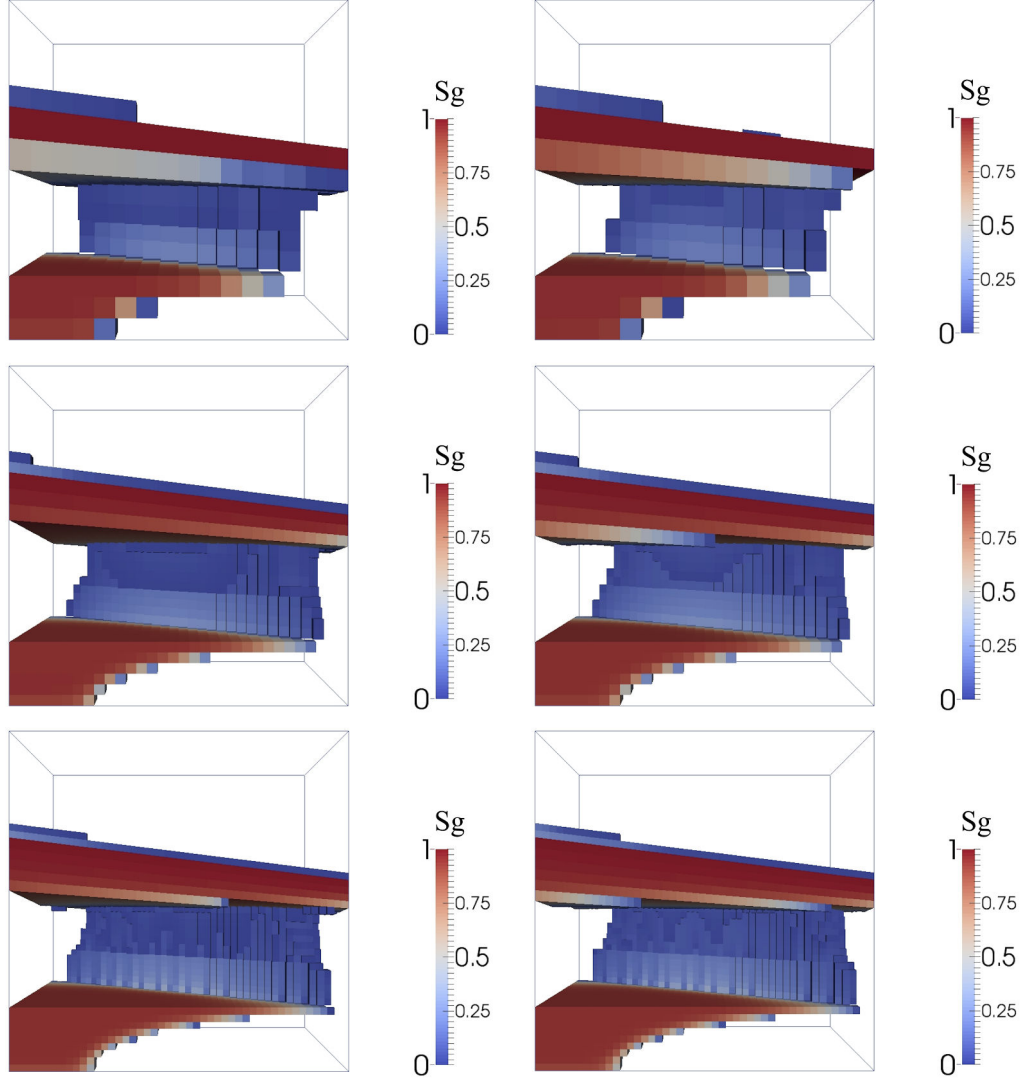


Figure 1.18: Gas saturation s^g above the threshold 10^{-6} at final time for the PPF (left) and PSF (right) formulations on the meshes $16 \times 16 \times 16$, $32 \times 32 \times 32$, $48 \times 48 \times 48$ of the 3D basin.

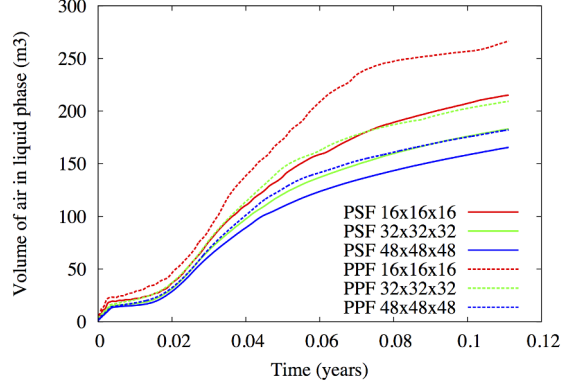


Figure 1.19: Volume of air dissolved in the liquid phase in the 3D basin function of time for both formulations PSF and PPF and for the family of meshes.

formulation	mesh	$N_{\Delta t}$	N_{Chop}	N_{Newton}	N_{GMRes}	CPU(s)	α_{CPU}
PSF	$n = 16$	405	0	2.92	13.4	35	
PSF	$n = 32$	405	0	3.77	21.6	217	1.32
PSF	$n = 64$	405	0	4.75	37.6	1480	1.38
PSF	$n = 128$	409	3	6.28	66.7	11820	1.50
PPF	$n = 16$	405	0	3.93	13.5	46	
PPF	$n = 32$	408	2	7.70	20.0	421	1.60
PPF	$n = 64$	525	61	17.65	31.2	6252	1.95
PPF	$n = 128$	1175	297	23.78	49.4	98549	1.99

Table 1.4: For each mesh $n \times 1 \times n$ of the 2D basin and both formulations PPF and PSF: number $N_{\Delta t}$ of successful time steps, number N_{Chop} of time step chops, number N_{Newton} of Newton iterations per successful time step, number N_{GMRes} of GMRes iterations by Newton iteration, CPU time in seconds, and scaling of CPU time (α_{CPU}) by $CPU \sim \text{cells}^{\alpha_{CPU}}$.

formulation	mesh	$N_{\Delta t}$	N_{Chop}	N_{Newton}	N_{GMRes}	CPU(s)	α_{CPU}
PSF	$n = 16$	405	0	3.87	24.8	781	
PSF	$n = 32$	405	0	4.72	48.7	10296	1.24
PSF	$n = 48$	407	1	5.34	74.7	49170	1.29
PPF	$n = 16$	407	1	5.96	24.7	1146	
PPF	$n = 32$	717	151	15.3	43.4	54205	1.85
PPF	$n = 48$	1803	472	16.1	56.5	543706	1.90

Table 1.5: For each mesh $n \times n \times n$ of the 3D basin and both formulations PPF and PSF: number $N_{\Delta t}$ of successful time steps, number N_{Chop} of time step chops, number N_{Newton} of Newton iterations per successful time step, number N_{GMRes} of GMRes iterations by Newton iteration, CPU time in seconds, and scaling of CPU time (α_{CPU}) by $CPU \sim \text{cells}^{\alpha_{CPU}}$.

1.4 Conclusion

In this Chapter three formulations of compositional gas liquid two phase flows with phase transitions have been shown to lead to equivalent definitions of the phase transitions. They have been compared in terms of non linear solver convergence and solutions on different 1D and 3D test cases involving gas appearance and liquid disappearance. The VAG discretization has been used in 3D taking into account discontinuous capillary pressures to capture accurately the saturation jump at different rocktype interfaces.

On the drying by suction 1D and 3D test cases, the three formulations lead to quite similar results with a better behavior of the PPF formulation on the finest meshes. On the other hand the PPF formulation has severe difficulties to deal with the gas phase appearance and liquid disappearance in the gas injection test cases, both in 1D and 3D. This difficulty is due to the degeneracy of the inverse of the capillary function \mathcal{S}^l at the phase transition points $s^l = 1$ and $s^l = 0$. The Newton convergence has been improved by forcing the Newton iterates to pass through these phase transition points, nevertheless it has not been sufficient to obtain large enough time steps on the gas injection test cases especially when the mesh is refined. This drastic difference of behaviour of the PPF formulation between the two test cases is probably due to the fact that the gas front is dominated by the capillary effect and well approximated by the Richards equation for the drying by suction test case, while it is more dominated by the Buckley Leverett equation and the gravity or pressure gradient terms for the gas injection test cases.

All together, the PSF and PSC formulations clearly outperform the PPF formulation for compositional gas liquid Darcy flows on our set of numerical experiments.

Chapter 2

Coupling of a liquid gas compositional 3D Darcy flow with a 1D compositional free gas flow

Abstract A model coupling a three dimensional gas liquid compositional Darcy flow in a fractured porous medium, and a one dimensional compositional free gas flow is presented. The coupling conditions at the interface between the gallery and the porous medium account for the molar normal fluxes continuity for each component, the gas liquid thermodynamical equilibrium, the gas pressure continuity and the gas molar fractions continuity. The fractures are represented as interfaces of codimension one immersed in the surrounding 3D porous medium, the matrix. Pressure continuity is assumed for both phases at the interfaces between the fracture and the matrix. The spatial discretization is based on the Vertex Approximate Gradient (VAG) scheme in the porous medium coupled with a non conforming control volume finite element discretization in the gallery. This model is applied to the simulation of the mass exchanges at the interface between the repository and the ventilation excavated gallery in a nuclear waste geological repository.

2.1 Introduction

Flow and transport processes in domains composed of a porous medium and an adjacent free-flow region appear in a wide range of industrial and environmental applications. This is in particular the case for radioactive waste deep geological repositories where such models must be used to predict the mass and energy exchanges occurring at the interface between the repository and the ventilation excavated galleries. Typically, in this example, the porous medium initially saturated with the liquid phase is dried by suction in the neighbourhood of the interface. To model such physical processes, one needs to account in the porous medium for the flow of the liquid and gas phases including the vaporization of the water component in the gas phase and the dissolution of the gaseous component in the liquid phase. In the gallery, a single phase gas free flow can be consid-

ered assuming that the liquid phase is instantaneously vaporized at the interface. This single phase gas free flow has to be compositional to account for the change of the relative humidity in the gallery which has a strong feedback on the liquid flow rate at the interface.

In this Chapter we consider a reduced model coupling a gas liquid Darcy flow in the porous medium with a 1D free flow in the gallery. It assumes that the longitudinal dimension of the gallery is large compared with its diameter. The liquid and gas phases are considered as a mixture of two components, the water component denoted by e which can vaporize in the gas phase, and the gaseous component a standing for air which can dissolve in the liquid phase. The matching conditions at the porous medium gallery interface are a simplified version of those proposed in [49, 6] taking into account the low permeability of the repository. In this case, it can be assumed that the gas pressure, and the gas molar fractions are both continuous at the interface. In addition, following [49, 6], the thermodynamical equilibrium between the gas and liquid phases is assumed to hold at the interface.

The flow in the porous medium takes into account the mass exchanges between a network of discrete fractures and the surrounding 3D porous medium, the matrix. Following [2, 53, 12, 13] we consider the asymptotic model for which the fractures are represented as interfaces of codimension one immersed in the matrix domain. The pressures at the interfaces between the matrix and the fracture network are assumed continuous corresponding to a large ratio between the normal permeability of the fracture and the width of the fracture compared with the ratio between the permeability of the matrix and the size of the domain.

The coupled model is formulated in terms of a single set of unknowns used in the matrix, in the fracture network and in the gallery corresponding to the liquid and gas pressures. Its discretization is based on the VAG scheme introduced in [32] for the single phase Darcy flow, in [36] for compositional Darcy flows, and in [12] for two phase Darcy flows in discrete fracture networks. The VAG scheme is roughly speaking a finite volume nodal approximation. Its main advantage compared with typical nodal finite volume schemes such as Control Volume Finite Element (CVFE) methods [6] is to avoid the mixing of different material properties inside the control volumes. This idea is here extended to take into account the coupling with the 1D free gas flow using a 1D finite element mesh non necessarily matching with the porous medium mesh.

In order to introduce the reduced model and its functional setting, we first consider a model problem corresponding to a single phase Darcy flow coupling the 3D flow in the matrix, the 2D flow in the fracture network and the 1D flow in the gallery. The VAG discretization is also first described for this model problem using a non conforming discretization between the porous medium domain and the gallery. This non conformity is necessary to allow for fairly general meshes at the interface Γ . The convergence analysis of the VAG scheme is performed for the model problem using the gradient scheme framework introduced in [32] and [29].

The outline of the Chapter is the following: section 2.2 deals with the single phase Darcy flow. The geometry and the functional framework is introduced in subsection 2.2.1 and the VAG discretization of this model problem is described in subsection 2.2.3. The gradient scheme framework is extended to this model problem in subsection 2.2.2 in order to perform the convergence analysis of the VAG discretization in subsection 2.2.4. Two numerical examples are provided in subsection 2.2.5 to compare the numerical convergence and the error estimates of subsection 2.2.4. Section 2.3 extends the model and its VAG discretization to compositional flows. The formulation of the model uses a single set of unknowns corresponding to the gas and liquid pressures both in the porous medium and in the gallery. Then, our discrete model is assessed numerically in section 2.4 on three test cases without fractures including a comparison with an approximate stationary solution. A more advanced model is also tested in subsection 2.4.3 including on the gallery side a gas molar fraction at the interface and a normal diffusion term between the interface and the gallery modelling the concentration boundary layer in the spirit of [48, 49]. The previous model corresponds to the limit when the diffusion coefficient tends to infinity. Then, section 2.5 gives two examples including 1 and 4 fractures. Finally, we prove in section 2.6 the convergence of the scheme to a weak solution for a simplified model coupling the Richards equation in the porous medium with the 1D Poiseuille flow in the gallery. This analysis also applies to the coupling between the Richards equation and a 1D convection diffusion equation in the gallery at given velocity which is a rather good approximation of the full model.

2.2 Model problem

This section deals with a single phase Darcy flow coupling a 3D Darcy flow in the matrix, a 2D Darcy flow in the fracture network and a 1D Darcy (or Poiseuille) flow in the gallery. The coupling between the matrix and the fracture network uses the reduced model introduced in [2] where the pressure is assumed continuous at the interface between the fractures and the matrix. In addition, the pressure is also assumed continuous at fracture intersections. We refer to [12] for a detailed analysis of this model including a complex network of planar fractures. The coupling between the Darcy flow in the fractured porous medium and the Darcy 1D flow is obtained assuming the continuity of the pressure at the interface between the porous medium and the gallery. This implies in particular that the pressure at the gallery porous medium interface depends only on the x coordinate along the gallery. In the physical framework of this thesis, this model problem corresponds to the stationary state where only the gas is assumed present in the porous medium.

2.2.1 Geometry and functional setting

Let ω and $S \subset \omega$ be two simply connected polygonal domains of \mathbb{R}^2 and $\Omega = (0, L) \times (\omega \setminus \overline{S})$ be the cylindrical domain defining the porous medium. The excavated gallery corresponds

to the domain $(0, L) \times S$ and it will be assumed that the flow in the gallery depends only on the x coordinate along the gallery. Let us denote by $\Gamma = (0, L) \times \partial S$ the interface between the gallery and the porous medium and by γ the trace operator from $H^1(\Omega)$ to $L^2(\Gamma)$. We define on Γ the coordinate system (x, s) where s is the curvilinear coordinate along ∂S .

Let $\bar{\Gamma}_f = \bigcup_{i \in I} \bar{\Gamma}_{f,i}$ and its interior $\Gamma_f = \bar{\Gamma}_f \setminus \partial \bar{\Gamma}_f$ denote the network of fractures $\Gamma_{f,i} \subset \Omega$, $i \in I$, such that each $\Gamma_{f,i}$ is a planar polygonal simply connected open domain included in a plane \mathcal{P}_i of \mathbb{R}^3 . It is assumed that the angles of $\Gamma_{f,i}$ are strictly smaller than 2π , that $\Gamma_{f,i} \cap \bar{\Gamma}_{f,j} = \emptyset$ for all $i \neq j$, and that $\Gamma_f \cap \partial\Omega = \emptyset$.

For all $i \in I$, let us set

$$\left\{ \begin{array}{l} \Sigma_i = \partial\Gamma_{f,i}, \\ \Sigma_{i,j} = \Sigma_i \cap \Sigma_j, j \in I \setminus \{i\}, \\ \Sigma_{i,D} = \Sigma_i \cap (\partial\Omega \setminus \bar{\Gamma}), \\ \Sigma_{i,\Gamma} = \Sigma_i \cap \Gamma, \\ \Sigma_{i,N} = \Sigma_i \setminus (\bigcup_{j \in I \setminus \{i\}} \Sigma_{i,j} \cup \Sigma_{i,D} \cup \Sigma_{i,\Gamma}), \end{array} \right.$$

and

$$\left\{ \begin{array}{l} \Sigma_\Gamma = \bigcup_{i \in I} \Sigma_{i,\Gamma}, \\ \Sigma_D = \bigcup_{i \in I} \Sigma_{i,D}, \\ \Sigma_N = \bigcup_{i \in I} \Sigma_{i,N}, \\ \Sigma = (\bigcup_{(i,j) \in I \times I, i \neq j} \Sigma_{i,j}) \setminus (\Sigma_D \cup \Sigma_\Gamma), \end{array} \right.$$

We refer to Figure 2.1 for an illustration of the notations in a simplified Cartesian geometry.

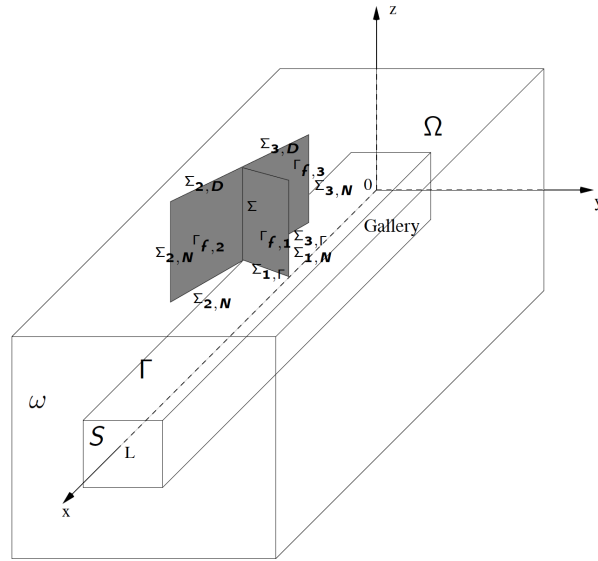


Figure 2.1: Simplified Cartesian geometry with the porous medium domain Ω , the gallery $(0, L) \times S$, the interface Γ , and 3 fractures $\Gamma_{f,i}$, $i = 1, \dots, 3$, their boundaries $\Sigma_{1,N}$, $\Sigma_{1,\Gamma}$, $\Sigma_{2,N}$, $\Sigma_{2,D}$, $\Sigma_{2,\Gamma}$, and their intersection Σ .

The space $H^1(\Gamma_f) \subset L^2(\Gamma_f)$ is defined as the subspace of functions with restriction to $\Gamma_{f,i}$ in $H^1(\Gamma_{f,i})$ for all $i \in I$, and with continuous trace at fracture intersections. Let us define the trace operators from $H^1(\Gamma_f)$ to $L^2(\Sigma_\Gamma)$ and from $H^1(\Gamma)$ to $L^2(\Sigma_\Gamma)$, both denoted by γ_{Σ_Γ} for convenience. Let γ_f denote the trace operator from $H^1(\Omega)$ to $L^2(\Gamma_f)$.

The space of solutions is defined as follows

$$V = \{u \in H^1(\Omega) \mid \gamma_f u \in H^1(\Gamma_f), \gamma u \in H^1(\Gamma), \partial_s \gamma u = 0\}.$$

Note that in the above definition of the space V , the fact that $u \in H^1(\Omega)$ and that $\gamma_f u \in H^1(\Gamma_f)$, $\gamma u \in H^1(\Gamma)$ implies that $\gamma_{\Sigma_\Gamma} \gamma_f u = \gamma_{\Sigma_\Gamma} \gamma u$. Keeping the same notation for convenience, the trace operator γ maps V to $H^1(0, L)$. The subspace of V taking into account homogeneous Dirichlet boundary conditions for u on $\Gamma_D = \partial\Omega \setminus \bar{\Gamma}$, for $\gamma_f u$ on Σ_D , and for γu at $x = 0$ and $x = L$, is denoted by

$$V^0 = \{u \in V \mid u = 0 \text{ on } \Gamma_D, \gamma_f u = 0 \text{ on } \Sigma_D, \gamma u(0) = \gamma u(L) = 0\},$$

and endowed with the Hilbertian norm

$$\|u\|_{V^0} = \left(\int_{\Omega} |\nabla u(\mathbf{x})|^2 d\mathbf{x} + \int_{\Gamma_f} |\nabla_\tau \gamma_f u(\mathbf{x})|^2 d\tau(\mathbf{x}) + \int_0^L |\partial_x \gamma u(x)|^2 dx \right)^{\frac{1}{2}},$$

where ∇_τ denote the tangential gradient operator. The following density result is needed for the convergence analysis.

Lemma 2.2.1 *The smooth function subspace of V^0 defined by $C_{V^0}^\infty = C^\infty(\bar{\Omega}) \cap V^0$ is a dense subspace of V^0 .*

Proof: the proof is similar to the one presented in [13]. \square

Let us define the following function space for the fluxes.

$$W = \left\{ \begin{array}{l} \mathbf{q} = (\mathbf{q}_m, \mathbf{q}_f, q_g) \in H_{\text{div}}(\Omega \setminus \bar{\Gamma}_f) \times L^2(\Gamma_f)^{d-1} \times L^2(0, L) \mid \\ \text{there exists } (r_f(\mathbf{q}), r_g(\mathbf{q})) \in L^2(\Gamma_f) \times L^2(0, L) \text{ such that} \\ \int_{\Omega \setminus \Gamma_f} (\mathbf{q}_m \cdot \nabla v + v \operatorname{div}(\mathbf{q}_m)) d\mathbf{x} + \int_{\Gamma_f} (\mathbf{q}_f \cdot \nabla_\tau \gamma_f v + r_f(\mathbf{q}) \gamma_f v) d\tau(\mathbf{x}) \\ + \int_0^L q_g (\partial_x \gamma v) + r_g(\mathbf{q}) \gamma v dx = 0 \text{ for all } v \in V^0 \end{array} \right\}. \quad (2.1)$$

The uniqueness of $(r_f(\mathbf{q}), r_g(\mathbf{q}))$ is clear using liftings from $C_c^\infty(0, L)$ and from $C_c^\infty(\Gamma_{f,i})$, $i \in I$, to $C_{V^0}^\infty$. The function space W is an Hilbert space endowed with the following scalar product: for all $(\mathbf{p}, \mathbf{q}) \in W \times W$

$$\begin{aligned} \langle \mathbf{p}, \mathbf{q} \rangle_W &= \int_{\Omega \setminus \Gamma_f} (\mathbf{p}_m \cdot \mathbf{q}_m + \operatorname{div}(\mathbf{p}_m) \operatorname{div}(\mathbf{q}_m)) d\mathbf{x} \\ &\quad + \int_{\Gamma_f} (\mathbf{p}_f \cdot \mathbf{q}_f + r_f(\mathbf{p}) r_f(\mathbf{q})) d\tau(\mathbf{x}) + \int_0^L (p_g q_g + r_g(\mathbf{p}) r_g(\mathbf{q})) dx. \end{aligned}$$

Let $\Omega_\alpha, \alpha \in \mathcal{A}$ denote the connected components of $\Omega \setminus \bar{\Gamma}$. For all $i \in I$, we can define the two sides \pm of the fracture $\Gamma_{f,i}$ and the corresponding unit normal vector \mathbf{n}_i^\pm at $\Gamma_{f,i}$ outward to the sides \pm . Each side \pm corresponds to the subdomain $\alpha_i^\pm \in \mathcal{A}$ with possibly $\alpha_i^+ = \alpha_i^-$. For all $\mathbf{q}_m \in H_{\text{div}}(\Omega \setminus \bar{\Gamma})$, let $\mathbf{q}_m|_{\Omega_{\alpha_i^\pm}} \cdot \mathbf{n}_i^\pm|_{\Gamma_{f,i}}$ denote the two normal traces at the fracture $\Gamma_{f,i}$ and let us define the jump operator $H_{\text{div}}(\Omega \setminus \bar{\Gamma}) \rightarrow \mathcal{D}'(\Gamma_{f,i})$ in the sense of distributions by

$$\llbracket \mathbf{q}_m \cdot \mathbf{n}_i \rrbracket = (\mathbf{q}_m|_{\Omega_{\alpha_i^+}} \cdot \mathbf{n}_i^+)|_{\Gamma_{f,i}} + (\mathbf{q}_m|_{\Omega_{\alpha_i^-}} \cdot \mathbf{n}_i^-)|_{\Gamma_{f,i}}.$$

In order to define a “smooth” function subspace of W , we need to consider the set of points $(\hat{x}_k)_{k \in S_{\Sigma_\Gamma}}$ such that $\hat{x}_k \in (0, L)$ and $\int_{(\{\hat{x}_k\} \times \partial S) \cap \Sigma_\Gamma} ds \neq 0$. Then, for all $k \in S_{\Sigma_\Gamma}$, we denote by H_k the Heaviside step function on $(0, L)$ such that $H_k(x) = 0$ if $x < \hat{x}_k$ and $H_k(x) = 1$ if $x > \hat{x}_k$.

For all $\alpha \in \mathcal{A}$ let us denote by $C_b^\infty(\Omega_\alpha)$ the set of functions φ such that for all $\mathbf{x} \in \bar{\Omega}_\alpha$, there exists $r > 0$ such that for all connected component ω of the domain $\{\mathbf{x} \in \mathbb{R}^d \mid |\mathbf{x}| < r\} \cap \Omega_\alpha$, one has $\varphi|_\omega \in C^\infty(\bar{\omega})^d$.

Then we set

$$C_W^\infty = \left\{ \begin{array}{l} \mathbf{q} = (\mathbf{q}_m, \mathbf{q}_f, q_g) \mid \mathbf{q}_m|_{\Omega_\alpha} \in C_b^\infty(\Omega_\alpha), \alpha \in \mathcal{A}, \mathbf{q}_f|_{\Gamma_{f,i}} \in C^\infty(\bar{\Gamma}_{f,i})^{d-1}, i \in I, \\ q_g - \sum_{k \in S_{\Sigma_\Gamma}} \sum_{i \in I} \left(\int_{(\{\hat{x}_k\} \times \partial S) \cap \Sigma_{i,\Gamma}} \mathbf{q}_f|_{\Gamma_{f,i}} \cdot \mathbf{n}_{\Sigma_i} dl(\mathbf{x}) \right) H_k(x) \in C^\infty([0, L]), \\ \sum_{i \in I} \mathbf{q}_f|_{\Gamma_{f,i}} \cdot \mathbf{n}_{\Sigma_i} = 0 \text{ on } \Sigma, \mathbf{q}_f|_{\Gamma_{f,i}} \cdot \mathbf{n}_{\Sigma_i} = 0 \text{ on } \Sigma_{i,N}, i \in I \end{array} \right\},$$

where, for all $i \in I$, we denote by \mathbf{n}_{Σ_i} the unit vector normal to Σ_i outward (and tangent) to $\Gamma_{f,i}$. Note that the definition of W incorporates the physical assumption that the sum of the normal fluxes at fracture intersections as well as the normal flux at the immersed fracture boundary Σ_N vanish.

Lemma 2.2.2 *The function space C_W^∞ is a dense subspace of W .*

Proof: To prove that C_W^∞ is a subspace of W , we need to check for all $\mathbf{q} \in C_W^\infty$ that $(r_f(\mathbf{q}), r_g(\mathbf{q}))$ satisfying (2.1) is in $L^2(\Gamma_f) \times L^2(0, L)$. Let us consider the function $r_f(\mathbf{q}) \in L^2(\Gamma_f)$ such that

$$r_f(\mathbf{q})|_{\Gamma_{f,i}} = \text{div}_{\tau_i}(\mathbf{q}_f|_{\Gamma_{f,i}}) - \llbracket \mathbf{q}_m \cdot \mathbf{n}_i \rrbracket \quad (2.2)$$

for all $i \in I$, where div_{τ_i} is the tangential divergence operator on $\Gamma_{f,i}$. Let $r_g(\mathbf{q}) \in \mathcal{D}'(0, L)$ be defined by

$$\int_0^L r_g(\mathbf{q}) \varphi dx = - \int_0^L q_g \partial_x \varphi dx - \int_\Gamma (\mathbf{q}_m \cdot \mathbf{n}) \varphi d\tau(\mathbf{x}) - \sum_{i \in I} \int_{\Sigma_{i,\Gamma}} (\mathbf{q}_f|_{\Gamma_{f,i}} \cdot \mathbf{n}_{\Sigma_i}) \varphi dl(\mathbf{x}) \quad (2.3)$$

for all $\varphi \in C_c^\infty(0, L)$, using implicitly the extension $\varphi(\mathbf{x}) = \varphi(x)$ for all $\mathbf{x} \in \Gamma$. From the definition of C_W^∞ , we deduce that $r_g(\mathbf{q}) \in L^2(0, L)$. Using that $C_c^\infty(0, L)$ is dense in

$H_0^1(0, L)$, that $\gamma v \in H_0^1(0, L)$ for all $v \in V^0$ and integration by part, it is easy to check that \mathbf{q} and the above defined functions $r_f(\mathbf{q})$ and $r_g(\mathbf{q})$ satisfy (2.1).

From the Riesz representation theorem, for any linear form $\xi \in W'$, there exist $a_m \in L^2(\Omega)$, $\mathbf{A}_m \in L^2(\Omega)^d$, $a_f \in L^2(\Gamma_f)$, $\mathbf{A}_f \in L^2(\Gamma_f)^{d-1}$, $a_g \in L^2(0, L)$ and $A_g \in L^2(0, L)$ such that for all $\mathbf{q} \in W$

$$\begin{aligned} \langle \xi, \mathbf{q} \rangle_{W', W} &= \int_{\Omega \setminus \Gamma_f} (\mathbf{q}_m \cdot \mathbf{A}_m + a_m \operatorname{div}(\mathbf{q}_m)) d\mathbf{x} + \int_{\Gamma_f} (\mathbf{q}_f \cdot \mathbf{A}_f + r_f(\mathbf{q}) a_f) d\tau(\mathbf{x}) \\ &\quad + \int_0^L (q_g A_g + r_g(\mathbf{q}) a_g) dx. \end{aligned} \quad (2.4)$$

Let us assume that $\langle \xi, \mathbf{q} \rangle_{W', W} = 0$ for all $\mathbf{q} \in C_W^\infty$. Then, in order to prove the density of C_W^∞ in W , it suffices to prove that $a_m \in V^0$, $\mathbf{A}_m = \nabla a_m$, $a_f = \gamma_f a_m$, $\mathbf{A}_f = \nabla_\tau a_f$, $a_g = \gamma a_m$ and $A_g = \partial_x a_g$. From Lemma 8 in [13], it is already known that $a_m \in H^1(\Omega)$, $a_f \in H^1(\Gamma)$ with $a_m = 0$ on $\partial\Omega \setminus \bar{\Gamma}$, $a_f = 0$ on Σ_D , and $a_f = \gamma_f a_m$, $\mathbf{A}_m = \nabla a_m$, $\mathbf{A}_f = \nabla_\tau a_f$.

Taking $\mathbf{q} = (0, 0, q_g)$ in (2.4) with $q_g \in C^\infty([0, L])$, it follows that $a_g \in H_0^1(0, L)$ with $A_g = \partial_x a_g$. Next setting $\mathbf{q} = (\mathbf{q}_m, 0, 0)$ in (2.4) with $\mathbf{q}_m|_{\Omega_\alpha} \in C_b^\infty(\Omega_\alpha)$ for all $\alpha \in \mathcal{A}$, it follows from the definitions (2.3) and (2.2) of $r_g(\mathbf{q})$ and $r_f(\mathbf{q})$ that

$$\int_{\Gamma} (\mathbf{q}_m \cdot \mathbf{n})(\gamma a_m - a_g) d\tau(\mathbf{x}) = 0,$$

which implies that $a_g = \gamma a_m$. \square

Model Problem

In the matrix domain $\Omega \setminus \bar{\Gamma}_f$ (resp. in the fracture network Γ_f), let us denote by $\mathbf{K}_m \in L^\infty(\Omega)^{d \times d}$ (resp. $\mathbf{K}_f \in L^\infty(\Gamma_f)^{(d-1) \times (d-1)}$) the permeability tensor such that there exist $\bar{\lambda}_m \geq \underline{\lambda}_m > 0$ (resp. $\bar{\lambda}_f \geq \underline{\lambda}_f > 0$) with

$$\underline{\lambda}_m |\boldsymbol{\xi}|^2 \leq (\mathbf{K}_m(\mathbf{x}) \boldsymbol{\xi}, \boldsymbol{\xi}) \leq \bar{\lambda}_m |\boldsymbol{\xi}|^2 \text{ for all } \boldsymbol{\xi} \in \mathbb{R}^d, \mathbf{x} \in \Omega,$$

(resp. $\underline{\lambda}_f |\boldsymbol{\xi}|^2 \leq (\mathbf{K}_f(\mathbf{x}) \boldsymbol{\xi}, \boldsymbol{\xi}) \leq \bar{\lambda}_f |\boldsymbol{\xi}|^2$ for all $\boldsymbol{\xi} \in \mathbb{R}^{d-1}, \mathbf{x} \in \Gamma_f$).

We denote by $d_f \in L^\infty(\Gamma_f)$ the width of the fractures assumed to be such that there exist $\bar{d}_f \geq \underline{d}_f > 0$ with $\underline{d}_f \leq d_f(\mathbf{x}) \leq \bar{d}_f$ for all $\mathbf{x} \in \Gamma_f$.

Let us also denote by $\alpha_g \in L^\infty(0, L)$ the pressure drop parameter in the gallery such that there exist $\bar{\alpha}_g \geq \underline{\alpha}_g > 0$ with $\underline{\alpha}_g \leq \alpha_g(x) \leq \bar{\alpha}_g$ for all $x \in (0, L)$.

Let $g_m \in L^2(\Omega)$, $g_f \in L^2(\Gamma_f)$, and $g_g \in L^2(0, L)$ denote respectively the source terms in the matrix, in the fracture network, and in the gallery. Let us consider the linear model coupling a single phase Darcy flow in the fractured porous medium with a single phase

1D Darcy flow in the gallery: find $u \in V^0$ and $\mathbf{q} = (\mathbf{q}_m, \mathbf{q}_f, q_g) \in W$ such that

$$\begin{cases} \operatorname{div}(\mathbf{q}_m) = g_m, \\ r_f(\mathbf{q}) = d_f g_f, \\ r_g(\mathbf{q}) = |S| g_g, \\ \mathbf{q}_m = -\mathbf{K}_m \nabla u, \\ \mathbf{q}_f = -d_f \mathbf{K}_f \nabla_\tau \gamma_f u, \\ q_g = -\frac{|S|}{\alpha_g} \partial_x \gamma u. \end{cases} \quad (2.5)$$

Its variational formulation amounts to find $u \in V^0$ such that

$$\begin{aligned} & \int_{\Omega} \mathbf{K}_m \nabla u \cdot \nabla v \, d\mathbf{x} + \int_{\Gamma_f} d_f \mathbf{K}_f \nabla_\tau \gamma_f u \cdot \nabla_\tau \gamma_f v \, d\tau(\mathbf{x}) \\ & \quad + \int_0^L \frac{|S|}{\alpha_g} \partial_x \gamma u \partial_x \gamma v \, dx \\ & = \int_{\Omega} g_m v \, d\mathbf{x} + \int_{\Gamma_f} d_f g_f \gamma_f v \, d\tau(\mathbf{x}) + \int_0^L |S| g_g \gamma v \, dx. \end{aligned} \quad (2.6)$$

for all $v \in V^0$. The existence and uniqueness of a solution to (2.6) is readily obtained from the Poincaré inequality and the Lax Milgram theorem.

2.2.2 Gradient scheme discretization of the model problem

The gradient scheme framework has been introduced in [32], [29] to analyse the convergence of numerical methods for linear and nonlinear second order diffusion problems. As shown in [29], this framework accounts for various conforming and non conforming discretizations such as Finite Element methods, Mixed and Mixed Hybrid Finite Element methods, and some Finite Volume schemes like symmetric MPFA, Vertex Approximate Gradient (VAG) schemes [32], and Hybrid Finite Volume (HFV) schemes [31]. Let us also refer to [10] for an alternative general framework based on the concept of compatible discrete operator for the discretization of diffusion problems on polyhedral meshes.

In this subsection, the gradient scheme framework is extended to the model problem 2.2.1. It will be used in subsection 2.2.4 to perform the convergence analysis of the VAG discretization introduced in subsection 2.2.3.

A gradient discretization \mathcal{D} of (2.6) is defined by a vector space of degrees of freedom $X_{\mathcal{D}}$, its subspace associated with homogeneous Dirichlet boundary conditions $X_{\mathcal{D}}^0$, and the following set of linear operators:

- Three discrete gradient operators:
 $\nabla_{\mathcal{D}_m} : X_{\mathcal{D}} \rightarrow L^2(\Omega)^d$, $\nabla_{\mathcal{D}_f} : X_{\mathcal{D}} \rightarrow L^2(\Gamma_f)^{d-1}$, and $\nabla_{\mathcal{D}_g} : X_{\mathcal{D}} \rightarrow L^2(0, L)$
- Three function reconstruction operators:
 $\Pi_{\mathcal{D}_m} : X_{\mathcal{D}} \rightarrow L^2(\Omega)$, $\Pi_{\mathcal{D}_f} : X_{\mathcal{D}} \rightarrow L^2(\Gamma_f)$ and $\Pi_{\mathcal{D}_g} : X_{\mathcal{D}} \rightarrow L^2(0, L)$.

The vector space $X_{\mathcal{D}}$ is endowed with the semi-norm

$$\|v_{\mathcal{D}}\|_{\mathcal{D}} = \left(\|\nabla_{\mathcal{D}_m} v_{\mathcal{D}}\|_{L^2(\Omega)^d}^2 + \|\nabla_{\mathcal{D}_f} v_{\mathcal{D}}\|_{L^2(\Gamma_f)^{d-1}}^2 + \|\nabla_{\mathcal{D}_g} v_{\mathcal{D}}\|_{L^2(0,L)}^2 \right)^{\frac{1}{2}},$$

which is assumed to define a norm on $X_{\mathcal{D}}^0$. Next, we define the coercivity, consistency, and limit conformity properties for sequences of gradient discretizations.

Coercivity: Let $C_{\mathcal{D}} > 0$ be defined by

$$\max_{0 \neq v_{\mathcal{D}} \in X_{\mathcal{D}}^0} \frac{\|\Pi_{\mathcal{D}_m} v_{\mathcal{D}}\|_{L^2(\Omega)} + \|\Pi_{\mathcal{D}_f} v_{\mathcal{D}}\|_{L^2(\Gamma_f)} + \|\Pi_{\mathcal{D}_g} v_{\mathcal{D}}\|_{L^2(0,L)}}{\|v_{\mathcal{D}}\|_{\mathcal{D}}}. \quad (2.7)$$

Then, a sequence of gradient discretizations $(\mathcal{D}^l)_{l \in \mathbb{N}}$ is said to be coercive if there exists $C_P > 0$ such that $C_{\mathcal{D}^l} \leq C_P$ for all $l \in \mathbb{N}$.

Consistency: For all $u \in V^0$ and $v_{\mathcal{D}} \in X_{\mathcal{D}}^0$ let us define

$$\begin{aligned} S_{\mathcal{D}}(u, v_{\mathcal{D}}) &= \|\nabla_{\mathcal{D}_m} v_{\mathcal{D}} - \nabla u\|_{L^2(\Omega)^d} + \|\nabla_{\mathcal{D}_f} v_{\mathcal{D}} - \nabla_{\tau} \gamma_f u\|_{L^2(\Gamma_f)^{d-1}} + \|\nabla_{\mathcal{D}_g} v_{\mathcal{D}} - \partial_x \gamma u\|_{L^2(0,L)} \\ &\quad + \|\Pi_{\mathcal{D}_m} v_{\mathcal{D}} - u\|_{L^2(\Omega)} + \|\Pi_{\mathcal{D}_f} v_{\mathcal{D}} - \gamma_f u\|_{L^2(\Gamma_f)} + \|\Pi_{\mathcal{D}_g} v_{\mathcal{D}} - \gamma u\|_{L^2(0,L)}, \end{aligned} \quad (2.8)$$

and

$$\mathcal{S}_{\mathcal{D}}(u) = \min_{v_{\mathcal{D}} \in X_{\mathcal{D}}^0} S_{\mathcal{D}}(u, v_{\mathcal{D}}). \quad (2.9)$$

Then, a sequence of gradient discretizations $(\mathcal{D}^l)_{l \in \mathbb{N}}$ is said to be consistent if for all $u \in V^0$ one has $\lim_{l \rightarrow +\infty} \mathcal{S}_{\mathcal{D}^l}(u) = 0$.

Limit Conformity: For all $\mathbf{q} = (\mathbf{q}_m, \mathbf{q}_f, q_g) \in W$ and $v_{\mathcal{D}} \in X_{\mathcal{D}}^0$, let us define

$$\begin{aligned} W_{\mathcal{D}}(\mathbf{q}, v_{\mathcal{D}}) &= \int_{\Omega \setminus \Gamma_f} (\mathbf{q}_m \cdot \nabla_{\mathcal{D}_m} v_{\mathcal{D}} + \Pi_{\mathcal{D}_m} v_{\mathcal{D}} \operatorname{div}(\mathbf{q}_m)) d\mathbf{x} \\ &\quad + \int_{\Gamma_f} (\mathbf{q}_f \cdot \nabla_{\mathcal{D}_f} v_{\mathcal{D}} + r_f(\mathbf{q}) \Pi_{\mathcal{D}_f} v_{\mathcal{D}}) d\tau(\mathbf{x}) \\ &\quad + \int_0^L (q_g \nabla_{\mathcal{D}_g} v_{\mathcal{D}} + r_g(\mathbf{q}) \Pi_{\mathcal{D}_g} v_{\mathcal{D}}) dx. \end{aligned} \quad (2.10)$$

and

$$\mathcal{W}_{\mathcal{D}}(\mathbf{q}) = \max_{0 \neq v_{\mathcal{D}} \in X_{\mathcal{D}}^0} \frac{|W_{\mathcal{D}}(\mathbf{q}_m, \mathbf{q}_f, q_g, v_{\mathcal{D}})|}{\|v_{\mathcal{D}}\|_{\mathcal{D}}}. \quad (2.11)$$

Then, a sequence of gradient discretizations $(\mathcal{D}^l)_{l \in \mathbb{N}}$ is said to be limit conforming if for all $\mathbf{q} \in W$ one has $\lim_{l \rightarrow +\infty} \mathcal{W}_{\mathcal{D}^l}(\mathbf{q}) = 0$.

Application to 2.2.1

The gradient discretization of (2.6) with homogeneous Dirichlet boundary conditions is defined by: $u_{\mathcal{D}} \in X_{\mathcal{D}}^0$ such that

$$\begin{aligned} & \int_{\Omega} \mathbf{K}_m \nabla_{\mathcal{D}_m} u_{\mathcal{D}} \cdot \nabla_{\mathcal{D}_m} v_{\mathcal{D}} \, d\mathbf{x} + \int_{\Gamma_f} d_f \mathbf{K}_f \nabla_{\mathcal{D}_f} u_{\mathcal{D}} \cdot \nabla_{\mathcal{D}_f} v_{\mathcal{D}} \, d\tau(\mathbf{x}) \\ & + \int_0^L \frac{|S|}{\alpha_g} \nabla_{\mathcal{D}_g} u_{\mathcal{D}} \nabla_{\mathcal{D}_g} v_{\mathcal{D}} \, dx \\ & = \int_{\Omega} g_m \Pi_{\mathcal{D}_m} v_{\mathcal{D}} \, d\mathbf{x} + \int_{\Gamma_f} d_f g_f \Pi_{\mathcal{D}_f} v_{\mathcal{D}} \, d\tau(\mathbf{x}) + \int_0^L |S| g_g \Pi_{\mathcal{D}_g} v_{\mathcal{D}} \, dx, \end{aligned} \quad (2.12)$$

for all $v_{\mathcal{D}} \in X_{\mathcal{D}}^0$. Using the gradient scheme framework, we can state the following propositions providing the well posedness and the error estimates for (2.12).

Proposition 2.2.1 *Let \mathcal{D} be a gradient discretization of (2.6). Then (2.12) has a unique solution $u_{\mathcal{D}} \in X_{\mathcal{D}}^0$ satisfying the a priori estimate*

$$\|u_{\mathcal{D}}\|_{\mathcal{D}} \leq \frac{C_{\mathcal{D}}}{\min(\underline{\lambda}_m, \underline{\lambda}_f \underline{d}_f, \frac{|S|}{\alpha_g})} \left(\|g_m\|_{L^2(\Omega)} + \|d_f g_f\|_{L^2(\Gamma_f)} + |S| \|g_g\|_{L^2(0,L)} \right).$$

Proof: For any solution $u_{\mathcal{D}} \in X_{\mathcal{D}}^0$ of (2.12), setting $v_{\mathcal{D}} = u_{\mathcal{D}}$ in (2.12), and using the Cauchy Schwarz inequality, the definition (2.7) of $C_{\mathcal{D}}$, and the assumption that $\|\cdot\|_{\mathcal{D}}$ defines a norm on $X_{\mathcal{D}}^0$, we obtain the a priori estimate and hence the uniqueness and existence of a solution. \square

Proposition 2.2.2 Error estimates. *Let $u \in V^0$ be the solution of (2.6) and let us set $(\mathbf{q}_m, \mathbf{q}_f, q_g) = (-\mathbf{K}_m \nabla u, -d_f \mathbf{K}_f \nabla_{\tau} \gamma_f u, -\frac{|S|}{\alpha_g} \partial_x \gamma u) \in W$. Let \mathcal{D} be a gradient discretization of (2.6), and let $u_{\mathcal{D}} \in X_{\mathcal{D}}^0$ be the solution of (2.12). Then, there exist C_1, C_2 depending only on $\bar{\lambda}_m, \underline{\lambda}_m, \bar{\lambda}_f, \underline{\lambda}_f, \bar{d}_f, \underline{d}_f, \frac{|S|}{\alpha_g}, \frac{|S|}{\alpha_g}$, and C_3, C_4 depending only on $C_{\mathcal{D}}, \bar{\lambda}_m, \underline{\lambda}_m, \bar{\lambda}_f, \underline{\lambda}_f, \bar{d}_f, \underline{d}_f, \frac{|S|}{\alpha_g}, \frac{|S|}{\alpha_g}$, such that one has the following error estimates:*

$$\left\{ \begin{array}{l} \|\nabla u - \nabla_{\mathcal{D}_m} u_{\mathcal{D}}\|_{L^2(\Omega)^d} + \|\nabla_{\tau} \gamma_f u - \nabla_{\mathcal{D}_f} u_{\mathcal{D}}\|_{L^2(\Gamma_f)^{d-1}} + \|\partial_x \gamma u - \nabla_{\mathcal{D}_g} u_{\mathcal{D}}\|_{L^2(0,L)} \\ \leq C_1 \mathcal{S}_{\mathcal{D}}(u) + C_2 \mathcal{W}_{\mathcal{D}}(\mathbf{q}_m, \mathbf{q}_f, q_g), \\ \|\Pi_{\mathcal{D}_m} u_{\mathcal{D}} - u\|_{L^2(\Omega)} + \|\Pi_{\mathcal{D}_f} u_{\mathcal{D}} - \gamma_f u\|_{L^2(\Gamma_f)} + \|\gamma u - \Pi_{\mathcal{D}_g} u_{\mathcal{D}}\|_{L^2(0,L)} \\ \leq C_3 \mathcal{S}_{\mathcal{D}}(u) + C_4 \mathcal{W}_{\mathcal{D}}(\mathbf{q}_m, \mathbf{q}_f, q_g). \end{array} \right.$$

Proof: Using the definition of $\mathcal{W}_{\mathcal{D}}$ and the definition of the solution $u_{\mathcal{D}}$ of (2.12), we obtain that for all $v_{\mathcal{D}} \in X_{\mathcal{D}}^0$

$$\begin{aligned} & \left| \int_{\Omega} \left(\mathbf{K}_m \nabla_{\mathcal{D}_m} v_{\mathcal{D}} \cdot (\nabla u - \nabla_{\mathcal{D}_m} u_{\mathcal{D}}) \right) d\mathbf{x} + \int_{\Gamma_f} \left(d_f(\mathbf{x}) \mathbf{K}_f \nabla_{\mathcal{D}_f} v_{\mathcal{D}} \cdot (\nabla_{\tau} \gamma_f u - \nabla_{\mathcal{D}_f} u_{\mathcal{D}}) \right) d\tau(\mathbf{x}) \right. \\ & \quad \left. + \int_0^L \left(\frac{|S|}{\alpha_g} \nabla_{\mathcal{D}_g} v_{\mathcal{D}} \cdot (\partial_x \gamma u - \nabla_{\mathcal{D}_g} u_{\mathcal{D}}) \right) dx \right| \leq \|v_{\mathcal{D}}\|_{\mathcal{D}} \mathcal{W}_{\mathcal{D}}(\mathbf{q}_m, \mathbf{q}_f, q_g). \end{aligned}$$

Let us introduce $w_{\mathcal{D}} \in X_{\mathcal{D}}^0$ defined as

$$w_{\mathcal{D}} = \operatorname{argmin}_{v_{\mathcal{D}} \in X_{\mathcal{D}}^0} S_{\mathcal{D}}(u, v_{\mathcal{D}}),$$

and let us set in the previous estimate $v_{\mathcal{D}} = w_{\mathcal{D}} - u_{\mathcal{D}}$. Applying the Cauchy Schwarz inequality, we obtain the first estimate. In addition, from the definition of $C_{\mathcal{D}}$, we have that

$$\|\Pi_{\mathcal{D}_m}(w_{\mathcal{D}} - u_{\mathcal{D}})\|_{L^2(\Omega)} + \|\Pi_{\mathcal{D}_f}(w_{\mathcal{D}} - u_{\mathcal{D}})\|_{L^2(\Gamma_f)} + \|\Pi_{\mathcal{D}_g}(w_{\mathcal{D}} - u_{\mathcal{D}})\|_{L^2(0,L)} \leq C_{\mathcal{D}} \|w_{\mathcal{D}} - u_{\mathcal{D}}\|_{\mathcal{D}},$$

which proves the second estimate using the definition of $w_{\mathcal{D}}$. \square

2.2.3 VAG Discretization of the model problem

The VAG discretization [32] is a finite volume discretization of diffusion problem adapted to general meshes and heterogenous anisotropic media. It is here extended to our model problem coupling the 3D Darcy flow in the porous medium, the 2D Darcy flow in the fracture network and the 1D Darcy flow in the gallery.

On the porous medium side, we follow the discretization introduced in [12] accounting for general fracture networks. At the interface Γ between the porous medium and the gallery, a non conforming discretization is considered to allow for fairly general meshes at the interface. A simple matching condition is used by imposing the jump of u to vanish at the nodes on the porous medium side located at the interface Γ . This simple strategy is shown in subsection 2.2.4 to preserve the optimal order of convergence provided that the meshes in the gallery and in the porous medium satisfy compatibility conditions which are not very restrictive in practice (see Proposition 2.2.3).

Alternatively, we could investigate the use of a mixed formulation with Lagrange multipliers at the interface Γ in the spirit of Mortar methods [8] to avoid such condition on the meshes. The main advantage of our approach is to avoid the solution of a saddle point problem and to easily extend to compositional models.

We consider a conforming polyhedral mesh of the domain Ω . Let \mathcal{M} denote the set of cells K , \mathcal{V} the set of vertices \mathbf{s} , \mathcal{E} the set of edges e , and \mathcal{F} the set of faces σ , of the mesh. We denote by \mathcal{V}_K the set of vertices of each cell $K \in \mathcal{M}$, by \mathcal{M}_s the set of cells sharing the node s , by \mathcal{V}_{σ} the set of nodes and by \mathcal{E}_{σ} the set of edges of the face $\sigma \in \mathcal{F}$. The set \mathcal{M}_{σ} is the set of cells shared by the face $\sigma \in \mathcal{F}$. We denote by $\mathcal{V}_{\Gamma} = \mathcal{V} \cap \bar{\Gamma}$ the

set of nodes belonging to the boundary Γ of the gallery, and by $\mathcal{V}_D = \mathcal{V} \cap \Gamma_D$ the set of Dirichlet boundary nodes. In the following, for a d dimensional domain A , $|A|$ will denote the Lebesgue d -dimensional measure of A .

It is assumed that for each face $\sigma \in \mathcal{F}$, there exists a so-called “centre” of the face \mathbf{x}_σ such that $\mathbf{x}_\sigma = \frac{1}{\text{Card}(\mathcal{V}_\sigma)} \sum_{\mathbf{s} \in \mathcal{V}_\sigma} \mathbf{x}_\mathbf{s}$. The face σ is assumed to be star-shaped w.r.t. its centre \mathbf{x}_σ which means that the face σ matches with the union of the triangles $\tau_{\sigma,e}$ defined by the face centre \mathbf{x}_σ and each of its edge $e \in \mathcal{E}_\sigma$.

The porous medium mesh is assumed to be conforming with respect to the fracture network as well as with the boundary $\partial\Omega$. In particular, there exists $\mathcal{F}_{\Gamma_f} \subset \mathcal{F}$ such that

$$\bar{\Gamma}_f = \bigcup_{\sigma \in \mathcal{F}_{\Gamma_f}} \bar{\sigma}.$$

Let us denote by $\mathcal{F}_{\Gamma_f, \mathbf{s}}$ the set of fracture faces sharing the node $\mathbf{s} \in \mathcal{V}_{\Gamma_f} = \mathcal{V} \cap \bar{\Gamma}_f$.

A finite element 1D mesh is defined in the gallery $(0, L)$ by the set of nodal points $0 = x_0 < \dots < x_m < x_{m+1} < \dots < x_{m_x+1} = L$ and we set $h_{m+\frac{1}{2}} = |x_{m+1} - x_m|$ for all $m = 0, \dots, m_x$.

The \mathbb{P}_1 finite element nodal basis defined on this 1D mesh is denoted by η_m , $m = 0, \dots, m_x + 1$.

Setting $x_{m+\frac{1}{2}} = \frac{x_m + x_{m+1}}{2}$ for all $m = 1, \dots, m_x - 1$, and $x_{\frac{1}{2}} = 0$, $x_{m_x+\frac{1}{2}} = L$, we define the m_x 1D cells $k_m = (x_{m-\frac{1}{2}}, x_{m+\frac{1}{2}})$.

The previous discretization is denoted by \mathcal{D} . Let us define the vector space

$$X_{\mathcal{D}_p} = \{v_K \in \mathbb{R}, v_{\mathbf{s}} \in \mathbb{R}, v_\sigma \in \mathbb{R}, K \in \mathcal{M}, \mathbf{s} \in \mathcal{V}, \sigma \in \mathcal{F}_{\Gamma_f}\},$$

of degrees of freedom (d.o.f.) located at the cell centres, fracture face centres, and at the nodes of the porous medium mesh, and the vector space

$$X_{\mathcal{D}_g} = \{v_m \in \mathbb{R}, m = 0, \dots, m_x + 1\},$$

of d.o.f. located at the nodal points of the gallery $(0, L)$ (see Figure 2.2).

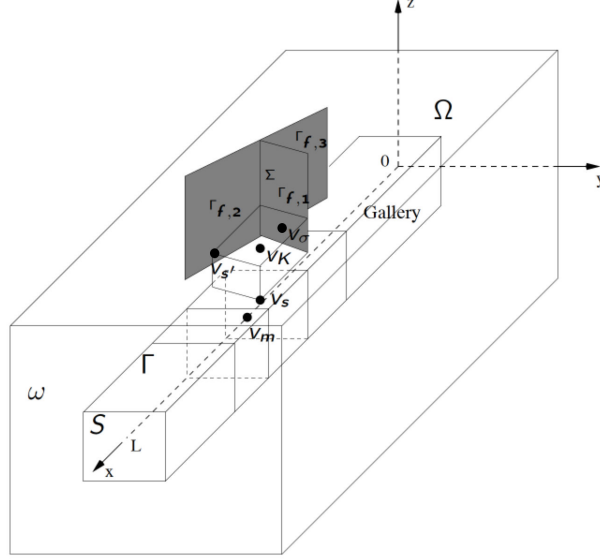


Figure 2.2: Simplified Cartesian geometry with the d.o.f. located at the cell centres, fracture face centres, nodes of the porous medium mesh, and at the nodal points of the gallery $(0, L)$.

The extension of the VAG discretization [32] to our coupled model is based on conforming Finite Element reconstructions of the gradient operators on Ω , on Γ_f , and on $(0, L)$, and on non conforming piecewise constant function reconstructions on Ω , on Γ_f , and on $(0, L)$.

For all $\sigma \in \mathcal{F}$, let us first define the operator $I_\sigma : X_{\mathcal{D}_p} \rightarrow \mathbb{R}$ such that

$$I_\sigma(v_{\mathcal{D}}) = \frac{1}{\text{Card}(\mathcal{V}_\sigma)} \sum_{\mathbf{s} \in \mathcal{V}_\sigma} v_{\mathbf{s}},$$

which is by definition of \mathbf{x}_σ a second order interpolation operator at point \mathbf{x}_σ .

Let us introduce the tetrahedral sub-mesh $\mathcal{T} = \{T_{K,\sigma,e}, e \in \mathcal{E}_\sigma, \sigma \in \mathcal{F}_K, K \in \mathcal{M}\}$ of the porous medium mesh, where $T_{K,\sigma,e}$ is the tetrahedron defined by the cell center \mathbf{x}_K and the triangle $\tau_{\sigma,e}$. For a given $v_{\mathcal{D}_p} \in X_{\mathcal{D}_p}$, we define the function $\Pi_{\mathcal{T}} v_{\mathcal{D}_p} \in C^0(\overline{\Omega})$ as the continuous piecewise affine function on each tetrahedron of \mathcal{T} such that $\Pi_{\mathcal{T}} v_{\mathcal{D}_p}(\mathbf{x}_K) = v_K$, $\Pi_{\mathcal{T}} v_{\mathcal{D}_p}(\mathbf{s}) = v_{\mathbf{s}}$, $\Pi_{\mathcal{T}} v_{\mathcal{D}_p}(\mathbf{x}_\sigma) = v_\sigma$, and $\Pi_{\mathcal{T}} v_{\mathcal{D}_p}(\mathbf{x}_{\sigma'}) = I_{\sigma'}(v)$ for all $K \in \mathcal{M}$, $\mathbf{s} \in \mathcal{V}$, $\sigma \in \mathcal{F}_{\Gamma_f}$, and $\sigma' \in \mathcal{F} \setminus \mathcal{F}_{\Gamma_f}$.

The nodal finite element basis of $\Pi_{\mathcal{T}} X_{\mathcal{D}_p}$ is denoted by η_ν , $\nu \in \mathcal{M} \cup \mathcal{V} \cup \mathcal{F}_{\Gamma_f}$ such that $\eta_\nu(\mathbf{x}_{\nu'}) = \delta_{\nu,\nu'}$ for all $\nu, \nu' \in \mathcal{M} \cup \mathcal{V} \cup \mathcal{F}_{\Gamma_f}$.

Then, we define for all $v_{\mathcal{D}_p} \in X_{\mathcal{D}_p}$ the following gradient operators

$$\nabla_{\mathcal{D}_m} v_{\mathcal{D}_p} : X_{\mathcal{D}_p} \rightarrow L^2(\Omega)^d \text{ such that } \nabla_{\mathcal{D}_m} v_{\mathcal{D}_p} = \nabla \Pi_{\mathcal{T}} v_{\mathcal{D}_p}, \quad (2.13)$$

in the matrix, and

$$\nabla_{\mathcal{D}_f} v_{\mathcal{D}_p} : X_{\mathcal{D}_p} \rightarrow L^2(\Gamma_f)^{d-1} \text{ such that } \nabla_{\mathcal{D}_f} v_{\mathcal{D}_p} = \nabla_\tau \gamma_f \Pi_{\mathcal{T}} v_{\mathcal{D}_p}. \quad (2.14)$$

in the fracture network. In the gallery, the gradient operator $\nabla_{\mathcal{D}_g}$ from $X_{\mathcal{D}_g}$ to $L^2(0, L)$ is defined by

$$\nabla_{\mathcal{D}_g} v_{\mathcal{D}_g}(x) = \frac{v_{m+1} - v_m}{h_{m+\frac{1}{2}}} \text{ for all } x \in (x_m, x_{m+1}), m = 0, \dots, m_x. \quad (2.15)$$

In addition to these conforming gradient operators, the VAG discretization uses non conforming piecewise constant reconstructions of functions from $X_{\mathcal{D}_p}$ into $L^2(\Omega)$ and $L^2(\Gamma_f)$, and from $X_{\mathcal{D}_g}$ into $L^2(0, L)$.

Let us introduce the following partition of each cell $K \in \mathcal{M}$

$$\overline{K} = \overline{\omega}_K \bigcup \left(\bigcup_{\mathbf{s} \in \mathcal{V}_K \setminus (\mathcal{V}_D \cup \mathcal{V}_\Gamma \cup \mathcal{V}_{\Gamma_f})} \overline{\omega}_{K,\mathbf{s}} \right)$$

Then, we define the function reconstruction operator in the matrix

$$\Pi_{\mathcal{D}_m} v_{\mathcal{D}_p}(\mathbf{x}) = \begin{cases} v_K & \text{for all } \mathbf{x} \in \omega_K, K \in \mathcal{M}, \\ v_{\mathbf{s}} & \text{for all } \mathbf{x} \in \omega_{K,\mathbf{s}}, \mathbf{s} \in \mathcal{V}_K \setminus (\mathcal{V}_D \cup \mathcal{V}_\Gamma \cup \mathcal{V}_{\Gamma_f}), K \in \mathcal{M}. \end{cases} \quad (2.16)$$

Similarly, let us define the partition of each fracture face $\sigma \in \mathcal{F}_{\Gamma_f}$ by

$$\overline{\sigma} = \overline{\omega}_\sigma \bigcup \left(\bigcup_{\mathbf{s} \in \mathcal{V}_\sigma \setminus (\mathcal{V}_D \cup \mathcal{V}_\Gamma)} \overline{\omega}_{\sigma,\mathbf{s}} \right),$$

and the function reconstruction operator in the fracture network by

$$\Pi_{\mathcal{D}_f} v_{\mathcal{D}_p}(\mathbf{x}) = \begin{cases} v_\sigma & \text{for all } \mathbf{x} \in \omega_\sigma, \sigma \in \mathcal{F}_{\Gamma_f}, \\ v_{\mathbf{s}} & \text{for all } \mathbf{x} \in \omega_{\sigma,\mathbf{s}}, \mathbf{s} \in \mathcal{V}_\sigma \setminus (\mathcal{V}_D \cup \mathcal{V}_\Gamma), \sigma \in \mathcal{F}_{\Gamma_f}. \end{cases} \quad (2.17)$$

In the gallery, the reconstruction operator is defined by

$$\Pi_{\mathcal{D}_g} v_{\mathcal{D}_g}(x) = v_m \text{ for all } x \in (x_{m-\frac{1}{2}}, x_{m+\frac{1}{2}}), m = 1, \dots, m_x. \quad (2.18)$$

Note that $\Pi_{\mathcal{D}_m} v_{\mathcal{D}_p}$ does not depend on $v_{\mathbf{s}}$ for $\mathbf{s} \in \mathcal{V}_\Gamma \cup \mathcal{V}_{\Gamma_f}$ and that $\Pi_{\mathcal{D}_f} v_{\mathcal{D}_p}$ does not depend on $v_{\mathbf{s}}$ for $\mathbf{s} \in \mathcal{V}_\Gamma \cap \mathcal{V}_{\Gamma_f}$. This property of the operators $\Pi_{\mathcal{D}_m}$ and $\Pi_{\mathcal{D}_f}$ avoids the mixing of the matrix and fractures in the control volumes located at nodes $\mathbf{s} \in \mathcal{V}_{\Gamma_f}$, as well as the mixing of the porous medium and the gallery in control volumes located at nodes $\mathbf{s} \in \mathcal{V}_\Gamma$. This is a crucial property to extend the VAG discretization to the compositional model taking into account the highly contrasted material properties or the different models in the gallery, in the fractures, and in the matrix.

Finally, let us define the interpolation operator $\mathcal{P}_{\mathbf{s}}$ reconstructing the value $u_{\mathbf{s}}$ at point $\mathbf{x}_{\mathbf{s}}$ for $\mathbf{s} \in \mathcal{V}_\Gamma$ as a function of the vector of d.o.f. $u_{\mathcal{D}_g} \in X_{\mathcal{D}_g}$ in the gallery:

$$\mathcal{P}_{\mathbf{s}} u_{\mathcal{D}_g} = \sum_{m=0}^{m_x+1} \alpha_{m,\mathbf{s}} u_m,$$

with $\alpha_{m,\mathbf{s}} = \eta_m(x_{\mathbf{s}})$. From this definition of $\mathcal{P}_{\mathbf{s}}$, we can define the vector space $X_{\mathcal{D}}$ of discrete unknowns as the following subspace of $X_{\mathcal{D}_p} \times X_{\mathcal{D}_g}$

$$X_{\mathcal{D}} = \{(v_{\mathcal{D}_p}, v_{\mathcal{D}_g}) \in X_{\mathcal{D}_p} \times X_{\mathcal{D}_g} \mid v_{\mathbf{s}} = \mathcal{P}_{\mathbf{s}} v_{\mathcal{D}_g} \text{ for all } \mathbf{s} \in \mathcal{V}_{\Gamma}\}.$$

Its subspace with homogeneous Dirichlet boundary conditions is denoted by

$$X_{\mathcal{D}}^0 = \{v_{\mathcal{D}} \in X_{\mathcal{D}} \mid v_{\mathbf{s}} = 0 \text{ for all } \mathbf{s} \in \mathcal{V}_D, \text{ and } v_0 = v_{m_x+1} = 0\}. \quad (2.19)$$

The previous gradient and function reconstruction operators will be applied on vectors of $X_{\mathcal{D}}$ keeping the same notations for convenience sake.

The VAG gradient discretization is defined by the vector space of d.o.f. (2.19), by the discrete gradient operators (2.13), (2.14), (2.15), and by the function reconstruction operators (2.16), (2.17), (2.18). Then, the VAG discretization of the model problem (2.6) is directly given by (2.12).

In order to write the equivalent finite volume formulation of (2.12), let us define for all $u_{\mathcal{D}} \in X_{\mathcal{D}}$ the matrix fluxes

$$V_{K,\nu}(u_{\mathcal{D}}) = \sum_{\nu' \in \Xi_K} T_K^{\nu,\nu'}(u_K - u_{\nu'}), \quad (2.20)$$

connecting each cell K to its d.o.f. $\nu \in \Xi_K$ with $\Xi_K = \mathcal{V}_K \cup (\mathcal{F}_K \cap \mathcal{F}_{\Gamma_f})$ and

$$T_K^{\nu,\nu'} = \int_K \mathbf{K}_m \nabla \eta_{\nu} \cdot \nabla \eta_{\nu'} d\mathbf{x}.$$

Similarly, the fracture fluxes defined by

$$V_{\sigma,\mathbf{s}}(u_{\mathcal{D}}) = \sum_{\nu' \in \mathcal{V}_{\sigma}} T_{\sigma}^{\mathbf{s},\nu'}(u_{\sigma} - u_{\nu'}), \quad (2.21)$$

connect each fracture face σ to its nodes $\mathbf{s} \in \mathcal{V}_{\sigma}$ where

$$T_{\sigma}^{\mathbf{s},\mathbf{s}'} = \int_{\sigma} d_f \mathbf{K}_f \nabla_{\tau} \gamma_f \eta_{\mathbf{s}} \cdot \nabla_{\tau} \gamma_f \eta_{\mathbf{s}'} d\tau(\mathbf{x}).$$

On the gallery side, we similarly define for all $u_{\mathcal{D}} \in X_{\mathcal{D}}$ the fluxes

$$V_{m,m+1}(u_{\mathcal{D}}) = T_{m+\frac{1}{2}}(u_m - u_{m+1}), \quad (2.22)$$

connecting m to $m+1$ for all $m = 0, \dots, m_x$, where

$$T_{m+\frac{1}{2}} = \frac{|S|}{h_{m+\frac{1}{2}}^2} \int_{x_m}^{x_{m+1}} \frac{dx}{\alpha_g(x)}.$$

Let us set for the source terms in the matrix

$$g_{m,K} = \frac{1}{|\omega_K|} \int_{\omega_K} g_m(\mathbf{x}) d\mathbf{x}, \quad g_{m,K,\mathbf{s}} = \frac{1}{|\omega_{K,\mathbf{s}}|} \int_{\omega_{K,\mathbf{s}}} g_m(\mathbf{x}) d\mathbf{x},$$

and $\alpha_{K,\mathbf{s}} = \frac{|\omega_{K,\mathbf{s}}|}{|K|}$ for all $\mathbf{s} \in \mathcal{V}_K \setminus (\mathcal{V}_D \cup \mathcal{V}_\Gamma \cup \mathcal{V}_{\Gamma_f})$ and $K \in \mathcal{M}$. Similarly, we set in the fracture network

$$g_{f,\sigma} = \frac{1}{|\omega_\sigma|} \int_{\omega_\sigma} d_f(\mathbf{x}) g_f(\mathbf{x}) d\tau(\mathbf{x}), \quad g_{f,\sigma,\mathbf{s}} = \frac{1}{|\omega_{\sigma,\mathbf{s}}|} \int_{\omega_{\sigma,\mathbf{s}}} d_f(\mathbf{x}) g_f(\mathbf{x}) d\tau(\mathbf{x}),$$

and $\alpha_{\sigma,\mathbf{s}} = \frac{|\omega_{\sigma,\mathbf{s}}|}{|\sigma|}$ for all $\mathbf{s} \in \mathcal{V}_\sigma \setminus (\mathcal{V}_D \cup \mathcal{V}_\Gamma)$ and $\sigma \in \mathcal{F}_{\Gamma_f}$.

Then, the variational formulation (2.12) is equivalent to find $u_{\mathcal{D}} \in X_{\mathcal{D}}^0$ satisfying the discrete conservation equations in the porous medium

$$\left\{ \begin{array}{l} \sum_{\nu \in \Xi_K} V_{K,\nu}(u_{\mathcal{D}}) = (1 - \sum_{\mathbf{s} \in \mathcal{V}_K \setminus (\mathcal{V}_D \cup \mathcal{V}_\Gamma \cup \mathcal{V}_{\Gamma_f})} \alpha_{K,\mathbf{s}}) |K| g_{m,K}, \quad K \in \mathcal{M}, \\ \sum_{\mathbf{s} \in \mathcal{V}_\sigma} V_{\sigma,\mathbf{s}}(u_{\mathcal{D}}) - \sum_{K \in \mathcal{M}_\sigma} V_{K,\sigma}(u_{\mathcal{D}}) = (1 - \sum_{\mathbf{s} \in \mathcal{V}_\sigma \setminus (\mathcal{V}_D \cup \mathcal{V}_\Gamma)} \alpha_{\sigma,\mathbf{s}}) |\sigma| g_{f,\sigma}, \quad \sigma \in \mathcal{F}_{\Gamma_f}, \\ - \sum_{K \in \mathcal{M}_\mathbf{s}} V_{K,\mathbf{s}}(u_{\mathcal{D}}) = \sum_{K \in \mathcal{M}_\mathbf{s}} \alpha_{K,\mathbf{s}} |K| g_{m,K,\mathbf{s}}, \quad \mathbf{s} \in \mathcal{V} \setminus (\mathcal{V}_D \cup \mathcal{V}_\Gamma \cup \mathcal{V}_{\Gamma_f}), \\ - \sum_{K \in \mathcal{M}_\mathbf{s}} V_{K,\mathbf{s}}(u_{\mathcal{D}}) - \sum_{\sigma \in \mathcal{F}_{\Gamma_f,\mathbf{s}}} V_{\sigma,\mathbf{s}}(u_{\mathcal{D}}) \\ = \sum_{\sigma \in \mathcal{F}_{\Gamma_f,\mathbf{s}}} \alpha_{\sigma,\mathbf{s}} |\sigma| g_{f,\sigma,\mathbf{s}}, \quad \mathbf{s} \in \mathcal{V}_{\Gamma_f} \setminus (\mathcal{V}_D \cup \mathcal{V}_\Gamma), \end{array} \right. \quad (2.23)$$

coupled with the conservation equations in the gallery for $m = 1, \dots, m_x$

$$\begin{aligned} V_{m,m+1}(u_{\mathcal{D}}) - V_{m-1,m}(u_{\mathcal{D}}) &= \int_{x_{m-1/2}}^{x_{m+1/2}} |S| g_g dx \\ &+ \sum_{\mathbf{s} \in \mathcal{V}_\Gamma} \alpha_{m,\mathbf{s}} \left(\sum_{K \in \mathcal{M}_\mathbf{s}} V_{K,\mathbf{s}}(u_{\mathcal{D}}) + \sum_{\sigma \in \mathcal{F}_{\Gamma_f,\mathbf{s}}} V_{\sigma,\mathbf{s}}(u_{\mathcal{D}}) \right). \end{aligned} \quad (2.24)$$

2.2.4 Convergence analysis of the VAG discretization of the model problem

It will be assumed for the convergence analysis that the family of tetrahedral submeshes \mathcal{T} of the porous medium domain Ω is shape regular. Hence we consider the mesh shape regularity parameter

$$\theta_{\mathcal{T}} = \max_{T \in \mathcal{T}} \frac{h_T}{\rho_T},$$

and the mesh size

$$h_{\mathcal{T}} = \max_{T \in \mathcal{T}} h_T,$$

where h_T denotes the diameter of the tetrahedron T and ρ_T the diameter of the insphere of T . For the 1D mesh in the gallery we set

$$h_{\mathcal{D}_g} = \max_{m=0, \dots, m_x} h_{m+\frac{1}{2}}.$$

Let us define the linear mapping $\bar{\Pi}_{\mathcal{D}_g}$ from $X_{\mathcal{D}}^0$ to $H_0^1(0, L)$ such that

$$\bar{\Pi}_{\mathcal{D}_g} v_{\mathcal{D}} = \sum_{m=0}^{m_x+1} u_m \eta_m(x)$$

and let us recall that

$$\nabla_{\mathcal{D}_g} = \partial_x \bar{\Pi}_{\mathcal{D}_g}.$$

Lemma 2.2.3 *For all $v_{\mathcal{D}} \in X_{\mathcal{D}}$ one has the estimate*

$$\|\gamma \Pi_{\mathcal{T}} v_{\mathcal{D}} - \bar{\Pi}_{\mathcal{D}_g} v_{\mathcal{D}}\|_{L^2(\Gamma)} \leq (8|\partial S|)^{\frac{1}{2}} (h_{\mathcal{T}} + h_{\mathcal{D}_g}) \|\nabla_{\mathcal{D}_g} v_{\mathcal{D}}\|_{L^2(0, L)}.$$

Proof: Let us consider the points $\bar{x}_k \in (0, L)$, $k = 0, \dots, N$ such that $\bar{x}_0 = 0$, $\bar{x}_N = L$, $\bar{x}_{k+1} - \bar{x}_k = h_{\mathcal{T}}$ for all $k = 0, \dots, N-2$, and $0 < \bar{x}_N - \bar{x}_{N-1} \leq h_{\mathcal{T}}$. We consider the overlapping decomposition of Γ defined by $(\bar{x}_k, \bar{x}_{k+2}) \times \partial S$ for $k = 0, \dots, N-2$. Let $k \in \{0, \dots, N-2\}$ be given, and let us set $m_{1,k} = \operatorname{argmax}\{m \in \{0, \dots, m_x+1\} \mid \bar{x}_k \geq x_m\}$, $m_{2,k} = \operatorname{argmin}\{m \in \{0, \dots, m_x+1\} \mid \bar{x}_{k+2} \leq x_m\}$, and $\mathcal{F}_{\Gamma}^k = \{\sigma \in \mathcal{F}_{\Gamma} \mid \sigma \subset [\bar{x}_k, \bar{x}_{k+2}] \times \partial S\}$. Then, it follows that

$$\begin{aligned} & \|\gamma \Pi_{\mathcal{T}} v_{\mathcal{D}} - \bar{\Pi}_{\mathcal{D}_g} v_{\mathcal{D}}\|_{L^2(\Gamma)}^2 \\ & \leq \sum_{k \in \{0, \dots, N-2\} \mid m_{2,k} > m_{1,k}+1} \sum_{\sigma \in \mathcal{F}_{\Gamma}^k} |\sigma| \left(\max_{m \in \{m_{1,k}, \dots, m_{2,k}\}} v_m - \min_{m \in \{m_{1,k}, \dots, m_{2,k}\}} v_m \right)^2 \\ & \leq 2h_{\mathcal{T}}(2h_{\mathcal{T}} + 2h_{\mathcal{D}_g}) |\partial S| \sum_{k \in \{0, \dots, N-2\} \mid m_{2,k} > m_{1,k}+1} \sum_{m_{1,k}}^{m_{2,k}-1} \frac{|v_{m+1} - v_m|^2}{h_{m+\frac{1}{2}}} \\ & \leq 4h_{\mathcal{T}}(2h_{\mathcal{T}} + 2h_{\mathcal{D}_g}) |\partial S| \sum_{m=0}^{m_x} \frac{|v_{m+1} - v_m|^2}{h_{m+\frac{1}{2}}} = 8|\partial S| h_{\mathcal{T}} (h_{\mathcal{T}} + h_{\mathcal{D}_g}) \|\nabla_{\mathcal{D}_g} v_{\mathcal{D}}\|_{L^2(0, L)}^2. \end{aligned}$$

□

Lemma 2.2.4 *For all $v_{\mathcal{D}} \in X_{\mathcal{D}}$, there exists a constant C depending only on the fracture network and on the domain Ω such that*

$$\|\gamma_{\Sigma_{\Gamma}} \gamma_f \Pi_{\mathcal{T}} v_{\mathcal{D}} - \gamma_{\Sigma_{\Gamma}} \bar{\Pi}_{\mathcal{D}_g} v_{\mathcal{D}}\|_{L^2(\Sigma_{\Gamma})} \leq C(h_{\mathcal{T}} + h_{\mathcal{D}_g}) \|\nabla_{\mathcal{D}_g} v_{\mathcal{D}}\|_{L^2(0, L)}.$$

Proof: the set $\bar{\Sigma}_\Gamma$ is the union of a finite number of segments depending only on Γ_f and Γ . Let us consider such a segment denoted by $[\mathbf{x}_{s_1}, \mathbf{x}_{s_2}]$, and let us define $\mathcal{E}_{\mathbf{x}_{s_1}\mathbf{x}_{s_2}} = \{e \in \mathcal{E} \mid e \subset [\mathbf{x}_{s_1}, \mathbf{x}_{s_2}]\}$, $m_1 = \operatorname{argmax}\{m \in \{0, \dots, m_x + 1\} \mid x_{s_1} \geq x_m\}$ and $m_2 = \operatorname{argmin}\{m \in \{0, \dots, m_x + 1\} \mid x_{s_2} \leq x_m\}$, $m_1(e) = \operatorname{argmax}\{m \in \{0, \dots, m_x + 1\} \mid x_s \geq x_m, \forall \mathbf{s} \in \mathcal{V}_e\}$ and $m_2(e) = \operatorname{argmin}\{m \in \{0, \dots, m_x + 1\} \mid x_s \leq x_m, \forall \mathbf{s} \in \mathcal{V}_e\}$. It follows that

$$\begin{aligned}
& \|\gamma_{\Sigma_\Gamma} \gamma_f \Pi_T v_D - \gamma_{\Sigma_\Gamma} \bar{\Pi}_{\mathcal{D}_g} v_D\|_{L^2(\mathbf{x}_{s_1}, \mathbf{x}_{s_2})}^2 \\
& \leq \sum_{e \in \mathcal{E}_{\mathbf{x}_{s_1}\mathbf{x}_{s_2}} \mid m_2(e) > m_1(e)+1} |e| \left(\max_{m \in \{m_1(e), \dots, m_2(e)\}} v_m - \min_{m \in \{m_1(e), \dots, m_2(e)\}} v_m \right)^2 \\
& \leq \sum_{e \in \mathcal{E}_{\mathbf{x}_{s_1}\mathbf{x}_{s_2}} \mid m_2(e) > m_1(e)+1} |e| \sum_{m_1(e)}^{m_2(e)-1} \frac{|v_{m+1} - v_m|^2}{h_{m+\frac{1}{2}}} (h_\mathcal{T} + 2h_{\mathcal{D}_g}) \\
& \leq 2h_\mathcal{T}(h_\mathcal{T} + 2h_{\mathcal{D}_g}) \sum_{m=m_1}^{m_2-1} \frac{|v_{m+1} - v_m|^2}{h_{m+\frac{1}{2}}} = 2h_\mathcal{T}(h_\mathcal{T} + 2h_{\mathcal{D}_g}) \|\nabla_{\mathcal{D}_g} v_D\|_{L^2(0,L)}^2.
\end{aligned}$$

□

For all $u \in \mathcal{C}_{V_0}^\infty$, let us define $P_{\mathcal{D}_g} u \in X_{\mathcal{D}_g}$ such that $(P_{\mathcal{D}_g} u)_m = \gamma u(x_m)$ for all $m = 0, \dots, m_x + 1$, and $P_{\mathcal{D}_p} u \in X_{\mathcal{D}_p}$ such that $(P_{\mathcal{D}_p} u)_\mathbf{s} = u(\mathbf{x}_\mathbf{s})$ for all $\mathbf{s} \in \mathcal{V}$, $(P_{\mathcal{D}_p} u)_\sigma = u(\mathbf{x}_\sigma)$ for all $\sigma \in \mathcal{F}_{\Gamma_f}$, $(P_{\mathcal{D}_p} u)_K = u(\mathbf{x}_K)$ for all $K \in \mathcal{M}$.

Let us also define for all $u \in \mathcal{C}_{V_0}^\infty$, $P_{\mathcal{D}} u \in X_{\mathcal{D}}^0$ such that $(P_{\mathcal{D}} u)_\mathbf{s} = u(\mathbf{x}_\mathbf{s})$ for all $\mathbf{s} \in \mathcal{V} \setminus \mathcal{V}_\Gamma$, $(P_{\mathcal{D}} u)_\sigma = u(\mathbf{x}_\sigma)$ for all $\sigma \in \mathcal{F}_{\Gamma_f}$, $(P_{\mathcal{D}} u)_K = u(\mathbf{x}_K)$ for all $K \in \mathcal{M}$, $(P_{\mathcal{D}} u)_\mathbf{s} = \mathcal{P}_\mathbf{s}(P_{\mathcal{D}_g} u)$ for all $\mathbf{s} \in \mathcal{V}_\Gamma$, and $(P_{\mathcal{D}} u)_m = \gamma u(x_m)$ for all $m = 0, \dots, m_x + 1$.

Lemma 2.2.5 *For all $u \in \mathcal{C}_{V_0}^\infty$, there exists a constant $C(u, \theta_\mathcal{T})$ depending on u and $\theta_\mathcal{T}$ such that*

$$\|\nabla_{\mathcal{D}_m} P_{\mathcal{D}} u - \nabla u\|_{L^2(\Omega)^d} \leq C(u, \theta_\mathcal{T}) \left(h_\mathcal{T} + h_{\mathcal{D}_g} \max_{\sigma \in \mathcal{F}_\Gamma} \left(\frac{h_\sigma}{\operatorname{diam}(\sigma)^{\frac{1}{2}}} \right) \right),$$

where $h_\sigma = \max_{\mathbf{s} \in \mathcal{V}_\sigma} \left(|x_\mathbf{s} - x_{m(\mathbf{s})}| |x_\mathbf{s} - x_{m(\mathbf{s})+1}| \right)^{\frac{1}{2}}$ with $m(\mathbf{s}) \in \{0, \dots, m_x\}$ such that $x_\mathbf{s} \in [x_{m(\mathbf{s})}, x_{m(\mathbf{s})+1}]$.

Proof: From Lemma 3.2 of [14], there exist two constants $C(u)$ and $C(\theta_\mathcal{T})$ such that

$$\begin{aligned}
\|\nabla_{\mathcal{D}_m} (P_{\mathcal{D}} u - P_{\mathcal{D}_p} u)\|_{L^2(\Omega)^d}^2 & \leq C(\theta_\mathcal{T}) \sum_{\sigma \in \mathcal{F}_\Gamma} \sum_{\mathbf{s} \in \mathcal{V}_\sigma} \operatorname{diam}(\sigma) \left(u(\mathbf{x}_\mathbf{s}) - \mathcal{P}_\mathbf{s}(P_{\mathcal{D}_g} u) \right)^2 \\
& \leq C(\theta_\mathcal{T}) C(u) \sum_{\sigma \in \mathcal{F}_\Gamma} h_\sigma^4 \operatorname{diam}(\sigma).
\end{aligned}$$

It is classical from \mathbb{P}_1 finite element approximation that there exists a constant $C(\theta_\mathcal{T}, u)$ such that $\|\nabla_{\mathcal{D}_m} P_{\mathcal{D}_p} u - \nabla u\|_{L^2(\Omega)^d} \leq C(\theta_\mathcal{T}, u) h_\mathcal{T}$. Combining the two previous estimates, we obtain the estimate of Lemma 2.2.5. □

Lemma 2.2.6 *For all $u \in C_{V0}^\infty$, there exist a constant $C(u, \theta_\mathcal{T})$ depending on u and $\theta_\mathcal{T}$ such that*

$$\|\nabla_{\mathcal{D}_f} P_{\mathcal{D}} u - \nabla_\tau \gamma_f u\|_{L^2(\Gamma_f)^{d-1}} \leq C(u, \theta_\mathcal{T}) \left(h_\mathcal{T} + h_{\mathcal{D}_g} \max_{e \in \mathcal{E}_\Gamma \cap \mathcal{E}_{\Gamma_f}} \left(\frac{h_e}{\text{diam}(e)^{\frac{1}{2}}} \right) \right),$$

where $h_e = \max_{\mathbf{s} \in \mathcal{V}_e} \left(|x_{\mathbf{s}} - x_{m(\mathbf{s})}| |x_{\mathbf{s}} - x_{m(\mathbf{s})+1}| \right)^{\frac{1}{2}}$ with $m(\mathbf{s}) \in \{0, \dots, m_x\}$ such that $x_{\mathbf{s}} \in [x_{m(\mathbf{s})}, x_{m(\mathbf{s})+1}]$.

Proof: From Lemma 3.2 of [14], there exist two constants $C(u)$ and $C(\theta_\mathcal{T})$ such that

$$\begin{aligned} \|\nabla_{\mathcal{D}_f} (P_{\mathcal{D}} u - P_{\mathcal{D}_p} u)\|_{L^2(\Gamma_f)^{d-1}}^2 &\leq C(\theta_\mathcal{T}) \sum_{e \in \mathcal{E}_\Gamma \cap \mathcal{E}_{\Gamma_f}} \sum_{\mathbf{s} \in \mathcal{V}_e} \left(u(\mathbf{x}_{\mathbf{s}}) - \mathcal{P}_{\mathbf{s}}(P_{\mathcal{D}_g} u) \right)^2 \\ &\leq C(\theta_\mathcal{T}) C(u) \sum_{e \in \mathcal{E}_\Gamma \cap \mathcal{E}_{\Gamma_f}} h_e^4. \end{aligned}$$

It is classical from \mathbb{P}_1 finite element approximation that there exists a constant $C(\theta_\mathcal{T}, u)$ such that $\|\nabla_{\mathcal{D}_f} P_{\mathcal{D}_p} u - \nabla_\tau \gamma_f u\|_{L^2(\Gamma_f)^{d-1}} \leq C(\theta_\mathcal{T}, u) h_\mathcal{T}$. Combining the two previous estimates, we obtain the estimate of Lemma 2.2.6. \square

Lemma 2.2.7 *For all $u \in C_{V0}^\infty$, there exist a constant $C(u, \theta_\mathcal{T})$ depending on u and $\theta_\mathcal{T}$ such that*

$$\|\Pi_{\mathcal{D}_m} P_{\mathcal{D}} u - u\|_{L^2(\Omega)} + \|\Pi_{\mathcal{D}_f} P_{\mathcal{D}} u - \gamma_f u\|_{L^2(\Gamma_f)} \leq C(u, \theta_\mathcal{T}) \left(h_\mathcal{T} + h_{\mathcal{D}_g}^2 h_\mathcal{T}^{\frac{1}{2}} \right).$$

Proof: Let us prove for example the estimate for the matrix function reconstruction operator. From Lemma 3.2 of [14], we have the estimates

$$\begin{aligned} \|\Pi_\mathcal{T} (P_{\mathcal{D}} u - P_{\mathcal{D}_p} u)\|_{L^2(\Omega)}^2 &\leq C(\theta_\mathcal{T}) \sum_{\sigma \in \mathcal{F}_\Gamma} \sum_{\mathbf{s} \in \mathcal{V}_\sigma} \text{diam}(\sigma)^3 \left(u(\mathbf{x}_{\mathbf{s}}) - \mathcal{P}_{\mathbf{s}}(P_{\mathcal{D}_g} u) \right)^2 \\ &\leq C(\theta_\mathcal{T}) C(u) \sum_{\sigma \in \mathcal{F}_\Gamma} h_\sigma^4 \text{diam}(\sigma)^3. \end{aligned}$$

The proof follows from a classical \mathbb{P}_1 finite element approximation and Lemma 3.3 of [14]. \square

The following Lemma follows from classical \mathbb{P}_1 finite element estimates.

Lemma 2.2.8 *For all $u \in C_{V0}^\infty$, there exists a constant $C(u)$ depending on u such that*

$$\|\Pi_{\mathcal{D}_g} P_{\mathcal{D}} u - \gamma u\|_{L^2(0,L)} + \|\nabla_{\mathcal{D}_g} P_{\mathcal{D}} u - \partial_x \gamma u\|_{L^2(0,L)} \leq C(u) h_{\mathcal{D}_g}.$$

The following Lemma, which provides an estimate of the consistency error for smooth solutions, directly follows from Lemmas 2.2.5, 2.2.6, 2.2.7, 2.2.8.

Lemma 2.2.9 For all $u \in C_{V_0}^\infty$, there exists a constant $C(u, \theta_{\mathcal{T}})$ depending on u and $\theta_{\mathcal{T}}$ such that

$$\mathcal{S}_{\mathcal{D}}(u) \leq C(u, \theta_{\mathcal{T}}) \left(h_{\mathcal{T}} + h_{\mathcal{D}_g} \left(1 + \max_{\sigma \in \mathcal{F}_{\Gamma}} \left(\frac{h_{\sigma}}{\text{diam}(\sigma)^{\frac{1}{2}}} \right) \right) \right)$$

where $h_{\sigma} = \max_{\mathbf{s} \in \mathcal{V}_{\sigma}} \left(|x_{\mathbf{s}} - x_{m(\mathbf{s})}| |x_{\mathbf{s}} - x_{m(\mathbf{s})+1}| \right)^{\frac{1}{2}}$ with $m(\mathbf{s}) \in \{0, \dots, m_x\}$ such that $x_{\mathbf{s}} \in [x_{m(\mathbf{s})}, x_{m(\mathbf{s})+1}]$.

Remark 2.2.1 To obtain the first order estimate of Lemma 2.2.9, it suffices that u is $C^2(\overline{K})$ for each cell $K \in \mathcal{M}$ and $\gamma u \in C^2([x_m, x_{m+1}])$ for all $m = 0, \dots, m_x$. From the definition of W , and since the solution satisfies $q_g = -\frac{|S|}{\alpha_g} \partial_x \gamma u$, in order to obtain such a smoothness on the solution, one should clearly include the points $\hat{x}_k, k \in S_{\Sigma_{\Gamma}}$ in the 1D mesh of $(0, L)$.

We now state in the following Lemma an estimate of the conformity error for fluxes in C_W^∞ .

Lemma 2.2.10 For all $\mathbf{q} = (\mathbf{q}_m, \mathbf{q}_f, q_g) \in C_W^\infty$ there exists a constant $C(\mathbf{q}, \theta_{\mathcal{T}})$ depending on \mathbf{q} and $\theta_{\mathcal{T}}$ such that

$$\mathcal{W}_{\mathcal{D}}(\mathbf{q}) \leq C(\mathbf{q}, \theta_{\mathcal{T}}) (h_{\mathcal{T}} + h_{\mathcal{D}_g}).$$

Proof: Let $\mathbf{q} = (\mathbf{q}_m, \mathbf{q}_f, q_g)$ be in C_W^∞ . Let us define for all $v_{\mathcal{D}} \in X_{\mathcal{D}}^0$

$$\begin{aligned} \overline{W}_{\mathcal{D}}(\mathbf{q}, v_{\mathcal{D}}) &= \int_{\Omega \setminus \Gamma_f} (\mathbf{q}_m \cdot \nabla \Pi_{\mathcal{T}} v_{\mathcal{D}} + \Pi_{\mathcal{T}} v_{\mathcal{D}} \text{div}(\mathbf{q}_m)) d\mathbf{x} \\ &\quad + \int_{\Gamma_f} (\mathbf{q}_f \cdot \nabla_{\tau} \gamma_f \Pi_{\mathcal{T}} v_{\mathcal{D}} + r_f(\mathbf{q}) \gamma_f \Pi_{\mathcal{T}} v_{\mathcal{D}}) d\tau(\mathbf{x}) \\ &\quad + \int_0^L (q_g \partial_x \overline{\Pi}_{\mathcal{D}_g} v_{\mathcal{D}} + r_g(\mathbf{q}) \overline{\Pi}_{\mathcal{D}_g} v_{\mathcal{D}}) dx. \end{aligned}$$

Using integration by part, we can derive that

$$\begin{aligned} \overline{W}_{\mathcal{D}}(\mathbf{q}, v_{\mathcal{D}}) &= \int_{\Gamma} (\mathbf{q}_m \cdot \mathbf{n}) (\gamma \Pi_{\mathcal{T}} v_{\mathcal{D}} - \overline{\Pi}_{\mathcal{D}_g} v_{\mathcal{D}}) d\tau(\mathbf{x}) \\ &\quad + \sum_{i \in I} \int_{\Sigma_{i, \Gamma}} (\mathbf{q}_f|_{\Gamma_{f,i}} \cdot \mathbf{n}_{\Sigma_i}) (\gamma_{\Sigma_{\Gamma}} \gamma_f \Pi_{\mathcal{T}} v_{\mathcal{D}} - \gamma_{\Sigma_{\Gamma}} \overline{\Pi}_{\mathcal{D}_g} v_{\mathcal{D}}) dl(\mathbf{x}). \end{aligned}$$

It follows from Lemmas 2.2.3 and 2.2.4 that there exists a constant $C(\mathbf{q})$ such that

$$\overline{W}_{\mathcal{D}}(\mathbf{q}, v_{\mathcal{D}}) \leq C(\mathbf{q}) (h_{\mathcal{T}} + h_{\mathcal{D}_g}) \|\nabla_{\mathcal{D}_g} v_{\mathcal{D}}\|_{L^2(0, L)}.$$

Next, from Lemma 3.4 of [14] it follows that there exists $C(\mathbf{q}, \theta_{\mathcal{T}})$

$$|\overline{W}_{\mathcal{D}}(\mathbf{q}, v_{\mathcal{D}}) - W_{\mathcal{D}}(\mathbf{q}, v_{\mathcal{D}})| \leq C(\mathbf{q}, \theta_{\mathcal{T}}) (h_{\mathcal{T}} + h_{\mathcal{D}_g}) \|v_{\mathcal{D}}\|_{\mathcal{D}},$$

Combining the two previous estimates, we can conclude the proof of Lemma 2.2.10. \square

We can now state the main result of this section.

Proposition 2.2.3 *Let us consider a family of discretizations $(\mathcal{D}^l)_{l \in \mathbb{N}}$ such that there exist constants θ, β with $\theta_{\mathcal{T}^l} \leq \theta$ and $\max_{\sigma \in \mathcal{F}_\Gamma^l} (\frac{h_\sigma}{\text{diam}(\sigma)^{\frac{1}{2}}}) \leq \beta$ for all $l \in \mathbb{N}$, where*

$$h_\sigma = \max_{\mathbf{s} \in \mathcal{V}_\sigma} \left(|x_{\mathbf{s}} - x_{m(\mathbf{s})}| |x_{\mathbf{s}} - x_{m(\mathbf{s})+1}| \right)^{\frac{1}{2}},$$

with $m(\mathbf{s}) \in \{0, \dots, m_x\}$ such that $x_{\mathbf{s}} \in [x_{m(\mathbf{s})}, x_{m(\mathbf{s})+1}]$, and such that $\lim_{l \rightarrow +\infty} h_{\mathcal{T}^l} = 0$ and $\lim_{l \rightarrow +\infty} h_{\mathcal{D}_g^l} = 0$.

Then, the corresponding family of VAG discretizations defined in subsection 2.2.3 is coercive, consistent and limit conforming in the sense of subsection 2.2.2 and hence convergent.

Proof: The coercivity follows from Proposition 9 of [13] and from the classical estimate $\|\Pi_{\mathcal{D}_g} v_{\mathcal{D}}\|_{L^2(0,L)} \leq L^{\frac{1}{2}} \|\nabla_{\mathcal{D}_g} v_{\mathcal{D}}\|_{L^2(0,L)}$ for all $v_{\mathcal{D}} \in X_{\mathcal{D}}^0$. The consistency derives from Lemmas 2.2.9 and 2.2.1 and the limit conformity from Lemmas 2.2.10 and 2.2.2. \square

Remark 2.2.2 *If the mesh is conforming at the interface Γ in the sense that for all $\mathbf{s} \in \mathcal{V}_\Gamma$ there exists $m \in \{0, \dots, m_x + 1\}$ such that $x_{\mathbf{s}} = x_m$, then one has $h_\sigma = 0$ for all $\sigma \in \mathcal{F}_\Gamma$ in the previous proposition.*

In addition, if the discretization is conforming in the sense that $\Pi_{\mathcal{T}} X_{\mathcal{D}} \subset V$ and $\nabla_{\mathcal{D}_g} = \gamma \Pi_{\mathcal{T}}$, then, the terms in Lemmas 2.2.3 and 2.2.4 vanish. This is the case if, in addition to the previous condition on \mathcal{V}_Γ , denoting by \mathcal{V}_m the set of nodes along $\{x_m\} \times \partial S = \{\mathbf{s}_1, \dots, \mathbf{s}_{k_m}\}$ in cyclic order, all the edges $(\mathbf{s}_k, \mathbf{s}_{k+1})$, $k = 1, \dots, k_m - 1$ and $(\mathbf{s}_{k_m}, \mathbf{s}_1)$ belong to \mathcal{E} .

2.2.5 Numerical examples

In order to ease the mesh generation, we consider in both test cases the simpler geometry of Figure 2.1 for which the porous medium is defined by the domain $\Omega = (0, 1)^3$ and the gallery is defined by the domain $(0, 1) \times (-1, 0) \times (0, 1)$ with longitudinal axis x . The porous medium gallery interface is defined by $\Gamma = (0, 1) \times \{0\} \times (0, 1)$.

For the first test case the porous medium contains a single fracture $\Gamma_f = \{0.5\} \times (0, 1) \times (0, 1)$ orthogonal to the axis x of the gallery (see Figure 2.3). Both the matrix and the fracture are considered homogeneous and isotropic and we set $\mathbf{K}_m = I$ and $d_f \mathbf{K}_f = I$.

Let us choose the function $u \in V$ defined by

$$u(x, y, z) = \begin{cases} y \cos(x + y + z) + e^{\cos(x+y)} & \text{if } x \leq \frac{1}{2}, \\ y \cos(1 - x + y + z) + e^{\cos(1-x+y)} & \text{if } x > \frac{1}{2}. \end{cases}$$

The function u is solution of (2.5) (with non homogeneous Dirichlet boundary conditions and right hand sides obtained from u), if the flux

$$(\mathbf{q}_m, \mathbf{q}_f, q_g) = \left(-\nabla u, -\nabla_{\mathcal{T}} \gamma_f u, -\frac{1}{\alpha_g} \partial_x \gamma u \right)$$

is in the space C_W^∞ . We can check that this condition is satisfied for a constant choice of $\alpha_g > 0$ defined by

$$\alpha_g = \frac{2 \sin(\frac{1}{2}) e^{\cos(\frac{1}{2})}}{\sin(\frac{1}{2}) e^{\cos(\frac{1}{2})} - \sin(\frac{3}{2}) + \sin(\frac{1}{2})}.$$

The convergence of the VAG scheme to this solution is tested on two families of meshes (see Figure 2.3). The first family is a family of uniform Cartesian meshes of the domain Ω of sizes $n \times n \times n$ with $n = 2, 4, 8, 16, 32, 64, 128$. The second family is the family of tetrahedral meshes of the domain Ω taken from the FVCA6 3D benchmark [34]. In both cases the 1D mesh in the gallery contains the point $x = \frac{1}{2}$ and is uniform in both intervals $(0, \frac{1}{2})$ and $(\frac{1}{2}, 1)$ with a total number of points roughly equal to 1.2 times the power one third of the number of cells of the mesh of the domain Ω . We have checked, for this choice of the 1D mesh, that roughly 95 percent of the nodes of Γ are not matching with the nodes of the 1D mesh.

In all test cases, the linear system obtained after elimination of the cell and Dirichlet unknowns is solved using the GMRes iterative solver with the stopping criteria 10^{-10} and a maximum Krylov subspace dimension fixed to 1000 (not attained in our tests). The GMRes solver is preconditioned by ILUT [54], [55] using the thresholding parameter 10^{-4} .

The convergence of the sum of the relative L^2 errors in the matrix, fracture and gallery for the function and gradient reconstructions as a function of the number of degrees of freedom after elimination of the cell and Dirichlet unknowns is plotted in Figure 2.4. Tables 2.1 and 2.2 exhibit in addition the number of unknowns before and after elimination of the cells and Dirichlet nodes, the number of non zero elements of the reduced Jacobian, the CPU time in seconds for the linear solve and the order of convergence for the function and gradient reconstructions. The order of convergence is computed w.r.t. the number of cells to the power one third.

We can checked that we obtain as expected for both families of meshes a first order of convergence for the gradient reconstructions. A second order of convergence is obtained for the function reconstructions which is classically better than the obtained error estimate.

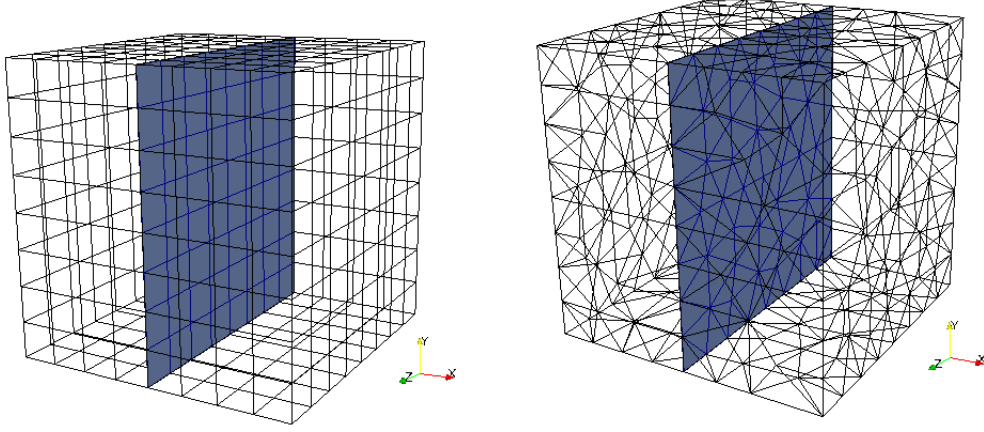


Figure 2.3: For the first test case: third Cartesian mesh and first tetrahedral mesh of the porous medium domain with one fracture orthogonal to the gallery axis x .

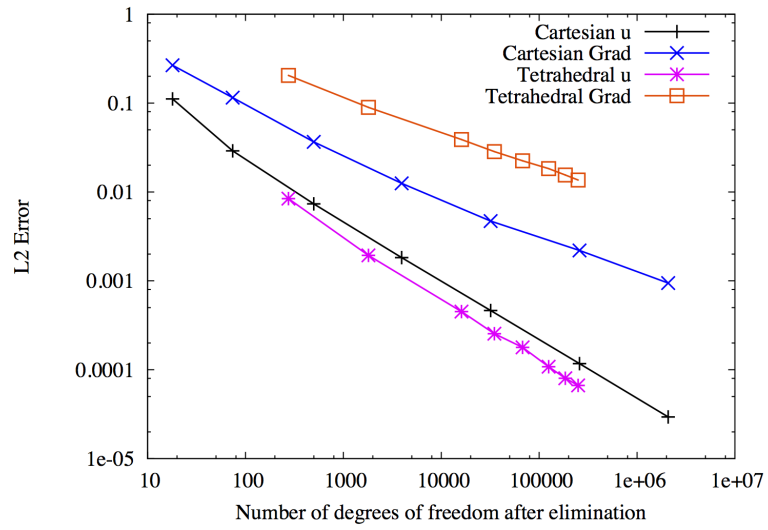


Figure 2.4: For the first test case and both families of Cartesian and tetrahedral meshes: sum of the relative L2 errors in the matrix, fracture and gallery for the function reconstructions (u) and the gradient reconstructions (Grad) as a function of the number of degrees of freedom after elimination of the cell and Dirichlet unknowns.

mesh	cells	d.o.f.	red. d.o.f.	nz jac	error u	error ∇	order u	order ∇	cpu (s)	α_{cpu}
1	8	43	18	72	0.11	0.27			$2.7 \cdot 10^{-4}$	
2	64	211	74	852	$2.9 \cdot 10^{-2}$	0.11	1.94	1.2	$6.2 \cdot 10^{-4}$	0.40
3	512	1316	499	9.2k	$7.3 \cdot 10^{-3}$	$3.7 \cdot 10^{-2}$	2.0	1.7	$1.1 \cdot 10^{-2}$	1.38
4	4k	9.2k	3.9k	90k	$1.8 \cdot 10^{-3}$	$1.2 \cdot 10^{-2}$	2.0	1.5	0.12	1.16
5	32k	69k	32k	798k	$4.6 \cdot 10^{-4}$	$4.7 \cdot 10^{-3}$	2.0	1.4	1.14	1.08
6	262k	540k	258k	6721k	$1.2 \cdot 10^{-4}$	$2.2 \cdot 10^{-3}$	2.0	1.1	10.3	1.05
7	2097k	4260k	2081k	55182k	$2.9 \cdot 10^{-5}$	$9.4 \cdot 10^{-4}$	2.0	1.2	102	1.10

Table 2.1: For the first test case and the family of 7 Cartesian meshes: number of cells (cells), number of unknowns (d.o.f.), number of unknowns after elimination without fill in of the cells and Dirichlet nodes (red. d.o.f.), number of non zero elements in the reduced Jacobian (nz jac), L2 error for the function reconstructions (error u), L2 error for the gradient reconstructions (error ∇), order of convergence for the function reconstructions (order u), order of convergence for the gradient reconstructions (order ∇), cpu time in seconds for the linear solution (cpu), and scaling of cpu time (α_{cpu}) by $cpu \sim cells^{\alpha_{cpu}}$.

mesh	cells	d.o.f.	red. d.o.f.	nz jac	error u	error ∇	order u	order ∇	cpu (s)	α_{cpu}
1	1.3k	1.8k	275	2.6k	$8.4 \cdot 10^{-3}$	0.20			$5.0 \cdot 10^{-3}$	
2	11k	13k	1.8k	23k	$1.9 \cdot 10^{-3}$	$8.9 \cdot 10^{-2}$	2.1	1.2	$5.5 \cdot 10^{-2}$	1.12
3	100k	120k	16k	231k	$4.5 \cdot 10^{-4}$	$3.9 \cdot 10^{-2}$	1.95	1.1	0.72	1.17
4	220k	260k	35k	513k	$2.5 \cdot 10^{-4}$	$2.8 \cdot 10^{-2}$	2.2	1.2	1.7	1.09
5	428k	505k	68k	1012k	$1.8 \cdot 10^{-4}$	$2.2 \cdot 10^{-2}$	1.6	1.1	3.5	1.09
6	794k	933k	125k	1889k	$1.1 \cdot 10^{-4}$	$1.8 \cdot 10^{-2}$	2.4	1.0	7.0	1.12
7	1175k	1379k	185k	2810k	$8.0 \cdot 10^{-5}$	$1.6 \cdot 10^{-2}$	2.3	1.2	11	1.15
8	1592k	1864k	250k	3815k	$6.7 \cdot 10^{-5}$	$1.4 \cdot 10^{-2}$	1.85	1.3	15	1.02

Table 2.2: For the first test case and the family of 8 tetrahedral meshes: number of cells (cells), number of unknowns (d.o.f.), number of unknowns after elimination without fill in of the cells and Dirichlet nodes (red. d.o.f.), number of non zero elements in the reduced Jacobian (nz jac), L2 error for the function reconstructions (error u), L2 error for the gradient reconstructions (error ∇), order of convergence for the function reconstructions (order u), order of convergence for the gradient reconstructions (order ∇), cpu time in seconds for the linear solution (cpu), and scaling of cpu time (α_{cpu}) by $cpu \sim cells^{\alpha_{cpu}}$.

The second test case consider a single fracture $\Gamma_f = (0, 1) \times (0, 1) \times \{0.5\}$ parallel to the axis x of the gallery (see Figure 2.5). The families of meshes are obtained from the previous ones by rotation and the 1D mesh in the gallery is uniform with the same number of nodes as in the previous test case.

Let us choose the function $u \in V$ defined by

$$u(x, y, z) = \begin{cases} y \cos(x + y + z) + e^{\cos(x+y)} & \text{if } z \leq \frac{1}{2}, \\ y \cos(x + y + 1 - z) + e^{\cos(x+y)} & \text{if } z > \frac{1}{2}, \end{cases}$$

and set $\mathbf{K}_m = I$ and $d_f \mathbf{K}_f = I$, $\alpha_g = 1$. Since the flux

$$(\mathbf{q}_m, \mathbf{q}_f, q_g) = (-\nabla u, -\nabla_\tau \gamma_f u, -\partial_x \gamma u)$$

is in the space C_W^∞ , the function u is solution of (2.5) with non homogeneous Dirichlet boundary conditions and right hand sides obtained from u . The results exhibited in Figure 2.6 and in Tables 2.3 and 2.4 are similar than for the previous test case.

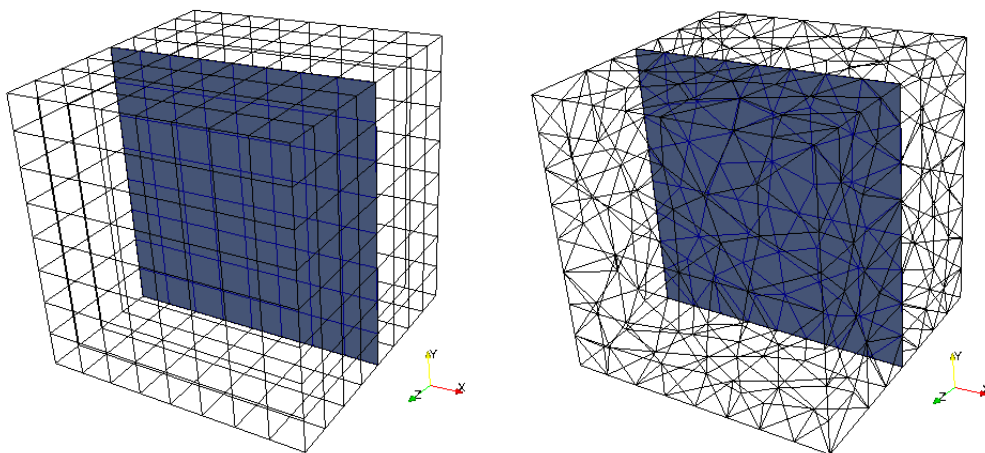


Figure 2.5: For the second test case: third Cartesian mesh and first tetrahedral mesh of the porous medium domain with one fracture parallel to the gallery axis x .

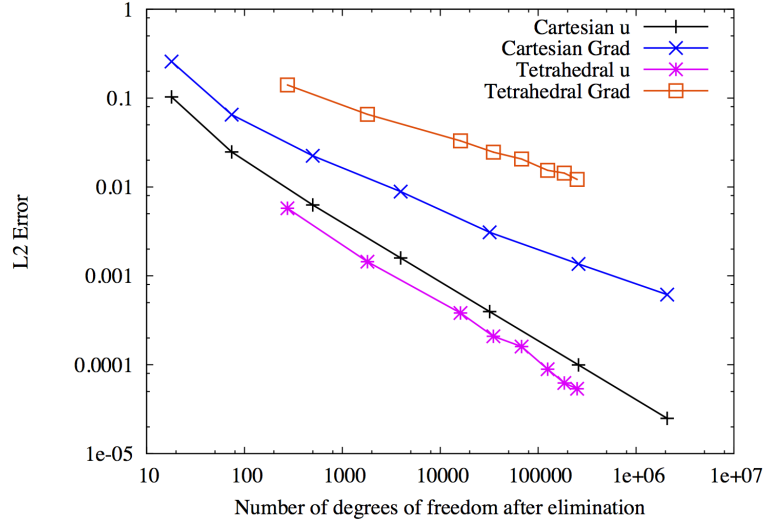


Figure 2.6: For the second test case and both families of Cartesian and tetrahedral meshes: sum of the relative L2 errors in the matrix, fracture and gallery for the function reconstructions (u) and the gradient reconstructions (Grad) as a function of the number of degrees of freedom after elimination of the cell and Dirichlet unknowns.

mesh	cells	d.o.f.	red. d.o.f.	nz jac	error u	error ∇	order u	order ∇	cpu (s)	α_{cpu}
1	8	43	18	87	0.10	0.26			$2.8 \cdot 10^{-4}$	
2	64	211	74	869	$2.5 \cdot 10^{-2}$	$6.5 \cdot 10^{-2}$	2.1	2.0	$8.8 \cdot 10^{-4}$	0.55
3	512	1.3	499	9.3k	$6.3 \cdot 10^{-3}$	$2.2 \cdot 10^{-2}$	2.0	1.5	$9.5 \cdot 10^{-3}$	1.14
4	4k	9.2k	3.9k	90k	$1.6 \cdot 10^{-3}$	$8.9 \cdot 10^{-3}$	2.0	1.3	0.13	1.27
5	32k	69k	32k	798k	$4.0 \cdot 10^{-4}$	$3.1 \cdot 10^{-3}$	2.0	1.5	1.2	1.07
6	262k	540k	258k	6723k	$9.9 \cdot 10^{-5}$	$1.4 \cdot 10^{-3}$	2.0	1.2	11	1.05
7	2097k	4260k	2081k	55183k	$2.5 \cdot 10^{-5}$	$6.2 \cdot 10^{-4}$	2.0	1.1	104	1.08

Table 2.3: For the second test case and the family of 7 Cartesian meshes: number of cells (cells), number of unknowns (d.o.f.), number of unknowns after elimination without fill in of the cells and Dirichlet nodes (red. d.o.f.), number of non zero elements in the reduced Jacobian (nz jac), L2 error for the function reconstructions (error u), L2 error for the gradient reconstructions (error ∇), order of convergence for the function reconstructions (order u), order of convergence for the gradient reconstructions (order ∇), cpu time in seconds for the linear solution (cpu), and scaling of cpu time (α_{cpu}) by $cpu \sim cells^{\alpha_{cpu}}$.

mesh	cells	d.o.f.	red. d.o.f.	nz jac	error u	error ∇	order u	order ∇	cpu (s)	α_{cpu}
1	1.3k	1.8k	275	2.6k	$5.8 \cdot 10^{-3}$	0.14			$6.1 \cdot 10^{-3}$	
2	11k	13k	1.8k	23k	$1.4 \cdot 10^{-3}$	$6.6 \cdot 10^{-2}$	2.0	1.1	$6.2 \cdot 10^{-2}$	1.09
3	100k	120k	16k	231k	$3.8 \cdot 10^{-4}$	$3.3 \cdot 10^{-2}$	1.8	0.9	1.1	1.30
4	220k	260k	34k	513k	$2.1 \cdot 10^{-4}$	$2.5 \cdot 10^{-2}$	2.3	1.1	1.8	0.62
5	428k	505k	67k	1012k	$1.6 \cdot 10^{-4}$	$2.1 \cdot 10^{-2}$	1.2	0.8	3.9	1.16
6	794k	932k	125k	1889k	$8.9 \cdot 10^{-5}$	$1.5 \cdot 10^{-2}$	2.8	1.4	7.0	0.95
7	1175k	1378k	185k	2809k	$6.2 \cdot 10^{-5}$	$1.4 \cdot 10^{-2}$	2.7	0.55	10	0.91
8	1592k	1864k	250k	3815k	$5.4 \cdot 10^{-5}$	$1.2 \cdot 10^{-2}$	1.5	1.6	16	1.55

Table 2.4: For the second test case and the family of 8 tetrahedral meshes: number of cells (cells), number of unknowns (d.o.f.), number of unknowns after elimination without fill in of the cells and Dirichlet nodes (red. d.o.f.), number of non zero elements in the reduced Jacobian (nz jac), L2 error for the function reconstructions (error u), L2 error for the gradient reconstructions (error ∇), order of convergence for the function reconstructions (order u), order of convergence for the gradient reconstructions (order ∇), cpu time in seconds for the linear solution (cpu), and scaling of cpu time (α_{cpu}) by $cpu \sim cells^{\alpha_{cpu}}$.

2.3 Extension to the Compositional Model

2.3.1 Compositional Model

Let $\alpha = g, l$ denote the gas and liquid phases assumed to be both defined by a mixture of two components, the water component denoted by e which can vaporize in the gas phase, and the gaseous component a standing for air which can dissolve in the liquid phase. The generalization to the case of N components is straightforward following Chapter 1. Following [11] (see also Chapter 1 or [47] for the case of N components), the gas liquid Darcy flow formulation uses the gas pressure p^g and the liquid pressure p^l as primary unknowns, denoted by $\mathcal{U} = (p^g, p^l)$ in the following. In this formulation, the component molar fractions of the gas and liquid phases are defined by some functions $c_i^\alpha(\mathcal{U})$ of the phase pressures such that $c_e^\alpha(\mathcal{U}) + c_a^\alpha(\mathcal{U}) = 1$. Consequently the molar and mass densities, as well as the viscosities can be defined as functions of \mathcal{U} and will be denoted by respectively $\zeta^\alpha(\mathcal{U})$, $\rho^\alpha(\mathcal{U})$, $\mu^\alpha(\mathcal{U})$ for $\alpha = g, l$.

In the matrix domain $\Omega \setminus \bar{\Gamma}_f$ let us use the following notations:

- The saturations s^α are given by the functions $\mathcal{S}_m^\alpha(\mathbf{x}, p_c)$ of the capillary pressure $p_c = p^g - p^l$ with $\mathcal{S}_m^l(\mathbf{x}, p_c) + \mathcal{S}_m^g(\mathbf{x}, p_c) = 1$.
- The relative permeabilities are denoted by $k_{r,m}^\alpha(\mathbf{x}, s^\alpha)$ for $\alpha = g, l$.
- The porosity is denoted by $\phi_m(\mathbf{x})$, and the permeability tensor by $\mathbf{K}_m(\mathbf{x})$

Similarly, in the fracture network Γ_f let us use the following notations:

- The saturations are given by the functions $\mathcal{S}_f^\alpha(\mathbf{x}, p_c)$ of the capillary pressure with $\mathcal{S}_f^l(\mathbf{x}, p_c) + \mathcal{S}_f^g(\mathbf{x}, p_c) = 1$.
- The relative permeabilities are denoted by $k_{r,f}^\alpha(\mathbf{x}, s^\alpha)$ for $\alpha = g, l$.
- The porosity is denoted by $\phi_f(\mathbf{x})$, the fracture width by $d_f(\mathbf{x})$, and the tangential permeability tensor by $\mathbf{K}_f(\mathbf{x})$.

Following [12], it is assumed that both phase pressures are continuous at the matrix fracture interfaces such that the pressures in the fracture network are defined by $\gamma_f p^\alpha$ for $\alpha = g, l$. Then, the Darcy velocities in the fracture network is obtained for $\alpha = g, l$ by the reduced model

$$\mathbf{V}_f^\alpha = -\frac{k_{r,f}^\alpha(\mathbf{x}, \mathcal{S}_f^\alpha(\gamma_f(p^g - p^l)))}{\mu^\alpha(\gamma_f \mathcal{U})} d_f(\mathbf{x}) \mathbf{K}_f(\mathbf{x}) \left(\nabla_\tau \gamma_f p^\alpha - \rho^\alpha(\gamma_f \mathcal{U}) \mathbf{g}_\tau \right),$$

where \mathbf{g} denote the gravity vector, $\mathbf{g}_\tau = \mathbf{g} - (\mathbf{g} \cdot \mathbf{n})\mathbf{n}$ with \mathbf{n} a unit normal vector to the fracture. At fracture intersections Σ , for $\alpha = g, l$, it is assumed that the pressures $\gamma_f p^\alpha$ are continuous and that the normal fluxes of the Darcy velocities \mathbf{V}_f^α sum to zero. At the immersed fracture boundaries Σ_N , the normal flux of the Darcy velocity \mathbf{V}_f^α is also assumed to vanish.

In the matrix domain, the Darcy velocities are classically defined by

$$\mathbf{V}_m^\alpha = -\frac{k_{r,m}^\alpha(\mathbf{x}, \mathcal{S}_m^\alpha(p^g - p^l))}{\mu^\alpha(\mathcal{U})} \mathbf{K}_m(\mathbf{x}) \left(\nabla p^\alpha - \rho^\alpha(\mathcal{U}) \mathbf{g} \right),$$

for both phases $\alpha = g, l$.

In the gallery, the primary unknowns, depending only on the x coordinate along the gallery and on the time t , are the gas pressure p and the gas molar fractions $c = (c_e, c_a)$. The gas flow model is defined by a No Pressure Wave (NPW) [57] isothermal pipe flow model. In connection with the previous model problem, we assume that the velocity in the gallery is given by

$$w = -\frac{1}{\alpha_g(x)} \partial_x p,$$

corresponding to a Poiseuille flow. A more general pressure drop law such as the Forchheimer law to fix ideas

$$w = h(\partial_x p) = \frac{\alpha_g - \sqrt{\alpha_g^2 + 4\beta_g |\partial_x p|}}{2\beta_g} \frac{\partial_x p}{|\partial_x p|},$$

with $\alpha_g(x) > 0$, $\beta_g(x) > 0$, will be considered in the discretization subsection 2.3.2.

At the interface Γ between the gallery and the porous medium the coupling conditions are an adaptation to a 1D configuration for the free flow to those stated in [49]. Compared with [49], the gas pressure jump $p - p^g$ at the interface is neglected since a small flow

rate between the porous medium and the gallery is assumed due to the low permeability of the disposal. Hence the coupling conditions account first for the continuity of the gas phase pressure $p^g = p$. Second, as in [49], we impose the continuity of the gas molar fractions $c^g = c$. Third the thermodynamical equilibrium between the gas phase and the liquid phase at the interface Γ is assumed. All together, we obtain the following coupling conditions at the interface Γ

$$\begin{cases} p = \gamma p^g, \\ c_i = c_i^g(\gamma \mathcal{U}), i = e, a. \end{cases} \quad (2.25)$$

Using these coupling conditions (2.25), we can formulate the 1D free flow model in the gallery using the same unknown \mathcal{U} as in the porous medium.

For $\alpha = g, l$, $i = e, a$, let us denote the number of mole per unit matrix volume by

$$n_{i,m}(\mathbf{x}, \mathcal{U}) = \sum_{\alpha=g,l} \zeta^\alpha(\mathcal{U}) \mathcal{S}_m^\alpha(\mathbf{x}, p^g - p^l) c_i^\alpha(\mathcal{U})$$

and the number of mole per unit fracture surface by

$$n_{i,f}(\mathbf{x}, \gamma_f \mathcal{U}) = \sum_{\alpha=g,l} \zeta^\alpha(\gamma_f \mathcal{U}) \mathcal{S}_f^\alpha(\mathbf{x}, \gamma_f(p^g - p^l)) c_i^\alpha(\gamma_f \mathcal{U}).$$

For $\alpha = g, l$, $i = e, a$, let us denote the mobility of the component i in phase α by

$$m_{i,m}^\alpha(\mathbf{x}, \mathcal{U}) = \zeta^\alpha(\mathcal{U}) c_i^\alpha(\mathcal{U}) \frac{k_{r,m}^\alpha(\mathbf{x}, \mathcal{S}_m^\alpha(\mathbf{x}, p^g - p^l))}{\mu^\alpha(\mathcal{U})}$$

in the matrix, and by

$$m_{i,f}^\alpha(\mathbf{x}, \gamma_f \mathcal{U}) = \zeta^\alpha(\gamma_f \mathcal{U}) c_i^\alpha(\gamma_f \mathcal{U}) \frac{k_{r,f}^\alpha(\mathbf{x}, \mathcal{S}_f^\alpha(\mathbf{x}, \gamma_f(p^g - p^l)))}{\mu^\alpha(\gamma_f \mathcal{U})}$$

in the fracture network.

We can now state formally the formulation of the model coupling the 3D gas liquid Darcy flow in the matrix domain, the 2D gas liquid Darcy flow in the fracture network, and the 1D free gas flow in the gallery. The model amounts to find $\mathcal{U} = (p^g, p^l) \in L^2(0, T; V) \times L^2(0, T; V)$ and $(\mathbf{q}_a, \mathbf{q}_e) \in L^2(0, T; W) \times L^2(0, T; W)$ with $\mathbf{q}_i = (\mathbf{q}_{m,i}, \mathbf{q}_{f,i}, q_{g,i})$, $i = a, e$,

such that for all $i = a, e$ one has

$$\left\{ \begin{array}{l} \phi_m \partial_t n_{i,m}(\mathbf{x}, \mathcal{U}) + \operatorname{div}(\mathbf{q}_{m,i}) = 0 \\ \phi_f d_f \partial_t n_{i,f}(\mathbf{x}, \mathcal{U}) + r_f(\mathbf{q}_i) = 0, \\ |S| \partial_t \left(\zeta^g(\gamma \mathcal{U}) c_i^g(\gamma \mathcal{U}) \right) + r_g(\mathbf{q}_i) = 0, \\ - \sum_{\alpha=g,l} m_{i,m}^\alpha(\mathbf{x}, \mathcal{U}) \mathbf{K}_m \left(\nabla p^\alpha - \rho^\alpha(\mathcal{U}) \mathbf{g} \right) = \mathbf{q}_{m,i}, \\ - \sum_{\alpha=g,l} m_{i,f}^\alpha(\mathbf{x}, \gamma_f \mathcal{U}) d_f \mathbf{K}_f \left(\nabla_\tau \gamma_f p^\alpha - \rho^\alpha(\gamma_f \mathcal{U}) \mathbf{g}_\tau \right) = \mathbf{q}_{f,i}, \\ - \frac{|S|}{\alpha_g} \zeta^g(\gamma \mathcal{U}) c_i^g(\gamma \mathcal{U}) \partial_x \gamma p^g = q_{g,i}, \end{array} \right. \quad (2.26)$$

together with initial conditions in the matrix, the fracture and the gallery domains, as well as Dirichlet boundary conditions at Γ_D , Σ_D and at both sides of the gallery.

2.3.2 VAG discretization of the compositional model

The VAG scheme has been extended to multiphase Darcy flows in [36] for compositional models. In [35] it is adapted to the case of discontinuous capillary pressures using a phase pressures formulation in order to take into account accurately the saturation jump at the interfaces between different rocktypes. This motivates the choice of the phase pressures as primary unknowns in our model. In [12] it is extended to the case of immiscible two phase Darcy flows in discrete fracture networks coupling the flow in the fractures with the flow in the surrounding matrix. The current discretization combines ideas of [35] and [12] and extend them to compositional models and to the coupling with the 1D free gas flow.

Let us define $\mathcal{U}_D = (p_D^g, p_D^l) \in (X_D)^2$ as the vector of the discrete unknowns of the coupled model (2.26). The discretization of the Darcy matrix fluxes for each component $i = e, a$ combines the VAG fluxes and a phase by phase upwinding of the mobility terms w.r.t. the sign of the flux

$$V_{K,\nu}^{\alpha,i}(\mathcal{U}_D) = m_{i,m}^\alpha(\mathbf{x}_K, \mathcal{U}_{K,\nu}^{\alpha,up}) \left(V_{K,\nu}(p_D^\alpha) + g \rho_{K,\nu}^\alpha V_{K,\nu}(z_D) \right),$$

for all $K \in \mathcal{M}$, $\nu \in \Xi_K$, with the upwinding

$$\mathcal{U}_{K,\nu}^{\alpha,up} = \begin{cases} \mathcal{U}_K & \text{if } V_{K,\nu}(p_D^\alpha) + g \rho_{K,\nu}^\alpha V_{K,\nu}(z_D) \geq 0, \\ \mathcal{U}_\nu & \text{else,} \end{cases}$$

the averaged density $\rho_{K,\nu}^\alpha = \frac{\rho^\alpha(\mathcal{U}_K) + \rho^\alpha(\mathcal{U}_\nu)}{2}$, and the vector of the vertical coordinates at all d.o.f. $z_D = (z_\mu, \mu \in \mathcal{M} \cup \mathcal{V} \cup \mathcal{F}_{\Gamma_f})$.

Similarly, the discretization of the Darcy fracture fluxes for $\sigma \in \mathcal{F}_{\Gamma_f}$, $\mathbf{s} \in \mathcal{V}_\sigma$ is defined by

$$V_{\sigma,\mathbf{s}}^{\alpha,i}(\mathcal{U}_D) = m_{i,f}^\alpha(\mathbf{x}_\sigma, \mathcal{U}_{\sigma,\mathbf{s}}^{\alpha,up}) \left(V_{\sigma,\mathbf{s}}(p_D^\alpha) + g \rho_{\sigma,\mathbf{s}}^\alpha V_{\sigma,\mathbf{s}}(z_D) \right),$$

with the upwinding

$$\mathcal{U}_{\sigma,\mathbf{s}}^{\alpha,up} = \begin{cases} \mathcal{U}_\sigma & \text{if } V_{\sigma,\mathbf{s}}(p_{\mathcal{D}}^\alpha) + g\rho_{\sigma,\mathbf{s}}^\alpha V_{\sigma,\mathbf{s}}(z_{\mathcal{D}}) \geq 0, \\ \mathcal{U}_{\mathbf{s}} & \text{else,} \end{cases}$$

and the averaged density $\rho_{\sigma,\mathbf{s}}^\alpha = \frac{\rho^\alpha(\mathcal{U}_\sigma) + \rho^\alpha(\mathcal{U}_{\mathbf{s}})}{2}$.

The VAG fluxes in the gallery (2.22) are extended to the Darcy-Forchheimer law using a one quadrature point formula as follows

$$\begin{aligned} V_{m,m+1}(p_{\mathcal{D}}^g) &= |S|h \left(\alpha_g(x_{m+\frac{1}{2}}), \beta_g(x_{m+\frac{1}{2}}), \nabla_{\mathcal{D}_g} p_{\mathcal{D}}^g(x_{m+\frac{1}{2}}) \right) \\ &= |S|h \left(\alpha_g(x_{m+\frac{1}{2}}), \beta_g(x_{m+\frac{1}{2}}), \frac{p_{m+1}^g - p_m^g}{h_{m+\frac{1}{2}}} \right), \end{aligned}$$

and the discretization of the Darcy-Forchheimer fluxes for each component $i = e, a$ is defined by

$$V_{m,m+1,i}(\mathcal{U}_{\mathcal{D}}) = \zeta^g(\mathcal{U}_{m,m+1}^{up}) c_i^g(\mathcal{U}_{m,m+1}^{up}) V_{m,m+1}(p_{\mathcal{D}}^g),$$

with the upwinding

$$\mathcal{U}_{m,m+1}^{up} = \begin{cases} \mathcal{U}_m, & \text{if } V_{m,m+1}(p_{\mathcal{D}}^g) \geq 0, \\ \mathcal{U}_{m+1}, & \text{else,} \end{cases}$$

for all $m = 0, \dots, m_x$.

For $N \in \mathbb{N}^*$, let us consider the time discretization $t^0 = 0 < t^1 < \dots < t^{n-1} < t^n \dots < t^N = T$ of the time interval $[0, T]$. We denote the time steps by $\Delta t^n = t^n - t^{n-1}$ for all $n = 1, \dots, N$.

The initial conditions are given in the porous medium by $\mathcal{U}_\nu^0 = (p_{ini,\nu}^g, p_{ini,\nu}^l)$ for all $\nu \in \mathcal{M} \cup \mathcal{F}_{\Gamma_f} \cup (\mathcal{V} \setminus (\mathcal{V}_D \cup \mathcal{V}_\Gamma))$. In the gallery, they are defined for all $m = 1, \dots, m_x$ by $p_m^{g,0} = p_{ini,m}^g$, and $p_m^{l,0} = p_{ini,m}^l$.

Let us set $\phi_K = \int_K \phi_m(\mathbf{x}) d\mathbf{x}$ and $\phi_\sigma = \int_\sigma \phi_f(\mathbf{x}) d_f(\mathbf{x}) d\tau(\mathbf{x})$. The system of discrete equations in the porous medium at time step t^n accounts for the discrete molar conservation of each component $i = e, a$ in each control volume $K \in \mathcal{M}$, $\sigma \in \mathcal{F}_{\Gamma_f}$, and

$$\mathbf{s} \in \mathcal{V} \setminus (\mathcal{V}_D \cup \mathcal{V}_\Gamma),$$

$$\left\{ \begin{array}{l} (1 - \sum_{\mathbf{s} \in \mathcal{V}_K \setminus (\mathcal{V}_D \cup \mathcal{V}_\Gamma)} \alpha_{K,\mathbf{s}}) \phi_K \frac{n_{i,m}(\mathbf{x}_K, \mathcal{U}_K^n) - n_{i,m}(\mathbf{x}_K, \mathcal{U}_K^{n-1})}{\Delta t^n} \\ + \sum_{\alpha=g,l} \sum_{\nu \in \Xi_K} V_{K,\nu}^{\alpha,i}(\mathcal{U}_D^n) = 0, \quad K \in \mathcal{M}, \\ (1 - \sum_{\mathbf{s} \in \mathcal{V}_\sigma \setminus (\mathcal{V}_D \cup \mathcal{V}_\Gamma)} \alpha_{\sigma,\mathbf{s}}) \phi_\sigma \frac{n_{i,f}(\mathbf{x}_\sigma, \mathcal{U}_\sigma^n) - n_{i,f}(\mathbf{x}_\sigma, \mathcal{U}_\sigma^{n-1})}{\Delta t^n} \\ + \sum_{\alpha=g,l} \left(\sum_{\mathbf{s} \in \mathcal{V}_\sigma} V_{\sigma,\mathbf{s}}^{\alpha,i}(\mathcal{U}_D^n) - \sum_{K \in \mathcal{M}_\sigma} V_{K,\sigma}^{\alpha,i}(\mathcal{U}_D^n) \right) = 0, \quad \sigma \in \mathcal{F}_{\Gamma_f}, \\ \sum_{K \in \mathcal{M}_\mathbf{s}} \alpha_{K,\mathbf{s}} \phi_K \frac{n_{i,m}(\mathbf{x}_K, \mathcal{U}_\mathbf{s}^n) - n_{i,m}(\mathbf{x}_K, \mathcal{U}_\mathbf{s}^{n-1})}{\Delta t^n} \\ - \sum_{\alpha=g,l} \sum_{K \in \mathcal{M}_\mathbf{s}} V_{K,\mathbf{s}}^{\alpha,i}(\mathcal{U}_D^n) = 0, \quad \mathbf{s} \in \mathcal{V} \setminus (\mathcal{V}_D \cup \mathcal{V}_\Gamma \cup \mathcal{V}_{\Gamma_f}), \\ \sum_{\sigma \in \mathcal{F}_{\Gamma_f}, \mathbf{s}} \alpha_{\sigma,\mathbf{s}} \phi_\sigma \frac{n_{i,f}(\mathbf{x}_\sigma, \mathcal{U}_\mathbf{s}^n) - n_{i,f}(\mathbf{x}_\sigma, \mathcal{U}_\mathbf{s}^{n-1})}{\Delta t^n} \\ - \sum_{\alpha=g,l} \left(\sum_{K \in \mathcal{M}_\mathbf{s}} V_{K,\mathbf{s}}^{\alpha,i}(\mathcal{U}_D^n) + \sum_{\sigma \in \mathcal{F}_{\Gamma_f}, \mathbf{s}} V_{\sigma,\mathbf{s}}^{\alpha,i}(\mathcal{U}_D^n) \right) = 0, \quad \mathbf{s} \in \mathcal{V}_{\Gamma_f} \setminus (\mathcal{V}_D \cup \mathcal{V}_\Gamma), \end{array} \right.$$

together with the Dirichlet boundary conditions $\mathcal{U}_\mathbf{s}^n = (\bar{p}_\mathbf{s}^g, \bar{p}_\mathbf{s}^l)$ for all $\mathbf{s} \in \mathcal{V}_D$. This system is coupled to the equations in the gallery at time step t^n accounting for the discrete molar conservation of each component $i = e, a$

$$\begin{aligned} & |K_m| \frac{\zeta^g(\mathcal{U}_m^n) c_i^g(\mathcal{U}_m^n) - \zeta^g(\mathcal{U}_m^{n-1}) c_i^g(\mathcal{U}_m^{n-1})}{\Delta t^n} \\ & + V_{m,m+1,i}(\mathcal{U}_D^n) - V_{m-1,m,i}(\mathcal{U}_D^n) \\ & = \sum_{\mathbf{s} \in \mathcal{V}_\Gamma} \alpha_{m,\mathbf{s}} \sum_{\alpha=g,l} \left(\sum_{K \in \mathcal{M}_\mathbf{s}} V_{K,\mathbf{s}}^{\alpha,i}(\mathcal{U}_D^n) + \sum_{\sigma \in \mathcal{F}_{\Gamma_f}, \mathbf{s}} V_{\sigma,\mathbf{s}}^{\alpha,i}(\mathcal{U}_D^n) \right), \quad m = 1, \dots, m_x, \end{aligned}$$

and the Dirichlet conditions at both sides of the gallery $\mathcal{U}_0^n = \bar{\mathcal{U}}_0$, $\mathcal{U}_{m_x+1}^n = \bar{\mathcal{U}}_L$.

2.4 Numerical experiments without fractures

To assess the coupled model and its discretisation, let us consider in this section three test cases all sharing the following setting.

Let ω and S be the disks of center 0 and radius respectively $r_\omega = 10$ m and $r_S = 2$ m. We consider a radial mesh of the domain $(0, L) \times (\omega \setminus \bar{S})$, $L = 1000$ m, exponentially refined at the interface of the gallery Γ to account for the steep gradient of the capillary pressure at the porous medium gallery interface. The porous medium radial mesh matches

at the interface Γ with the 1D mesh of the gallery. The geometry of the porous medium domain and of the gallery is shown in Figure 2.7.

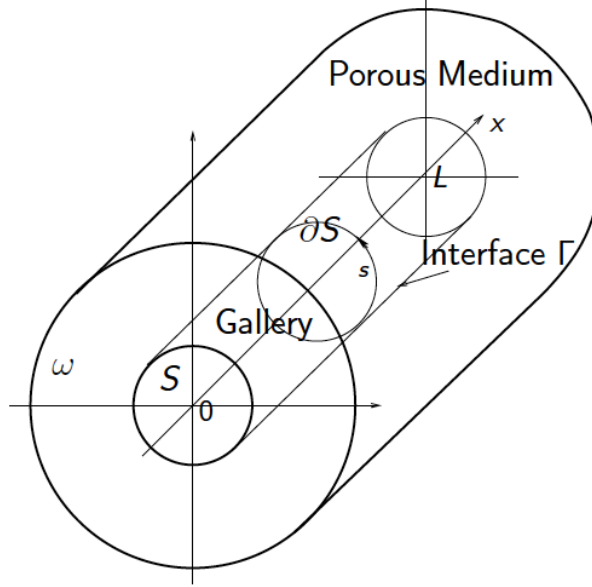


Figure 2.7: Geometry of the test cases

In addition to the water component e , we consider the air gaseous component denoted by a with the Henry constant $H_a = 6 \cdot 10^9$ Pa at the fixed temperature $T_e = 300$ K. The gas molar density is given by $\zeta^g(p^g) = \frac{p^g}{RT_e}$ mol.m⁻³ with $R = 8.314$ J K⁻¹ mol⁻¹, and the liquid molar density is fixed to $\zeta^l = 55555$ mol.m⁻³. The phase viscosities are fixed to $\mu^g = 18.51 \cdot 10^{-6}$ Pa.s⁻¹ and $\mu^l = 10^{-3}$ Pa.s⁻¹. The mass densities are defined by

$$\rho^\alpha = \zeta^\alpha \sum_{i \in \mathcal{C}} c_i^\alpha M_i$$

with the molar masses of the components $M_a = 29 \cdot 10^{-3}$ Kg mol⁻¹, $M_e = 18 \cdot 10^{-3}$ Kg mol⁻¹. The fugacities of the water and air components in the gas phase f_e^g and f_a^g are given by Dalton's law for an ideal mixture of perfect gas (1.1). The fugacities of the components in the liquid phase are given by Henry's law (1.2) for the dissolution of the air component in the liquid phase, and by Raoult-Kelvin's law (1.3) for the water component in the liquid phase. The solutions of the equations $f_i^g(c^g, p^g, p^l) = f_i^l(c^l, p^g, p^l)$ and $\sum_{i=e,a} c_i^\alpha = 1$, $\alpha = g, l$ leads to the following component molar fractions c^g and c^l as functions of \mathcal{U} :

$$\left\{ \begin{array}{ll} c_e^l = \frac{H_a - p^g}{H_a - \tilde{p}_{sat}}, & c_a^l = \frac{p^g - \tilde{p}_{sat}}{H_a - \tilde{p}_{sat}}, \\ c_e^g = \frac{\tilde{p}_{sat}}{p^g} c_e^l, & c_a^g = \frac{H_a}{p^g} c_a^l, \end{array} \right. \quad (2.27)$$

with the vapor pressure defined by (1.24) and

$$\tilde{p}_{sat} = p_{sat}(T_e) e^{\frac{p^l - p^g}{\zeta^l R T_e}}.$$

The porous medium is initially saturated by the liquid phase with imposed pressure $p_{init}^l = 40 \cdot 10^5$ Pa and composition $c_{a,init}^l = 0$, $c_{e,init}^l = 1$. At the external boundary $r = r_\omega$ the water pressure is fixed to $p_{ext}^l = p_{init}^l$, with an input composition $c_{a,ext}^l = 0$, $c_{e,ext}^l = 1$. On both sides $x = 0$ and $x = L$ of the porous medium, zero flux boundary conditions are imposed for all components. The initial condition in the gallery is given by $p_{init} = 10^5$ Pa and $c_{e,init}$ is defined by the relative humidity

$$H_{r,init} = \frac{c_{e,init} p_{init}}{p_{sat}(T_e)} = 0.5.$$

We consider an input gas velocity w_{in} depending on time (see Figures 2.9, 2.14), a fixed input water molar fraction $c_{e,in} = c_{e,init}$ at the left side $x = 0$ of the gallery, and a fixed output pressure $p_{out} = p_{init}$ at the right side $x = L$ of the gallery (see Figure 2.8). The relative permeabilities and capillary pressure in the porous medium are given by the Van-Genuchten laws (1.20)-(1.21)-(1.22). The Darcy Forchheimer parameters defining the pressure drop in the gallery are set to $\alpha = 0$ and $\beta_g = 10^{-3}$ Kg.m⁻⁴.

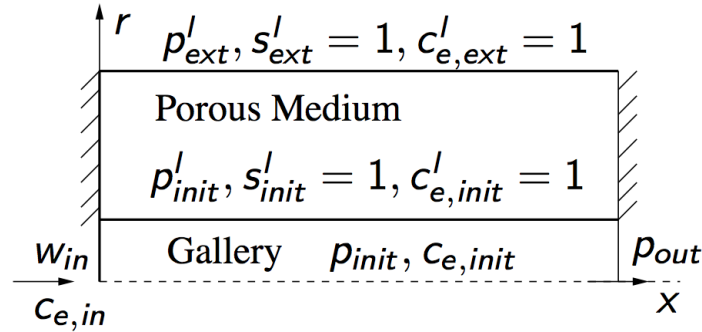


Figure 2.8: (x, r) cut of the disposal and initial and boundary conditions of the test case.

2.4.1 Comparison with an approximate stationary solution

In this first test case, we consider a single rocktype in the porous medium defined by the parameters $n = 1.49$, $s_r^l = 0.4$, $s_r^g = 0$, $P_r = 15 \cdot 10^6$ Pa of the Van-Genuchten laws accounting for the Callovo-Oxfordian argillites (COx). The permeability is assumed isotropic with $\mathbf{K}_m = 5 \cdot 10^{-20}$ m² the porosity is set to $\phi_m = 0.15$.

The simulation is run over a period of 10000 days with an initial time step of 100 seconds and a maximum time step of 50 days. The input velocity w_{in} is fixed to 1 m.s⁻¹ during the first 4000 days, 0.01 m.s⁻¹ during the next 4000 days, and 0 m.s⁻¹ during the remaining of the simulation (see Figure 2.9).

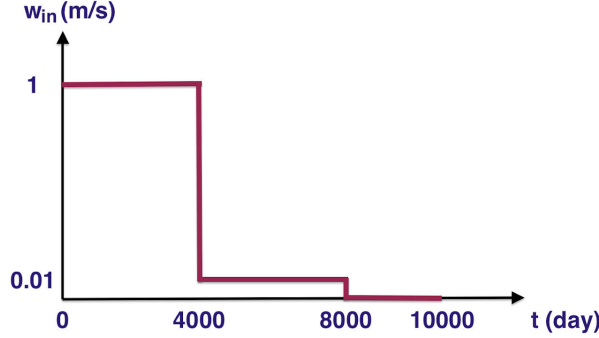


Figure 2.9: Input velocity w_{in} as a function of time.

Approximate Stationary Solution

In order to validate the simulation, an approximate stationary solution is computed for each value of the input gas velocity w_{in} . In this approximate model, the vaporization of the water component is kept but the dissolution of air is neglected. The gravity is also set to zero since the gravity forces are small compared with the capillary and pressure gradient forces. The pressure drop along the gallery can also be neglected meaning that the pressure in the gallery is equal to p_{init} . Last but not least, it is observed in the porous medium that the longitudinal derivatives are small compared with the radial derivatives due to the strong gradient of the capillary pressure at the porous medium gallery interface. Hence they will be neglected in our approximate model. Thanks to these assumptions, the stationary solution can be reduced to a single ordinary differential equation (ODE) for the water molar fraction in the gas phase along the gallery $c_e(x)$.

From the above assumptions, the approximate stationary solution $\mathcal{U}(x, r)$ depends only on x and r and satisfy the following simplified system in the porous medium

$$\begin{cases} \frac{\partial}{\partial r} \left(\frac{\zeta^g k_r^g}{\mu^g} \mathbf{K}_m r \frac{\partial}{\partial r} p^g \right) + \frac{\partial}{\partial r} \left(\frac{\zeta^l k_r^l}{\mu^l} \mathbf{K}_m r \frac{\partial}{\partial r} p^l \right) = 0, \\ \frac{\partial}{\partial r} \left(\frac{c_a^g \zeta^g k_r^g}{\mu^g} \mathbf{K}_m r \frac{\partial}{\partial r} p^g \right) = 0. \end{cases} \quad (2.28)$$

From the coupling conditions, at the porous medium gallery interface $r = r_S$, the gas pressure is fixed to $p^g(x, r_S) = p(x) = p_{init}$ and $c_e^g(x, r_S) = c_e(x)$. From the thermodynamical equilibrium of the water component at the interface, we can compute the capillary pressure at the interface as a function of $c_e(x)$ by the following formula:

$$p_c(c_e(x)) = -\zeta^l R T_e \ln \left(\frac{c_e(x) p_{init}}{p_{sat}(T_e)} \right)$$

Let us define $V_a = \frac{c_a^g \zeta^g k_r^g}{\mu^g} \mathbf{K}_m r \frac{\partial}{\partial r} p^g$ and the total velocity $V_T = \sum_{\alpha=l,g} \frac{\zeta^\alpha k_r^\alpha}{\mu^\alpha} \mathbf{K}_m r \frac{\partial}{\partial r} p^\alpha$.

We can deduce by integration of (2.28) taking into account the boundary conditions

$p^g(x, r_S) = p_{init}$, $c_e^g(x, r_S) = c_e(x)$, $c_a^g(x, r_S) = 1 - c_e(x)$, $p_c(x, r_S) = p_c(c_e(x))$, $p^l(x, r_\omega) = p_{ext}^l$, $c_e^l(x, r_\omega) = 1$, $c_a^l(x, r_\omega) = 0$, that $V_a = 0$ and that V_T depends only on x and is given by the following function of $c_e(x)$:

$$V_T(c_e(x)) = \frac{\zeta^l \mathbf{K}_m}{\mu^l \log(\frac{r_\omega}{r_S})} \left(p_{ext}^l - p_{init} + \int_0^{p_c(c_e(x))} k_r^l(s^l(-u)) du \right).$$

Turning to the equations in the gallery, $c_e(x)$ and $w(x)$ are solutions of the following system of ODEs

$$\begin{cases} \frac{d}{dx} \left(\zeta^g(p_{init}) w(x) c_e(x) \right) = \frac{2}{r_S^2} V_T(c_e(x)), & x \in (0, L), \\ \frac{d}{dx} \left(\zeta^g(p_{init}) w(x) (1 - c_e(x)) \right) = 0, & x \in (0, L), \\ c_e(0) = c_{e,in}, \\ w(0) = w_{in}. \end{cases}$$

The second equation yields $w(x) = w_{in} \frac{(1 - c_{e,in})}{1 - c_e(x)}$, $\forall x \in (0, L)$ and the above system reduces to the following ODE for $c_e(x)$:

$$\begin{cases} \zeta^g(p_{init}) w_{in} (1 - c_{e,in}) \frac{d}{dx} \left(\frac{c_e(x)}{1 - c_e(x)} \right) = \frac{2}{r_S^2} V_T(c_e(x)), & x \in (0, L), \\ c_e(0) = c_{e,in}, \end{cases} \quad (2.29)$$

which is numerically integrated.

Numerical results

The numerical solution obtained with the mesh $80 \times 50 \times 80$ is exhibited in Figures 2.10, 2.11 and 2.12. Figure 2.10 plots the average relative humidity in the gallery defined by $H_r(t) = \frac{1}{L} \int_0^L \frac{c_e(x,t) p(x,t)}{p_{sat}(T_e)} dx$ as a function of time. It also compares the numerical stationary relative humidities obtained as a function of x for each value of w_{in} with the ones obtained with the approximate stationary analytical model (2.29). A very good match can be checked in Figure 2.10 for the three input velocities. Figure 2.11 plots as a function of time the gas volume in the porous medium and the volumetric flow rates at the porous medium gallery interface for both phases. Figure 2.12 plots the stationary numerical liquid saturation at the porous medium gallery interface (represented in the gallery) and in the porous medium for each value of w_{in} . At the opening of the gallery at $t = 0$, we observe in Figures 2.10 an increase of the average relative humidity $H_r(t)$ up to almost 0.95 in a few seconds due to a large liquid flow rate (see Figure 2.11) at the interface. Then, the flow rate decreases and we observe a drying of the gallery due to the ventilation at $w_{in} = 1 \text{ m.s}^{-1}$ down to an average relative humidity slightly above $H_{r,init}$ in a few days. Meanwhile the gas penetrate slowly into the porous medium reaching a stationary state with around 167 m^3 of gas in say 4000 days (see Figure 2.11). When the input velocity is reduced to 0.01 m.s^{-1} , we observe first a rapid increase of $H_r(t)$ in say

100 days due to the reduced ventilation followed by a convergence to a second stationary state with $H_r(t) = 0.74$ in the gallery and around 137 m^3 of gas in the porous medium. Note in Figure 2.11 that the gas flow rate is entering in the porous medium between say 4600 and 7000 days although the volume of gas in the porous medium is still decreasing. This is due to a larger mass of air dissolved in the liquid phase entering into the gallery than the mass of air entering into the porous medium in the gas phase. At equilibrium, at time say between 7000 and 8000 days, the mass of air entering into the gallery dissolved in the liquid phase is compensated by the mass of air entering into the porous media in the gas phase. When w_{in} is set to 0 m.s^{-1} , $H_r(t)$ reaches a value above 1 corresponding to a negative capillary pressure and $s^l = 1$ at the interface and the gas disappears from the porous medium in around 1400 days. The value above 1 of the relative humidity is due to the fact that the model does not take into account the appearance of the liquid phase in the gallery side.

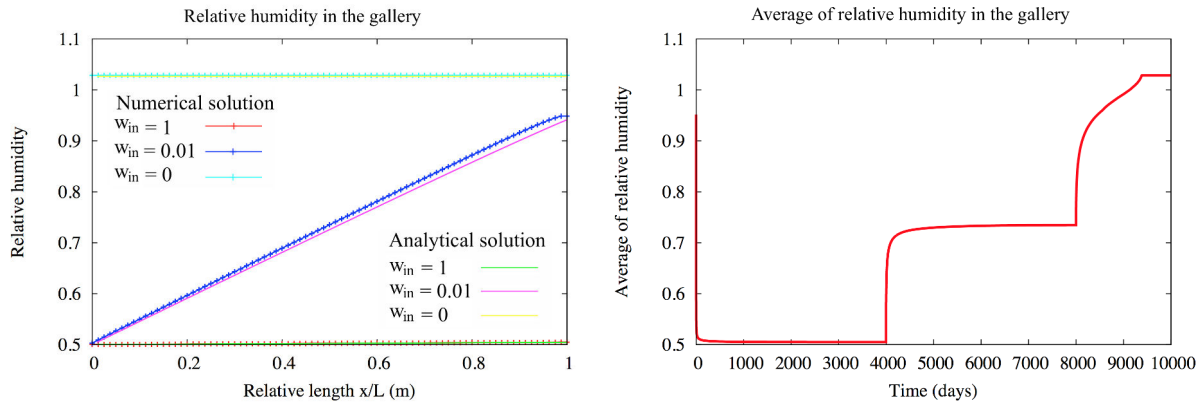


Figure 2.10: Stationary relative humidity in the gallery for each value of w_{in} compared with its approximate “analytical” solution (left); average of the relative humidity in the gallery as a function of time (right).

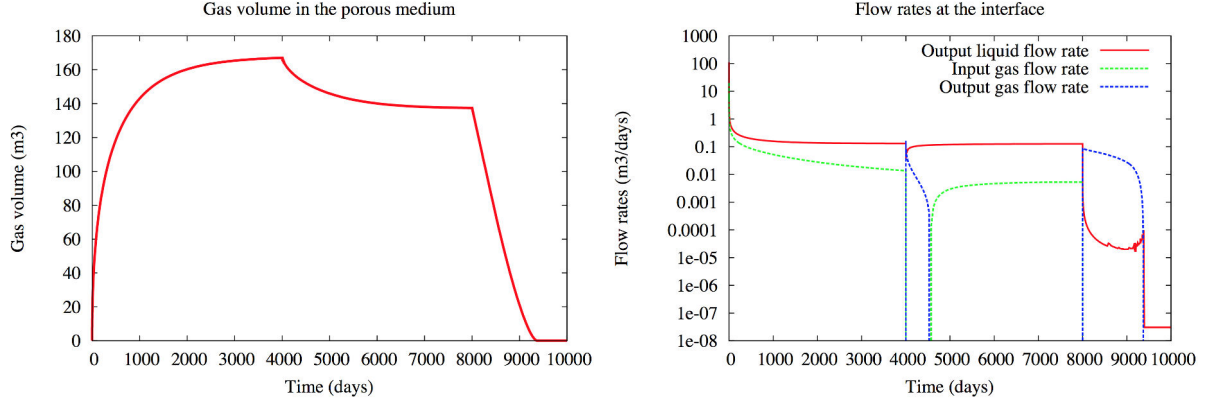


Figure 2.11: Gas Volume in the porous medium as a function of time (left); input and output flow rates at the interface Γ for the gas and liquid phases (right) as a function of time (an input flow rate enters into the porous medium).

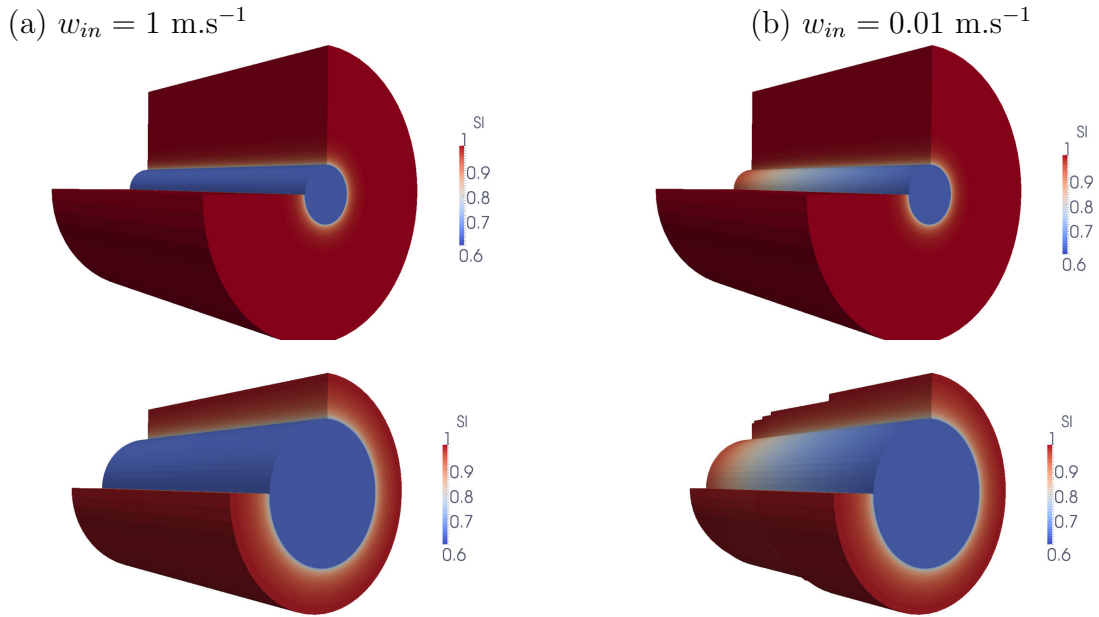


Figure 2.12: Stationary liquid saturation s^l obtained for $w_{in} = 1 \text{ m.s}^{-1}$ (a) and for $w_{in} = 0.01 \text{ m.s}^{-1}$ (b). The bottom figures zoom the liquid saturation in the porous medium below the threshold value 0.99. In the gallery the liquid saturation corresponds to the saturation at the interface function of x .

Figure 2.13 exhibits the convergence of the volume of gas in the porous medium as a function of time and of $H_r(t)$ for the five different meshes $20 \times 20 \times 20$, $40 \times 40 \times 40$, $60 \times 50 \times 60$, $70 \times 50 \times 70$ and $80 \times 50 \times 80$. Table 2.5 shows the numerical behaviour of the simulations for these five meshes. A rather good scalability of the linear and nonlinear solvers and of the CPU time w.r.t. the mesh size is obtained. The linear system is solved

using the GMRES iterative solver preconditioned by ILU0, and the linear and nonlinear stopping criteria are fixed to respectively 10^{-6} and 10^{-5} for the relative residuals.

mesh	$N_{\Delta t}$	N_{Chop}	N_{Newton}	N_{GMRes}	CPU(s)	α_{CPU}
$20 \times 20 \times 20$	615	0	3.12	11.5	890	
$30 \times 30 \times 30$	615	0	3.12	15	3250	1.06
$40 \times 40 \times 40$	615	0	3.12	19	8050	1.05
$60 \times 50 \times 60$	615	0	3.15	24.5	17300	0.74
$70 \times 50 \times 70$	640	6	3.27	57	105200	5.86
$80 \times 50 \times 80$	666	10	3.35	77	135300	0.94

Table 2.5: For each mesh : number $N_{\Delta t}$ of successful time steps, number N_{Chop} of time step chops, number N_{Newton} of Newton iterations per successful time step, number N_{GMRes} of GMRes iterations by Newton iteration, CPU time in seconds, and scaling of CPU time (α_{CPU}) by $CPU \sim \text{cells}^{\alpha_{CPU}}$.

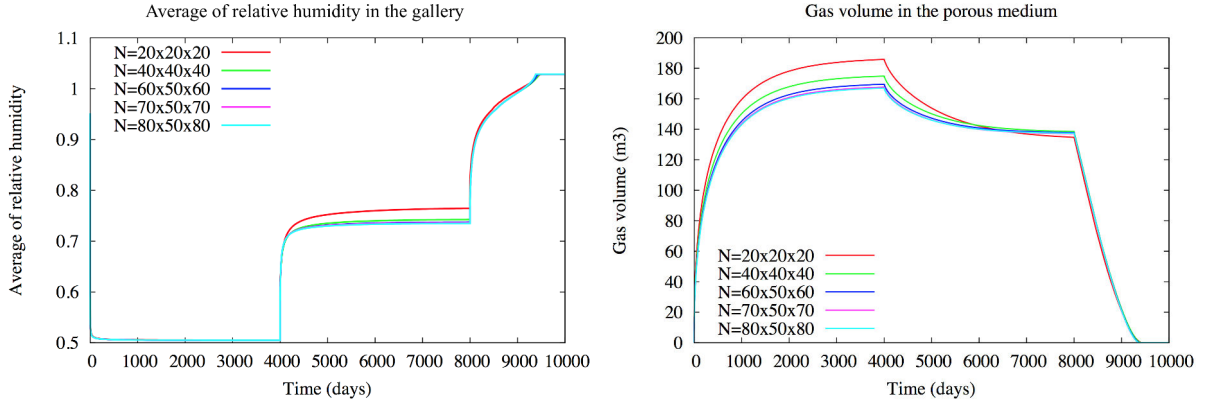


Figure 2.13: Average relative humidity in the gallery $H_r(t)$ (left) and gas volume in the porous medium as a function of time (right) for the five meshes.

2.4.2 Heterogeneous anisotropic test case

This second test case considers two different rocktypes in the porous medium. For $r_S < r < r_I = 3$ m we consider a damaged rock with isotropic permeability $\mathbf{K}_m = 5 \cdot 10^{-18} \text{ m}^2$ and a porosity $\phi_m = 0.15$, and for $r > r_I$ we consider the Callovo-Oxfordian argillites (COx) with the same porosity $\phi_m = 0.15$ and the anisotropic permeability defined by

$$\mathbf{K}_m = \begin{pmatrix} \lambda & 0 & 0 \\ 0 & \lambda & 0 \\ 0 & 0 & \frac{\lambda}{10} \end{pmatrix} \quad (2.30)$$

with $\lambda = 5 \cdot 10^{-20} \text{ m}^2$ in the x, y, z Cartesian coordinates where z is the vertical coordinate and x the direction of the Gallery. The Van-Genuchten parameters are defined by $n = 1.50$, $s_r^l = 0.2$, $s_r^g = 0$, $P_r = 5 \cdot 10^6 \text{ Pa}$ in the damaged zone, and by $n = 1.49$, $s_r^l = 0.4$, $s_r^g = 0$, $P_r = 15 \cdot 10^6 \text{ Pa}$ in the COx region.

The simulation is run over a period of 20000 days with an initial time step of 100 second and a maximum time step of 1000 days. The input velocity w_{in} is fixed to 1 m.s^{-1} during the first 3000 days, to 0.1 m.s^{-1} during the next 3000 days, and to 0.01 m.s^{-1} during the remaining of the simulation (see Figure 2.14). All the other parameters of the data set are the same as in the previous test case.

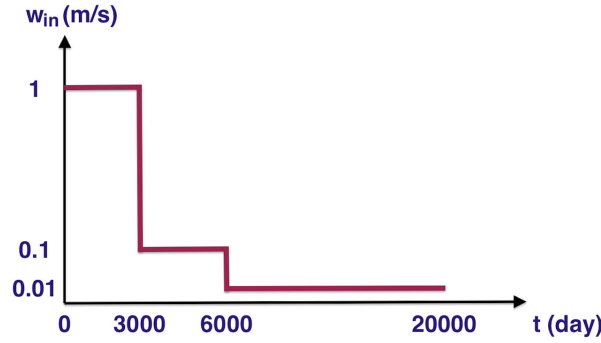


Figure 2.14: Input velocity w_{in} as a function of time.

As in the previous test case, the Figures 2.15, 2.16, and 2.17 exhibit the numerical solution obtained with the mesh $60 \times 60 \times 60$. Figure 2.15 plots the relative humidity in the gallery at the end of the simulation as a function of x , as well as the average relative humidity $H_r(t)$. Figure 2.16 shows the gas volume in the porous medium as a function of time, and the volumetric flow rates for both phases at the porous medium gallery interface as a function of time. Figure 2.17 plots the liquid saturation at the end of the simulation. Compared with the previous test case, a larger volume of gas enters into the porous medium due to the larger permeability of the damaged zone. The effect of the anisotropy along the vertical direction in the COx region is also clear in the right liquid saturation plot in Figure 2.17.

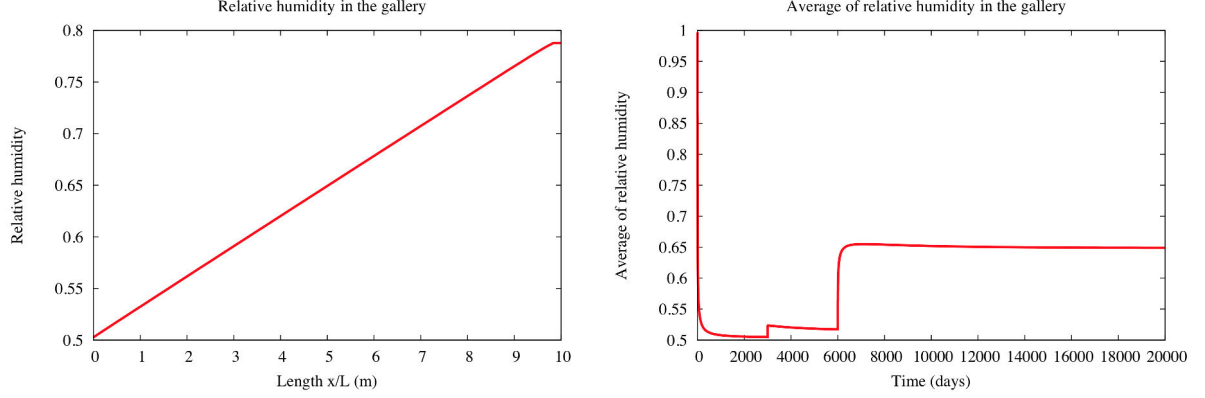


Figure 2.15: Relative humidity in the gallery at the end of the simulation (left); average of the relative humidity in the gallery as a function of time (right).

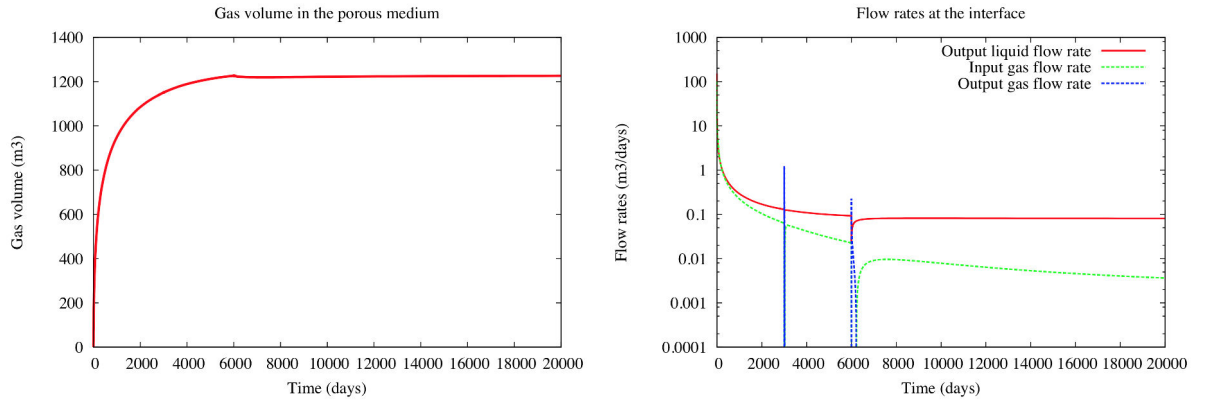


Figure 2.16: Gas Volume in the porous medium as a function of time (left); input and output flow rates at the interface Γ for the gas and liquid phases (right) as a function of time (an input flow rate enters into the porous medium).

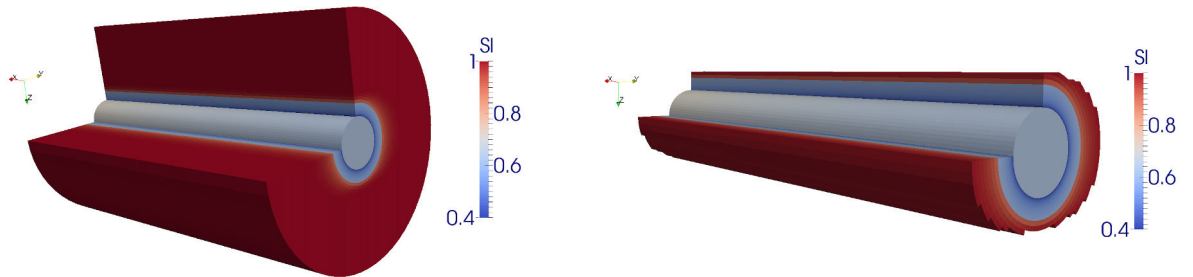


Figure 2.17: Liquid saturation s^l at the end of the simulation. At the right, the liquid saturation in the porous medium is plotted only below the threshold value 0.99. In the gallery the liquid saturation corresponds to the saturation at the interface function of x .

Figure 2.18 exhibits the convergence of the volume of gas in the porous medium as a function of time and of $H_r(t)$ for the five different meshes $30 \times 30 \times 30$, $40 \times 40 \times 40$, $50 \times 50 \times 50$, $60 \times 60 \times 60$ and $70 \times 70 \times 70$. Table 2.6 shows the numerical behaviour of the simulations for these five meshes with again a rather good scalability of the linear and nonlinear solvers and of the CPU time w.r.t. the mesh size.

mesh	$N_{\Delta t}$	N_{Chop}	N_{Newton}	N_{GMRes}	CPU(s)	α_{CPU}
$30 \times 30 \times 30$	409	0	3.31	15	2200	
$40 \times 40 \times 40$	409	0	3.34	18	6800	1.31
$50 \times 50 \times 50$	409	0	3.37	20	14050	1.08
$60 \times 60 \times 60$	409	0	3.40	23	20100	0.65
$70 \times 70 \times 70$	409	0	3.45	25	34700	1.18

Table 2.6: For each mesh : number $N_{\Delta t}$ of successful time steps, number N_{Chop} of time step chops, number N_{Newton} of Newton iterations per successful time step, number N_{GMRes} of GMRes iterations by Newton iteration, CPU time in seconds, and scaling of CPU time (α_{CPU}) by $CPU \sim \text{cells}^{\alpha_{CPU}}$.

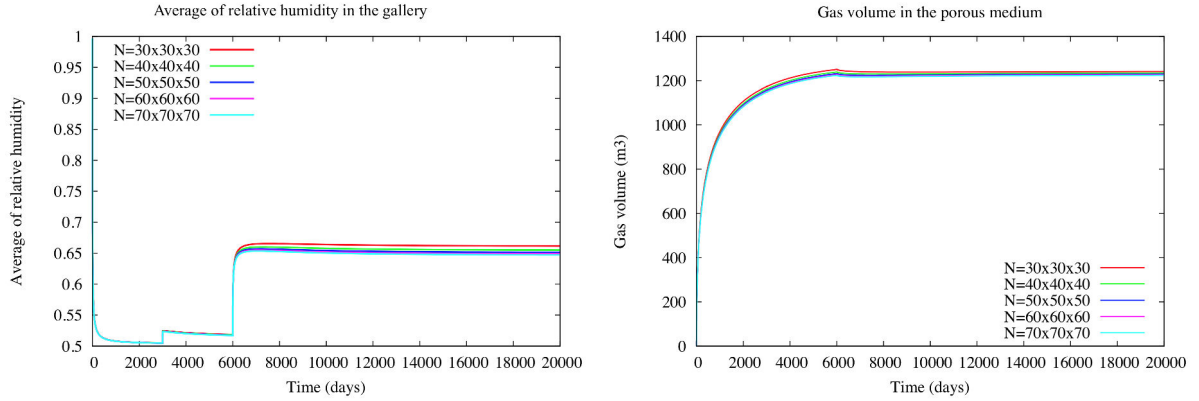


Figure 2.18: Average in space of the relative humidity in the gallery (left) and gas volume in the porous medium (right) as a function of time.

2.4.3 Model with gas molar fraction and diffusion at the interface

The previous model can be improved by the introduction of two gas molar fractions in the gallery instead of a single one. The first one corresponds to the gas molar fraction in the viscous boundary layer at the interface Γ on the gallery side. By the assumption of continuity of the gas molar fraction, it is equal to $c^g(\gamma\mathcal{U})$. Outside of this boundary layer, the second gas molar fraction is assumed to be constant in the section of the gallery thanks to a strong turbulent mixing. This second gas molar fraction is denoted by c

which is now an additional independent unknown. Another additional unknown is the gas normal velocity at the interface Γ denoted by v_n with the normal oriented outward of the porous medium (see Figure 2.19).

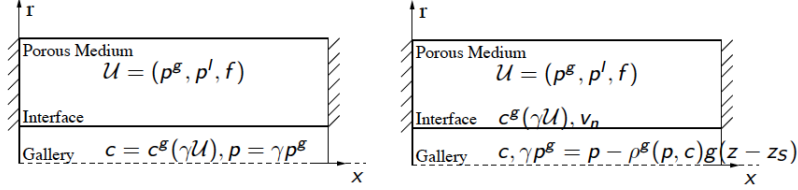


Figure 2.19: Main unknowns in the porous medium, at the interface and in the gallery for the previous model (left) and the new model (right) with $z_S = \frac{1}{|S|} \int_S dz$.

The new system unknowns are the porous medium unknowns $\mathcal{U} \in L^2(0, T; H^1(\Omega)) \times L^2(0, T; H^1(\Omega))$, the gas molar fractions in the gallery $c = (c_i)_{i \in \mathcal{C}}$ with $c_i \in L^\infty((0, L) \times (0, T))$, as well as the gas normal velocity at the interface $v_n \in L^\infty(\Gamma \times (0, T))$. They satisfy formally the porous medium equations (without fractures)

$$\begin{cases} \phi_m \partial_t n_{i,m}(\mathbf{x}, \mathcal{U}) + \operatorname{div}(\mathbf{q}_{m,i}) = 0, \quad i = a, e, \\ - \sum_{\alpha=g,l} m_{i,m}^\alpha(\mathbf{x}, \mathcal{U}) \mathbf{K}_m \left(\nabla p^\alpha - \rho^\alpha(\mathcal{U}) \mathbf{g} \right) = \mathbf{q}_{m,i}, \quad i = a, e, \end{cases} \quad (2.31)$$

coupled with the following modified conditions at the interface Γ

$$\begin{cases} \mathbf{q}_{m,i} \cdot \mathbf{n} = \zeta^g(\gamma\mathcal{U}) \left(c_i^g(\gamma\mathcal{U}) (v_n)^+ + c_i(v_n)^- + \frac{D^g}{\delta} (c_i^g(\gamma\mathcal{U}) - c_i) \right), \quad i = a, e, \\ \sum_{i \in \mathcal{C}} c_i^\alpha(\gamma\mathbf{u}) = 1, \quad \alpha = g, l, \\ \gamma p^g = p - \rho^g(p, c)g(z - \frac{1}{|S|} \int_S dz), \end{cases} \quad (2.32)$$

and the conservation equations along the gallery

$$\begin{cases} \partial_t \left(|S| \zeta^g(\gamma p^g, c) c_i \right) + \partial_x (q_{g,i}) = \int_{\partial S} \mathbf{q}_{m,i} \cdot \mathbf{n} \, ds, \quad i = a, e, \\ q_{g,i} = - \frac{|S|}{\alpha_g} \zeta^g(\gamma p^g, c) c_i \partial_x \gamma p^g, \quad i = a, e, \\ \sum_{i=a,e} c_i = 1, \end{cases} \quad (2.33)$$

where we have used the notation $a^+ = \max(a, 0)$ and $a^- = \min(a, 0)$. The interface conditions (2.32) account for the gas pressure continuity, the thermodynamical equilibrium,

and the molar flux continuity. The gas pressure γp^g at the interface assumes an hydrostatic pressure in the section S . In most cases, this hydrostatic correction can actually be neglected.

Following [49], the molar flux continuity takes into account the two point diffusion flux $\frac{D^g}{\delta}(c_i^g(\gamma\mathcal{U}) - c_i)$ between the gas molar fraction at the interface $c^g(\gamma\mathcal{U})$ and the mean gas molar fraction c in the gallery, where D^g is the Fickian diffusion coefficient set to $D^g = 2 \cdot 10^{-5} \text{ m}^2.\text{s}^{-1}$ in the following tests. The parameter δ is a convection diffusion boundary layer thickness at the interface Γ for the H_2O molar fraction in the gallery. It depends on the velocity and on the turbulent diffusion in the gallery. In practice, it can be obtained using a diagonal approximation of the Steklov Poincaré operator associated to the stationary convection diffusion equation in the gallery (see in subsection 3.3.2 of Chapter 3).

This diffusion term is essential to allow the component molar fluxes $\mathbf{q}_{m,i} \cdot \mathbf{n}$ at the interface to take different signs (typically positive for the water component and negative for the air component). Note also that the previous model is recovered at the limit when δ goes to zero implying that $\gamma c^g(\gamma\mathcal{U}) = c$.

In the following tests, the influence of the parameter δ on the solution of the previous test case is investigated for $\delta = 10^{-1}, 10^{-2}, 10^{-3}, 10^{-4}, 10^{-5} \text{ m}$. It is compared with the previous model solution corresponding to $\delta \rightarrow 0^+$. All the physical and numerical parameters are the same than in the previous test case including the input velocity w_{in} (see Figure 2.14). The initial time step is changed to $\Delta t = 0.1 \text{ s}$ and the mesh size is fixed to $40 \times 40 \times 40$. It is clear from the numerical results exhibited in Figures 2.20, 2.21 and 2.22 that the larger δ , the higher the average relative humidity at the interface, the lower the output liquid flux at the interface, and the lower the average relative humidity in the gallery. The convergence of the model for decreasing δ to the previous limit model obtained for $\delta \rightarrow 0^+$ is also checked.

The difference between both models is also seen to be much larger at small times when the liquid flux at the interface is high due to the instantaneous opening of the gallery. At larger times, once the liquid flux at the interface has sufficiently decreased (the threshold value depending on δ) both models roughly match. Table 2.7 exhibits the good numerical behavior of the Newton solver for a large range of δ .

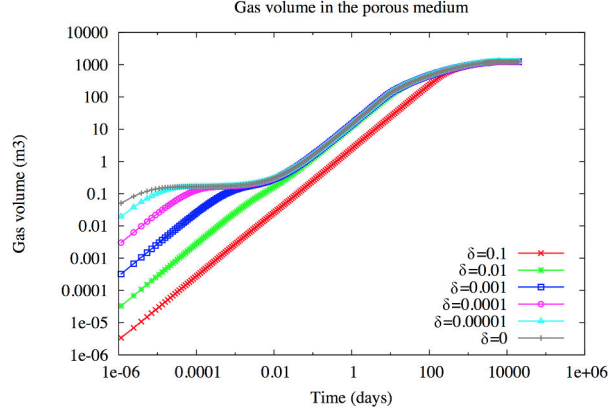


Figure 2.20: Gas volume in the porous medium as a function of time.

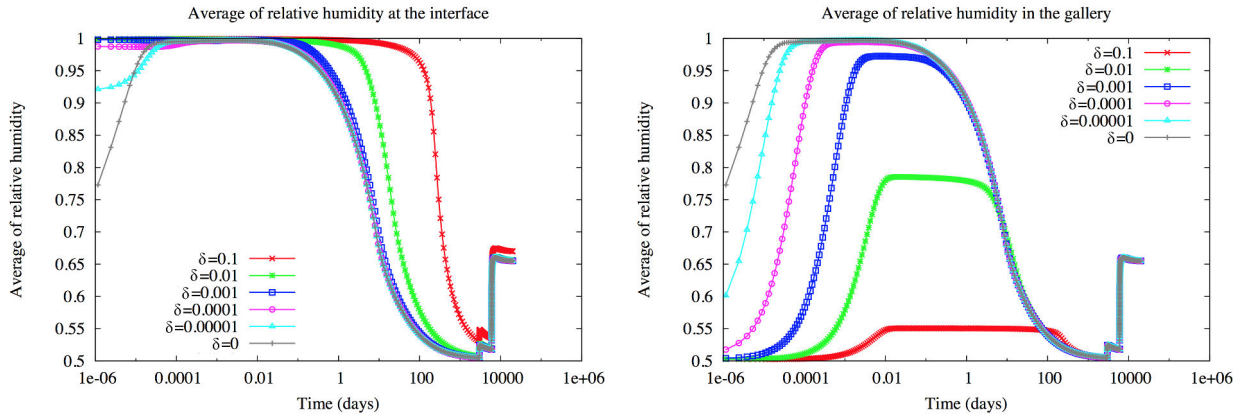


Figure 2.21: Average in space of the relative humidity at the interface (left) and in the gallery (right) as a function of time.

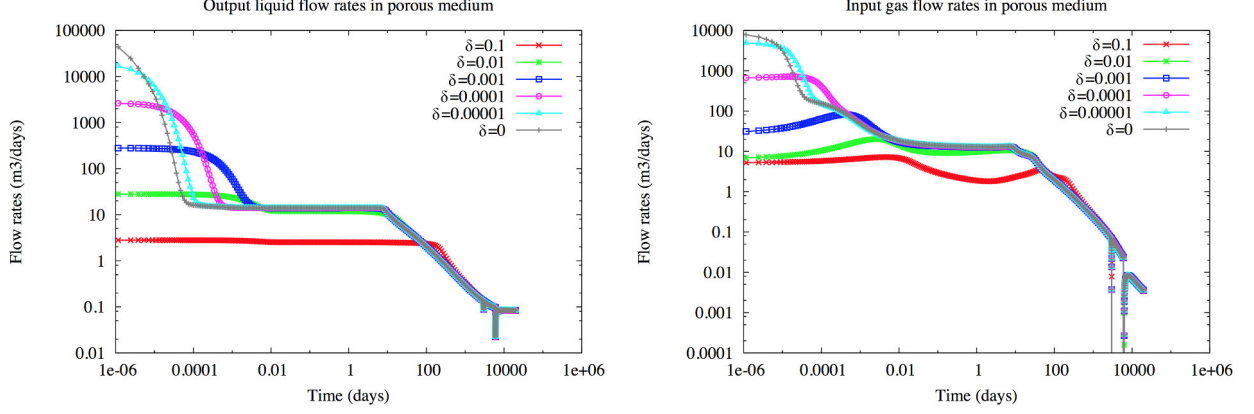


Figure 2.22: Output liquid flow rates (left) and input gas flow rates (right) in the porous medium as a function of time.

δ	$N_{\Delta t}$	N_{Chop}	N_{Newton}	N_{GMRes}	CPU(s)
10^{-1}	464	0	3.26	11.9	7064
10^{-2}	464	0	3.36	14.6	5971
10^{-3}	464	0	3.43	15.6	7631
10^{-4}	464	0	3.55	16.5	6353
10^{-5}	464	0	3.67	18.1	6630
0	464	0	3.71	19.7	6863

Table 2.7: For the mesh $40 \times 40 \times 40$ and each value of δ : number $N_{\Delta t}$ of successful time steps, number N_{Chop} of time step chops, number N_{Newton} of Newton iterations per successful time step, number N_{GMRes} of GMRes iterations by Newton iteration, CPU time in seconds.

2.5 Numerical experiments with fractures

2.5.1 Test case with 1 fracture

Let ω and S be the disks of center 0 and radius respectively $r_\omega = 15$ m and $r_S = 2$ m. We consider a radial mesh of the domain $(0, L) \times (\omega \setminus \overline{S})$, $L = 100$ m of size $n_x = 40$, $n_r = 30$, $n_\theta = 32$ in the cylindrical coordinates x, r, θ . The porous medium radial mesh is exponentially refined at the interface of the gallery Γ and matches at the interface Γ with the 1D mesh of the gallery.

The porous medium includes a single fracture defined by $x = 50$ m, $\theta \in [0, 2\pi)$, $r \in (r_S, r_f)$ with $r_f = 10$ m. The mesh is uniform in the x and θ directions and is exponentially refined at the interface of the gallery Γ to account for the steep gradient of the capillary pressure at the porous medium gallery interface. The mesh in the gallery is

conforming with the porous medium mesh in the sense that $m_x = n_x$ and that the points x_m , $m = 0, \dots, m_x + 1$ match with the x coordinates of the nodes along the x direction in the porous medium.

The thermodynamical laws are like in Section 2.4 for the fixed temperature $T_e = 300$ K. The Darcy Forchheimer parameters are set to $\alpha_g = 0$ and $\beta_g = 10^{-3}$ Kg.m⁻⁴. The relative permeabilities and capillary pressure are given by the Van-Genuchten laws (1.20)-(1.21)-(1.22).

Two different rocktypes are considered in the matrix domain $\Omega \setminus \bar{\Gamma}_f$. For $r_S < r < r_I = 3$ m we consider a damaged rock with isotropic permeability $\mathbf{K}_m = 5 \cdot 10^{-18}$ m² and a porosity $\phi_m = 0.15$, and for $r > r_I$ we consider the Callovo-Oxfordian argillites (COx) with the same porosity $\phi_m = 0.15$ and the anisotropic permeability defined by (2.30) with $\lambda = 5 \cdot 10^{-20}$ m². The Van-Genuchten parameters are defined by $n = 1.50$, $s_r^l = 0.2$, $s_r^g = 0$, $P_r = 5 \cdot 10^6$ Pa in the damaged zone, and by $n = 1.49$, $s_r^l = 0.4$, $s_r^g = 0$, $P_r = 15 \cdot 10^6$ Pa in the COx region. In the fracture Γ_f , the fracture width is equal to $d_f = 0.01$ m, the porosity is set to $\phi_f = 0.3$, the permeability is isotropic and set to $\mathbf{K}_f = 10^{-13}$ m², and The Van-Genuchten parameters are defined by $n = 4$, $s_r^l = 0$, $s_r^g = 0$, $P_r = 5 \cdot 10^5$ Pa.

The porous medium is initially saturated by the liquid phase with imposed pressure $p_{ini}^l = 40 \cdot 10^5$ Pa and composition $c_{a,ini}^l = 0$, $c_{e,ini}^l = 1$. At the external boundary $r = r_\omega$ the water pressure is fixed to $\bar{p}^l = p_{ini}^l$, with an input composition $\bar{c}_a^l = 0$, $\bar{c}_e^l = 1$. At both sides $x = 0$ and $x = L$ of the porous medium, zero flux boundary conditions are imposed. The initial condition in the gallery is given by $p_{ini} = 10^5$ Pa and $c_{e,ini}$ defined by the relative humidity

$$H_{r,ini} = \frac{c_{e,ini} p_{ini}}{p_{sat}(T_e)} = 0.5.$$

We consider an input gas velocity $w_{in} = 1$ m.s⁻¹, a fixed input water molar fraction $\bar{c}_{e,0} = c_{e,ini}$ at the left side $x = 0$ of the gallery, and a fixed output pressure $\bar{p}_L = p_{ini}$ at the right side $x = L$ of the gallery. The simulation is run over a period of 20000 days with an initial time step of 0.1 seconds and a maximum time step of 1000 days.

At the opening of the gallery at $t = 0$, we observe in Figure 2.25 an increase of the mean relative humidity up to say 0.98 in a few seconds due to a large liquid flow rate at the interface. Then, the flow rate decreases and we observe a drying of the gallery due to the ventilation at $w_{in} = 1$ m.s⁻¹ down to an average relative humidity slightly above $H_{r,ini}$ in a few tens days. Meanwhile the gas penetrates slowly into the porous medium reaching a stationary state with around 160 m³ of gas in say 10000 days (see Figure 2.24). As can be seen in Figure 2.23, the gas penetrates much deeper and at a much higher saturation in the fracture than in the porous medium due to the higher permeability and to the lower capillary pressure in the fracture than in the porous medium.

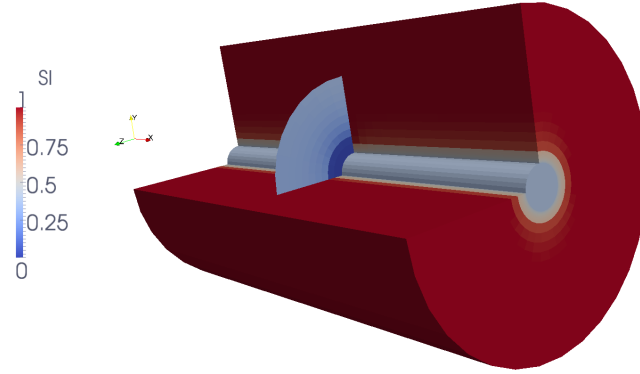


Figure 2.23: One fracture test case: liquid saturation s^l at the end of the simulation. In the gallery the liquid saturation corresponds to the saturation at the interface as a function of x .

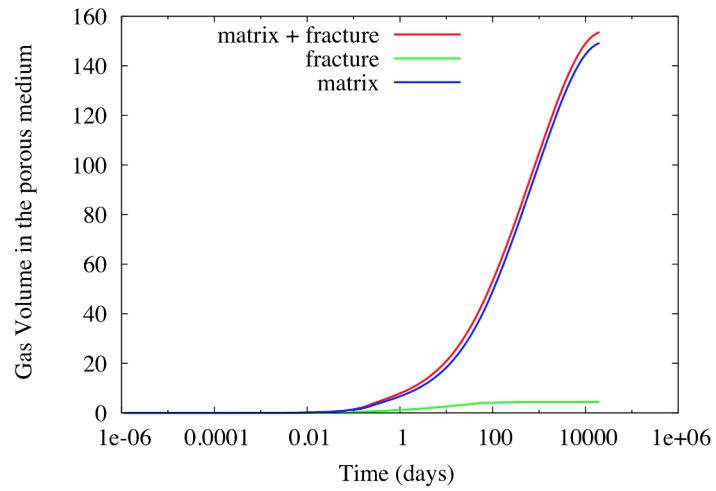


Figure 2.24: One fracture test case: volume of gas in the matrix, in the fracture and in the porous medium (matrix + fracture) as a function of time.

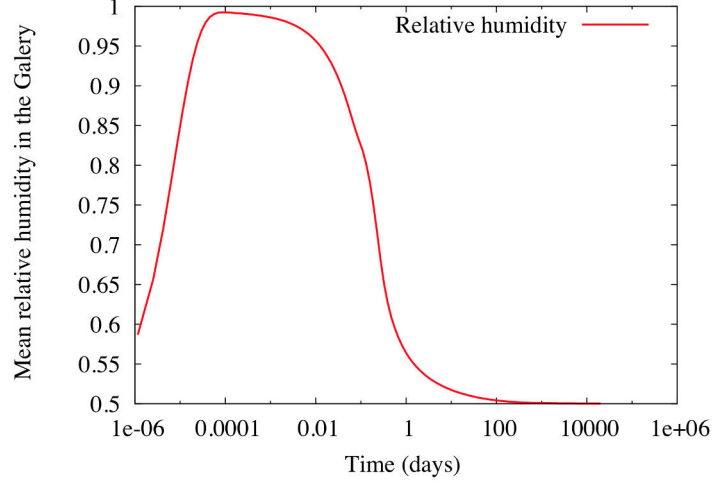


Figure 2.25: One fracture test case: mean relative humidity in the gallery as a function of time (equal to 0.5 at initial time).

2.5.2 Test case with 4 fractures

We consider the same test case as the previous one but including 4 fractures defined by $x = 35$ m, $\theta \in [0, 2\pi)$, $r \in (r_S, r_f)$ for the first fracture, by $x = 65$ m, $\theta \in [0, 2\pi)$, $r \in (r_S, r_f)$ for the second fracture, by $\theta = \frac{\pi}{4}$, $r \in (r_S, r_f)$, $x \in (25, 75)$ for the third one, and by $\theta = \frac{5\pi}{4}$, $r \in (r_S, r_f)$, $x \in (25, 75)$ for the last one. The numerical results exhibited in Figures 2.26, 2.27, 2.28 are similar to those of the previous test case with, as expected, a larger amount of gas in the fracture network, and a slightly higher relative humidity in the transient phase.

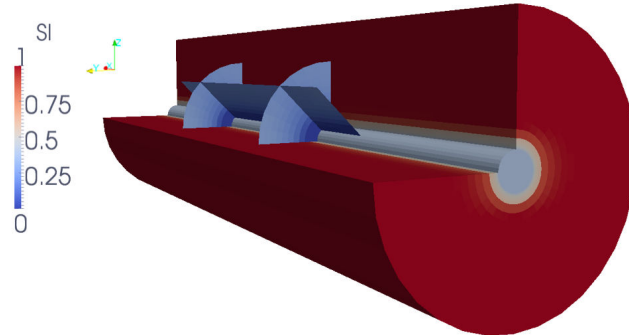


Figure 2.26: Four fractures test case: liquid saturation s^l at the end of the simulation. In the gallery the liquid saturation corresponds to the saturation at the interface as a function of x .

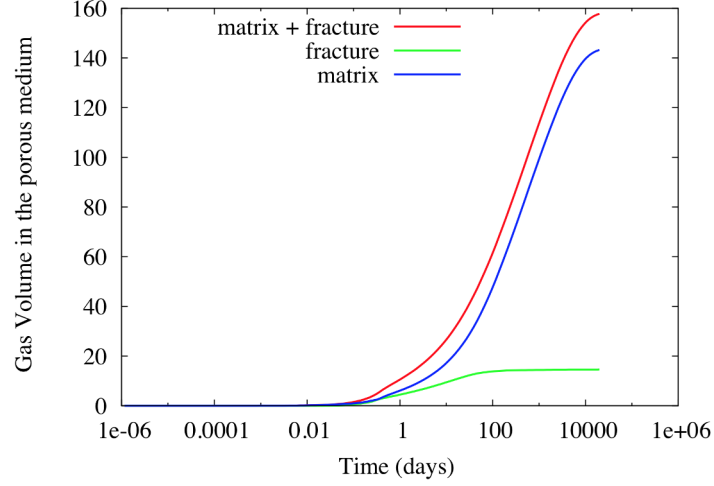


Figure 2.27: Four fractures test case: volume of gas in the matrix, in the fracture and in the porous medium (matrix + fracture) as a function of time.

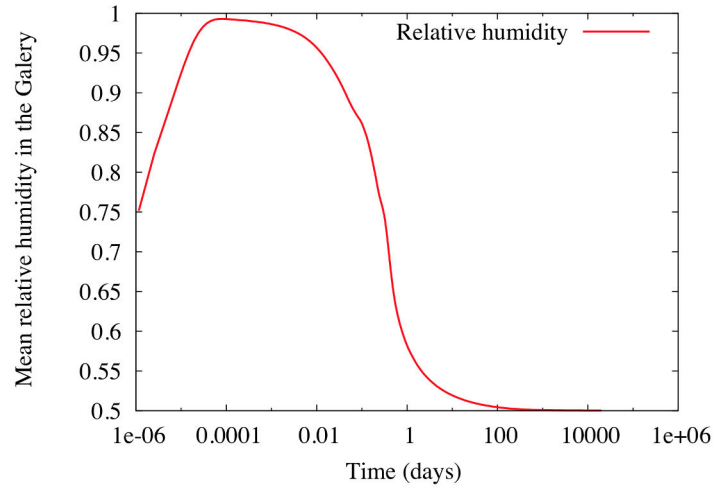


Figure 2.28: Four fractures test case: mean relative humidity in the gallery as a function of time (equal to 0.5 at initial time).

2.6 Convergence analysis of a simplified model

In this section it is assumed that there is no fracture i.e. $\Gamma_f = \emptyset$, and we consider the following simplified model using the Richards approximation in the porous medium and

a single component equation in the gallery with linear pressure drop.

$$\begin{cases} \phi_m \partial_t(\zeta^l \mathbf{S}^l(., u)) + \operatorname{div}(\zeta^l \mathbf{V}^l) = Q, \\ \partial_t(|S| \zeta^g(p)) + \partial_x(-\frac{1}{\alpha_g} |S| \tilde{\zeta}^g(p) \partial_x p) = \int_{\partial S} \zeta^l \mathbf{V}^l \cdot \mathbf{n} \, ds + |S| q, \\ \mathbf{V}^l = -\frac{k_r^\alpha(., \mathbf{S}^l(., u))}{\mu^l} \mathbf{K}_m(\nabla u - M^l \zeta^l \mathbf{g}), \quad p = g(\gamma(u)), \end{cases} \quad (2.34)$$

where we have used the notation $\mathbf{S}^l(\mathbf{x}, u) = \mathbf{S}^l(\mathbf{x}, -u)$. The only primary unknown in the porous medium is the liquid pressure denoted by u . The liquid mass density is assumed to be fixed to $M^l \zeta^l$ where M^l is the molar mass of the liquid phase and ζ^l is considered constant. The thermodynamical equilibrium at the interface Γ is accounted for by the relation $p = g(\gamma(u))$ with $g \in C^1(\mathbb{R}, \mathbb{R}^+)$, $0 < g'(q) \leq c_2$ for all $q \in \mathbb{R}$ and for a given constant $c_2 > 0$. The function g is a regularization for large positive u of $p = \frac{p_{\text{sat}}(T_e)}{c_e} e^{\frac{u}{\zeta^l R T_e}}$ for given constants $1 \geq c_e > 0$ and $T_e > 0$. The molar gas density is set to $\zeta^g(p) = \frac{p}{R T_e}$ and is truncated in the flux term such that $\tilde{\zeta}^g(p)$ is assumed to be a non decreasing function in $C^1(\mathbb{R}^+, \mathbb{R}^+)$ bounded from below and above by two strictly positive constants and with a bounded derivative.

Let us define the function space

$$U = \{u \in H^1(\Omega) \mid \partial_s \gamma u = 0\},$$

and its subspace $U^0 = U \cap H_{\Gamma_D}^1(\Omega)$ with zero trace on Γ_D . Let us also define the function space

$$V = \{u \in U \mid \gamma u \in H^1(\Gamma)\}.$$

Let $\mathcal{C}(\Omega \times [0, T])$ be the subspace of functions φ of $C^\infty(\overline{\Omega} \times [0, T])$ vanishing in a neighbourhood of $t = T$, $\bar{\Gamma}_D$ and $\partial\omega \times \{0, L\}$, and such that $\partial_s \varphi = 0$ in a neighbourhood of $\bar{\Gamma}$. Given $\bar{u} \in V$, $u_{\text{init},p} \in L^2(\Omega)$, and $u_{\text{init},g} \in L^2(0, L)$ the variational formulation of the simplified coupled model amounts to find $u \in L^2(0, T; U)$ with $u - \bar{u} \in L^2(0, T; U^0)$ and $g(\gamma u) - g(\gamma \bar{u}) \in L^2(0, T; H_0^1(\Gamma))$ such that for all $\varphi \in \mathcal{C}(\Omega \times [0, T])$ one has

$$\begin{cases} - \int_0^T \int_{\Omega} \phi_m(\mathbf{x}) \zeta^l \mathbf{S}^l(\mathbf{x}, u(\mathbf{x}, t)) \partial_t \varphi(\mathbf{x}, t) d\mathbf{x} dt - \int_{\Omega} \phi_m \zeta^l \mathbf{S}^l(\mathbf{x}, u_{\text{init},p}(\mathbf{x})) \varphi(\mathbf{x}, 0) d\mathbf{x} \\ - \int_0^T \int_0^L |S| \zeta^g(g(\gamma u)(x, t)) \partial_t \gamma \varphi(x, t) dx dt - \int_0^L |S| \zeta^g(g(u_{\text{init},g})(x)) \gamma \varphi(x, 0) dx \\ + \int_0^T \int_{\Omega} \zeta^l \frac{k_r^l(\mathbf{x}, \mathbf{S}^l(u(\mathbf{x}, t)))}{\mu^l} \mathbf{K}_m(\nabla u(\mathbf{x}, t) - M^l \zeta^l \mathbf{g}) \cdot \nabla \varphi(\mathbf{x}, t) d\mathbf{x} dt \\ + \int_0^T \int_0^L \frac{1}{\alpha_g(x)} |S| \tilde{\zeta}^g(g(\gamma u)(x, t)) \partial_x g(\gamma u)(x, t) \partial_x \gamma \varphi(x, t) dx dt \\ = \int_0^T \left(\int_{\Omega} Q(\mathbf{x}, t) \varphi(\mathbf{x}, t) d\mathbf{x} + \int_0^L |S| q(x, t) \gamma \varphi(x, t) dx \right) dt. \end{cases} \quad (2.35)$$

We make the following additional *assumptions on the data*:

- It is assumed that $k_r^l(\mathbf{x}, s)$ is a measurable function w.r.t. \mathbf{x} and continuous w.r.t. s , and such that $0 < k_{min} \leq k_r^l(\mathbf{x}, s) \leq k_{max}$ for all $(\mathbf{x}, s) \in \Omega \times [0, 1]$.
- $S^l(\mathbf{x}, u) \in [0, 1]$ for all $(\mathbf{x}, u) \in \Omega \times \mathbb{R}$ with $S^l(\mathbf{x}, u) = S_j^l(u)$ for a.e. $\mathbf{x} \in \Omega_j$ and all $u \in \mathbb{R}$, where S_j^l is a non decreasing Lipschitz continuous function with constant L_s and $(\Omega_j)_{j \in J}$ is a finite family of disjoint connected polyhedral open sets such that $\bigcup_{j \in J} \overline{\Omega_j} = \overline{\Omega}$.
- It is assumed that there exists a constant L_{sp} such that $|S^l(x, v) - S^l(x, u)| \leq L_{sp}|g(v) - g(u)|$ for all $\mathbf{x} \in \Omega$ and $(u, v) \in \mathbb{R}^2$.
- The permeability tensor \mathbf{K}_m is a measurable function on the space of symmetric 3 dimensional matrices such that there exist $0 < \underline{\lambda}_m \leq \overline{\lambda}_m$ with $\underline{\lambda}_m|\xi|^2 \leq (\mathbf{K}_m(\mathbf{x})\xi, \xi) \leq \overline{\lambda}_m|\xi|^2$ for all $\mathbf{x} \in \overline{\Omega}$.
- $\alpha_g \in L^\infty(0, L)$ is such that $0 < \underline{\alpha}_g \leq \alpha_g(x) \leq \overline{\alpha}_g$ for all $x \in (0, L)$.
- The porosity ϕ_m belongs to $L^\infty(\Omega)$ with $0 < \underline{\phi}_m \leq \phi_m(\mathbf{x}) \leq \overline{\phi}_m$ for all $\mathbf{x} \in \Omega$.
- It is assumed that $Q \in L^2(\Omega \times (0, T))$ and $q \in L^2((0, L) \times (0, T))$.

Remark 2.6.1 *The VAG discretization and convergence analysis detailed below for the model (2.34) can be readily adapted to another simplified model coupling the Richards equation in the porous medium to a 1D convection diffusion equation for the water molar fraction c_e at given constant velocity w , constant diffusion coefficient $D^g > 0$, and at given constant pressure p .*

$$\left\{ \begin{array}{l} \phi_m \partial_t(\zeta^l S^l(\cdot, u)) + \operatorname{div}(\zeta^l \mathbf{V}^l) = Q, \\ \partial_t(|S|\zeta^g(p)c_e) + \partial_x(|S|\zeta^g(p)(wc_e - D^g \partial_x c_e)) = \int_{\partial S} \zeta^l \mathbf{V}^l \cdot \mathbf{n} \, ds + |S|q, \\ \mathbf{V}^l = -\frac{k_r^\alpha(\cdot, S^l(\cdot, u))}{\mu^l} \mathbf{K}_m(\nabla u - M^l \zeta^l \mathbf{g}), \quad c_e = \bar{g}(\gamma(u)), \end{array} \right. \quad (2.36)$$

As for (2.34), the thermodynamical equilibrium at the interface Γ is accounted for by the relation $c_e = \bar{g}(\gamma(u))$ with $\bar{g} \in C^1(\mathbb{R}, \mathbb{R}^+)$, $0 < \bar{g}'(q) \leq c_2$ for all $q \in \mathbb{R}$ and for a given constant $c_2 > 0$. Here the function \bar{g} is a regularization for large positive u of $c_e = \frac{p_{sat}(T_e)}{p} e^{\frac{u}{\zeta^l R T_e}}$ for given constants $p > 0$ and $T_e > 0$.

The model (2.36) is a rather good approximation of the full model thanks to the weak liquid inflow from the porous medium to the gallery.

2.6.1 Vertex Approximate Gradient Discretization

We restrict ourself to the conforming case for which $\Pi_{\mathcal{T}} X_{\mathcal{D}} \subset V$ and $\nabla_{\mathcal{D}_g} = \partial_x \gamma \Pi_{\mathcal{T}}$. It is obtained by assuming that

- for all $\mathbf{s} \in \mathcal{V}_\Gamma$ there exists $m \in \{0, \dots, m_x + 1\}$ such that $x_{\mathbf{s}} = x_m$

- denoting by \mathcal{V}_m the set of nodes along $\{x_m\} \times \partial S = \{\mathbf{s}_1, \dots, \mathbf{s}_{k_m}\}$ in cyclic order, all the edges $(\mathbf{s}_k, \mathbf{s}_{k+1})$, $k = 1, \dots, k_m - 1$ and $(\mathbf{s}_{k_m}, \mathbf{s}_1)$ belong to \mathcal{E} .

For $v \in X_{\mathcal{D}}$, and a function $k \in C^0(\mathbb{R}, \mathbb{R})$, we define $k(v) \in X_{\mathcal{D}}$ as follows: $k(v)_{\mathbf{s}} = k(v_{\mathbf{s}})$ for all $\mathbf{s} \in \mathcal{V}$ and $k(v)_K = k(v_K)$ for all $K \in \mathcal{M}$.

Given $u_{\mathcal{D}}^0 \in X_{\mathcal{D}}$ and $\bar{u}_{\mathcal{D}} \in X_{\mathcal{D}}$, the discrete unknowns $u_{\mathcal{D}}^n \in X_{\mathcal{D}}$ at all time step $n = 1, \dots, N$ are such that they satisfy $u_{\mathcal{D}}^n - \bar{u}_{\mathcal{D}} \in X_{\mathcal{D}}^0$ and the following discrete variational formulation

$$\left\{ \begin{aligned} & \int_{\Omega} \phi_m(\mathbf{x}) \zeta^l \frac{S^l(\mathbf{x}, \Pi_{\mathcal{D}_m} u_{\mathcal{D}}^n(\mathbf{x})) - S^l(\mathbf{x}, \Pi_{\mathcal{D}_m} u_{\mathcal{D}}^{n-1}(\mathbf{x}))}{\Delta t^n} \Pi_{\mathcal{D}_m} v_{\mathcal{D}}(\mathbf{x}) d\mathbf{x} \\ & + \int_0^L |S| \frac{\zeta^g(\Pi_{\mathcal{D}_g} g(u_{\mathcal{D}}^n)(x)) - \zeta^g(\Pi_{\mathcal{D}_g} g(u_{\mathcal{D}}^{n-1})(x))}{\Delta t^n} \Pi_{\mathcal{D}_g} v_{\mathcal{D}}(x) dx \\ & + \int_{\Omega} \zeta^l \frac{k_r^l(\mathbf{x}, S^l(\mathbf{x}, \Pi_{\mathcal{D}_m} u_{\mathcal{D}}^n(\mathbf{x})))}{\mu^l} \mathbf{K}_m (\nabla_{\mathcal{D}_m} u_{\mathcal{D}}^n(\mathbf{x}) - M^l \zeta^l \mathbf{g}) \cdot \nabla_{\mathcal{D}_m} v_{\mathcal{D}}(\mathbf{x}) d\mathbf{x} \\ & + \int_0^L \frac{1}{\alpha_g(x)} |S| \tilde{\zeta}^g(\Pi_{\mathcal{D}_g} g(u_{\mathcal{D}}^n)(x)) \nabla_{\mathcal{D}_g} g(u_{\mathcal{D}}^n)(x) \nabla_{\mathcal{D}_g} v_{\mathcal{D}}(x) dx \\ & = \frac{1}{\Delta t^n} \int_{t^{n-1}}^{t^n} \left(\int_{\Omega} Q(\mathbf{x}, t) \Pi_{\mathcal{D}_m} v_{\mathcal{D}}(\mathbf{x}) d\mathbf{x} + \int_0^L |S| q(x, t) \Pi_{\mathcal{D}_g} v_{\mathcal{D}}(x) dx \right) dt, \end{aligned} \right. \quad (2.37)$$

for all $v_{\mathcal{D}} \in X_{\mathcal{D}}^0$.

2.6.2 Convergence analysis

Let ρ_T denote the insphere diameter of a given tetrahedron $T \in \mathcal{T}$, h_T its diameter, and $h_{\mathcal{T}} = \max_{T \in \mathcal{T}} h_T$. We will assume in the convergence analysis that the family of tetrahedral submeshes \mathcal{T} is shape regular in the sense that $\theta_{\mathcal{T}} = \max_{T \in \mathcal{T}} \frac{h_T}{\rho_T}$ is bounded for the family of meshes. The following Lemmas are simple adaptations of the Lemmas already obtained in [14].

Lemma 2.6.1 *There exist $C_1, C_2 > 0$ depending only on $\theta_{\mathcal{T}}$ such that for all $u_{\mathcal{D}} \in X_{\mathcal{D}}$*

$$\|\Pi_{\mathcal{D}_m} u_{\mathcal{D}}\|_{L^2(\Omega)} \leq C_1 \|\Pi_{\mathcal{T}} u_{\mathcal{D}}\|_{L^2(\Omega)} \quad \text{and} \quad \|\Pi_{\mathcal{D}_g} u_{\mathcal{D}}\|_{L^2(0,L)} \leq C_2 \|\gamma \Pi_{\mathcal{T}} u_{\mathcal{D}}\|_{L^2(0,L)}. \quad (2.38)$$

We deduce from Lemma 2.6.1, the following discrete Poincaré inequalities.

Lemma 2.6.2 *There exist $C_5, C_6 > 0$ depending only on $\theta_{\mathcal{T}}$ such that for all $u_{\mathcal{D}} \in X_{\mathcal{D}}^0$*

$$\|\Pi_{\mathcal{D}_m} u_{\mathcal{D}}\|_{L^2(\Omega)} \leq C_5 \|\nabla_{\mathcal{D}_m} u_{\mathcal{D}}\|_{L^2(\Omega)^3} \quad \text{and} \quad \|\Pi_{\mathcal{D}_g} u_{\mathcal{D}}\|_{L^2(0,L)} \leq C_6 \|\nabla_{\mathcal{D}_g} u_{\mathcal{D}}\|_{L^2(0,L)}. \quad (2.39)$$

Lemma 2.6.3 *There exists $C_3 > 0$ depending only on $\theta_{\mathcal{T}}$ such that, for all $u_{\mathcal{D}} \in X_{\mathcal{D}}$,*

$$\|\Pi_{\mathcal{D}_m} u_{\mathcal{D}} - \Pi_{\mathcal{T}} u_{\mathcal{D}}\|_{L^2(\Omega)} + \|\Pi_{\mathcal{D}_g} u_{\mathcal{D}} - \gamma \Pi_{\mathcal{T}} u_{\mathcal{D}}\|_{L^2(0,L)} \leq C_3 h_{\mathcal{T}} \|\Pi_{\mathcal{T}} u_{\mathcal{D}}\|_V. \quad (2.40)$$

Lemma 2.6.3 imply in particular that there exists $C > 0$ depending only on $\theta_{\mathcal{T}}$ such that

$$\|\Pi_{\mathcal{D}_m} \bar{u}_{\mathcal{D}} - \bar{u}\|_{L^2(\Omega)} + \|\Pi_{\mathcal{D}_g} \bar{u}_{\mathcal{D}} - \bar{u}\|_{L^2(0,L)} \leq C \left((1 + h_{\mathcal{T}}) \|\Pi_{\mathcal{T}} \bar{u}_{\mathcal{D}} - \bar{u}\|_V + h_{\mathcal{T}} \|\bar{u}\|_V \right).$$

Next, for any smooth function $\varphi \in C^\infty(\bar{\Omega})$ such that $\partial_s \varphi = 0$ on Γ , let us define the projection $P_{\mathcal{D}} \varphi$ on $X_{\mathcal{D}}$ by $(P_{\mathcal{D}} \varphi)_K = \varphi(\mathbf{x}_K)$, $K \in \mathcal{M}$, $(P_{\mathcal{D}} \varphi)_{\mathbf{s}} = \varphi(\mathbf{x}_{\mathbf{s}})$, $\mathbf{s} \in \mathcal{V}$. We have the following classical finite element approximation result.

Lemma 2.6.4 *For all $\varphi \in C^\infty(\bar{\Omega})$ such that $\partial_s \varphi = 0$ on Γ , there exists $C(\varphi) > 0$ depending only on φ and $\theta_{\mathcal{T}}$ such that*

$$\|\varphi - \Pi_{\mathcal{T}} P_{\mathcal{D}} \varphi\|_V \leq C(\varphi) h_{\mathcal{T}}.$$

Let us set $X_{\mathcal{D}, \Delta t} = (X_{\mathcal{D}})^N$, and for all $v_{\mathcal{D}} = (v_{\mathcal{D}}^n)_{n=1, \dots, N} \in X_{\mathcal{D}, \Delta t}$ let us define for all $n = 1, \dots, N$

$$\begin{aligned} \Pi_{\mathcal{D}_p, \Delta t} v_{\mathcal{D}}(\mathbf{x}, t) &= \Pi_{\mathcal{D}_m} v_{\mathcal{D}}^n(\mathbf{x}) \text{ for all } (\mathbf{x}, t) \in \Omega \times (t^{n-1}, t^n], \\ \Pi_{\mathcal{D}_g, \Delta t} v_{\mathcal{D}}(x, t) &= \Pi_{\mathcal{D}_g} v_{\mathcal{D}}^n(x) \text{ for all } (x, t) \in (0, L) \times (t^{n-1}, t^n], \\ \Pi_{\mathcal{T}, \Delta t} v_{\mathcal{D}}(\mathbf{x}, t) &= \Pi_{\mathcal{T}} v_{\mathcal{D}}^n(\mathbf{x}) \text{ for all } (\mathbf{x}, t) \in \Omega \times (t^{n-1}, t^n], \\ \nabla_{\mathcal{D}_p, \Delta t} v_{\mathcal{D}}(\mathbf{x}, t) &= \nabla_{\mathcal{D}_m} v_{\mathcal{D}}^n(\mathbf{x}) \text{ for all } (\mathbf{x}, t) \in \Omega \times (t^{n-1}, t^n], \\ \nabla_{\mathcal{D}_g, \Delta t} v_{\mathcal{D}}(x, t) &= \nabla_{\mathcal{D}_g} v_{\mathcal{D}}^n(x) \text{ for all } (x, t) \in (0, L) \times (t^{n-1}, t^n]. \end{aligned}$$

Let $u_{\mathcal{D}} = (u_{\mathcal{D}}^n)_{n=1, \dots, N}$, the given solution to (2.37), we also define the functions

$$s_{\mathcal{D}_m, \Delta t}^l(\mathbf{x}, t) = S^l(\mathbf{x}, \Pi_{\mathcal{D}_p, \Delta t} u_{\mathcal{D}}(\mathbf{x}, t)), \quad p_{\mathcal{D}_g, \Delta t}(x, t) = g(\Pi_{\mathcal{D}_g, \Delta t} u_{\mathcal{D}}(x, t)),$$

and

$$\begin{aligned} \delta_{\mathcal{D}} s_{\mathcal{D}_p, \Delta t}^l(\mathbf{x}, t) &= \frac{S^l(\mathbf{x}, \Pi_{\mathcal{D}_m} u_{\mathcal{D}}^n(\mathbf{x})) - S^l(\mathbf{x}, \Pi_{\mathcal{D}_m} u_{\mathcal{D}}^{n-1}(\mathbf{x}))}{\Delta t^n} \text{ for all } (\mathbf{x}, t) \in \Omega \times (t^{n-1}, t^n], \\ \delta_{\mathcal{D}} p_{\mathcal{D}_g, \Delta t}(x, t) &= \frac{\Pi_{\mathcal{D}_g} g(u_{\mathcal{D}}^n)(x) - \Pi_{\mathcal{D}_g} g(u_{\mathcal{D}}^{n-1})(x)}{\Delta t^n} \text{ for all } (x, t) \in (0, L) \times (t^{n-1}, t^n]. \end{aligned}$$

Let us set for all $v_{\mathcal{D}} \in X_{\mathcal{D}}^0$

$$\begin{aligned} A_{\mathcal{D}_m}^n(v_{\mathcal{D}}) &= \int_{\Omega} \phi_m(\mathbf{x}) \zeta^l \frac{S^l(\mathbf{x}, \Pi_{\mathcal{D}_m} u_{\mathcal{D}}^n(\mathbf{x})) - S^l(\mathbf{x}, \Pi_{\mathcal{D}_m} u_{\mathcal{D}}^{n-1}(\mathbf{x}))}{\Delta t^n} \Pi_{\mathcal{D}_m} v_{\mathcal{D}}(\mathbf{x}) d\mathbf{x} \\ &= \frac{1}{\Delta t^n} \int_{t^{n-1}}^{t^n} \int_{\Omega} \phi_m(\mathbf{x}) \zeta^l \delta_{\mathcal{D}} s_{\mathcal{D}_p, \Delta t}^l(\mathbf{x}, t) \Pi_{\mathcal{D}_m} v_{\mathcal{D}}(\mathbf{x}) d\mathbf{x} dt, \end{aligned} \tag{2.41}$$

$$\begin{aligned} A_{\mathcal{D}_g}^n(v_{\mathcal{D}}) &= \int_0^L \frac{|S|}{RT_e} \frac{\Pi_{\mathcal{D}_g} g(u_{\mathcal{D}}^n)(x) - \Pi_{\mathcal{D}_g} g(u_{\mathcal{D}}^{n-1})(x)}{\Delta t^n} \Pi_{\mathcal{D}_g} v_{\mathcal{D}}(x) dx \\ &= \frac{1}{\Delta t^n} \int_{t^{n-1}}^{t^n} \int_0^L \frac{|S|}{RT_e} \delta_{\mathcal{D}} p_{\mathcal{D}_g, \Delta t}(x, t) \Pi_{\mathcal{D}_g} v_{\mathcal{D}}(x) dx dt, \end{aligned} \tag{2.42}$$

$$\begin{aligned}
B_{\mathcal{D}_m}^n(v_{\mathcal{D}}) &= \int_{\Omega} \zeta^l \frac{k_r^l(\mathbf{x}, S^l(\mathbf{x}, \Pi_{\mathcal{D}_m} u_{\mathcal{D}}^n(\mathbf{x})))}{\mu^l} \mathbf{K}_m \left(\nabla_{\mathcal{D}_m} u_{\mathcal{D}}^n(\mathbf{x}) - M^l \zeta^l \mathbf{g} \right) \cdot \nabla_{\mathcal{D}_m} v_{\mathcal{D}}(\mathbf{x}) d\mathbf{x} \\
&= \frac{1}{\Delta t^n} \int_{t^{n-1}}^{t^n} \int_{\Omega} \zeta^l \frac{k_r^l(\mathbf{x}, s_{\mathcal{D}_m, \Delta t}^l(\mathbf{x}, t))}{\mu^l} \mathbf{K}_m \left(\nabla \Pi_{\mathcal{T}, \Delta t} u_{\mathcal{D}}(\mathbf{x}, t) - M^l \zeta^l \mathbf{g} \right) \\
&\quad \cdot \nabla_{\mathcal{D}_m} v_{\mathcal{D}}(\mathbf{x}) d\mathbf{x} dt,
\end{aligned} \tag{2.43}$$

$$\begin{aligned}
B_{\mathcal{D}_g}^n(v_{\mathcal{D}}) &= \int_0^L \frac{1}{\alpha_g(x)} |S| \tilde{\zeta}^g(\Pi_{\mathcal{D}_g} g(u_{\mathcal{D}}^n)(x)) \nabla_{\mathcal{D}_g} g(u_{\mathcal{D}}^n)(x) \nabla_{\mathcal{D}_g} v_{\mathcal{D}}(x) dx \\
&= \frac{1}{\Delta t^n} \int_{t^{n-1}}^{t^n} \int_0^L \frac{1}{\alpha_g(x)} |S| \tilde{\zeta}^g(p_{\mathcal{D}_g, \Delta t}(x, t)) \partial_x \gamma \Pi_{\mathcal{T}, \Delta t} g(u_{\mathcal{D}})(x, t) \nabla_{\mathcal{D}_g} v_{\mathcal{D}}(x) dx dt
\end{aligned} \tag{2.44}$$

and

$$C_{\mathcal{D}_m}^n(v_{\mathcal{D}}) = \frac{1}{\Delta t^n} \int_{t^{n-1}}^{t^n} \int_{\Omega} Q(\mathbf{x}, t) \Pi_{\mathcal{D}_m} v_{\mathcal{D}}(\mathbf{x}) d\mathbf{x} dt, \tag{2.45}$$

$$C_{\mathcal{D}_g}^n(v_{\mathcal{D}}) = \frac{1}{\Delta t^n} \int_{t^{n-1}}^{t^n} \int_0^L |S| q(x, t) \Pi_{\mathcal{D}_g} v_{\mathcal{D}}(x) dx dt, \tag{2.46}$$

in such a way that the system (2.37) is equivalent to: find $u_{\mathcal{D}} \in X_{\mathcal{D}, \Delta t}$ with $u_{\mathcal{D}}^n - \bar{u}_{\mathcal{D}} \in X_{\mathcal{D}}^0$, $n = 1, \dots, N$, such that

$$A_{\mathcal{D}_m}^n(v_{\mathcal{D}}) + A_{\mathcal{D}_g}^n(v_{\mathcal{D}}) + B_{\mathcal{D}_m}^n(v_{\mathcal{D}}) + B_{\mathcal{D}_g}^n(v_{\mathcal{D}}) = C_{\mathcal{D}_m}^n(v_{\mathcal{D}}) + C_{\mathcal{D}_g}^n(v_{\mathcal{D}}), \tag{2.47}$$

for all $v_{\mathcal{D}} \in X_{\mathcal{D}}^0$.

A priori estimates and existence of a discrete solution

Proposition 2.6.1 *There exists at least one solution $u_{\mathcal{D}} \in X_{\mathcal{D}, \Delta t}$ to (2.37), and there exists a constant $C > 0$ depending only on the data, on $\theta_{\mathcal{T}}$, and on $\|\Pi_{\mathcal{D}_m} u_{\mathcal{D}}^0 - u_{init, p}\|_{L^2(\Omega)}$, $\|\Pi_{\mathcal{D}_g} u_{\mathcal{D}}^0 - u_{init, g}\|_{L^2(0, L)}$, $\|\Pi_{\mathcal{T}} \bar{u}_{\mathcal{D}} - \bar{u}\|_V$ such that any solution $u_{\mathcal{D}} \in X_{\mathcal{D}, \Delta t}$ to (2.37) satisfies*

$$\begin{aligned}
&\|\Pi_{\mathcal{D}_g, \Delta t} g(u_{\mathcal{D}})\|_{L^\infty(0, T; L^2(0, L))} + \|\nabla_{\mathcal{D}_p, \Delta t} u_{\mathcal{D}}\|_{L^2(0, T; L^2(\Omega))} \\
&\quad + \|\nabla_{\mathcal{D}_g, \Delta t} g(u_{\mathcal{D}})\|_{L^2(0, T; L^2(\Gamma))} \leq C.
\end{aligned} \tag{2.48}$$

Proof: We first prove the a priori estimate (2.48). Let us set

$$T_1 = \sum_{n=1}^N \Delta t^n A_{\mathcal{D}_m}^n(u_{\mathcal{D}}^n), \quad T_2 = \sum_{n=1}^N \Delta t^n A_{\mathcal{D}_g}^n(u_{\mathcal{D}}^n), \quad T_5 = \sum_{n=1}^N \Delta t^n A_{\mathcal{D}_m}^n(\bar{u}_{\mathcal{D}}),$$

and

$$T_6 = \sum_{n=1}^N \Delta t^n A_{\mathcal{D}_g}^n(\bar{u}_{\mathcal{D}}), \quad T_8 = \sum_{n=1}^N \Delta t^n (C_{\mathcal{D}_m}^n(u_{\mathcal{D}}^n - \bar{u}_{\mathcal{D}}) + C_{\mathcal{D}_g}^n(u_{\mathcal{D}}^n - \bar{u}_{\mathcal{D}})).$$

We also define

$$T_3 = \sum_{n=1}^N \Delta t^n \int_{\Omega} \zeta^l \frac{k_r^l(\mathbf{x}, S^l(\mathbf{x}, \Pi_{\mathcal{D}_m} u_{\mathcal{D}}^n(\mathbf{x})))}{\mu^l} \mathbf{K}_m \nabla_{\mathcal{D}_m} (u_{\mathcal{D}}^n - \bar{u}_{\mathcal{D}})(\mathbf{x}) \cdot \nabla_{\mathcal{D}_m} (u_{\mathcal{D}}^n - \bar{u}_{\mathcal{D}})(\mathbf{x}) d\mathbf{x}, \quad (2.49)$$

$$T_7 = \sum_{n=1}^N \Delta t^n \int_{\Omega} \zeta^l \frac{k_r^l(\mathbf{x}, S^l(\mathbf{x}, \Pi_{\mathcal{D}_m} u_{\mathcal{D}}^n(\mathbf{x})))}{\mu^l} \mathbf{K}_m \left(M^l \zeta^l \mathbf{g} - \nabla_{\mathcal{D}_m} \bar{u}_{\mathcal{D}}(\mathbf{x}) \right) \cdot \nabla_{\mathcal{D}_m} (u_{\mathcal{D}}^n - \bar{u}_{\mathcal{D}})(\mathbf{x}) d\mathbf{x}, \quad (2.50)$$

$$T_4 = \sum_{n=1}^N \Delta t^n \int_0^L \frac{1}{\alpha_g(x)} |S| \tilde{\zeta}^g(\Pi_{\mathcal{D}_g} g(u_{\mathcal{D}}^n)(x)) \nabla_{\mathcal{D}_g} g(u_{\mathcal{D}}^n)(x) \nabla_{\mathcal{D}_g} (u_{\mathcal{D}}^n - \bar{u}_{\mathcal{D}})(x) dx, \quad (2.51)$$

in such a way that

$$T_1 + T_2 + T_3 + T_4 = T_5 + T_6 + T_7 + T_8.$$

Accumulation terms: Firstly, using the assumption on S^l , the following estimate is a straightforward adaptation from Lemma 3.1 of [35].

$$T_1 \geq -\bar{\phi}_m \frac{\zeta^l L_s}{2} \|\Pi_{\mathcal{D}_m} u_{\mathcal{D}}^0\|_{L^2(\Omega)}^2. \quad (2.52)$$

Next, using $0 \leq S^l(\mathbf{x}, u) \leq 1$, we obtain the following estimate for T_5

$$T_5 \leq \zeta^l \bar{\phi}_m \sqrt{|\Omega|} \|\Pi_{\mathcal{D}_m} \bar{u}_{\mathcal{D}}\|_{L^2(\Omega)}. \quad (2.53)$$

From (2.18), we have that

$$T_2 = \frac{|S|}{RT_e} \sum_{n=1}^N \sum_{m=1}^{m_x} |x_{m-\frac{1}{2}} x_{m+\frac{1}{2}}| (g(u_m^n) - g(u_m^{n-1})) u_m^n.$$

Using $G(u) = \int_0^u v g'(v) dv$ which verifies $G(b) - G(a) = b(g(b) - g(a)) - \int_a^b (g(v) - g(a)) dv$ and hence $b(g(b) - g(a)) \geq G(b) - G(a)$ for all $(a, b) \in \mathbb{R} \times \mathbb{R}$, we obtain that

$$\begin{aligned} T_2 &\geq \frac{|S|}{RT_e} \sum_{n=1}^N \sum_{m=1}^{m_x} |x_{m-\frac{1}{2}} x_{m+\frac{1}{2}}| (G(u_m^n) - G(u_m^{n-1})), \\ &= \frac{|S|}{RT_e} \sum_{m=1}^{m_x} |x_{m-\frac{1}{2}} x_{m+\frac{1}{2}}| (G(u_m^N) - G(u_m^0)). \end{aligned}$$

Remark that $G(u) = \int_{g(0)}^{g(u)} g^{-1}(v) dv$, so that in view of assumption on g one has

$$\frac{(g(u) - g(0))^2}{2 \max_{v \in \mathbb{R}} g'(v)} \leq G(u) \leq \left(\max_{v \in \mathbb{R}} g'(v) \right) \frac{u^2}{2}.$$

Therefore

$$T_2 \geq \frac{|S|}{2RT_e \max_{v \in \mathbb{R}} g'(v)} \left(\|\Pi_{\mathcal{D}_g} g(u_{\mathcal{D}}^N) - g(0)\|_{L^2(0,L)}^2 \right) - \frac{|S| \max_{v \in \mathbb{R}} g'(v)}{2RT_e} \|\Pi_{\mathcal{D}_g} u_{\mathcal{D}}^0\|_{L^2(0,L)}^2. \quad (2.54)$$

Turning to T_6 , we obtain the estimate

$$T_6 \leq \frac{|S|}{RT_e} \|\Pi_{\mathcal{D}_g} \bar{u}_{\mathcal{D}}\|_{L^2(0,L)} \|\Pi_{\mathcal{D}_g} (g(u_{\mathcal{D}}^N) - g(u_{\mathcal{D}}^0))\|_{L^2(0,L)}.$$

We deduce that

$$T_6 \leq \frac{|S|}{RT_e} \max \left(\max_{v \in \mathbb{R}} g'(v), 1 \right) \|\Pi_{\mathcal{D}_g} \bar{u}_{\mathcal{D}}\|_{L^2(0,L)} \left(\|\Pi_{\mathcal{D}_g} g(u_{\mathcal{D}}^N)\|_{L^2(0,L)} + \|\Pi_{\mathcal{D}_g} u_{\mathcal{D}}^0\|_{L^2(0,L)} \right). \quad (2.55)$$

Transport terms: Thanks to the assumptions on \mathbf{K}_m and k_r^l we obtain the following estimates

$$T_3 \geq \frac{\zeta^l}{\mu^l} k_{\min} \bar{\lambda}_m \sum_{n=1}^N \Delta t^n \|\nabla_{\mathcal{D}_m} (u_{\mathcal{D}}^n - \bar{u}_{\mathcal{D}})\|_{L^2(\Omega)^3}^2 \quad (2.56)$$

and

$$T_7 \leq \frac{\zeta^l}{\mu^l} k_{\max} \bar{\lambda}_m \sum_{n=1}^N \Delta t^n \|\nabla_{\mathcal{D}_m} (u_{\mathcal{D}}^n - \bar{u}_{\mathcal{D}})\|_{L^2(\Omega)^3} \left(\|\nabla_{\mathcal{D}_m} \bar{u}_{\mathcal{D}}\|_{L^2(\Omega)^3} + M^l \zeta^l |\mathbf{g}| \sqrt{|\Omega|} \right). \quad (2.57)$$

From (2.15) and (2.18), setting $b_{m,m+\frac{1}{2}} = \int_{x_m}^{x_{m+\frac{1}{2}}} \frac{dx}{\alpha_g(x)}$, $b_{m+1,m+\frac{1}{2}} = \int_{x_{m+\frac{1}{2}}}^{x_{m+1}} \frac{dx}{\alpha_g(x)}$ and

$$a_{m+\frac{1}{2}} = \frac{\tilde{\zeta}^g(g(u_m^n)) b_{m,m+\frac{1}{2}} + \tilde{\zeta}^g(g(u_{m+1}^n)) b_{m+1,m+\frac{1}{2}}}{|x_m x_{m+1}|},$$

for $m = 0, \dots, m_x$ we have that

$$\begin{aligned} T_4 &= |S| \sum_{n=1}^N \Delta t^n \sum_{m=0}^{m_x} a_{m+\frac{1}{2}} \frac{(g(u_m^n) - g(u_{m+1}^n))(u_m^n - u_{m+1}^n)}{|x_m x_{m+1}|} \\ &\quad - |S| \sum_{n=1}^N \Delta t^n \sum_{m=0}^{m_x} a_{m+\frac{1}{2}} \frac{(g(u_m^n) - g(u_{m+1}^n))(\bar{u}_m - \bar{u}_{m+1})}{|x_m x_{m+1}|}. \end{aligned}$$

We deduce that

$$\begin{aligned} T_4 &\geq \frac{|S| \min_{v \in \mathbb{R}} \tilde{\zeta}^g(v)}{\bar{\alpha}_g \max_{v \in \mathbb{R}} g'(v)} \sum_{n=1}^N \Delta t^n \|\nabla_{\mathcal{D}_g} g(u_{\mathcal{D}}^n)\|_{L^2(0,L)}^2 \\ &\quad - \frac{|S|}{\bar{\alpha}_g} \left(\max_{v \in \mathbb{R}} \tilde{\zeta}^g(v) \right) \left(\sum_{n=1}^N \Delta t^n \|\nabla_{\mathcal{D}_g} g(u_{\mathcal{D}}^n)\|_{L^2(0,L)}^2 \right)^{1/2} \left(\sum_{n=1}^N \Delta t^n \|\nabla_{\mathcal{D}_g} \bar{u}_{\mathcal{D}}\|_{L^2(0,L)}^2 \right)^{1/2}. \end{aligned}$$

Using Young's inequality we obtain that

$$T_4 \geq \frac{|S| \min_{v \in \mathbb{R}} \tilde{\zeta}^g(v)}{2\bar{\alpha}_g \max_{v \in \mathbb{R}} g'(v)} \sum_{n=1}^N \Delta t^n \|\nabla_{\mathcal{D}_g} g(u_{\mathcal{D}}^n)\|_{L^2(0,L)}^2 - \frac{|S| \bar{\alpha}_g (\max_{v \in \mathbb{R}} g'(v)) (\max_{v \in \mathbb{R}} \tilde{\zeta}^g(v))}{2\bar{\alpha}_g \min_{v \in \mathbb{R}} \tilde{\zeta}^g(v)} \sum_{n=1}^N \Delta t^n \|\nabla_{\mathcal{D}_g} \bar{u}_{\mathcal{D}}\|_{L^2(0,L)}^2. \quad (2.58)$$

Using the discrete Poincaré inequalities of Lemma 2.6.2, we obtain the following estimate of the source terms

$$T_8 \leq C_5 \sum_{n=1}^N \Delta t^n \|\nabla_{\mathcal{D}_m} (u_{\mathcal{D}}^n - \bar{u}_{\mathcal{D}})\|_{L^2(\Omega)^3} \left(\frac{1}{\Delta t^n} \int_{t^{n-1}}^{t^n} \|Q(\cdot, t)\|_{L^2(\Omega)} dt \right) + C_6 |S| \sum_{n=1}^N \Delta t^n \|\nabla_{\mathcal{D}_g} (u_{\mathcal{D}}^n - \bar{u}_{\mathcal{D}})\|_{L^2(0,L)} \left(\frac{1}{\Delta t^n} \int_{t^{n-1}}^{t^n} \|q(\cdot, t)\|_{L^2(0,L)} dt \right). \quad (2.59)$$

Gathering the estimates (2.52), (2.54), (2.56), (2.58), (2.53), (2.55), (2.57), and (2.59), and using Young's and Cauchy-Schwarz inequalities, we conclude the proof of the a priori estimate (2.48).

To prove the existence of a solution $u_{\mathcal{D}}^n, n = 1, \dots, N$ to (2.37), let us consider the one parameter family of solutions obtained by setting $s^{l,\theta}(\mathbf{x}, u) = \theta s^l(\mathbf{x}, u) + 1 - \theta$, $\tilde{\zeta}^{g,\theta}(p) = \theta \tilde{\zeta}^g(p) + (1 - \theta) \zeta_0^g$ with a given $\zeta_0^g > 0$, and $g^\theta(u) = \theta g(u) + (1 - \theta)u$. Let us remark that for all values of $\theta \in [0, 1]$, the previous estimates still hold. Since for $\theta = 0$, the system (2.37) becomes linear, it results that it admits a unique solution. By topological degree argument (see e.g. [23]), we deduce the existence of at least one solution to (2.37) for $\theta = 1$. \square

Space and time translates estimates

The function space $L^2(\Omega) \times L^2(0, L)$ is equipped with the scalar product

$$\langle (u, p), (v, q) \rangle_{L^2(\Omega) \times L^2(0,L)} = \int_{\Omega} \zeta^l \phi_m u v d\mathbf{x} + \int_0^L \frac{|S|}{RT_e} p q dx.$$

For all $(u, p) \in L^2(\Omega) \times L^2(0, L)$ we also define the dual semi-norm $\|u\|_{-1,\mathcal{D}}$ by

$$\|(u, p)\|_{-1,\mathcal{D}} = \sup_{v_{\mathcal{D}} \in X_{\mathcal{D}}^0, v_{\mathcal{D}} \neq 0} \frac{\langle (u, p), (\Pi_{\mathcal{D}_m} v_{\mathcal{D}}, \Pi_{\mathcal{D}_g} v_{\mathcal{D}}) \rangle_{L^2(\Omega) \times L^2(0,L)}}{\|\Pi_{\mathcal{T}} v_{\mathcal{D}}\|_V}. \quad (2.60)$$

Lemma 2.6.5 *There exists a constant $C > 0$ depending only on the data, on $\theta_{\mathcal{T}}$, and on $\|\Pi_{\mathcal{D}_m} u_{\mathcal{D}}^0 - u_{init,p}\|_{L^2(\Omega)}$, $\|\Pi_{\mathcal{D}_g} u_{\mathcal{D}}^0 - u_{init,g}\|_{L^2(0,L)}$, $\|\Pi_{\mathcal{T}} \bar{u}_{\mathcal{D}} - \bar{u}\|_V$ such that any solution $u_{\mathcal{D}} \in X_{\mathcal{D},\Delta t}$ to (2.37) satisfies the estimate*

$$\int_0^T \left\| \left(\delta_{\mathcal{D}} s_{\mathcal{D}_p,\Delta t}^l(\cdot, t), \delta_{\mathcal{D}} p_{\mathcal{D}_g,\Delta t}(\cdot, t) \right) \right\|_{-1,\mathcal{D}}^2 dt \leq C. \quad (2.61)$$

Proof: Using (2.37), we obtain that for all $v_{\mathcal{D}} \in X_{\mathcal{D}}^0$

$$\begin{aligned} & \langle (\delta_{\mathcal{D}} s_{\mathcal{D}_p, \Delta t}^l(\cdot, t^n), \delta_{\mathcal{D}} p_{\mathcal{D}_g, \Delta t}(\cdot, t^n)), (\Pi_{\mathcal{D}_m} v_{\mathcal{D}}, \Pi_{\mathcal{D}_g} v_{\mathcal{D}}) \rangle_{L^2(\Omega) \times L^2(0, L)} = \\ & - \int_{\Omega} \zeta^l \frac{k_r^l(\mathbf{x}, s^l(\mathbf{x}, \Pi_{\mathcal{D}_m} u_{\mathcal{D}}^n(\mathbf{x})))}{\mu^l} \mathbf{K}_m(\nabla_{\mathcal{D}_m} u_{\mathcal{D}}^n(\mathbf{x}) - M^l \zeta^l \mathbf{g}) \cdot \nabla_{\mathcal{D}_m} v_{\mathcal{D}}(\mathbf{x}) d\mathbf{x} \\ & - \int_0^L \frac{1}{\alpha_g(x)} |S| \tilde{\zeta}^g(\Pi_{\mathcal{D}_g} g(u_{\mathcal{D}}^n)(x)) \nabla_{\mathcal{D}_g} g(u_{\mathcal{D}}^n)(x) \nabla_{\mathcal{D}_g} v_{\mathcal{D}}(x) dx \\ & + \frac{1}{\Delta t^n} \int_{t^{n-1}}^{t^n} \left(\int_{\Omega} Q(\mathbf{x}, t) \Pi_{\mathcal{D}_m} v_{\mathcal{D}}(\mathbf{x}) d\mathbf{x} + \int_0^L |S| q(x, t) \Pi_{\mathcal{D}_g} v_{\mathcal{D}}(x) dx \right) dt. \end{aligned}$$

Using the discrete Poincaré inequalities of Lemma 2.6.2, and the assumption on the function g , we obtain the estimate

$$\begin{aligned} & \langle (\delta_{\mathcal{D}} s_{\mathcal{D}_p, \Delta t}^l(\cdot, t^n), \delta_{\mathcal{D}} p_{\mathcal{D}_g, \Delta t}(\cdot, t^n)), (\Pi_{\mathcal{D}_m} v_{\mathcal{D}}, \Pi_{\mathcal{D}_g} v_{\mathcal{D}}) \rangle_{L^2(\Omega) \times L^2(0, L)} \leq \\ & \zeta^l k_{\max} \bar{\lambda}_m \left(\|\nabla_{\mathcal{D}_m} u_{\mathcal{D}}^n\|_{L^2(\Omega)^3} + M^l \zeta^l |\mathbf{g}| \sqrt{|\Omega|} \right) \|\nabla_{\mathcal{D}_m} v_{\mathcal{D}}\|_{L^2(\Omega)^3} \\ & + \frac{1}{\alpha_g} |S| \left(\max_{q \in \mathbb{R}} \tilde{\zeta}^g(q) \right) \|\nabla_{\mathcal{D}_g} g(u_{\mathcal{D}}^n)\|_{L^2(0, L)} \|\nabla_{\mathcal{D}_g} v_{\mathcal{D}}\|_{L^2(0, L)} \\ & + C_5 \left(\frac{1}{\Delta t^n} \int_{t^{n-1}}^{t^n} \|Q(\cdot, t)\|_{L^2(\Omega)} dt \right) \|\nabla_{\mathcal{D}_m} v_{\mathcal{D}}\|_{L^2(\Omega)^3} \\ & + C_6 |S| \left(\frac{1}{\Delta t^n} \int_{t^{n-1}}^{t^n} \|q(\cdot, t)\|_{L^2(0, L)} dt \right) \|\nabla_{\mathcal{D}_g} v_{\mathcal{D}}\|_{L^2(0, L)}. \end{aligned}$$

and the proof is achieved using Proposition 2.6.1 and the Cauchy-Schwarz inequality. \square .

Lemma 2.6.6 *There exists a constant $C > 0$ depending only on the data, on $\theta_{\mathcal{T}}$, and on $\|\Pi_{\mathcal{D}_m} u_{\mathcal{D}}^0 - u_{init, p}\|_{L^2(\Omega)}$, $\|\Pi_{\mathcal{D}_g} u_{\mathcal{D}}^0 - u_{init, g}\|_{L^2(0, L)}$, $\|\Pi_{\mathcal{T}} \bar{u}_{\mathcal{D}} - \bar{u}\|_V$ such that any solution $u_{\mathcal{D}} \in X_{\mathcal{D}, \Delta t}$ to (2.37) satisfies the estimate for all $\tau \in \mathbb{R}$*

$$\begin{aligned} & \int_{\mathbb{R}} \left(\|s_{\mathcal{D}_p, \Delta t}^l(\cdot, t + \tau) - s_{\mathcal{D}_p, \Delta t}^l(\cdot, t)\|_{L^2(\Omega)}^2 + \|p_{\mathcal{D}_g, \Delta t}(\cdot, t + \tau) - p_{\mathcal{D}_g, \Delta t}(\cdot, t)\|_{L^2(0, L)}^2 \right) dt \\ & \leq C \sqrt{|\tau|}, \end{aligned} \tag{2.62}$$

where $p_{\mathcal{D}_g, \Delta t}$ and $s_{\mathcal{D}_p, \Delta t}^l$ are extended by zero outside of respectively $(0, L) \times (0, T)$ and $\Omega \times (0, T)$.

Proof: From the Lipschitz assumptions on the functions S^l and g , and by definition of the semi-norm (2.60) we obtain the estimates

$$\begin{aligned}
& \int_{\Omega} \zeta^l \phi_m(\mathbf{x}) |s_{\mathcal{D}_p, \Delta t}^l(\mathbf{x}, t + \tau) - s_{\mathcal{D}_p, \Delta t}^l(\mathbf{x}, t)|^2 d\mathbf{x} \\
& + \int_0^L \frac{|S|}{RT_e} |p_{\mathcal{D}_g, \Delta t}(x, t + \tau) - p_{\mathcal{D}_g, \Delta t}(x, t)|^2 dx \\
& \leq L_{sp} \int_{\Omega} \zeta^l \phi_m(\mathbf{x}) \left(s_{\mathcal{D}_p, \Delta t}^l(\mathbf{x}, t + \tau) - s_{\mathcal{D}_p, \Delta t}^l(\mathbf{x}, t) \right) \\
& \quad \left(\Pi_{\mathcal{D}_p, \Delta t} g(u_{\mathcal{D}})(\mathbf{x}, t + \tau) - \Pi_{\mathcal{D}_p, \Delta t} g(u_{\mathcal{D}})(\mathbf{x}, t) \right) d\mathbf{x} \\
& + \int_0^L \frac{|S|}{RT_e} \left(p_{\mathcal{D}_g, \Delta t}(x, t + \tau) - p_{\mathcal{D}_g, \Delta t}(x, t) \right) \\
& \quad \left(\Pi_{\mathcal{D}_g, \Delta t} g(u_{\mathcal{D}})(x, t + \tau) - \Pi_{\mathcal{D}_g, \Delta t} g(u_{\mathcal{D}})(x, t) \right) dx \\
& \leq \max(1, L_{sp}) \|s_{\mathcal{D}_p, \Delta t}^l(\cdot, t + \tau) - s_{\mathcal{D}_p, \Delta t}^l(\cdot, t), p_{\mathcal{D}_g, \Delta t}(\cdot, t + \tau) - p_{\mathcal{D}_g, \Delta t}(\cdot, t)\|_{-1, \mathcal{D}} \\
& \quad \|\Pi_{\mathcal{T}, \Delta t} g(u_{\mathcal{D}})(\cdot, t + \tau) - \Pi_{\mathcal{T}, \Delta t} g(u_{\mathcal{D}})(\cdot, t)\|_V
\end{aligned}$$

Using Young's inequality, we obtain that there exists C such that for all $\tau \in (0, T)$

$$\begin{aligned}
& \int_0^{T-\tau} \left(\|s_{\mathcal{D}_p, \Delta t}^l(\cdot, t + \tau) - s_{\mathcal{D}_p, \Delta t}^l(\cdot, t)\|_{L^2(\Omega)} + \|p_{\mathcal{D}_g, \Delta t}(\cdot, t + \tau) - p_{\mathcal{D}_g, \Delta t}(\cdot, t)\|_{L^2(0, L)} \right) dt \\
& \leq \frac{C}{\sqrt{|\tau|}} \int_0^{T-\tau} \|s_{\mathcal{D}_p, \Delta t}^l(\cdot, t + \tau) - s_{\mathcal{D}_p, \Delta t}^l(\cdot, t), p_{\mathcal{D}_g, \Delta t}(\cdot, t + \tau) - p_{\mathcal{D}_g, \Delta t}(\cdot, t)\|_{-1, \mathcal{D}} dt \\
& + C\sqrt{|\tau|} \int_0^{T-\tau} \|\Pi_{\mathcal{T}, \Delta t} g(u_{\mathcal{D}})(\cdot, t + \tau) - \Pi_{\mathcal{T}, \Delta t} g(u_{\mathcal{D}})(\cdot, t)\|_V dt.
\end{aligned}$$

From BV properties of piecewise constant functions and from Lemma 2.6.5, we obtain that

$$\begin{aligned}
& \int_0^{T-\tau} \|s_{\mathcal{D}_p, \Delta t}^l(\cdot, t + \tau) - s_{\mathcal{D}_p, \Delta t}^l(\cdot, t), p_{\mathcal{D}_g, \Delta t}(\cdot, t + \tau) - p_{\mathcal{D}_g, \Delta t}(\cdot, t)\|_{-1, \mathcal{D}} dt \\
& \leq \tau \int_0^T \left\| \left(\delta_{\mathcal{D}} s_{\mathcal{D}_p, \Delta t}^l(\cdot, t), \delta_{\mathcal{D}} p_{\mathcal{D}_g, \Delta t}(\cdot, t) \right) \right\|_{-1, \mathcal{D}} dt \\
& \leq \tau \sqrt{T} \left(\int_0^T \left\| \left(\delta_{\mathcal{D}} s_{\mathcal{D}_p, \Delta t}^l(\cdot, t), \delta_{\mathcal{D}} p_{\mathcal{D}_g, \Delta t}(\cdot, t) \right) \right\|_{-1, \mathcal{D}}^2 dt \right)^{1/2} \\
& \leq C\sqrt{T}\tau.
\end{aligned}$$

Using $0 \leq S^l(\mathbf{x}, v) \leq 1$ as well as the boundedness of $\|p_{\mathcal{D}_g, \Delta t}(\cdot, t)\|_{L^2(0, L)}$ on $[0, T]$ from Proposition 2.6.1, we conclude the proof of Lemma 2.6.6. \square

Lemma 2.6.7 *Let $\hat{p}_{\mathcal{D}} \in X_{\mathcal{D}, \Delta t}$ be defined by $\hat{p}_{\mathcal{D}}^n = g(u_{\mathcal{D}}^n) - g(\bar{u}_{\mathcal{D}})$, we denote $\hat{p}_{\mathcal{D}_g, \Delta t} = \Pi_{\mathcal{D}_g, \Delta t} \hat{p}_{\mathcal{D}}$. There exists a constant $C > 0$ depending only on the data, on $\theta_{\mathcal{T}}$, and on $\|\Pi_{\mathcal{D}_m} u_{\mathcal{D}}^0 - u_{init, p}\|_{L^2(\Omega)}$, $\|\Pi_{\mathcal{D}_g} u_{\mathcal{D}}^0 - u_{init, g}\|_{L^2(0, L)}$, $\|\Pi_{\mathcal{T}} \bar{u}_{\mathcal{D}} - \bar{u}\|_V$ such that any solution*

$u_{\mathcal{D}} \in X_{\mathcal{D}, \Delta t}$ to (2.37) satisfies the following estimate for all $\xi \in \mathbb{R}^3$ and $\zeta \in \mathbb{R}$.

$$\begin{aligned} & \int_0^T \left(\|s_{\mathcal{D}_p, \Delta t}^l(\cdot + \xi, t) - s_{\mathcal{D}_p, \Delta t}^l(\cdot, t)\|_{L^2(\mathbb{R}^3)}^2 + \|\hat{p}_{\mathcal{D}_g, \Delta t}(\cdot + \zeta, t) - \hat{p}_{\mathcal{D}_g, \Delta t}(\cdot, t)\|_{L^2(\mathbb{R})}^2 \right) dt \\ & \leq C(|\xi| + |\zeta| + h_{\mathcal{T}}) \end{aligned} \quad (2.63)$$

where $s_{\mathcal{D}_p, \Delta t}^l$ and $\hat{p}_{\mathcal{D}_g, \Delta t}$ are extended on \mathbb{R}^3 (respectively on \mathbb{R}) by zero.

Proof: For any $\xi \in \mathbb{R}^3$ we define the set $\Omega_{\xi} = \{\mathbf{x} \in \Omega \mid \mathbf{x} + \xi \in \Omega\}$. From Proposition 2.6.1 there exists a constant C such that the following estimate holds for all $\xi \in \mathbb{R}^3$ and $\zeta \in \mathbb{R}$:

$$\begin{aligned} & \int_0^T \|\Pi_{\mathcal{T}, \Delta t} u_{\mathcal{D}}(\cdot + \xi, t) - \Pi_{\mathcal{T}, \Delta t} u_{\mathcal{D}}(\cdot, t)\|_{L^2(\Omega_{\xi})}^2 dt \\ & + \int_0^T \|\gamma \Pi_{\mathcal{T}, \Delta t} \hat{p}_{\mathcal{D}}(\cdot + \zeta, t) - \gamma \Pi_{\mathcal{T}, \Delta t} \hat{p}_{\mathcal{D}}(\cdot, t)\|_{L^2(\mathbb{R})}^2 dt \\ & \leq C(|\xi| + |\zeta|). \end{aligned} \quad (2.64)$$

We conclude the proof using Lemma 2.6.3 as well as Lipschitz properties and boundedness of S^l . \square .

Convergence

Lemma 2.6.8 *Let $(v^{(k)})_{k \in \mathbb{N}}$ be a sequence of functions in $L^2(0, T; U^0)$ such that there exists $C > 0$ with $\|v^{(k)}\|_{L^2(0, T; H^1(\Omega))} \leq C$ for all $k \in \mathbb{N}$. Then, there exists $v \in L^2(0, T; U^0)$ such that*

1. *up to a subsequence*

$$v^{(k)} \rightharpoonup v \text{ in } L^2(\Omega \times (0, T)) \text{ and } \nabla v^{(k)} \rightharpoonup \nabla v \text{ in } L^2(\Omega \times (0, T))^3.$$

2. *up to the same subsequence*

$$\gamma v^{(k)} \rightharpoonup \gamma v \text{ in } L^2((0, L) \times (0, T));$$

Proof: The proof of the first statement is classical, see e.g. the proof of Lemma 5.1 in [12]; moreover $v \in L^2(0, T; H_{\Gamma_D}^1(\Omega))$. Next, there exists $r \in L^2(0, T; L^2(0, L))$ such that $\gamma v^{(k)} \rightharpoonup r$ in $L^2(0, T; L^2(0, L))$. To conclude, let us prove that $\partial_s \gamma v = 0$ and $r = \gamma v$. For all $\varphi \in L^2((0, L) \times (0, T))$ and $\psi \in L^2(\partial S \times (0, T))$, there exist $\Psi \in L^2(0, T; H_{\text{div}}(\Omega))$ such that $\Psi \cdot \mathbf{n} = \varphi(x, t)\psi(s, t)$ on Γ . Hence, one has

$$\begin{aligned} & \int_0^T \int_{\Omega} (\nabla v^{(k)}(\mathbf{x}, t) \cdot \Psi(\mathbf{x}, t) + v^{(k)}(\mathbf{x}, t) \text{div} \Psi(\mathbf{x}, t)) d\mathbf{x} dt \\ & = \int_0^T \int_0^L \int_{\partial S} (\gamma v^{(k)})(x, t) \varphi(x, t) \psi(s, t) dx ds dt. \end{aligned}$$

Passing to the limit in this equality one obtains that

$$\begin{aligned} & \int_0^T \int_{\Omega} (\nabla v(\mathbf{x}, t) \cdot \Psi(\mathbf{x}, t) + v(\mathbf{x}, t) \operatorname{div} \Psi(\mathbf{x}, t)) d\mathbf{x} dt \\ &= \int_0^T \int_0^L \int_{\partial S} r(x, t) \varphi(x, t) \psi(s, t) dx ds dt, \end{aligned}$$

which implies that

$$\int_0^T \int_0^L \int_{\partial S} (\gamma v(x, s, t) - r(x, t)) \varphi(x, t) \psi(s, t) dx ds dt = 0,$$

and hence that $\partial_s \gamma v = 0$ and $\gamma v = r$. \square .

Theorem 2.6.1 *Let $\mathcal{D}^{(k)}, \Delta t^{n,(k)}, n = 1, \dots, N^{(k)}, k \in \mathbb{N}$ be a sequence of space time discretizations such that there exists $\theta > 0$ with $\theta_{\mathcal{T}^{(k)}} \leq \theta$. It is assumed that $\lim_{k \rightarrow +\infty} h_{\mathcal{T}^{(k)}} = 0$, and that $\Delta t^{(k)} = \max_{n=1, \dots, N^{(k)}} \Delta t^{n,(k)}$ tends to zero when $k \rightarrow +\infty$, and that $\|\Pi_{\mathcal{D}_m^{(k)}} u_{\mathcal{D}^{(k)}}^0 - u_{init,p}\|_{L^2(\Omega)}, \|\Pi_{\mathcal{D}_g^{(k)}} u_{\mathcal{D}^{(k)}}^0 - u_{init,g}\|_{L^2(0,L)}, \|\Pi_{\mathcal{T}^{(k)}} \bar{u}_{\mathcal{D}^{(k)}} - \bar{u}\|_V$ tends to zero when $k \rightarrow +\infty$. Then, there exist a subsequence of $k \in \mathbb{N}$ and a function $u \in L^2(0, T; V)$ solution of (2.35) such that up to this subsequence*

$$s_{\mathcal{D}_m^{(k)}, \Delta t^{(k)}}^l \rightarrow S^l(\cdot, u) \text{ strongly in } L^2(\Omega \times (0, T)),$$

$$\Pi_{\mathcal{D}_m^{(k)}, \Delta t^{(k)}} u_{\mathcal{D}^{(k)}} \rightharpoonup u \text{ weakly in } L^2(\Omega \times (0, T)),$$

and

$$p_{\mathcal{D}_g^{(k)}, \Delta t^{(k)}} \rightarrow g(\gamma u) \text{ strongly in } L^2((0, L) \times (0, T)).$$

Proof: From Proposition 2.6.1, Lemma 2.6.8, and the convergence to zero of $\|\Pi_{\mathcal{T}^{(k)}} \bar{u}_{\mathcal{D}^{(k)}} - \bar{u}\|_V$ we deduce that there exists $u \in L^2(0, T; U)$ with $u - \bar{u} \in L^2(0, T; U^0)$ such that up to a subsequence $\Pi_{\mathcal{T}^{(k)}, \Delta t^{(k)}} u_{\mathcal{D}^{(k)}} \rightharpoonup u$ weakly in $L^2(\Omega \times (0, T))$, $\gamma \Pi_{\mathcal{T}^{(k)}, \Delta t^{(k)}} u_{\mathcal{D}^{(k)}} \rightharpoonup \gamma u$ weakly in $L^2((0, L) \times (0, T))$, and $\nabla \Pi_{\mathcal{T}^{(k)}, \Delta t^{(k)}} u_{\mathcal{D}^{(k)}} \rightharpoonup \nabla u$ weakly in $L^2(\Omega \times (0, T))^3$.

In view of Lemma 2.6.6, Lemma 2.6.7, and Lemma B.2 of [30], the Kolmogorov-Fréchet theorem implies that there exist two functions $s \in L^2(\Omega \times (0, T))$ and $\hat{p} \in L^2((0, L) \times (0, T))$ such that up to a subsequence $s_{\mathcal{D}_m^{(k)}, \Delta t^{(k)}}^l \rightarrow S$ strongly in $L^2(\Omega \times (0, T))$ and $\hat{p}_{\mathcal{D}_g^{(k)}, \Delta t^{(k)}} \rightarrow \hat{p}$ strongly in $L^2((0, L) \times (0, T))$. The sequence $\gamma \Pi_{\mathcal{T}^{(k)}, \Delta t^{(k)}} \hat{p}_{\mathcal{D}^{(k)}}$ is uniformly bounded in $L^2(0, T; H_0^1(0, L))$, thus one can extract a subsequence of $\partial_x \gamma \Pi_{\mathcal{T}^{(k)}, \Delta t^{(k)}} \hat{p}_{\mathcal{D}^{(k)}}$ weakly converging to some function \hat{p}_x in $L^2((0, L) \times (0, T))$. Let $\varphi \in L^2(0, T; C_c^\infty(\mathbb{R}))$ and let $\gamma \Pi_{\mathcal{T}^{(k)}, \Delta t^{(k)}} \hat{p}_{\mathcal{D}^{(k)}}$ be extended by zero outside of $(0, L)$, passing to the limit in

$$\int_0^T \int_{\mathbb{R}} \left((\partial_x \gamma \Pi_{\mathcal{T}^{(k)}, \Delta t^{(k)}} \hat{p}_{\mathcal{D}^{(k)}}) \varphi(x, t) + \gamma \Pi_{\mathcal{T}^{(k)}, \Delta t^{(k)}} \hat{p}_{\mathcal{D}^{(k)}} \partial_x \varphi(x, t) \right) dx dt = 0,$$

we obtain that

$$\int_0^T \int_{\mathbb{R}} \left(\hat{p}_x \varphi(x, t) + \hat{p} \partial_x \varphi(x, t) \right) dx dt = 0,$$

and hence that $\hat{p}_x = \partial_x \hat{p}$ and $\hat{p} \in L^2(0, T; H_0^1(0, L))$. From the convergence to zero of $\|\Pi_{\mathcal{T}^{(k)}} \bar{u}_{\mathcal{D}^{(k)}} - \bar{u}\|_V$ and the assumptions on g we deduce that there exists $p \in L^2((0, L) \times (0, T))$ such that $p - g(\gamma \bar{u}) \in L^2(0, T; H_0^1(0, L))$ and such that $p_{\mathcal{D}_g^{(k)}, \Delta t^{(k)}} \rightarrow p$ strongly and $\partial_x \gamma \Pi_{\mathcal{T}^{(k)}, \Delta t^{(k)}} p_{\mathcal{D}^{(k)}}$ converges weakly to $\partial_x p$ up to subsequence. Using the Minty's trick stated in Lemma 3.6 of [35] one can show that $s = S^l(., u)$ and $p = g(\gamma u)$.

It remains to show that u is a solution to (2.35). We will drop the superscript (k) in the following for the sake of convenience. Let $\mathcal{C}(\Omega \times [0, T])$ be the subspace of functions φ of $C^\infty(\bar{\Omega} \times [0, T])$ vanishing at $t = T$ and on Γ_D and such that $\partial_s \varphi = 0$ on Γ . Then, let $\psi \in \mathcal{C}(\Omega \times [0, T])$ and consider the function $\bar{\psi}(t) = P_{\mathcal{D}} \psi(., t) \in X_{\mathcal{D}}^0$.

Next, setting $v_{\mathcal{D}} = \bar{\psi}(t^{n-1})$ in (2.47), multiplying the left and right hand sides by Δt^n and summing over n , we obtain that

$$\begin{aligned} & \sum_{n=1}^N \Delta t^n \left(A_{\mathcal{D}_m}^n(\bar{\psi}(t^{n-1})) + A_{\mathcal{D}_g}^n(\bar{\psi}(t^{n-1})) + B_{\mathcal{D}_m}^n(\bar{\psi}(t^{n-1})) + B_{\mathcal{D}_g}^n(\bar{\psi}(t^{n-1})) \right) \\ &= C_{\mathcal{D}_m}^n(\bar{\psi}(t^{n-1})) + C_{\mathcal{D}_g}^n(\bar{\psi}(t^{n-1})). \end{aligned}$$

First, using the chain rule and $\bar{\psi}(T) = 0$, we have that

$$\begin{aligned} \sum_{n=1}^N \Delta t^n A_{\mathcal{D}_m}^n(\bar{\psi}(t^{n-1})) &= - \sum_{n=1}^N \int_{t^{n-1}}^{t^n} \int_{\Omega} \zeta^l \phi_m(\mathbf{x}) s_{\mathcal{D}_m, \Delta t}^l(\mathbf{x}, t) \partial_t \Pi_{\mathcal{D}_m} \bar{\psi}(t)(\mathbf{x}) d\mathbf{x} dt \\ &\quad + \int_{\Omega} \zeta^l \phi_m(\mathbf{x}) s^l(\mathbf{x}, \Pi_{\mathcal{D}_m} u_{\mathcal{D}}^0(\mathbf{x})) \Pi_{\mathcal{D}_m} \bar{\psi}(0)(\mathbf{x}) d\mathbf{x}. \end{aligned}$$

We deduce from the strong convergence of $s_{\mathcal{D}_m, \Delta t}^l$ to $S^l(., u)$, the strong convergence of $\Pi_{\mathcal{D}_m} u_{\mathcal{D}}^0$ to $u_{init, p}$, and the regularity of ψ , that

$$\begin{aligned} \sum_{n=1}^N \Delta t^n A_{\mathcal{D}_m}^n(\bar{\psi}(t^{n-1})) &\rightarrow - \int_0^T \int_{\Omega} \zeta^l \phi_m(\mathbf{x}) S^l(\mathbf{x}, u(\mathbf{x}, t)) \partial_t \psi(\mathbf{x}, t) d\mathbf{x} dt \\ &\quad + \int_{\Omega} \zeta^l \phi_m(\mathbf{x}) S^l(\mathbf{x}, u_{init, p}(\mathbf{x})) \psi(\mathbf{x}, 0) d\mathbf{x}. \end{aligned}$$

Similarly, we have that

$$\begin{aligned} \sum_{n=1}^N \Delta t^n A_{\mathcal{D}_g}^n(\bar{\psi}(t^{n-1})) &= - \sum_{n=1}^N \int_{t^{n-1}}^{t^n} \int_0^L \frac{|S|}{RT_e} p_{\mathcal{D}_g, \Delta t}(x, t) \partial_t \Pi_{\mathcal{D}_g} \bar{\psi}(t)(x) dx dt \\ &\quad + \int_0^L \frac{|S|}{RT_e} g(\Pi_{\mathcal{D}_g} u_{\mathcal{D}}^0(x)) \Pi_{\mathcal{D}_g} \bar{\psi}(0)(x) dx. \end{aligned}$$

We deduce from the strong convergence of $p_{\mathcal{D}_g, \Delta t}$ to $g(\gamma u)$, the strong convergence of $\Pi_{\mathcal{D}_g} u_{\mathcal{D}}^0$ to $u_{init, g}$, and the regularity of ψ , that

$$\begin{aligned} \sum_{n=1}^N \Delta t^n A_{\mathcal{D}_g}^n(\bar{\psi}(t^{n-1})) &= - \int_0^T \int_0^L \frac{|S|}{RT_e} g(\gamma u)(x, t) \partial_t \gamma \psi(x, t) dx dt \\ &\quad + \int_0^L \frac{|S|}{RT_e} g(u_{init, g}(x)) \gamma \psi(x, 0) dx. \end{aligned}$$

Turning to the diffusion terms, we have from the weak convergence of $\nabla \Pi_{\mathcal{T}, \Delta t} u_{\mathcal{D}}$ to ∇u , the strong convergence of $s_{\mathcal{D}_m, \Delta t}^l$ to $S^l(\cdot, u)$, the assumption on k_r^l , and the regularity of ψ , that

$$\begin{aligned} & \sum_{n=1}^N \Delta t^n B_{\mathcal{D}_m}^n(\bar{\psi}(t^{n-1})) \\ & \rightarrow \int_0^T \int_{\Omega} \zeta^l \frac{k_r^l(\mathbf{x}, S^l(\mathbf{x}, u(\mathbf{x}, t)))}{\mu^l} \mathbf{K}_m(\nabla u(\mathbf{x}, t) - M^l \zeta^l \mathbf{g}) \cdot \nabla \psi(\mathbf{x}, t) d\mathbf{x} dt \end{aligned}$$

Similarly, we deduce from the weak convergence of $\partial_x \gamma \Pi_{\mathcal{T}, \Delta t} u_{\mathcal{D}}$ to $\partial_x g(\gamma u)$, the strong convergence of $p_{\mathcal{D}_g, \Delta t}$ to $g(\gamma u)$, the assumption on $\tilde{\zeta}^g$, and the regularity of ψ , that

$$\begin{aligned} & \sum_{n=1}^N \Delta t^n B_{\mathcal{D}_g}^n(\bar{\psi}(t^{n-1})) \\ & \rightarrow \int_0^T \int_0^L \frac{1}{\alpha_g(x)} |S| \tilde{\zeta}^g(g(\gamma u)(x, t)) \partial_x g(\gamma u)(x, t) \partial_x \gamma \psi(x, t) dx dt. \end{aligned}$$

Turning to the source terms, from the regularity of ψ , we obtain that

$$\begin{aligned} & \sum_{n=1}^N \Delta t^n \left(C_{\mathcal{D}_m}^n(\bar{\psi}(t^{n-1})) + C_{\mathcal{D}_g}^n(\bar{\psi}(t^{n-1})) \right) \\ & \rightarrow \int_0^T \int_{\Omega} Q(\mathbf{x}, t) \psi(\mathbf{x}, t) d\mathbf{x} dt + \int_0^T \int_0^L |S| q(x, t) \gamma \psi(x, t) dx dt. \end{aligned}$$

2.7 Conclusion

A reduced model coupling the 3D gas liquid compositional Darcy flow in the matrix, the 2D gas liquid compositional Darcy flow in the fracture network, and a 1D compositional gas free flow has been proposed and applied to predict the mass exchanges occurring at the interface between the repository and the ventilation excavated galleries. The model takes into account the low permeability of the disposal to simplify the coupling conditions and uses a No Pressure Wave approximation in the free flow domain. The VAG scheme has been extended to the discretization of such model. It has the advantage compared with classical CVFE approaches to avoid in a natural way the mixing of the porous and free media properties inside the control volumes at the nodes located at the interface. The discretization has been validated on a single phase Darcy flow model problem as well as on a compositional model using an approximate solution for the stationary state. Finally, the convergence of the VAG discretization to a weak solution has been proved for a simplified model coupling the 3D Richards approximation for the liquid pressure in the porous medium and the Darcy approximation of the 1D gas pressure equation in the gallery. In the next chapter, the reduced model of subsection 2.4.3 will be compared in a 2D geometry with a 2D-2D model using the Reynold Averaged Navier Stokes (RANS) equations in the

2D gallery with an algebraic turbulent model. To that end, the molar fraction boundary layer thickness δ of subsection 2.4.3 will be computed using a low frequency diagonal approximation of a Steklov Poincaré operator for the convection diffusion equation in the gallery.

Chapter 3

Coupling of a liquid gas compositional 2D Darcy flow with a 2D compositional free gas flow

Abstract: In this Chapter, a fixed point algorithm to solve the coupling between the gas liquid compositional Darcy flow and the free gas flow is developed. This algorithm takes advantage of the weak velocity and pressure perturbations in the gallery induced by the coupling with the porous medium. On the other hand it keeps in the Newton solver the strong coupling between the porous medium system and the convection diffusion equations for the gas molar fractions in the gallery at fixed velocity. The efficiency of the fixed point algorithm is assessed on a 2D model problem. The obtained solutions are compared with the solutions given by the reduced model presented in Chapter 2. To this end, a model to compute the molar fraction boundary layer thickness, which plays an essential role in the quality of the reduced model, is proposed.

3.1 Introduction

The study of the reduced model in Chapter 2 has made clear the strong coupling between the water molar fraction in the gallery and the liquid pressure and flux at the porous medium gallery interface. This strong coupling results from the liquid gas thermodynamical equilibrium at the interface.

This Chapter 3 develops a fixed point algorithm which preserves this strong coupling and relaxes the coupling between, on the one hand, the velocity and the pressure in the gallery, and, on the other hand, the porous medium unknowns and the gas molar fractions in the gallery. The idea of this algorithm is to solve in the first step of the fixed point algorithm the porous medium equations coupled to the convection diffusion equations for the gas molar fractions in the gallery. Then, the total molar flux at the interface is computed and used in the second step of the algorithm to compute the velocity and pressure in the gallery solving the Navier Stokes equations.

Compared with fully coupled approaches such as the ones developed in [6, 41, 48], our fixed point algorithm has the advantage to lead to the non linear and linear solutions of simpler sub-systems. Sequential algorithms, such as the ones described in [26, 24] (see also the review [25]) are frequently used for solving drying problems. As mentioned in [26, 24] they require a time step at the scale of the free flow due to the strong coupling between the water molar fraction in the gallery and the liquid pressure and flux at the porous medium gallery interface. In our context this is of course prohibited. In order to simulate a period of say 100 years, we need to be able to use time steps at the scale of the porous medium with a quasi stationary computation of the free flow at each time step.

The second objective of this chapter is to compare the solutions of the full model and of the reduced model developed in Chapter 2 using a 1D model in the free flow domain. To this end, we need to derive a model for the gas molar fraction boundary layer thickness introduced in section 2.4.3. This parameter plays an essential role on the liquid evaporation rate at the interface. The proposed model is based on a low frequency diagonal approximation of a Steklov Poincaré type operator for the stationary convection diffusion equation at fixed velocity. It leads to a boundary layer thickness depending on the longitudinal coordinate x along the gallery.

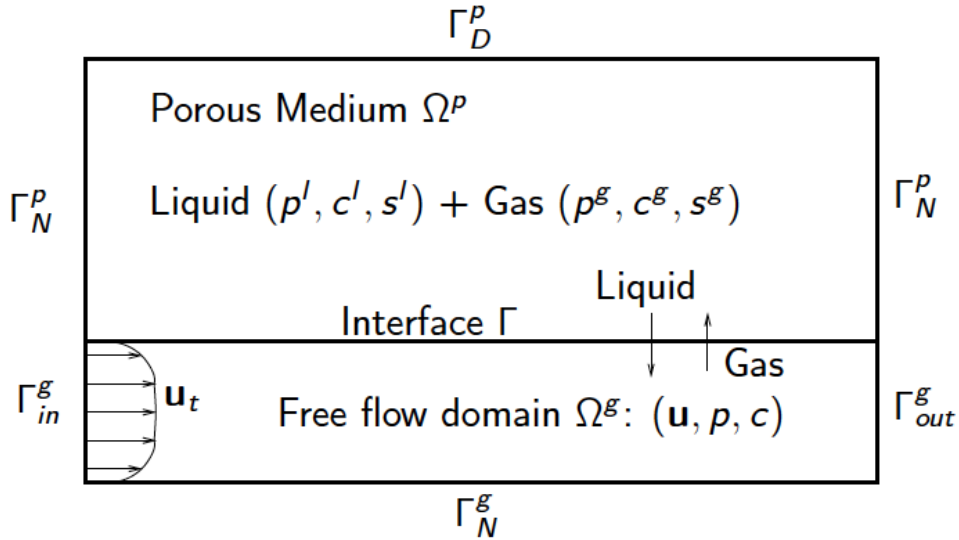


Figure 3.1: Free flow domain Ω^g , porous medium domain Ω^p , interface Γ , and remaining boundaries for our 2D test case.

In order to assess the efficiency of the fixed point algorithm and to compare the full and reduced models, a simple 2D setting exhibited in Figure 3.1 is used. In the porous medium domain Ω^p , we consider a compositional liquid gas Darcy flow using the phase pressures and component fugacities formulation of Chapter 1. In the gallery domain Ω^g , the turbulent nature of the flow is taken into account using an algebraic model leading to the computation of a turbulent profile. This longitudinal turbulent profile is a stationary

solution of the RANS model (Reynolds Averaged Navier Stokes, see e.g. [19, 9]) without the coupling with the porous medium flow. Then, this turbulent profile \mathbf{u}_t provides the turbulent dynamic viscosity μ_t and the turbulent diffusion D_t that are used to compute the velocity, pressure and gas molar fraction in Ω^g solving the RANS compositional model at fixed turbulent viscosity μ_t and diffusion D_t . The turbulent viscosity and diffusion can be fixed thanks to the small perturbation of the velocity and pressure induced by the coupling in the free flow region. Note also that the turbulent diffusion D_t plays an essential role in the liquid evaporation rate at the interface.

The 2D domain is discretized using a Cartesian mesh conforming at the interface and refined on both sides of the interface Γ in order to take into account the laminar boundary layer on the gallery side and the strong liquid pressure gradient on the porous medium side. The space discretization uses a Marker-And-Cell (MAC) scheme for the RANS model [40] and a cell centred finite volume scheme for the Darcy flow in Ω^p and for the convection diffusion equations in Ω^g . In both cases, the diffusive fluxes (Darcy and turbulent diffusion terms) are approximated by a two point flux and the convective numerical fluxes are obtained by a first order upwind scheme. The time integration uses an implicit Euler scheme.

Three test cases are considered. The first test case is roughly speaking the 2D-2D version of the Andra test case presented in subsection 2.4.2 with different values for the length of the gallery ranging from 25 m to 400 m and different input velocities ranging from 0.05 to 5 m s⁻¹. The second test case considers a vertical gallery with two different rocktypes along the direction of the gallery. The third test case goes away from the Andra order of magnitudes by considering a porous medium with a much higher permeability of 1 Darcy and spatial dimensions of order 1 meter.

The outline of the remaining of this Chapter is the following. In Section 3.2, the formulation of the coupled model is introduced using the phase pressures and component fugacities formulation in the porous medium. Then, the splitting algorithm is described. In Section 3.3 the reduced model using a 1D model in the free flow domain is described as well as the computation of the gas molar fraction boundary layer thickness. In Section 3.4, the 2D setting for our numerical experiments is detailed as well as the discretization in the porous medium and in the gallery. Then, the results of the three test cases are presented and discussed.

3.2 Formulation of the coupled model and fixed point algorithm

Let Ω^p denote the porous medium domain and Ω^g the free flow domain. The interface between the two domains is denoted by $\Gamma = \partial\Omega^p \cap \partial\Omega^g$.

3.2.1 Formulation of the coupled model

Let $\alpha = g, l$ denote the gas and liquid phases assumed to be both defined by a mixture of components $i \in \mathcal{C}$ among which the water component denoted by e which can vaporize in the gas phase, and a set of gaseous components $j \in \mathcal{C} \setminus \{e\}$ which can dissolve in the liquid phase. For the sake of simplicity, the model is assumed to be isothermal with a fixed temperature T_e . Following Chapter 1, the gas liquid Darcy flow formulation uses the gas pressure p^g , the liquid pressure p^l , and the component fugacities $f = (f_i)_{i \in \mathcal{C}}$ as primary unknowns, denoted by $\mathcal{U} = (p^g, p^l, f)$ in the following. In this formulation, following [45], the component molar fractions $c^\alpha = (c_i^\alpha)_{i \in \mathcal{C}}$ of each phase $\alpha = g, l$ are the functions $c_i^\alpha(\mathcal{U})$ of \mathcal{U} defined by inversion of the equations $f_i^\alpha(c^\alpha, p^\alpha, p^l) = f_i$, $i \in \mathcal{C}$, where f_i^α is the fugacity of the component i in the phase α . In addition, for $\alpha = g, l$, the phase pressure p^α is extended in the absence of the phase in such a way that the closure law $\sum_{i \in \mathcal{C}} c_i^\alpha(\mathcal{U}) = 1$ is always imposed. The phase molar and mass densities, as well as the phase viscosities are denoted in the following by respectively $\zeta^\alpha(p^\alpha, c^\alpha)$, $\rho^\alpha(p^\alpha, c^\alpha)$, $\mu^\alpha(p^\alpha, c^\alpha)$ for $\alpha = g, l$. For the sake of simplicity, for $\xi = \zeta^\alpha$, ρ^α , or μ^α , we will still use the notation $\xi(\mathcal{U})$ for the function $\xi(p^\alpha, c^\alpha(\mathcal{U}))$.

Finally, we define the liquid saturation as the function $\mathcal{S}^l(\mathbf{x}, p^g - p^l)$ of $p_c = p^g - p^l$ defined by the inverse of the monotone graph extension of the capillary pressure function $p_c(\mathbf{x}, \cdot)$, and we set $\mathcal{S}^g(\mathbf{x}, \cdot) = 1 - \mathcal{S}^l(\mathbf{x}, \cdot)$. This leads to the following set of equations for the unknowns \mathcal{U} in the porous medium

$$\left\{ \begin{array}{ll} \phi \partial_t n_i(\mathbf{x}, \mathcal{U}) + \operatorname{div} \left(\sum_{\alpha=g,l} m_i^\alpha(\mathbf{x}, \mathcal{U}) \mathbf{K} \left(\nabla p^\alpha - \rho^\alpha(\mathcal{U}) \mathbf{g} \right) \right) & = 0, \quad i \in \mathcal{C} \quad \text{on } \Omega^p \times (0, T), \\ \sum_{i \in \mathcal{C}} c_i^\alpha(\mathcal{U}) = 1, \quad \alpha = g, l & \quad \text{on } \Omega^p \times (0, T), \end{array} \right. \quad (3.1)$$

with the number of mole of the component i per unit pore volume defined by

$$n_i(\mathbf{x}, \mathcal{U}) = \sum_{\alpha=g,l} c_i^\alpha(\mathcal{U}) \zeta^\alpha(\mathcal{U}) \mathcal{S}^\alpha(\mathbf{x}, p^g - p^l),$$

and the mobility of the component i in phase α defined by

$$m_i^\alpha(\mathbf{x}, \mathcal{U}) = c_i^\alpha(\mathcal{U}) \zeta^\alpha(\mathcal{U}) \frac{k_r^\alpha(\mathbf{x}, \mathcal{S}^\alpha(\mathbf{x}, p^g - p^l))}{\mu^\alpha(\mathcal{U})}.$$

In the free flow domain it is assumed that the gas molar and mass densities are fixed which amounts to neglect the effect of the pressure and molar fraction variations on the gas densities. It is assumed that the coupling with the porous medium induces a small perturbation of a given stationary turbulent flow with velocity \mathbf{u}_t and pressure p_t solution of the following RANS model

$$\left\{ \begin{array}{ll} \rho^g \operatorname{div}(\mathbf{u}_t \otimes \mathbf{u}_t) + \operatorname{div} \left(-(\mu^g + \mu_t)(\nabla \mathbf{u}_t + \nabla^t \mathbf{u}_t) \right) + \nabla p_t = \rho^g \mathbf{g} & \text{on } \Omega^g, \\ \operatorname{div}(\mathbf{u}_t) = 0 & \text{on } \Omega^g, \end{array} \right. \quad (3.2)$$

with boundary condition $\mathbf{u}_t = 0$ at the interface Γ . In (3.2), μ_t is the turbulent viscosity which is modelled e.g. using an algebraic turbulent model or a more advanced $k - \epsilon$ model. Note that this turbulent viscosity μ_t vanishes at the interface Γ but is much larger than μ^g away from the viscous boundary layer. This turbulent flow is responsible for a turbulent diffusion denoted by D_t and typically given by $D_t = \frac{1}{S_c} \frac{\mu_t}{\rho^g}$ where S_c is the Schmidt number (see e.g. [9]) that will be assumed to be equal to 1 in the following to fix ideas. This turbulent diffusion, which is much larger than D^g away from the viscous boundary layer, plays an essential role in the order of magnitude of the evaporation rate. The gas molar fraction of the uncoupled flow corresponds to the initial condition $c = c_{init}$ of the coupled flow.

The coupling of the free flow with the porous medium flow leads to the new gas velocity $\mathbf{u} = \mathbf{u}_t + \tilde{\mathbf{u}}$, the new pressure $p = p_t + \tilde{p}$, and the gas molar fraction c solutions of the following RANS model

$$\left\{ \begin{array}{ll} \rho^g \operatorname{div}(\mathbf{u}_t \otimes \tilde{\mathbf{u}} + \tilde{\mathbf{u}} \otimes \mathbf{u}_t + \tilde{\mathbf{u}} \otimes \tilde{\mathbf{u}}) \\ \quad - \operatorname{div}((\mu^g + \mu_t)(\nabla \tilde{\mathbf{u}} + \nabla^t \tilde{\mathbf{u}})) + \nabla \tilde{p} = 0 & \text{on } \Omega^g \times (0, T), \\ \partial_t c_i + \operatorname{div}(c_i \mathbf{u}) + \operatorname{div}(-(D^g + D_t) \nabla c_i) = 0, i \in \mathcal{C} & \text{on } \Omega^g \times (0, T), \\ \sum_{i \in \mathcal{C}} c_i = 1 & \text{on } \Omega^g \times (0, T). \end{array} \right. \quad (3.3)$$

Due to the small perturbation assumption, the turbulent viscosity μ_t and diffusion D_t are assumed in (3.3) to be given functions of \mathbf{x} independent on $\tilde{\mathbf{u}}$, \tilde{p} , and c . A stationary model for the momentum equation is used in (3.3) due to the much larger porous medium flow time scale than the free flow time scale. The component molar conservations in the free flow domain are kept unstationary in order to ease the non linear solution of the coupled system at the start of the simulation.

At the interface Γ between the free flow domain and the porous medium the coupling conditions are an adaptation to those stated in [49]. The Beavers Joseph condition at the interface Γ is replaced by a no slip condition due to the low permeability of the porous medium. The remaining conditions are the continuity of the molar fluxes for each component $i \in \mathcal{C}$ assuming that the liquid phase is instantaneously vaporized, the continuity of the gas molar fractions, the continuity of the normal component of the normal stress, and the gas liquid thermodynamical equilibrium. We obtain the following

interface conditions

$$\left\{ \begin{array}{ll} \frac{1}{\zeta^g} \sum_{\alpha=l,g} -m_i^\alpha(\mathbf{x}, \mathcal{U}) \mathbf{K}(\nabla p^\alpha - \rho^\alpha(\mathcal{U}) \mathbf{g}) \cdot \mathbf{n} \\ \quad = c_i \mathbf{u} \cdot \mathbf{n} - D^g \nabla c_i \cdot \mathbf{n}, i \in \mathcal{C} & \text{on } \Gamma \times (0, T), \\ c_i^g(\mathcal{U}) = c_i, i \in \mathcal{C} & \text{on } \Gamma \times (0, T), \\ p^g = p + \mathbf{n} \cdot (\rho^g \mathbf{u} \otimes \mathbf{u} - \mu^g (\nabla \mathbf{u} + \nabla^t \mathbf{u})) \mathbf{n} & \text{on } \Gamma \times (0, T), \\ \sum_{i \in \mathcal{C}} c_i^\alpha(\mathcal{U}) = 1 \alpha = g, l, & \text{on } \Gamma \times (0, T), \\ \mathbf{u} \wedge \mathbf{n} = 0 & \text{on } \Gamma \times (0, T), \end{array} \right. \quad (3.4)$$

where \mathbf{n} denotes the unit normal vector at the interface Γ oriented outward of the porous medium domain. Note that in practice, the gas pressure jump $p - p^g$ at the interface can be neglected since a small flow rate between the porous medium and the free flow domain is expected.

3.2.2 Fixed point algorithm

In [6, 41, 48] all the Darcy and free flow unknowns corresponding in our case to \mathcal{U} , \mathbf{u} , p and c are solved using a monolithic Newton algorithm at each time step of a fully implicit Euler time integration scheme. Given the complexity of the full system, this approach naturally leads to difficulties in solving the non linear and linearized systems.

Alternatively, many coupling strategies simply rely on a sequential coupling algorithm of Dirichlet Neumann type using typically two different codes for the Darcy and free flows. This type of sequential coupling algorithm leads to very small time steps due to the strong coupling between the liquid pressure p^l and the water molar fraction c_e at the interface Γ which is induced by the thermodynamical equilibrium. For example, in [26, 24], a time step of 0.1 s is reported resulting in roughly 100h of CPU time for a few days of simulation. We refer to [25] for a recent review including a list of codes implementing sequential or fully implicit coupling algorithms for the modelling of drying processes at the interface between a porous medium and a free flow domain.

Our approach is rather to split the system in two simpler subsystems at each time step of the fully implicit Euler time integration scheme. In a first step, for given \mathbf{u} and p in Ω^g , the strongly coupled unknowns \mathcal{U} in Ω^p , c in Ω^g , and $\mathbf{u} \cdot \mathbf{n}$ at Γ are computed using a Newton algorithm solving the Darcy flow in the porous medium together with the tracer equations in the free flow domain and part of the interface conditions. The gas velocity \mathbf{u} and gas pressure p in Ω^g are then computed in a second step solving the momentum and divergence free equations using step 1 normal velocity $\mathbf{u} \cdot \mathbf{n}$ at the interface Γ . The two steps 1 and 2 are iterated, as a fixed point algorithm for the normal velocity $\mathbf{u} \cdot \mathbf{n}$ at the interface Γ , until the stopping criteria $\|1 - \sum_{i \in \mathcal{C}} c_i\|_{L^\infty(\Omega^g)} \leq \epsilon$ is satisfied for a given accuracy ϵ . The convergence of this fixed point method is expected

to be very fast due to the weak coupling of the unknowns \mathcal{U} , c , and $\mathbf{u} \cdot \mathbf{n}$ to the unknowns \mathbf{u} and p . We will see in the numerical Section 3.4 that, in practice, the sequential version of this algorithm, i.e. a single fixed point iteration, suffices to obtain a very accurate result.

We detail below the two steps of the fixed point algorithm at a given time step Δt^n between times t^{n-1} and t^n , which are iterated until convergence of the gas molar fractions such that $\|1 - \sum_{i \in \mathcal{C}} c_i\|_{L^\infty(\Omega^g)} \leq \epsilon$. To fix idea, an Euler implicit time integration is used in both domains. The unknowns at time n are denoted with the n superscript. The fixed point iteration count is denoted by k and the fixed point algorithm is initialized with the previous time step solution.

Step 1: it computes $\mathcal{U}^{n,k}$ in the porous medium, $c^{n,k}$ in the free flow domain and $\mathbf{u}^{n,k} \cdot \mathbf{n}$ at the interface, at fixed velocity $\mathbf{u}^{n,k-1}$ and pressure $p^{n,k-1}$ in the free flow domain, as the solution of the system coupling the Darcy flow model

$$\left\{ \begin{array}{ll} \phi \frac{n_i(\mathbf{x}, \mathcal{U}^{n,k}) - n_i(\mathbf{x}, \mathcal{U}^{n-1})}{\Delta t^n} \\ + \operatorname{div} \left(\sum_{\alpha=g,l} -m_i^\alpha(\mathbf{x}, \mathcal{U}^{n,k}) \mathbf{K} \left(\nabla p^{\alpha,n,k} - \rho^\alpha(\mathcal{U}^{n,k}) \mathbf{g} \right) \right) = 0, i \in \mathcal{C} & \text{on } \Omega^p, \\ \sum_{i \in \mathcal{C}} c_i^\alpha(\mathcal{U}^{n,k}) = 1, \alpha = g, l & \text{on } \Omega^p, \end{array} \right. \quad (3.5)$$

with the tracer equations in the free flow model

$$\frac{c_i^{n,k} - c_i^{n-1}}{\Delta t^n} + \operatorname{div} \left(c_i^{n,k} \mathbf{u}^{n,k-1} \right) + \operatorname{div} \left(-(D^g + D_t) \nabla c_i^{n,k} \right) = 0, i \in \mathcal{C}, \quad \text{on } \Omega^g, \quad (3.6)$$

and the following subset of the interface conditions

$$\left\{ \begin{array}{ll} \frac{1}{\zeta^g} \sum_{\alpha=l,g} -m_i^\alpha(\mathbf{x}, \mathcal{U}^{n,k}) \mathbf{K} \left(\nabla p^{\alpha,n,k} - \rho^\alpha(\mathcal{U}^{n,k}) \mathbf{g} \right) \cdot \mathbf{n} \\ = c_i^{n,k} \mathbf{u}^{n,k} \cdot \mathbf{n} - D^g \nabla c_i^{n,k} \cdot \mathbf{n}, i \in \mathcal{C} & \text{on } \Gamma, \\ c_i^g(\mathcal{U}^{n,k}) = c_i^{n,k}, i \in \mathcal{C} & \text{on } \Gamma, \\ p^{g,n,k} = p^{n,k-1} + \mathbf{n} \cdot \left(\rho^g \mathbf{u}^{n,k-1} \otimes \mathbf{u}^{n,k-1} - \mu^g (\nabla \mathbf{u}^{n,k-1} + \nabla^t \mathbf{u}^{n,k-1}) \right) \mathbf{n} & \text{on } \Gamma, \\ \sum_{i \in \mathcal{C}} c_i^\alpha(\mathcal{U}^{n,k}) = 1 \alpha = g, l, & \text{on } \Gamma. \end{array} \right. \quad (3.7)$$

Note that in (3.6) and (3.7), the normal gas velocity $\mathbf{u}^{n,k} \cdot \mathbf{n}$ is used for the convective flux at the interface Γ and not $\mathbf{u}^{n,k-1} \cdot \mathbf{n}$.

Step 2: Given the normal gas velocity $\mathbf{u}^{n,k} \cdot \mathbf{n}$ at the interface Γ computed at step 1, step 2 computes the gas velocity $\mathbf{u}^{n,k} = \mathbf{u}_t + \tilde{\mathbf{u}}^{n,k}$ and the gas pressure $p^{n,k} = p_t + \tilde{p}^{n,k}$ as the

solution at time t^n of the following RANS model

$$\left\{ \begin{array}{ll} \rho^g \operatorname{div}(\mathbf{u}_t \otimes \tilde{\mathbf{u}}^{n,k} + \tilde{\mathbf{u}}^{n,k} \otimes \mathbf{u}_t + \tilde{\mathbf{u}}^{n,k} \otimes \tilde{\mathbf{u}}^{n,k}) \\ \quad - \operatorname{div}((\mu^g + \mu_t)(\nabla \tilde{\mathbf{u}}^{n,k} + \nabla^t \tilde{\mathbf{u}}^{n,k})) + \nabla \tilde{p}^{n,k} = 0 & \text{on } \Omega^g, \\ \operatorname{div}(\tilde{\mathbf{u}}^{n,k}) = 0 & \text{on } \Omega^g. \end{array} \right. \quad (3.8)$$

3.3 Reduced model

It is assumed to fix ideas that the free flow domain is a cylindrical domain of length L and of section S with S an open simply connected subdomain of \mathbb{R}^2 . The free flow domain is defined by $\Omega^g = (0, L) \times S$ and the interface by $\Gamma = (0, L) \times \partial S$. In the following, γ denotes the trace operator on Γ and s is the curvilinear coordinate along ∂S .

The reduced model is motivated by the large longitudinal dimension compared with the transversal dimensions of the free flow domain in radioactive waste geological storage applications. It is assumed that the pressure p and the longitudinal velocity u in the section S depend only on the longitudinal coordinate x and on time t . The gas molar fraction c is also assumed to depend only on x and t . At the interface Γ , the gas molar fraction in the viscous boundary layer is given by $c^g(\gamma\mathcal{U})$ from the gas molar fraction continuity. The gas pressure γp^g at the interface assumes an hydrostatic pressure in the section S . In most cases, this hydrostatic correction can actually be neglected. Another unknown is the gas normal velocity at the interface Γ averaged along ∂S . It is denoted by v_n with the normal oriented outward of the porous medium.

3.3.1 Reduced 1D model in the free flow domain

The new system amounts to find the porous medium unknowns $\mathcal{U}(\mathbf{x}, t)$ on $\Omega^p \times (0, T)$, and the free flow domain unknowns $u(x, t)$, $c(x, t)$ on $(0, L) \times (0, T)$ and $v_n(\mathbf{x}, t)$ on $\Gamma \times (0, T)$ satisfying the Darcy flow system (3.1), coupled with the following modified system at the interface Γ

$$\left\{ \begin{array}{l} c_i^g(\gamma\mathcal{U})v_n^+ + c_i v_n^- + \frac{D^g}{\delta}(c_i^g(\gamma\mathcal{U}) - c_i) \\ = \frac{1}{\zeta^g} \sum_{\alpha=g,l} -m_i^\alpha(\mathbf{x}, \mathcal{U}) \mathbf{K}(\nabla p^\alpha - \rho^\alpha(\mathcal{U})\mathbf{g}) \cdot \mathbf{n}, \quad i \in \mathcal{C} \text{ on } \Gamma \times (0, T), \\ \sum_{i \in \mathcal{C}} c_i^\alpha(\gamma\mathcal{U}) = 1, \quad \alpha = g, l \text{ on } \Gamma \times (0, T), \\ \gamma p^g = p - \rho^g(p, c)g(z - \frac{1}{|S|} \int_S dz), \text{ on } \Gamma \times (0, T), \end{array} \right. \quad (3.9)$$

and with the conservation equations along the free flow domain

$$\left\{ \begin{array}{l} \partial_t c_i + \partial_x(c_i u) \\ = \frac{1}{|S|\zeta^g} \int_{\partial S} \sum_{\alpha=g,l} -m_i^\alpha(\mathbf{x}, \mathcal{U}) \mathbf{K}(\nabla p^\alpha - \rho^\alpha(\mathcal{U}) \mathbf{g}) \cdot \mathbf{n} \, ds, \, i \in \mathcal{C} \text{ on } (0, L) \times (0, T), \\ \sum_{i \in \mathcal{C}} c_i = 1 \text{ on } (0, L) \times (0, T). \end{array} \right. \quad (3.10)$$

To fix ideas the pressure drop is given by the Forchheimer model $(\alpha_g u + \beta_g |u|u) = -\partial_x \gamma p^g$ with $\alpha_g \geq 0$ and $\beta_g \geq 0$, $\alpha_g + \beta_g > 0$. In (3.9), we have used the notation $a^+ = \max(a, 0)$ and $a^- = \min(a, 0)$. The function $\delta > 0$ corresponds to the molar fraction boundary layer thickness that need to be modelled as discussed in the next subsection.

3.3.2 Molar fraction boundary layer thickness model

A simple choice of the boundary layer thickness δ is given by the following model. let \mathcal{L} denote the stationary convection diffusion operator defined for all $d \in H^1(\Omega^g)$ by

$$\mathcal{L}d = \operatorname{div}(\mathbf{u}_t d - (D^g + D_t) \nabla d),$$

recalling that $\operatorname{div}(\mathbf{u}_t) = 0$ and that $\mathbf{u}_t = 0$ on Γ . We define the solution d of the following stationary convection diffusion equation given a constant boundary condition $d_{in} \in \mathbb{R}$ on $\Gamma_{in}^g = \{0\} \times S$ and a boundary condition $d_\Gamma \in H^{\frac{1}{2}}(\Gamma)$ on Γ :

$$\left\{ \begin{array}{ll} \mathcal{L}d = 0 & \text{on } \Omega^g, \\ d = d_\Gamma & \text{on } \Gamma, \\ d = d_{in} & \text{on } \Gamma_{in}^g, \\ \nabla d \cdot \mathbf{n} = 0 & \text{on } \Gamma_{out}^g = \{L\} \times S. \end{array} \right. \quad (3.11)$$

Let us denote by \mathcal{S}_P the linear Steklov-Poincaré operator such that for all $d_\Gamma \in H^{\frac{1}{2}}(\Gamma)$

$$\mathcal{S}_P(d_\Gamma - d_{in}) = -\nabla d \cdot \mathbf{n} \in H^{-\frac{1}{2}}(\Gamma),$$

and let us denote by M the linear compact operator from $H^{\frac{1}{2}}(\Gamma)$ to $H^{\frac{1}{2}}(\Gamma)$ such that for all $d_\Gamma \in H^{\frac{1}{2}}(\Gamma)$

$$M(d_\Gamma - d_{in}) = -d_{in} + \frac{1}{|S|} \int_S d(\cdot, y, z) dy dz \in H^1(\Gamma).$$

Then, we define for $d_{in} \in \mathbb{R}$, $d_\Gamma = d_\gamma 1_\Gamma$ with $d_\gamma \in \mathbb{R}$, $d_{in} \neq d_\gamma$,

$$\delta = \frac{d_\Gamma - \frac{1}{|S|} \int_S d(\cdot, y, z) dy dz}{-\nabla d \cdot \mathbf{n}} = \frac{(I - M)1_\Gamma}{\mathcal{S}_P 1_\Gamma}$$

where 1_Γ denotes the function equal to 1 on Γ . This definition of δ is clearly independent on the choice of both d_γ and d_{in} . Also from the maximum principle, $\delta(\mathbf{x}) > 0$ for all $\mathbf{x} \in \Gamma$.

From the maximum principle and the Fredholm alternative, the linear operator $I - M$ defines a bijection from $H^{\frac{1}{2}}(\Gamma)$ to $H^{\frac{1}{2}}(\Gamma)$. Hence we can define the operator

$$\overline{\mathcal{S}}_P = \mathcal{S}_P(I - M)^{-1},$$

which relates the normal flux at Γ to the difference between the trace on Γ and the section mean values as follows

$$-\nabla d \cdot \mathbf{n} = \overline{\mathcal{S}}_P \left(d_\Gamma - \frac{1}{|S|} \int_S d(., y, z) dy dz \right).$$

In this framework, $\frac{1}{\delta}$ clearly appears as a diagonal approximation of the operator $\overline{\mathcal{S}}_P$ which is built to be exact for constant boundary conditions on Γ . A better approximation could be obtained using a second order approximation of the operator $\overline{\mathcal{S}}_P$ following the techniques used in Optimized Schwarz Methods [43].

It is more usual to relate the flux to the difference between the trace on Γ and d_{in} using the Steklov Poincaré operator. The diagonal approximation $\frac{D^g}{\delta} = D^g \mathcal{S}_P 1_\Gamma$ of the operator $D^g \mathcal{S}_P$ is referred to as the Convective Mass Transfer Coefficient *CMTC* (see the review [25] and the references there in for a discussion about CMTCs). In our context, our choice has the advantage to take into account the coupling of the interface conditions with the 1D gas free flow.

3.4 Numerical tests

In order to assess the efficiency of the fixed point algorithm and to compare the full and reduced models, we consider in the following tests a simple 2D setting with $\Omega^g = (0, L) \times (0, H_1)$, $\Omega^p = (0, L) \times (H_1, H_2)$ and $\Gamma = (0, L) \times \{H_1\}$. Figure 3.1 exhibits the two domains, the interface and the external boundaries Γ_D^p , Γ_N^p , Γ_{in}^g , Γ_{out}^g , and Γ_N^g .

We consider the set of components $\mathcal{C} = \{e, a\}$ where e denotes the water component, and a the gaseous air component with the fixed Henry constant $H_a = 6 \cdot 10^9$ Pa. The gas molar density is given by $\zeta^g(p^g) = \frac{p^g}{RT_e}$ mol.m⁻³, and the liquid molar density is fixed to $\zeta^l = 55555$ mol.m⁻³. The phase viscosities are fixed to $\mu^g = 18.51 \cdot 10^{-6}$ Pa.s⁻¹ and $\mu^l = 10^{-3}$ Pa.s⁻¹. The mass densities are defined by $\rho^\alpha = \zeta^\alpha \sum_{i \in \mathcal{C}} c_i^\alpha M_i$ with the molar masses of the components $M_a = 29 \cdot 10^{-3}$ Kg mol⁻¹, $M_e = 18 \cdot 10^{-3}$ Kg mol⁻¹. The fugacities of the water and air components in the gas phase f_e^g and f_a^g are given by Dalton's law for an ideal mixture of perfect gas (1.1). The fugacities of the components in the liquid phase are given by Henry's law (1.2) for the dissolution of the air component in the liquid phase, and by Raoult-Kelvin's law (1.3) for the water component in the liquid phase. The solution of the equation $f^\alpha(c^\alpha, p^g, p^l) = f$ leads to the following component

molar fractions c_i^α as functions of \mathcal{U} :

$$\begin{cases} c_e^l(\mathcal{U}) = \frac{f_e}{P_{sat}(T_e)} \exp\left(\frac{(p^g - p^l)}{\zeta^l(p^l)RT_e}\right), & c_a^l(\mathcal{U}) = \frac{f_a}{H_a}, \\ c_e^g(\mathcal{U}) = \frac{f_e}{p^g}, & c_a^g(\mathcal{U}) = \frac{f_a}{p^g}. \end{cases} \quad (3.12)$$

The relative permeabilities and capillary pressure in the porous medium are given by the Van-Genuchten laws (1.20)-(1.21)-(1.22). In our numerical tests, the stationary turbulent profile, corresponding to the velocity without the coupling with the porous medium, is obtained using the following Prandtl algebraic turbulent model for the turbulent viscosity (see [56, 19, 9])

$$\mu_t = \rho^g (l_m(y))^2 |u'_t(y)|, \quad l_m(y) = 0.41 \min(y, H_1 - y).$$

It leads to compute the solution (\mathbf{u}_t, p_t) with $\mathbf{u}_t(y) = \begin{pmatrix} u_t(y) \\ 0 \end{pmatrix}$ of the system

$$\begin{cases} \operatorname{div}(-(\mu^g + \mu_t)\nabla u_t) + \partial_x p_t = 0 & \text{on } \Omega^g, \\ \partial_y p_t = -\rho^g g & \text{on } \Omega^g, \\ \operatorname{div}(\mathbf{u}_t) = 0 & \text{on } \Omega^g, \end{cases} \quad (3.13)$$

which reduces to the following Ordinary Differential Equation (ODE) for $u_t(y)$

$$(\mu^g + \rho^g (l_m(y))^2 |u'_t|) u'_t = \alpha_t (H_1/2 - y),$$

to be integrated between $y = 0$ and $y = \frac{H_1}{2}$ by symmetry. The integration constant of this ODE and the constant α_t are obtained using the conditions $u_t(0) = 0$ and

$$\frac{1}{H_1} \int_0^{H_1} u_t(y) dy = w_{in},$$

where w_{in} is the prescribed mean value of the input velocity. Using the outflow boundary condition (3.14) specified below, the turbulent pressure is defined by

$$p_t(x, y) = p_{out} - \rho^g g y - \alpha_t (x - L),$$

where p_{out} is the outflow pressure for $y = 0$, and $g = 9.81 m.s^{-2}$ is the gravity acceleration. In our numerical tests, the turbulent diffusion is related to the turbulent viscosity by

$$D_t(y) = \frac{\mu_t(y)}{\rho^g}.$$

The porous medium is initially saturated by the liquid phase with imposed pressure p_{init}^l and composition $c_{a,init}^l = 0$, $c_{e,init}^l = 1$ which combined with the equation $c_e^g(\mathcal{U}_{init}) + c_a^g(\mathcal{U}_{init}) = 1$ defines the initial unknowns \mathcal{U}_{init} . At the top porous medium boundary Γ_D^p , a Dirichlet boundary condition is imposed equal to the initial condition $\mathcal{U}_D = \mathcal{U}_{init}$. At

both sides Γ_N^p of the porous medium, a zero normal flux boundary condition is imposed for all components. The initial condition in the free flow domain is given by $p_{init} = 10^5$ Pa and $c_{e,init} = 1 - c_{a,init}$ defined by the prescribed relative humidity

$$H_{r,init} = \frac{c_{e,init} p_{init}}{P_{sat}(T_e)}.$$

At the boundary Γ_{in}^g , the input molar fractions are set to $c_{in} = c_{init}$, and the stationary turbulent profile $\mathbf{u}_t(y)$ is imposed. At the boundary Γ_{out}^g , the following outflow boundary conditions are imposed

$$p - (\mu^g + \mu_t(y))\partial_x u = p^{out} - \rho^g g y, \quad \partial_x v = 0, \quad (3.14)$$

with $p_{out} = p_{init}$. The usual gradient is used in this outflow condition rather than the symmetric gradient in such a way that this condition can be satisfied by (\mathbf{u}_t, p_t) . The diffusive normal fluxes are set to zero for all components $i \in \mathcal{C}$ on Γ_{out}^g . At the bottom boundary Γ_N^g , the velocity \mathbf{u} is set to zero as well as the diffusive normal fluxes for all components $i \in \mathcal{C}$.

3.4.1 Finite Volume Discretization on a Cartesian mesh

The domain $(0, L) \times (0, H_2)$ is discretized by a non uniform Cartesian mesh refined at both sides of the interface Γ . A finite volume cell centered discretization with a Two Point Flux Approximation (TPFA) of the Darcy fluxes and an upwind of the mobility terms is used for the porous medium flow [52, 5]. For the free flow, a staggered MAC (Marker-And-Cell) scheme is used for the Navier Stokes equations [40, 51, 58] combined with a TPFA discretization of the diffusion fluxes.

TPFA discretization of Step 1

To write the discretization of the step 1 model, it is convenient to use the following unstructured mesh notations. Let \mathcal{M}^p (resp. \mathcal{M}^g) denotes the set of cells of Ω^p (resp. Ω^g). The set of edges of the mesh is denoted by \mathcal{E} , $\mathcal{M}_\sigma \subset \mathcal{M}^p \cup \mathcal{M}^g$ stands for the set of cells sharing the edge σ , and \mathcal{E}_K denote the set of edges of the cell $K \in \mathcal{M}^p \cup \mathcal{M}^g$. The set of edges \mathcal{E} is partitioned as follows:

\mathcal{E}_{int}^p the set of interior edges of Ω^p with $\mathcal{M}_\sigma = \{K, L\} \subset \mathcal{M}^p$ for all $\sigma \in \mathcal{E}_{int}^p$,

\mathcal{E}_b^p the set of edges of Γ_b^p with $\mathcal{M}_\sigma = \{K\} \subset \mathcal{M}^p$ for all $\sigma \in \mathcal{E}_b^p$ with $b = D$ or N ,

\mathcal{E}_Γ the set of edges of Γ with $\mathcal{M}_\sigma = \{K, L\}$, $K \in \mathcal{M}^p$, $L \in \mathcal{M}^g$ for all $\sigma \in \mathcal{E}_\Gamma$,

\mathcal{E}_{int}^g the set of interior edges of Ω^g with $\mathcal{M}_\sigma = \{K, L\} \subset \mathcal{M}^g$ for all $\sigma \in \mathcal{E}_{int}^g$

\mathcal{E}_b^f the set of edges of Γ_b^f with $\mathcal{M}_\sigma = \{K\} \subset \mathcal{M}^g$ for all $\sigma \in \mathcal{E}_b^f$, $b = in, out, N$.

The set of discrete unknowns is denoted by $\mathcal{U}_K = (p_K^g, p_K^l, f_K) \in \mathbb{R}^{C+2}$, $K \in \mathcal{M}^p$ in the porous medium, by $c_K \in \mathbb{R}^C$, $K \in \mathcal{M}^g$ in the free flow domain, and by $\mathcal{U}_\sigma = (p_\sigma^g, p_\sigma^l, f_\sigma) \in \mathbb{R}^{C+2}$ and $v_{n,\sigma} \in \mathbb{R}$ for all edges $\sigma \in \mathcal{E}_\Gamma$ at the interface where $v_{n,\sigma}$ is the normal gas velocity oriented outward of the free flow domain.

Let ϕ_K denote the mean porosity in the cell K . Let $\mathbf{x}_K = (x_K, y_K)$ denote the centre of the cell K and $\mathbf{x}_\sigma = (x_\sigma, y_\sigma)$ the centre of the edge σ , and let T_σ be the TPFA Darcy transmissibility of the edge σ . The TPFA Darcy fluxes at the interior edges $\sigma \in \mathcal{E}_{int}^p$ of the porous medium, oriented outward to the cell K with $\mathcal{M}_\sigma = \{K, L\}$ are defined for $\alpha = g, l$ by

$$V_{K,\sigma}^\alpha(\mathcal{U}_K, \mathcal{U}_L) = T_\sigma \left(p_K^\alpha - p_L^\alpha + \rho^\alpha \left(\frac{\mathcal{U}_K + \mathcal{U}_L}{2} \right) g(y_K - y_L) \right).$$

Similarly, at the edges $\sigma \in (\mathcal{E}_D^p \cup \mathcal{E}_\Gamma) \cap \mathcal{E}_K$, $K \in \mathcal{M}^p$, they are defined for $\alpha = g, l$ by

$$V_{K,\sigma}^\alpha(\mathcal{U}_K, \mathcal{U}_\sigma) = T_\sigma \left(p_K^\alpha - p_\sigma^\alpha + \rho^\alpha \left(\frac{\mathcal{U}_K + \mathcal{U}_\sigma}{2} \right) g(y_K - y_\sigma) \right),$$

Then, using an upwind approximation of the mobilities with respect to the sign of each phase Darcy flux, we set for all $\sigma \in \mathcal{E}_{int}^p$, $\mathcal{M}_\sigma = \{K, L\}$

$$V_{K,\sigma}^{\alpha,i}(\mathcal{U}_K, \mathcal{U}_L) = m_i^\alpha(\mathbf{x}_K, \mathcal{U}_K) V_{K,\sigma}^\alpha(\mathcal{U}_K, \mathcal{U}_L)^+ + m_i^\alpha(\mathbf{x}_L, \mathcal{U}_L) V_{K,\sigma}^\alpha(\mathcal{U}_K, \mathcal{U}_L)^-, \quad (3.15)$$

and for all $\sigma \in (\mathcal{E}_D^p \cup \mathcal{E}_\Gamma) \cap \mathcal{E}_K$, $K \in \mathcal{M}^p$

$$V_{K,\sigma}^{\alpha,i}(\mathcal{U}_K, \mathcal{U}_\sigma) = m_i^\alpha(\mathbf{x}_K, \mathcal{U}_K) V_{K,\sigma}^\alpha(\mathcal{U}_K, \mathcal{U}_\sigma)^+ + m_i^\alpha(\mathbf{x}_K, \mathcal{U}_\sigma) V_{K,\sigma}^\alpha(\mathcal{U}_K, \mathcal{U}_\sigma)^-. \quad (3.16)$$

The discrete conservation equations in the porous medium writes for all cells $K \in \mathcal{M}^p$

$$\left\{ \begin{array}{l} \phi_K |K| \frac{n_i(\mathbf{x}_K, \mathcal{U}_K^{n,k}) - n_i(\mathbf{x}_K, \mathcal{U}_K^{n-1})}{\Delta t^n} + \sum_{\alpha=l,g} \left(\sum_{\sigma \in \mathcal{E}_{int}^p \cap \mathcal{E}_K} V_{K,\sigma}^{\alpha,i}(\mathcal{U}_K^{n,k}, \mathcal{U}_L^{n,k}) \right. \\ \quad \left. + \sum_{\sigma \in \mathcal{E}_D^p \cap \mathcal{E}_K} V_{K,\sigma}^{\alpha,i}(\mathcal{U}_K^{n,k}, \mathcal{U}_D) + \sum_{\sigma \in \mathcal{E}_\Gamma \cap \mathcal{E}_K} V_{K,\sigma}^{\alpha,i}(\mathcal{U}_K^{n,k}, \mathcal{U}_\sigma^{n,k}) \right) = 0, \quad i \in \mathcal{C} \\ \sum_{i \in \mathcal{C}} c_i^\alpha(\mathcal{U}_K^{n,k}) = 1, \quad \alpha = g, l, \end{array} \right. \quad (3.17)$$

with $|K|$ denoting the volume of the cell K .

The normal gas velocities at the edges of the free flow domain are given by the step 2 at the fixed point iteration $k-1$ and denoted for all $\sigma \in \mathcal{E}_K \setminus \mathcal{E}_\Gamma$, $K \in \mathcal{M}^g$ by $\mathbf{u}^{n,k-1} \cdot \mathbf{n}_{K,\sigma}$, where $\mathbf{n}_{K,\sigma}$ is the unit normal vector at the edge σ outward to the cell K . The cell pressures $p_K^{n,k-1}$ for all $K \in \mathcal{M}^g$ are also given by the step 2 at the fixed point iteration $k-1$. The discretization of the tracer equation writes for all cells $K \in \mathcal{M}^g$ and all

component $i \in \mathcal{C}$:

$$\begin{aligned}
& \frac{c_{i,K}^{n,k} - c_{i,K}^{n-1}}{\Delta t^n} |K| \\
& + \sum_{\sigma \in \mathcal{E}_{int}^g \cap \mathcal{E}_K} \left(c_{i,K}^{n,k} |\sigma| (\mathbf{u}^{n,k-1} \cdot \mathbf{n}_{K,\sigma})^+ + c_{i,L}^n |\sigma| (\mathbf{u}^{n,k-1} \cdot \mathbf{n}_{K,\sigma})^- + T_\sigma^D (c_{i,K}^{n,k} - c_{i,L}^{n,k}) \right) \\
& + \sum_{\sigma \in \mathcal{E}_\Gamma \cap \mathcal{E}_K} \left(\bar{c}_{i,K}^{n,k} |\sigma| (v_{n,\sigma}^{n,k})^+ + c_i^g(\mathcal{U}_\sigma^{n,k}) |\sigma| (v_{n,\sigma}^{n,k})^- + T_\sigma^D (\bar{c}_{i,K}^{n,k} - c_i^g(\mathcal{U}_\sigma^{n,k})) \right) \\
& + \sum_{\sigma \in \mathcal{E}_{in}^g \cap \mathcal{E}_K} \left(c_{i,K}^{n,k} |\sigma| (\mathbf{u}^{n,k-1} \cdot \mathbf{n}_{K,\sigma})^+ + c_{i,in} |\sigma| (\mathbf{u}^{n,k-1} \cdot \mathbf{n}_{K,\sigma})^- + T_\sigma^D (c_{i,K}^{n,k} - c_{i,in}) \right) \\
& + \sum_{\sigma \in \mathcal{E}_{out}^g \cap \mathcal{E}_K} c_{i,K}^{n,k} |\sigma| (\mathbf{u}^{n,k-1} \cdot \mathbf{n}_{K,\sigma})^+ = 0,
\end{aligned} \tag{3.18}$$

where $|\sigma|$ is the length of the edge σ , T_σ^D is the diffusion TPFA transmissibility of the edge σ , and where $\bar{c}_i = \frac{c_i}{\sum_{j \in \mathcal{C}} c_j}$, $i \in \mathcal{C}$ stands for the normalized molar fractions.

The discrete conservation equations in the porous medium domain (3.17) and in the free flow domain (3.18) are coupled to the following interface conditions written for all edges $\sigma \in \mathcal{E}_\Gamma$, with $\mathcal{M}_\sigma = \{K, L\}$, $K \in \mathcal{M}^p$, $L \in \mathcal{M}^g$:

$$\left\{ \begin{array}{l} \frac{1}{\zeta^g} \sum_{\alpha=l,g} V_{K,\sigma}^{\alpha,i}(\mathcal{U}_K^{n,k}, \mathcal{U}_\sigma^{n,k}) \\ \quad = -\bar{c}_{i,L}^{n,k} |\sigma| (v_{n,\sigma}^{n,k})^+ - c_i^g(\mathcal{U}_\sigma^{n,k}) |\sigma| (v_{n,\sigma}^{n,k})^- - T_\sigma^D (\bar{c}_{i,L}^{n,k} - c_i^g(\mathcal{U}_\sigma^{n,k})), \quad i \in \mathcal{C}, \\ p_\sigma^{g,n,k} = p_L^{n,k} + (\mathbf{n} \cdot (\rho^g \mathbf{u} \otimes \mathbf{u} - \mu^g \nabla \mathbf{u}) \mathbf{n})_\sigma^{n,k-1}, \\ \sum_{i \in \mathcal{C}} c_i^\alpha(\mathcal{U}_\sigma^{n,k}) = 1, \quad \alpha = g, l, \end{array} \right. \tag{3.19}$$

with the gas pressure jump $(\mathbf{n} \cdot (\rho^g \mathbf{u} \otimes \mathbf{u} - \mu^g \nabla \mathbf{u}) \mathbf{n})_\sigma^{n,k-1}$ specified in step 2 below.

The coupled system (3.17-3.18-3.19) at each time step n and at each fixed point iteration k is solved using a Newton algorithm. For all cells $K \in \mathcal{M}^p$ and for all edges $\sigma \in \mathcal{E}_\Gamma$ both fugacities f_e and f_a can be eliminated from the non linear system using the closure equations $c_e^\alpha(\mathcal{U}) + c_a^\alpha(\mathcal{U}) = 1$, $\alpha = g, l$. Also, for all $\sigma \in \mathcal{E}_\Gamma$, the normal velocity v_n is eliminated using the equation from (3.19)

$$v_{n,\sigma}^{n,k} = -\frac{1}{|\sigma| \zeta^g} \sum_{i \in \mathcal{C}} \sum_{\alpha=l,g} V_{K,\sigma}^{\alpha,i}(\mathcal{U}_K^{n,k}, \mathcal{U}_\sigma^{n,k}).$$

Using these eliminations, the Jacobian system to be solved at each Newton iteration reduces to Cardinal(\mathcal{C}) equations and unknowns in each cell $K \in \mathcal{M}^p \cup \mathcal{M}^g$ and at each edge $\sigma \in \mathcal{E}_\Gamma$. This linear system is solved using the sequential version of the SuperLU direct sparse solver [46], [27].

MAC discretization of Step 2

It is convenient in order to write the MAC discretization of the RANS model (3.8) to use the following structured mesh notations. The non uniform Cartesian mesh of Ω^g is defined by the set of $N_x + 1$ points along the x axis

$$0 = x_{\frac{1}{2}} < \cdots < x_{i-\frac{1}{2}} < x_{i+\frac{1}{2}} < \cdots < x_{N_x+\frac{1}{2}} = L,$$

and by the set of $N_y + 1$ points along the y axis

$$0 = y_{\frac{1}{2}} < \cdots < y_{j-\frac{1}{2}} < y_{j+\frac{1}{2}} < \cdots < y_{N_y+\frac{1}{2}} = H_1.$$

Let us set

$$\Delta x_i = x_{i+\frac{1}{2}} - x_{i-\frac{1}{2}}, i = 1, \dots, N_x \text{ and } \Delta y_j = y_{j+\frac{1}{2}} - y_{j-\frac{1}{2}}, j = 1, \dots, N_y.$$

We also define $x_i = \frac{x_{i+\frac{1}{2}} + x_{i-\frac{1}{2}}}{2}$, $i = 1, \dots, N_x$, and $y_j = \frac{y_{j+\frac{1}{2}} + y_{j-\frac{1}{2}}}{2}$, $j = 1, \dots, N_y$ and we set

$$\Delta x_{i+\frac{1}{2}} = x_{i+1} - x_i, i = 1, \dots, N_x - 1, \Delta x_{\frac{1}{2}} = x_1 - x_{\frac{1}{2}}, \Delta x_{N_x+\frac{1}{2}} = x_{N_x+\frac{1}{2}} - x_{N_x},$$

and

$$\Delta y_{j+\frac{1}{2}} = y_{j+1} - y_j, j = 1, \dots, N_y - 1, \Delta y_{\frac{1}{2}} = y_1 - y_{\frac{1}{2}}, \Delta y_{N_y+\frac{1}{2}} = y_{N_y+\frac{1}{2}} - y_{N_y}.$$

The discrete unknowns of the staggered MAC discretization are the vertical edge normal velocity perturbations

$$\tilde{u}_{i+\frac{1}{2},j}, i = 0, \dots, N_x, j = 1, \dots, N_y,$$

the horizontal edge normal velocities

$$v_{i,j+\frac{1}{2}} = \tilde{v}_{i,j+\frac{1}{2}}, i = 1, \dots, N_x, j = 0, \dots, N_y,$$

and the cell centred pressure perturbations

$$\tilde{p}_{i,j}, i = 1, \dots, N_x, j = 1, \dots, N_y.$$

The convective fluxes are discretized using an upwind approximation of the velocities assuming in our case that $u_t(y_j) + \tilde{u}_{i+\frac{1}{2},j} \geq 0$ and $\tilde{v}_{i,j+\frac{1}{2}} \leq 0$.

Let us drop in the following equations the n, k subscript for \tilde{u} , \tilde{v} and \tilde{p} to simplify the notations. The discrete system couples the discrete $\tilde{u}_{i+\frac{1}{2},j}$ momentum conservation equation in the cell $(x_i, x_{i+1}) \times (y_{j-\frac{1}{2}}, y_{j+\frac{1}{2}})$ for all $i = 1, \dots, N_x - 1$, $j = 1, \dots, N_y$, and

the boundary conditions for \tilde{u} :

$$\left\{ \begin{array}{l} \rho^g \Delta y_j \left((u_t(y_j) + \frac{\tilde{u}_{i+\frac{1}{2},j} + \tilde{u}_{i+\frac{3}{2},j}}{2})(\tilde{u}_{i+\frac{1}{2},j} + u_t(y_j)) \right. \\ \quad \left. - (u_t(y_j) + \frac{\tilde{u}_{i+\frac{1}{2},j} + \tilde{u}_{i-\frac{1}{2},j}}{2})(\tilde{u}_{i-\frac{1}{2},j} + u_t(y_j)) \right) \\ + \frac{1}{2} \rho^g \Delta x_{i+\frac{1}{2}} \left((u_t(y_{j+1/2}) + \tilde{u}_{i+\frac{1}{2},j+1})(\tilde{v}_{i,j+\frac{1}{2}} + \tilde{v}_{i+1,j+\frac{1}{2}}) \right. \\ \quad \left. - (u_t(y_{j-1/2}) + \tilde{u}_{i+\frac{1}{2},j})(\tilde{v}_{i,j-\frac{1}{2}} + \tilde{v}_{i+1,j-\frac{1}{2}}) \right) \\ + 2(\mu^g + \mu_t(y_j)) \left(\Delta y_j \frac{\tilde{u}_{i+\frac{1}{2},j} - \tilde{u}_{i+\frac{3}{2},j}}{\Delta x_{i+1}} + \Delta y_j \frac{\tilde{u}_{i+\frac{1}{2},j} - \tilde{u}_{i-\frac{1}{2},j}}{\Delta x_i} \right) \\ + \Delta y_j (\tilde{p}_{i+1,j} - \tilde{p}_{i,j}) + (\mu^g + \mu_t(y_{j+\frac{1}{2}})) \Delta x_{i+\frac{1}{2}} \frac{\tilde{u}_{i+\frac{1}{2},j} - \tilde{u}_{i+\frac{1}{2},j+1}}{\Delta y_{j+\frac{1}{2}}} \\ + (\mu^g + \mu_t(y_{j-\frac{1}{2}})) \Delta x_{i+\frac{1}{2}} \frac{\tilde{u}_{i+\frac{1}{2},j} - \tilde{u}_{i+\frac{1}{2},j-1}}{\Delta y_{j-\frac{1}{2}}} \\ + \mu_t(y_{j+\frac{1}{2}})(\tilde{v}_{i,j+\frac{1}{2}} - \tilde{v}_{i+1,j+\frac{1}{2}}) - \mu_t(y_{j-\frac{1}{2}})(\tilde{v}_{i,j-\frac{1}{2}} - \tilde{v}_{i+1,j-\frac{1}{2}}) = 0, \\ \tilde{u}_{i+\frac{1}{2},0} = \tilde{u}_{i+\frac{1}{2},N_y+1} = 0, \\ \tilde{u}_{\frac{1}{2},j} = 0, (\mu^g + \mu_t(y_j)) \Delta y_j \frac{\tilde{u}_{N_x+\frac{1}{2},j} - \tilde{u}_{N_x-\frac{1}{2},j}}{\Delta x_{N_x}} - \Delta y_j \tilde{p}_{N_x,j} = 0, \end{array} \right. \quad (3.20)$$

the discrete $\tilde{v}_{i,j+\frac{1}{2}}$ momentum conservation equation in the cell $(x_{i-\frac{1}{2}}, x_{i+\frac{1}{2}}) \times (y_j, y_{j+1})$ for all $i = 1, \dots, N_x, j = 1, \dots, N_y - 1$, and the boundary conditions for v :

$$\left\{ \begin{array}{l} \rho^g \Delta y_{j+\frac{1}{2}} \left((u_t(y_{j+\frac{1}{2}}) + \frac{\tilde{u}_{i+\frac{1}{2},j} + \tilde{u}_{i+\frac{1}{2},j+1}}{2}) \tilde{v}_{i,j+\frac{1}{2}} \right. \\ \quad \left. - (u_t(y_{j+\frac{1}{2}}) + \frac{\tilde{u}_{i-\frac{1}{2},j} + \tilde{u}_{i-\frac{1}{2},j+1}}{2}) \tilde{v}_{i-1,j+\frac{1}{2}} \right) \\ + \rho^g \Delta x_i \left(\tilde{v}_{i,j+\frac{1}{2}} \frac{\tilde{v}_{i,j+\frac{1}{2}} + \tilde{v}_{i,j+\frac{3}{2}}}{2} - \tilde{v}_{i,j+\frac{1}{2}} \frac{\tilde{v}_{i,j+\frac{1}{2}} + \tilde{v}_{i,j-\frac{1}{2}}}{2} \right) \\ + (\mu^g + \mu_t(y_{j+\frac{1}{2}})) \left(\Delta y_{j+\frac{1}{2}} \frac{\tilde{v}_{i,j+\frac{1}{2}} - \tilde{v}_{i+1,j+\frac{1}{2}}}{\Delta x_{i+\frac{1}{2}}} + \Delta y_{j+\frac{1}{2}} \frac{\tilde{v}_{i,j+\frac{1}{2}} - \tilde{v}_{i-1,j+\frac{1}{2}}}{\Delta x_{i-\frac{1}{2}}} \right) \\ + \Delta x_i (\tilde{p}_{i,j+1} - \tilde{p}_{i,j}) + 2(\mu^g + \mu_t(y_{j+1})) \Delta x_i \frac{\tilde{v}_{i,j+\frac{1}{2}} - \tilde{v}_{i,j+\frac{3}{2}}}{\Delta y_{j+1}} \\ + 2(\mu^g + \mu_t(y_j)) \Delta x_i \frac{\tilde{v}_{i,j+\frac{1}{2}} - \tilde{v}_{i,j-\frac{1}{2}}}{\Delta y_j} \\ + \mu_t(y_{j+\frac{1}{2}})(\tilde{u}_{i+\frac{1}{2},j} - \tilde{u}_{i+\frac{1}{2},j+1}) - \mu_t(y_{j+\frac{1}{2}})(\tilde{u}_{i-\frac{1}{2},j} - \tilde{u}_{i-\frac{1}{2},j+1}) = 0, \\ \tilde{v}_{0,j+\frac{1}{2}} = 0, \tilde{v}_{N_x+1,j+\frac{1}{2}} = \tilde{v}_{N_x,j+\frac{1}{2}}, \\ \tilde{v}_{i,\frac{1}{2}} = 0, \tilde{v}_{i,N_y+\frac{1}{2}} = u_{n,\sigma(i)}^{n,k}, \end{array} \right. \quad (3.21)$$

and the divergence free volume conservation equation in the cell $(x_{i-\frac{1}{2}}, x_{i+\frac{1}{2}}) \times (y_{j-\frac{1}{2}}, y_{j+\frac{1}{2}})$ for all $i = 1, \dots, N_x, j = 1, \dots, N_y$

$$\Delta y_j (\tilde{u}_{i+\frac{1}{2},j} - \tilde{u}_{i-\frac{1}{2},j}) + \Delta x_i (\tilde{v}_{i,j+\frac{1}{2}} - \tilde{v}_{i,j-\frac{1}{2}}) = 0. \quad (3.22)$$

The coupled system (3.20,3.21,3.22) is solved at each time step n and at each fixed point iteration k using a Quasi Newton algorithm where the Jacobian matrix is approximated by dropping the non linear part of the system. The main advantage of this approach is that this approximate Jacobian does not depend on n nor on k . Hence it is factorized only once using a direct sparse linear solver and a forward-backward sweep is performed at each Quasi Newton iteration. In the above numerical experiments the sequential version of the direct sparse solver SuperLU (see e.g.[27, 46]) is used.

Communications between step 1 and 2: Step 1 sends to step 2 the normal velocities $u_{n,\sigma(i)}^{k,n}$ at the interface where $\sigma(i)$ is the one to one mapping between $i = 1, \dots, N_x$ and the set of edges \mathcal{E}_Γ . Step 2 sends to step 1 the normal velocities at the edges $\mathcal{E}_{int}^g \cup \mathcal{E}_{out}^g \cup \mathcal{E}_{in}^g$, as well as the pressure jumps at $\sigma(i)$, $i = 1, \dots, N_x$

$$(\mathbf{n} \cdot (\rho^g \mathbf{u} \otimes \mathbf{u} - \mu^g (\nabla \mathbf{u} + \nabla^t \mathbf{u}) \mathbf{n})_{\sigma(i)}^{n,k-1} = \rho^g (\tilde{v}_{i,N_y+\frac{1}{2}}^{n,k-1})^2 + 2\mu^g \frac{\tilde{v}_{i,N_y+\frac{1}{2}}^{n,k-1} - \tilde{v}_{i,N_y-\frac{1}{2}}^{n,k-1}}{\Delta y_{N_y}},$$

which in practice can be neglected.

In the following numerical experiments the non linear stopping criteria are fixed to

- $\epsilon_{Newton} = 10^{-7}$ for the relative l^2 norm of the residual of the non linear system (3.17-3.18-3.19),
- $\epsilon_{QuasiNewton} = 10^{-6}$ for the relative l^2 norm of the difference between two successive Quasi Newton iterates of the non linear system (3.20,3.21,3.22),
- $\epsilon_{FixedPoint} = 10^{-8}$ on $\|1 - \sum_{i \in \mathcal{C}} c_i\|_{l^\infty}$ for the fixed point iterations of the coupled problem.

In practice, it will suffice to set the stopping criterias $\epsilon_{QuasiNewton}$ and $\epsilon_{FixedPoint}$ to respectively 10^{-3} and 10^{-2} in order to obtain a good accuracy but our objective in the following tests is to assess the convergence of the Quasi Newton and Fixed Point algorithms.

3.4.2 Andra test case with an horizontal gallery

The setting of this test case is exhibited in Figure 3.2. The porous medium domain $\Omega^p = (0, L) \times (H_1, H_2)$, with $H_1 = 5$ m and $H_2 = 15$ m, includes two rocktypes. The concrete rocktype in the domain $(0, L) \times (H_1, H_1 + 1)$ is defined by the Van-Genuchten parameters $n = 1.54$, $s_r^l = 0.01$, $s_r^g = 0$, $P_r = 2 \cdot 10^6$ Pa, the isotropic permeability $\mathbf{K} = 10^{-18}$ m² and the porosity $\phi = 0.3$. The COx rocktype in the domain $(0, L) \times (H_1 + 1, H_2)$ is defined by the Van-Genuchten parameters $n = 1.49$, $s_r^l = 0.4$, $s_r^g = 0$, $P_r = 15 \cdot 10^6$ Pa, the isotropic permeability $\mathbf{K} = 5 \cdot 10^{-20}$ m², and the porosity $\phi = 0.15$. The initial and top boundary liquid pressure in the porous medium is set to $p_{init}^l = 40 \cdot 10^5$ Pa, and the temperature is fixed to $T_e = 303$ K both in the porous medium and in the gallery. The initial and input relative humidity in the gallery is fixed to $H_{r,init} = 0.5$ and the output

and initial pressure in the gallery to $p_{init} = p_{out} = 10^5$ Pa.

In the following tests, we evaluate the influence of the input velocity w_{in} and of the length L of the gallery on the mean relative humidity in the gallery and on the mean evaporation rate at the interface. The input velocity w_{in} is set to 0.05, 0.5 or 5 m. s⁻¹, and the length L is set to 25, 100 or 400 m. The simulation is run over a period of 200 years, chosen large enough to reach the stationary state (see subsection 2.4.1 for a description of the stationary state).

To assess the numerical convergence of the discrete solutions, a family of Cartesian meshes are tested with increasing sizes set to $Nx \times Ny = 25 \times 50$, 50×100 , 100×200 , and 200×400 . All these meshes are uniform in the x direction and are refined in the direction y on both sides of the interface Γ as well as at the COx and concrete rocktypes interface $y = H_1 + 1$. To fix ideas, the sizes of the first cells at both sides of the interface Γ are set to δy_1 in the gallery side and to δy_2 in the porous medium side with $(\delta y_1, \delta y_2)$ in meters equal to $(1.62 \cdot 10^{-2}, 6.95 \cdot 10^{-3})$, $(7.09 \cdot 10^{-3}, 3.06 \cdot 10^{-3})$, $(3.32 \cdot 10^{-3}, 1.44 \cdot 10^{-3})$, and $(1.61 \cdot 10^{-3}, 6.96 \cdot 10^{-4})$ for respectively the meshes 25×50 , 50×100 , 100×200 , and 200×400 . Note that, with these values of δy_1 on the gallery side, the meshes are refined down to the scale of the laminar boundary layer.

In order to understand the following numerical results, we need to have in mind the orders of magnitude at the interface Γ of the molar fractions which are such that $c_a^l \ll c_e^l$, $c_e^g \ll c_a^g$, $c_e \ll c_a$, and of the molar gas and liquid Darcy fluxes which are such that $|\mathbf{V}^g \cdot \mathbf{n}| \ll |\mathbf{V}^l \cdot \mathbf{n}|$.

It follows that, at the interface Γ , the water component convective flux $\zeta^g c_e \mathbf{u} \cdot \mathbf{n}$ is small compared to the water component diffusive flux $-\zeta^g D^g \nabla c_e \cdot \mathbf{n}$ with a ratio roughly equal to c_e . This can be checked numerically in Figure 3.3 plotting the mean water component convective and diffusion fluxes at the interface as a function of time.

Using this remark, we can explain the shape of the mean evaporation rate at the interface as a function of time exhibited in Figure 3.9. It classically includes two stages characterized for the first stage by a roughly constant evaporation rate followed for the second stage by a decrease of the evaporation rate down to the stationary state. It is also known that the evaporation rate of the first stage weakly depends on the properties of the porous medium but the duration of the stage does depends on the porous medium properties. This first stage actually corresponds to a value of the water component molar fraction c_e at the interface roughly equal to $\frac{P_{sat}(T_e)}{p_{out}}$ (relative humidity H_r equal to 1) due to a relatively large water influx in the gallery. Using this Dirichlet boundary condition and the previous remark, the value of the water influx can be roughly computed from the

solution c_e of the stationary convection diffusion equation in the gallery

$$\left\{ \begin{array}{ll} \operatorname{div}(\mathbf{u}_t c_e - (D^g + D_t) \nabla c_e) = 0 & \text{on } \Omega^g, \\ c_e = \frac{P_{sat}(T_e)}{p_{out}} & \text{on } \Gamma, \\ c_e = c_{in} & \text{on } \Gamma_{in}^g, \\ \nabla c_e \cdot \mathbf{n} = 0 & \text{on } \Gamma_{out}^g \cup \Gamma_N^g. \end{array} \right. \quad (3.23)$$

which roughly corresponds to the value observed in Figure 3.9 away from a short transient state. Once the porous medium is sufficiently dried at the interface, the water influx starts to decrease down to a much lower stationary state (case of a top boundary bringing water in the porous medium). This decreasing phase corresponds to the second stage of the drying process.

Similarly, as shown in Figure 3.8, after a rapid transient increase, the relative humidity in the gallery is roughly constant during the first stage with a value which can be computed from the solution c_e of (3.23). Then, it decreases down to the stationary state during the second stage. An approximate value of the stationary relative humidity in the gallery has been computed in subsection 2.4.1.

These two stages of the simulation and the final stationary state can also be observed in Figure 3.5 which shows at different times the gas saturation in the porous medium and the water molar fraction in the gallery.

Figures 3.6 and 3.7 show the velocities \tilde{u} , u and $v = \tilde{v}$ at the first stage of the drying process. It is observed that the x component of the velocity is slowed down by the coupling in a neighbourhood of the interface Γ .

Figures 3.8, 3.9 exhibit the good convergence in space of the gas volume in the porous medium, of the relative humidity in the gallery, of the mean gas velocity and of the mean evaporation rate at the interface. Tables 3.1-3.5 show the numerical behavior of the simulations for various choices of the length of the gallery L and of the input velocity w_{in} and for the four meshes. We can observe a good scalability of the Newton and Quasi Newton non linear solvers and a good convergence of the fixed point iterations with roughly two or three fixed point iterations by time step (see also Figure 3.4).

Finally, Figures 3.10-3.15 exhibit the comparison of the relative humidity, the evaporation rate at the interface and the gas volume in the porous medium obtained for the 2D-2D and the reduced 2D-1D models for various values of the length L and of the input velocity w_{in} . It is clear that the larger the length the better the approximation provided by the reduced model. In all cases, the reduced model provides a good order of magnitude of all quantities of interest.

Figure 3.16 clearly shows that the solutions of the sequential algorithm, obtained with a single fixed point iteration, and of the converged fixed point algorithm can hardly be distinguished.

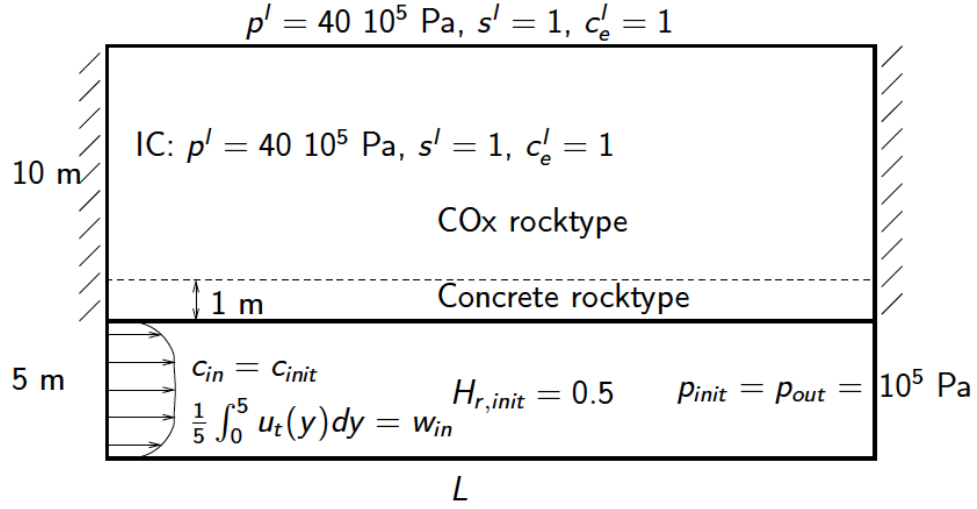


Figure 3.2: Setting of the Andra test case with an horizontal gallery.

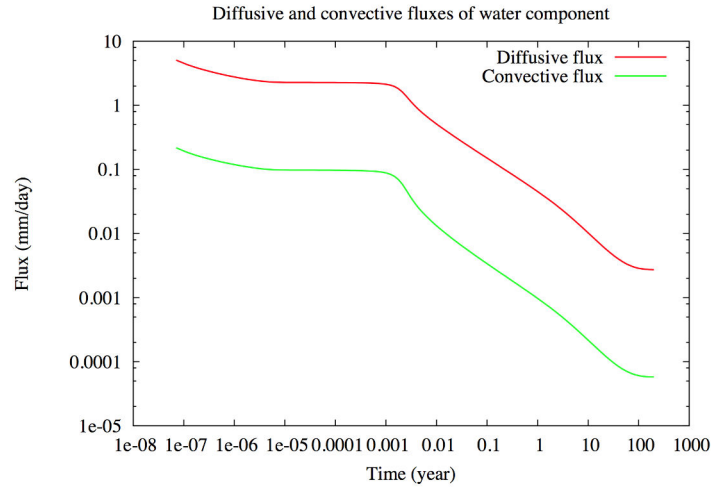


Figure 3.3: Mean diffusive and convective fluxes of the water component at the interface as a function of time with $L = 100 \text{ m}$, $w_{in} = 0.5 \text{ m.s}^{-1}$ and the mesh 100×200 .

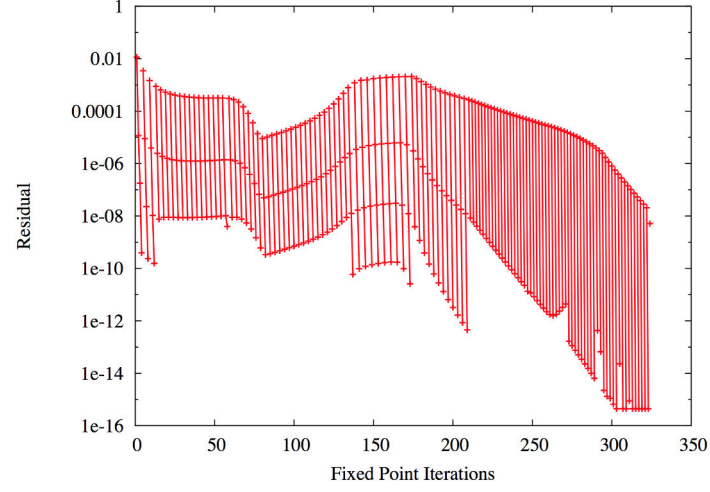


Figure 3.4: Convergence of the residual $\|1 - \sum_{i \in \mathcal{C}} c_i\|_{L^\infty(\Omega^g)}$ of the fixed point iterations for all time steps with $L = 100$ m, $w_{in} = 0.5$ m.s⁻¹ and with the mesh 100×200 .

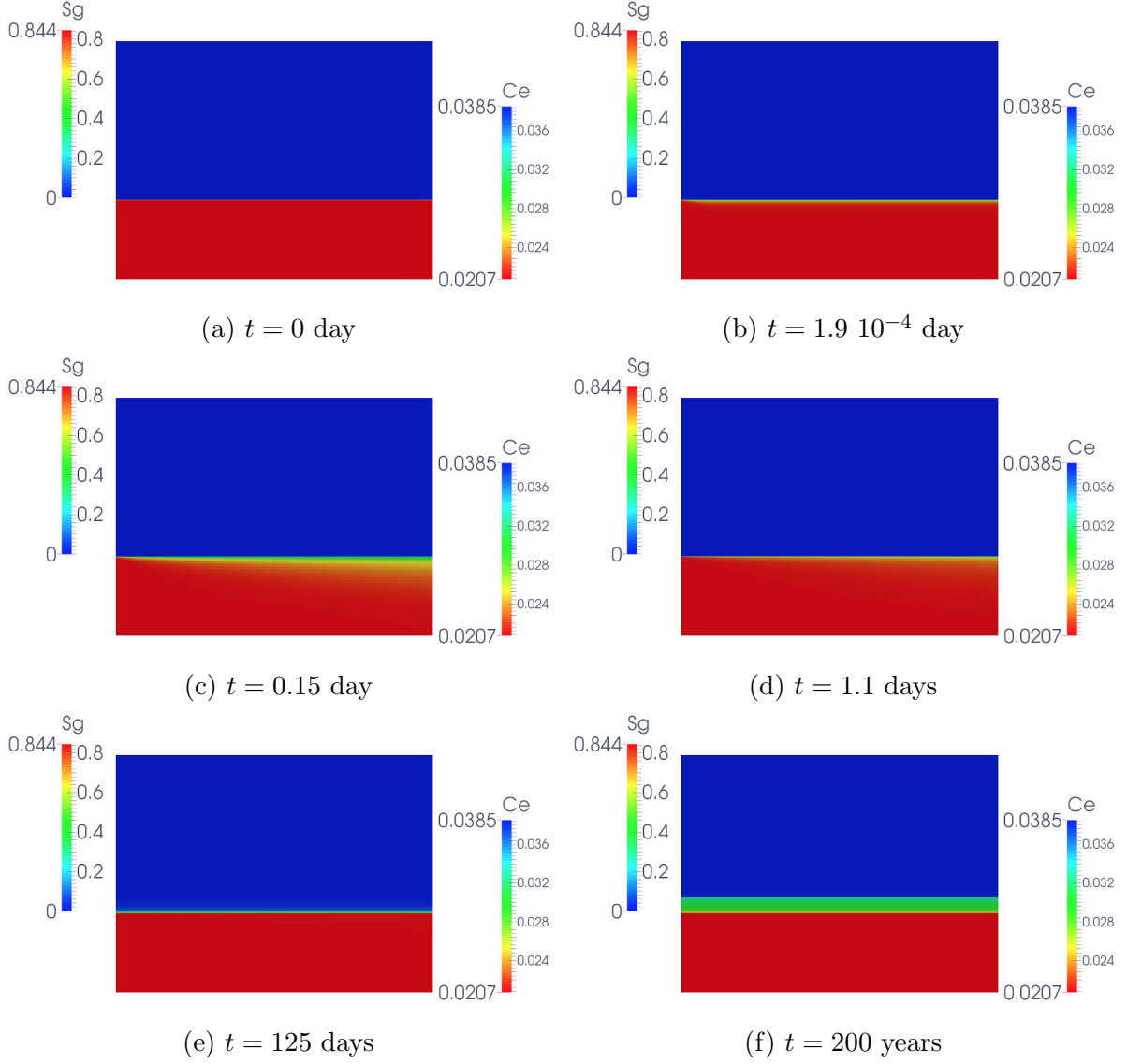


Figure 3.5: Gas saturation in the porous medium and water molar fraction in the gallery with $L = 100$ m, $w_{in} = 0.5$ m.s⁻¹ and the mesh 100×200 at (a) $t = 0$ day, (b) $t = 1.9 \cdot 10^{-4}$ day, (c) $t = 0.15$ day, (d) $t = 1.1$ days, (e) $t = 125$ days, (f) $t = 200$ years.

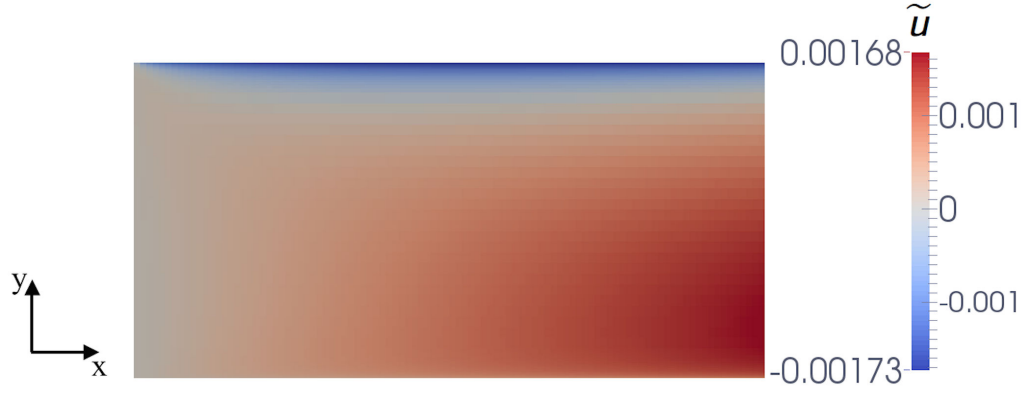


Figure 3.6: Perturbation \tilde{u} of the x component of the gas velocity at the first stage of the drying process obtained with $L = 100$ m, $w_{in} = 0.5$ m.s $^{-1}$ and with the mesh 100×200 .

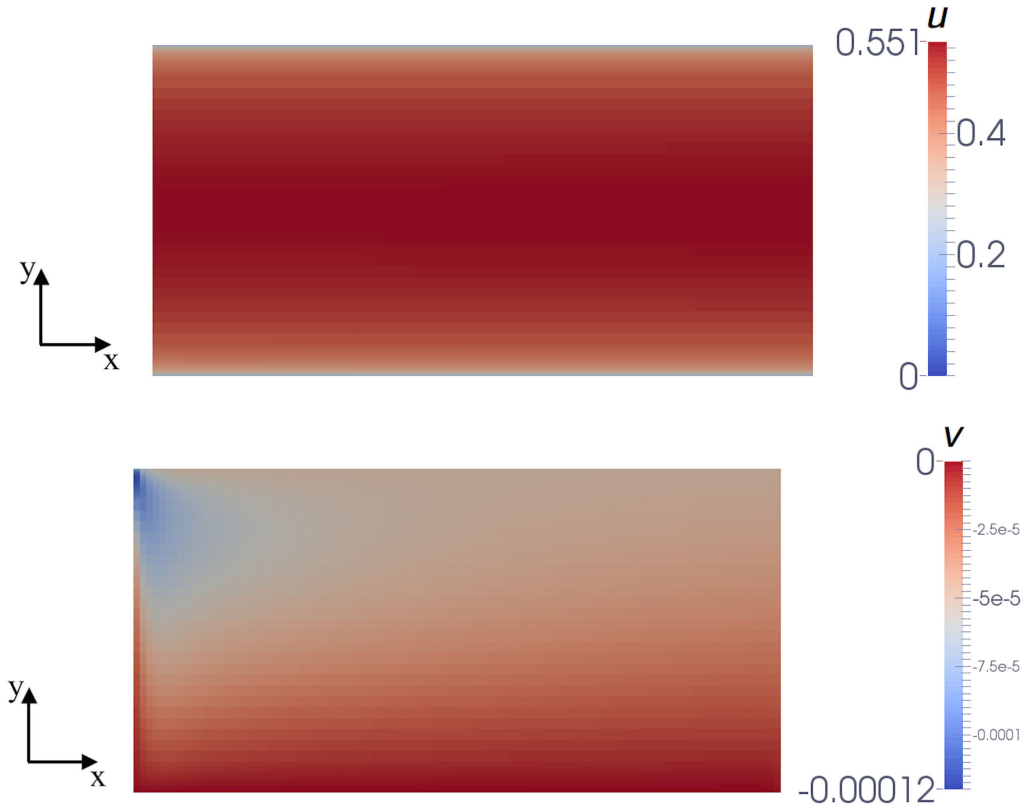


Figure 3.7: Gas velocities u (above) and $v = \tilde{v}$ (below) at the first stage of the drying process obtained with $L = 100$ m, $w_{in} = 0.5$ m.s $^{-1}$ and with the mesh 100×200 .

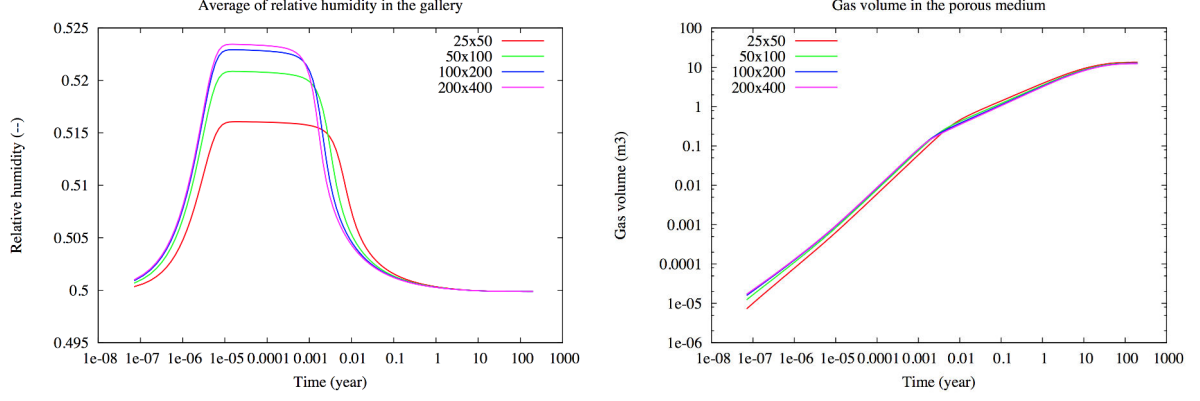


Figure 3.8: For each mesh and for $L = 100$ m, $w_{in} = 0.5 \text{ m.s}^{-1}$: average of the relative humidity in the gallery (left) and gas volume in the porous medium (right) as a function of time.

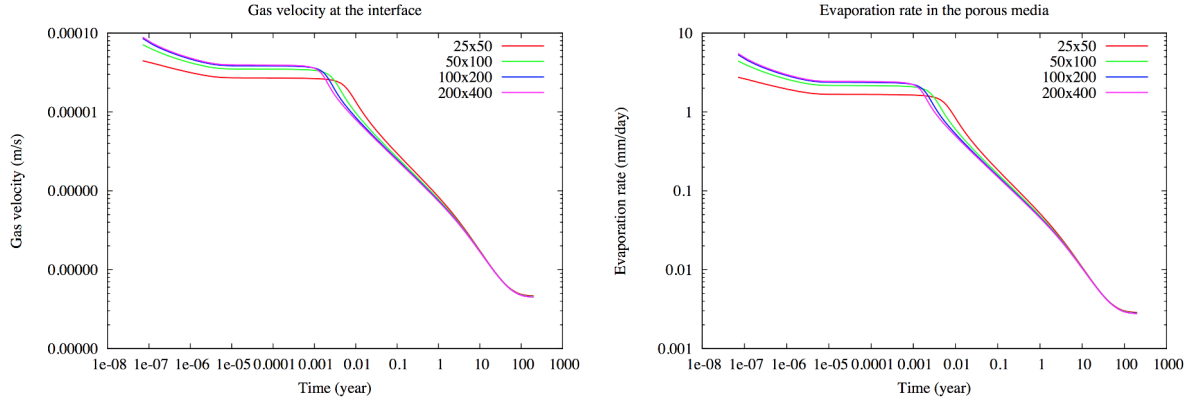


Figure 3.9: For each mesh and for $L = 100$ m, $w_{in} = 0.5 \text{ m.s}^{-1}$: average of the gas velocity at the interface (left) and evaporation rate at the interface (right) as a function of time.

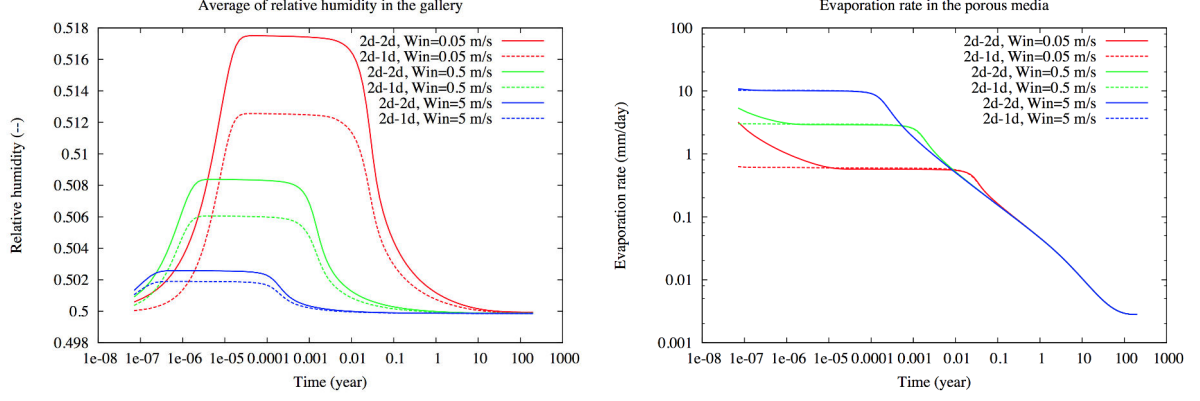


Figure 3.10: Comparison of the solutions obtained by the 2d-2d and 2d-1d models with $L = 25$ m and the mesh 100×200 : average of relative humidity in the gallery (left), evaporation rate at the interface (right) as a function of time.

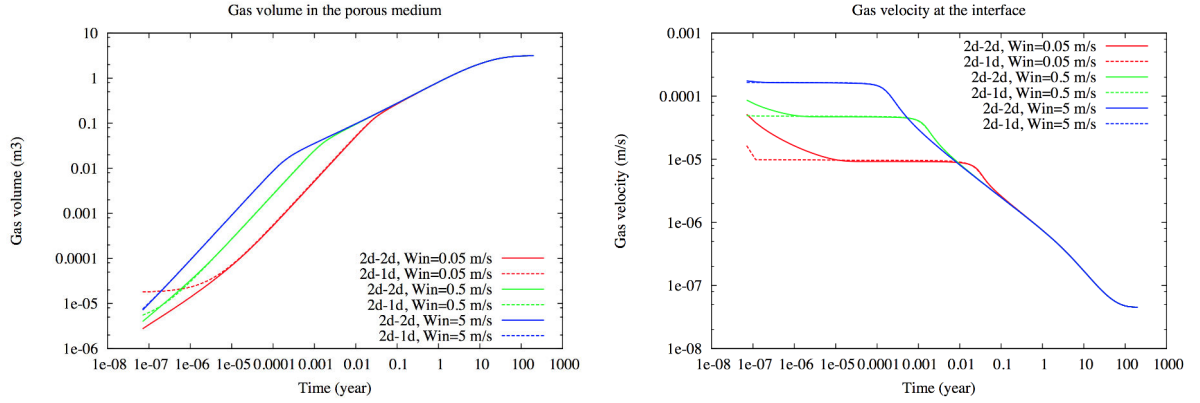


Figure 3.11: Comparison of the solutions obtained by the 2d-2d and 2d-1d models with $L = 25$ m and the mesh 100×200 : gas volume in porous medium (left), average of the gas velocity at the interface (right) as a function of time.

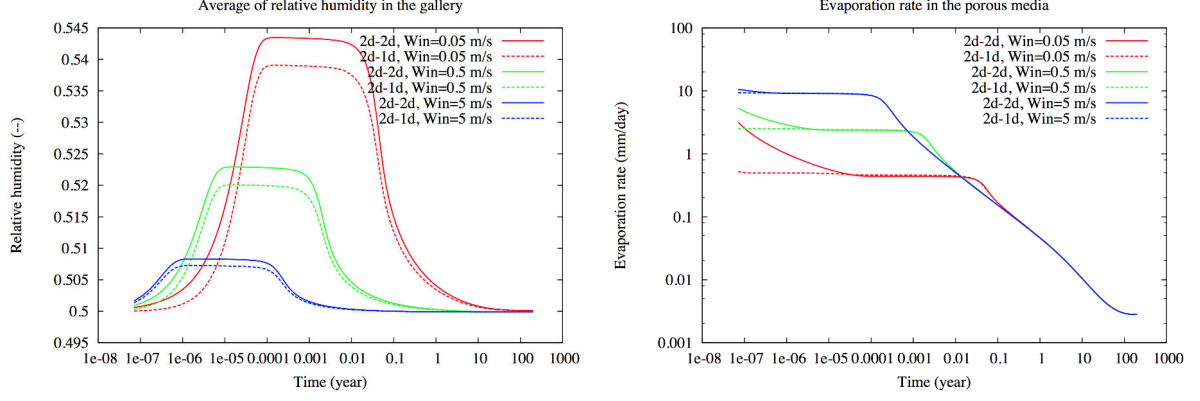


Figure 3.12: Comparison of the solutions obtained by the 2d-2d and 2d-1d models with $L = 100$ m and the mesh 100×200 : average of the relative humidity in the gallery (left), evaporation rate at the interface (right) as a function of time.

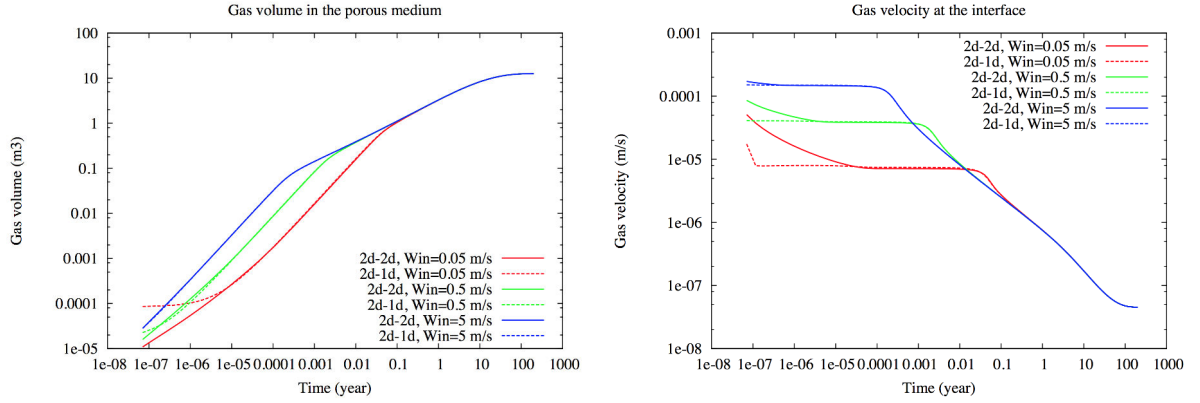


Figure 3.13: Comparison of the solutions obtained by the 2d-2d and 2d-1d models with $L = 100$ m and the mesh 100×200 : gas volume in porous medium (left), average of the gas velocity at the interface (right) as a function of time.

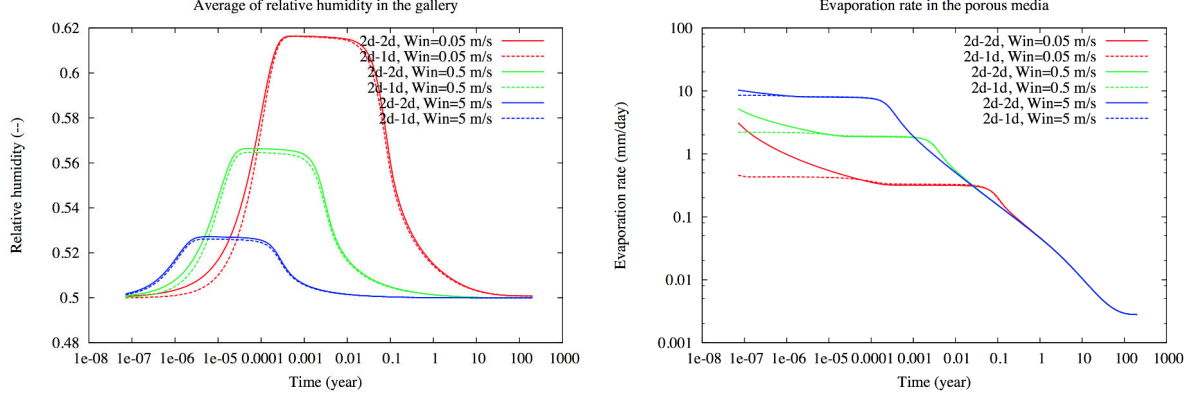


Figure 3.14: Comparison of the solutions obtained by the 2d-2d and 2d-1d models with $L = 400$ m and the mesh 100×200 : average of the relative humidity in the gallery (left), evaporation rate at the interface (right) as a function of time.

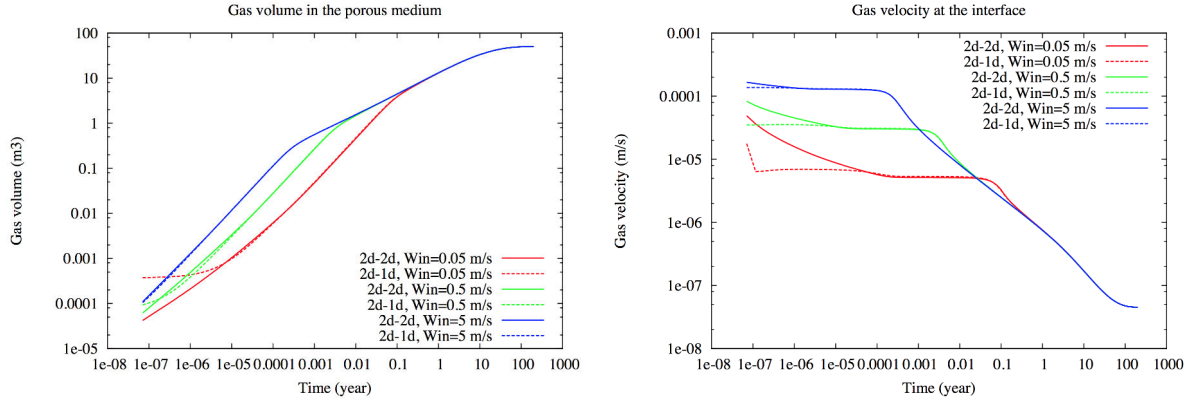


Figure 3.15: Comparison of the solutions obtained by the 2d-2d and 2d-1d models with $L = 400$ m and the mesh 100×200 : gas volume in porous medium (left), average of the gas velocity at the interface (right) as a function of time.

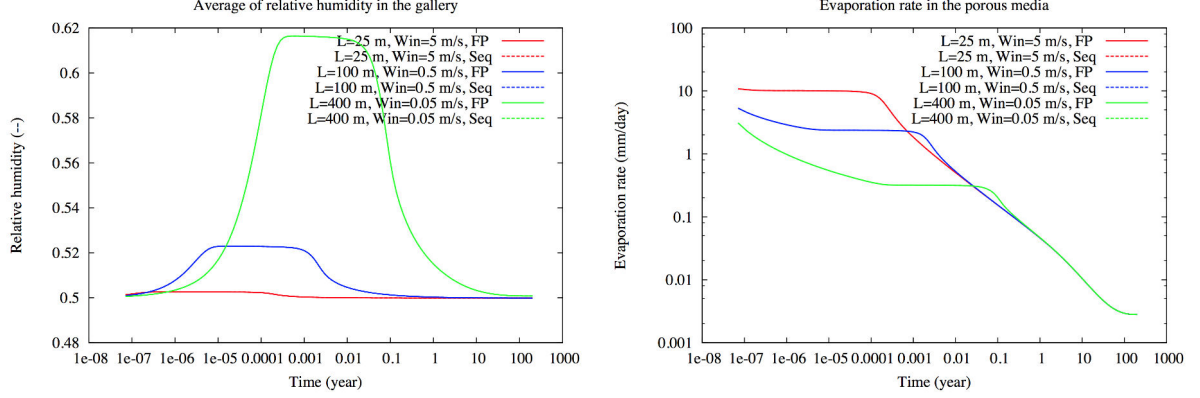


Figure 3.16: Comparison of the solutions obtained by the fixed-point (FP) and sequential (Seq) algorithms with the mesh 100×200 : average of the relative humidity in the gallery (left), evaporation rate at the interface (right) as a function of time.

We present in Tables 3.1 – 3.5 the numerical behavior of the simulations with different choices of L and w_{in} and for the four meshes:

(i) $L = 25$ m, $w_{in} = 5$ m.s $^{-1}$

<i>meshes</i>	$N_{\Delta t}$	N_{Chop}	N_{Newton}	N_{Pt}	N_{NVS}	CPU(s)	α_{CPU}
25×50	123	0	504	239	435	7.56	
50×100	123	0	527	257	480	48.64	1.34
100×200	123	0	552	277	525	388.47	1.50
200×400	123	0	582	287	552	3279.18	1.54

Table 3.1: For each mesh: number $N_{\Delta t}$ of successful time steps, number N_{Chop} of time step chops, number N_{Newton} of Newton iterations, number N_{Pt} of fixed point iterations, number N_{NVS} of quasi-newton iterations, CPU time in seconds, and scaling of CPU time (α_{CPU}) by $CPU \sim \text{cells}^{\alpha_{CPU}}$.

(ii) $L = 100$ m, $w_{in} = 5$ m.s $^{-1}$

<i>meshes</i>	$N_{\Delta t}$	N_{Chop}	N_{Newton}	N_{Pt}	N_{NVS}	CPU(s)	α_{CPU}
25×50	123	0	509	244	448	7.51	
50×100	123	0	543	266	499	49.79	1.36
100×200	123	0	564	284	538	409.81	1.52
200×400	123	0	593	290	556	4144.73	1.67

Table 3.2: For each mesh: number $N_{\Delta t}$ of successful time steps, number N_{Chop} of time step chops, number N_{Newton} of Newton iterations, number N_{Pt} of fixed point iterations, number N_{NVS} of quasi-newton iterations, CPU time in seconds, and scaling of CPU time (α_{CPU}) by $CPU \sim \text{cells}^{\alpha_{CPU}}$.

(iii) $L = 100$ m, $w_{in} = 0.5$ m.s⁻¹

<i>meshes</i>	$N_{\Delta t}$	N_{Chop}	N_{Newton}	N_{Pt}	N_{NVS}	CPU(s)	α_{CPU}
25×50	123	0	591	305	590	8.60	
50×100	123	0	636	315	615	58.86	1.39
100×200	123	0	690	324	634	486.11	1.52
200×400	123	0	753	343	661	4505.81	1.61

Table 3.3: For each mesh: number $N_{\Delta t}$ of successful time steps, number N_{Chop} of time step chops, number N_{Newton} of Newton iterations, number N_{Pt} of fixed point iterations, number N_{NVS} of quasi-newton iterations, CPU time in seconds, and scaling of CPU time (α_{CPU}) by $CPU \sim \text{cells}^{\alpha_{CPU}}$.

(iv) $L = 400$ m, $w_{in} = 5$ m.s⁻¹

<i>meshes</i>	$N_{\Delta t}$	N_{Chop}	N_{Newton}	N_{Pt}	N_{NVS}	CPU(s)	α_{CPU}
25×50	123	0	517	249	459	7.56	
50×100	123	0	599	278	520	55.76	1.44
100×200	123	0	628	292	553	460.47	1.52
200×400	123	0	652	291	557	5625.77	1.81

Table 3.4: For each mesh: number $N_{\Delta t}$ of successful time steps, number N_{Chop} of time step chops, number N_{Newton} of Newton iterations, number N_{Pt} of fixed point iterations, number N_{NVS} of quasi-newton iterations, CPU time in seconds, and scaling of CPU time (α_{CPU}) by $CPU \sim \text{cells}^{\alpha_{CPU}}$.

(v) $L = 400$ m, $w_{in} = 0.05$ m.s⁻¹

longer be valid even during the first stage of the drying process. Hence it is a good test case to challenge the reduced 2D-1D model.

The simulation is run over a period of 50 years with an initial time step of 1 s and a maximum time step of 10 years. The numerical solutions are obtained with the meshes $Ny \times Nx = 25 \times 73$, 50×143 , 100×283 , which are refined on both sides of the interface Γ as in the previous test case.

Figures 3.23-3.24 and 3.18 show as expected that the evaporation rate and the relative humidity are no longer constant during the first stage of the drying process due to the heterogeneity of the permeability along the gallery. Figure 3.20 also clearly shows the influence of the two different permeabilities along the gallery on the evaporation rate and on the desaturation of the porous medium. We see that the desaturation front propagates at different time scales in the two rocktype regions.

Figures 3.25-3.26 still exhibit a good match between the 2D-2D and the reduced 2D-1D models. However, as expected, it is not as good as in the previous test case.

Figure 3.27 exhibits as previously that the solutions of the sequential and converged fixed point algorithms are basically the same.

Tables 3.6-3.8 and Figure 3.19 exhibit, as in the previous test case, the good numerical behavior and scalability of the non linear solvers.

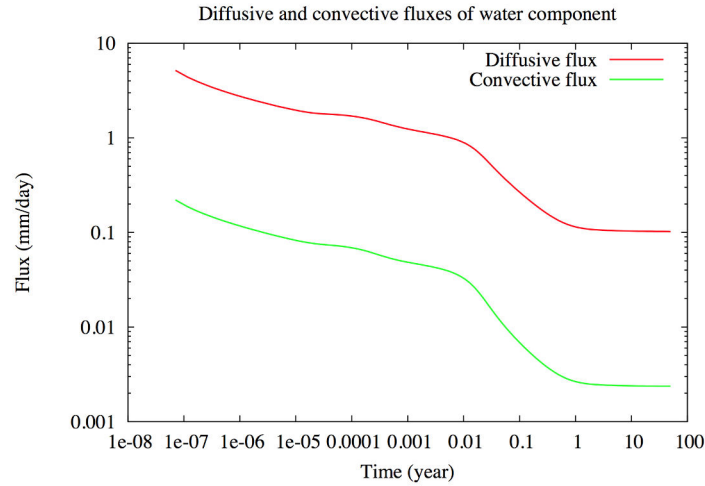


Figure 3.18: Mean diffusive and convective fluxes of water component at the interface as a function of time with $w_{in} = 0.5 \text{ m.s}^{-1}$ and the mesh 100×283 .

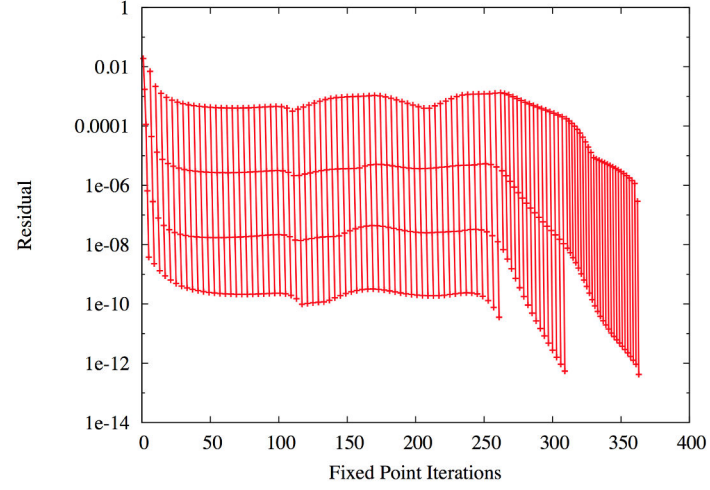


Figure 3.19: Convergence of the residual $\|1 - \sum_{i \in \mathcal{C}} c_i\|_{L^\infty(\Omega^g)}$ of the fixed point iterations for all time steps with $w_{in} = 0.5 \text{ m.s}^{-1}$ and with the mesh 100×283 .

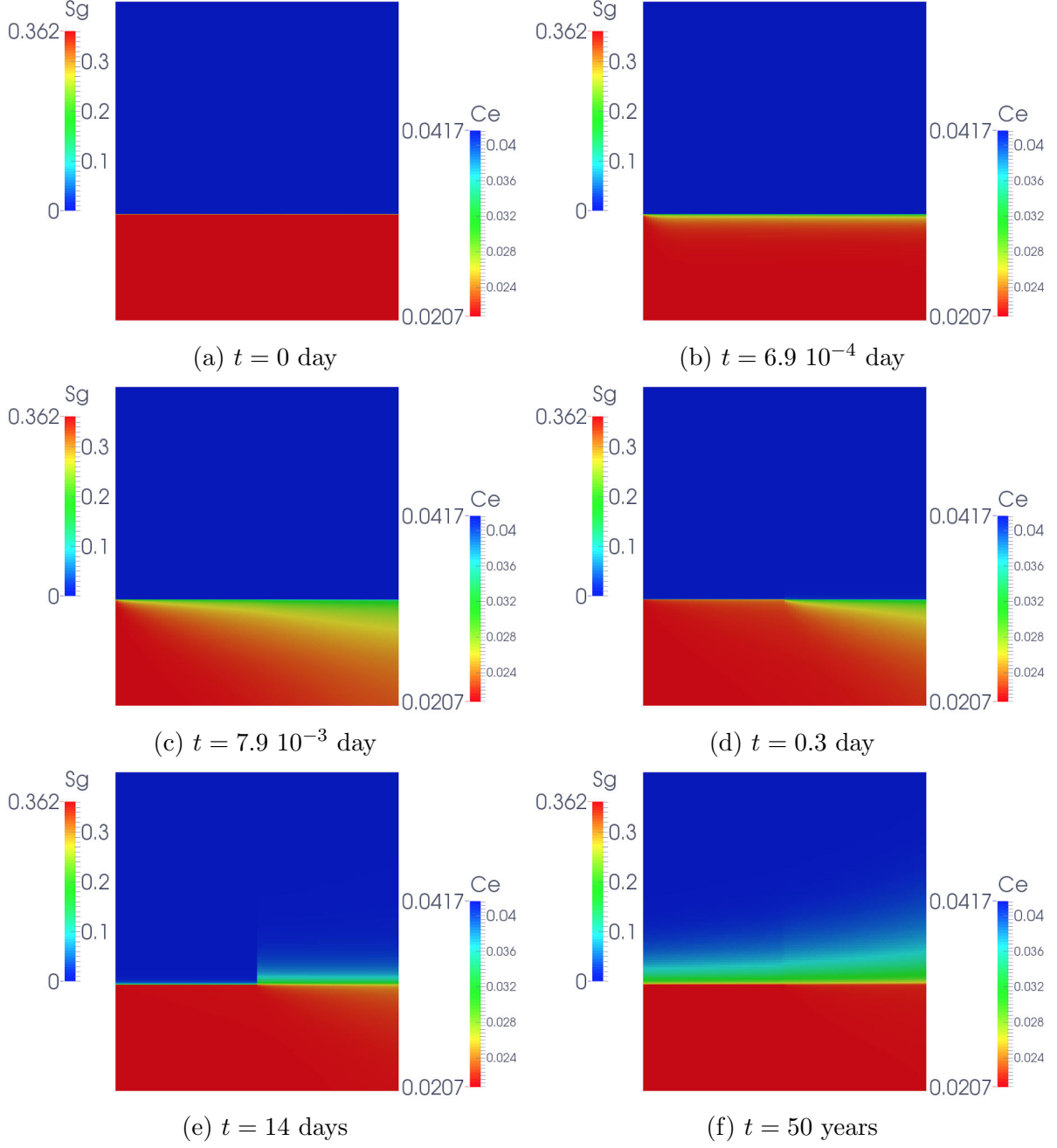


Figure 3.20: Gas saturation in the porous medium and water molar fraction in the gallery with $w_{in} = 0.5 \text{ m.s}^{-1}$ and the mesh 100×283 at (a) $t = 0$ day, (b) $t = 6.9 \cdot 10^{-4}$ day, (c) $t = 7.9 \cdot 10^{-3}$ day, (d) $t = 0.3$ day, (e) $t = 14$ days, (f) $t = 50$ years.

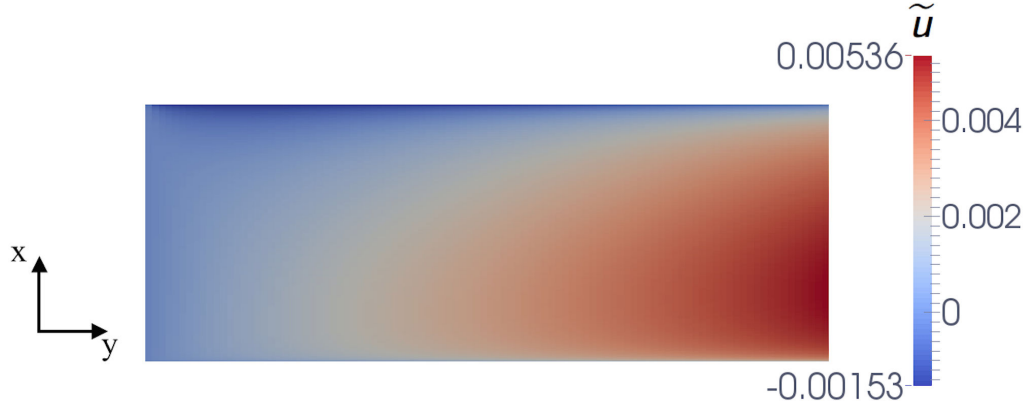


Figure 3.21: Perturbation \tilde{u} of the x component of the gas velocity at the first stage of the drying process obtained with $w_{in} = 0.5 \text{ m.s}^{-1}$ and with the mesh 100×283 .

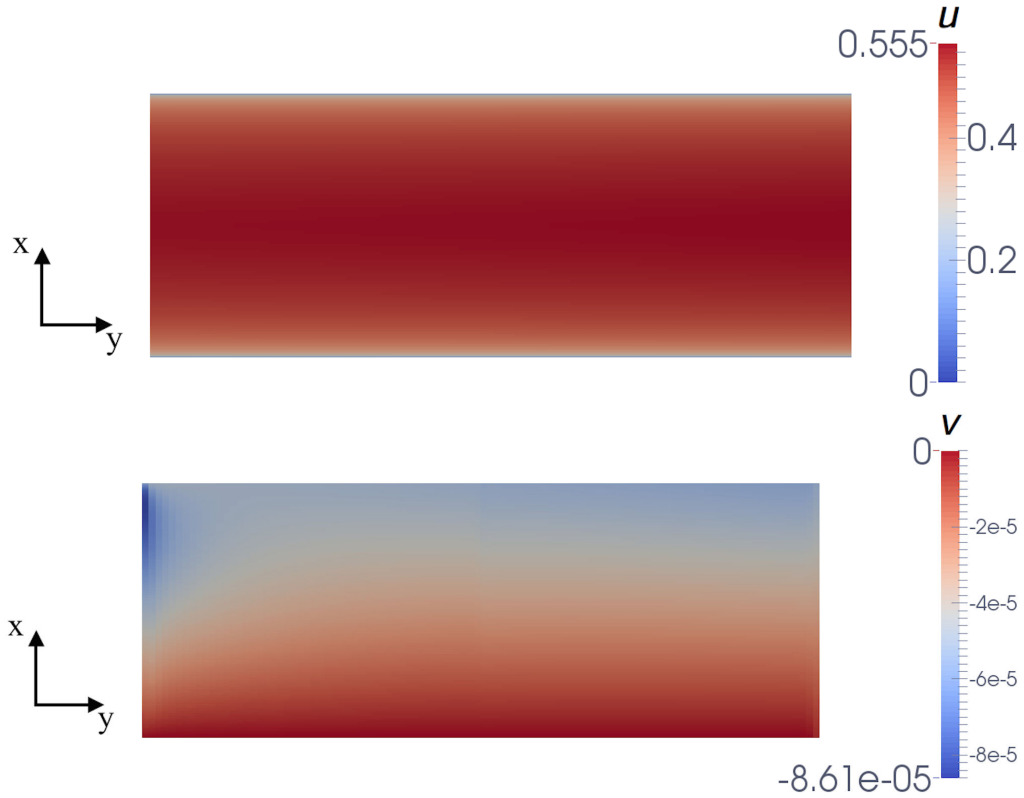


Figure 3.22: Gas velocities u (above) and $v = \tilde{v}$ (below) at the first stage of the drying process obtained with $w_{in} = 0.5 \text{ m.s}^{-1}$ and with the mesh 100×283 .

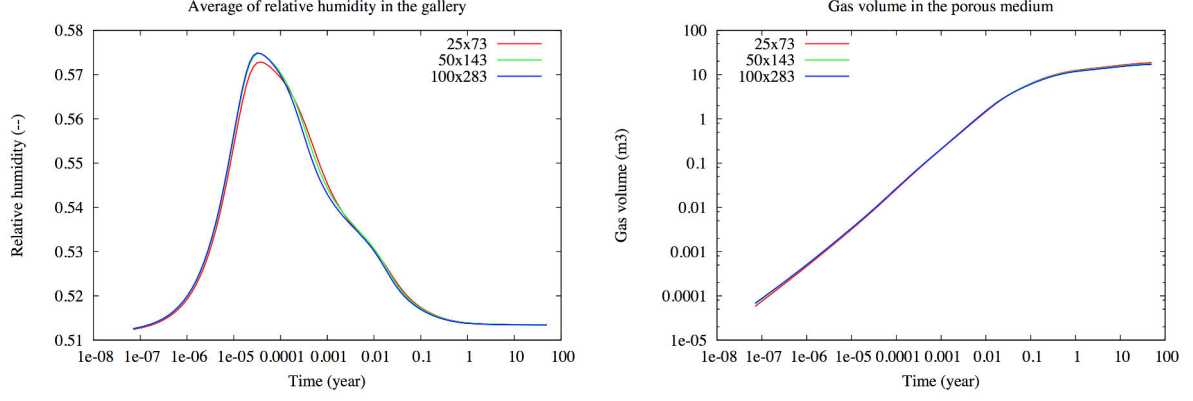


Figure 3.23: For each mesh and for $w_{in} = 0.5 \text{ m.s}^{-1}$: average of the relative humidity in the gallery (left) and gas volume in the porous medium (right) as a function of time.

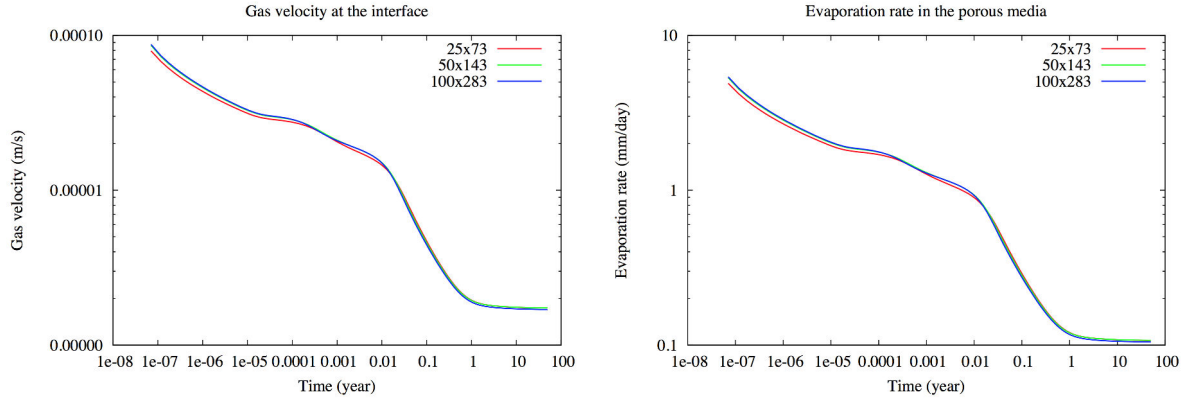


Figure 3.24: For each mesh and for $w_{in} = 0.5 \text{ m.s}^{-1}$: average of the gas velocity at the interface (left) and evaporation rate at the interface (right) as a function of time.

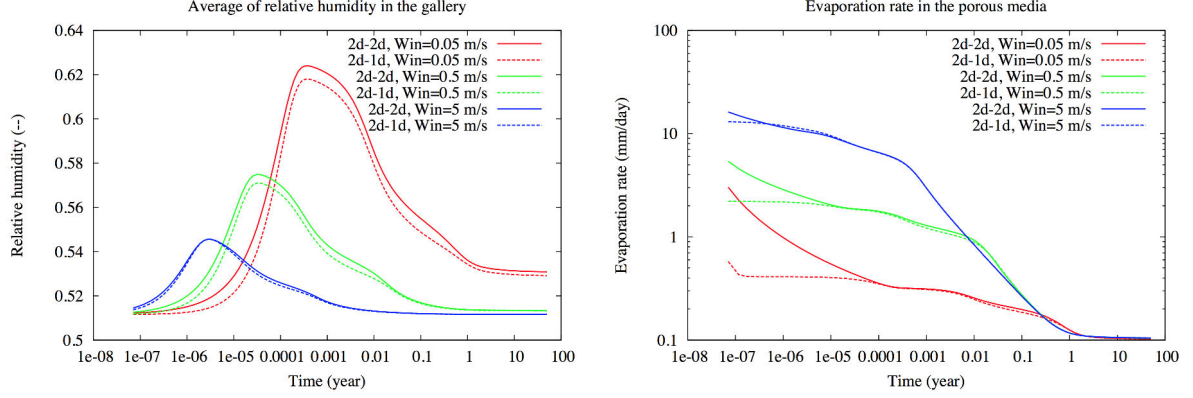


Figure 3.25: Comparison of the solutions obtained by the 2d-2d and 2d-1d models with the mesh 100×283 : average of the relative humidity in the gallery (left), evaporation rate at the interface (right) as a function of time.

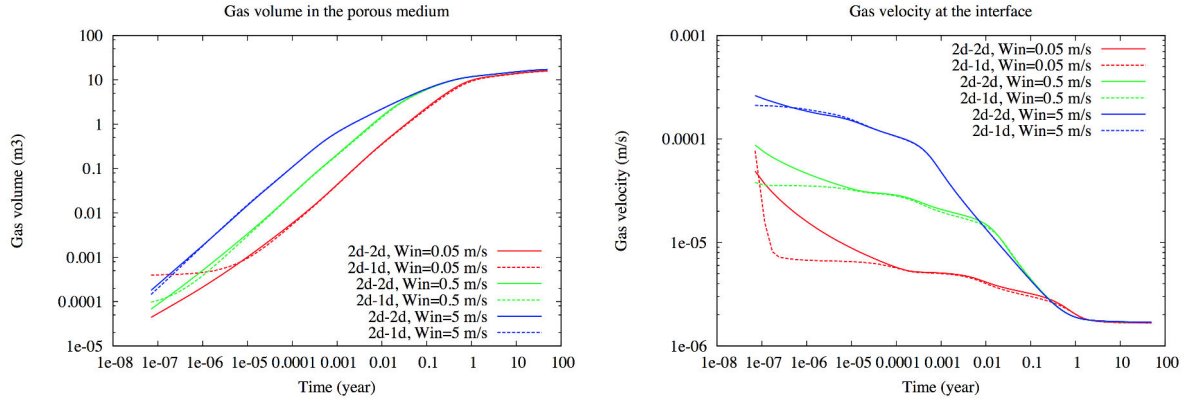


Figure 3.26: Comparison of the solutions obtained by the 2d-2d and 2d-1d models with the mesh 100×283 : gas volume in porous medium (left), average of the gas velocity at the interface (right) as a function of time.

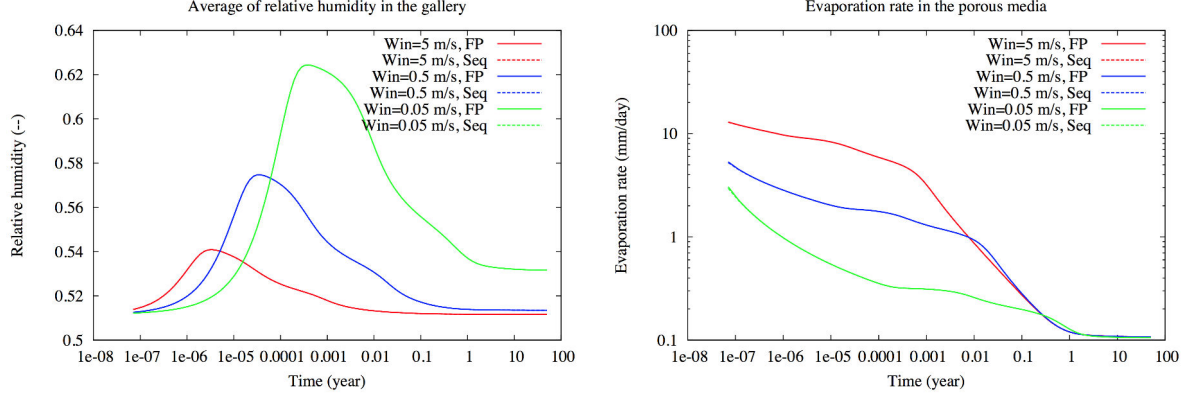


Figure 3.27: Comparison of the solutions obtained by the fixed-point (FP) and sequential (Seq) algorithms with the mesh 50×143 : average of the relative humidity in the gallery (left), evaporation rate at the interface (right) as a function of time.

We present in Tables 3.6 – 3.8 the numerical behavior of the simulations with different choices of w_{in} and for the three meshes:

(i) $w_{in} = 0.05 \text{ m.s}^{-1}$

<i>meshes</i>	$N_{\Delta t}$	N_{Chop}	N_{Newton}	N_{Pt}	N_{NVS}	CPU(s)	α_{CPU}
25×73	108	0	882	397	765	18.57	
50×143	108	0	963	406	805	123.43	1.39
100×283	108	0	1054	407	810	1155.48	1.63

Table 3.6: For each mesh: number $N_{\Delta t}$ of successful time steps, number N_{Chop} of time step chops, number N_{Newton} of Newton iterations, number N_{Pt} of fixed point iterations, number N_{NVS} of quasi-newton iterations, CPU time in seconds, and scaling of CPU time (α_{CPU}) by $CPU \sim \text{cells}^{\alpha_{CPU}}$.

(ii) $w_{in} = 0.5 \text{ m.s}^{-1}$

<i>meshes</i>	$N_{\Delta t}$	N_{Chop}	N_{Newton}	N_{Pt}	N_{NVS}	CPU(s)	α_{CPU}
25×73	108	0	759	328	619	15.63	
50×143	108	0	857	359	662	106.65	1.41
100×283	108	0	960	362	685	936.90	1.58

Table 3.7: For each mesh: number $N_{\Delta t}$ of successful time steps, number N_{Chop} of time step chops, number N_{Newton} of Newton iterations, number N_{Pt} of fixed point iterations, number N_{NVS} of quasi-newton iterations, CPU time in seconds, and scaling of CPU time (α_{CPU}) by $CPU \sim \text{cells}^{\alpha_{CPU}}$.

(iii) $w_{in} = 5 \text{ m.s}^{-1}$

<i>meshes</i>	$N_{\Delta t}$	N_{Chop}	N_{Newton}	N_{Pt}	N_{NVS}	CPU(s)	α_{CPU}
25×73	108	0	595	278	539	12.59	
50×143	108	0	648	278	540	85.77	1.41
100×283	108	0	706	288	551	760.54	1.59

Table 3.8: For each mesh: number $N_{\Delta t}$ of successful time steps, number N_{Chop} of time step chops, number N_{Newton} of Newton iterations, number N_{Pt} of fixed point iterations, number N_{NVS} of quasi-newton iterations, CPU time in seconds, and scaling of CPU time (α_{CPU}) by $CPU \sim \text{cells}^{\alpha_{CPU}}$.

3.4.4 Drying test case

In this test case exhibited in Figure 3.28, we consider the drying by convection of an homogeneous porous medium $\Omega^p = (0, L) \times (H_1, H_2)$ with $L = 1 \text{ m}$, $H_1 = 0.5 \text{ m}$, $H_2 = 1.5 \text{ m}$. The Porous medium is assumed to be closed at the lateral boundaries Γ_N^p and at the top boundary Γ_D^p . The rocktype is defined by the Van-Genuchten parameters $n = 4$, $s_r^l = s_r^g = 0$, $P_r = 15 \cdot 10^3 \text{ Pa}$, the isotropic permeability $\mathbf{K} = \mathbf{10}^{-12} \text{ m}^2$ and the porosity $\phi = 0.15$. The temperature is fixed to a rather high value $T_e = 333 \text{ K}$ in order to increase the liquid evaporation rate. Consequently the water molar fraction at a relative humidity equal to 1 is not so small any more and the water convection flux at the interface is not so negligible anymore compared with the water diffusive flux as exhibited in Figure 3.29.

The simulation is run over a period of 100 days with an initial time step of 10^{-4} s and a maximum time step of 1 day. The numerical solutions are obtained with the meshes $Nx \times Ny = 25 \times 73$, 50×143 , 100×283 , which are, as for the first test case, refined on both sides of the interface Γ to capture the steep gradient of the liquid pressure on the porous medium side and the laminar boundary layer on the gallery side.

Compared with the Andra test case of subsection 3.4.2, we can observe two main differences. First, the comparison of the 2D-2D and reduced 2D-1D models exhibited in Figures 3.36-3.37 shows as expected not such a good match for the relative humidity. This is due to the fact that the 1D flow assumption in the gallery is of course no longer verified. On the other hand the evaporation rate, the gas velocity and the gas volume still exhibit a very good match. This shows that the approximation provided by the boundary layer thickness model is still good.

Second, the effect of the gravity in the porous medium gas flow is very clear in Figure 3.31 which exhibits the gas rise up to the closed top boundary. For the horizontal Andra test case, the effect of the gravity was small due to the dominant capillary forces.

Figures 3.34-3.35 show that the spatial convergence is almost achieved for the coarsest mesh due to the strong refinement at the interface Γ . Figure 3.38 exhibits as before that the sequential algorithm provides basically the same accuracy than the converged fixed

point algorithm. The numerical behavior given by Tables 3.9-3.10 is still very good. We observe a small number of time step failures due to a non convergence of the Newton solver at the first step of the fixed point algorithm. It could probably be improved using another formulation for the Darcy flow since, as shown in Chapter 1, the phase pressures and component fugacities formulation is not very efficient when the capillary forces are not dominant.

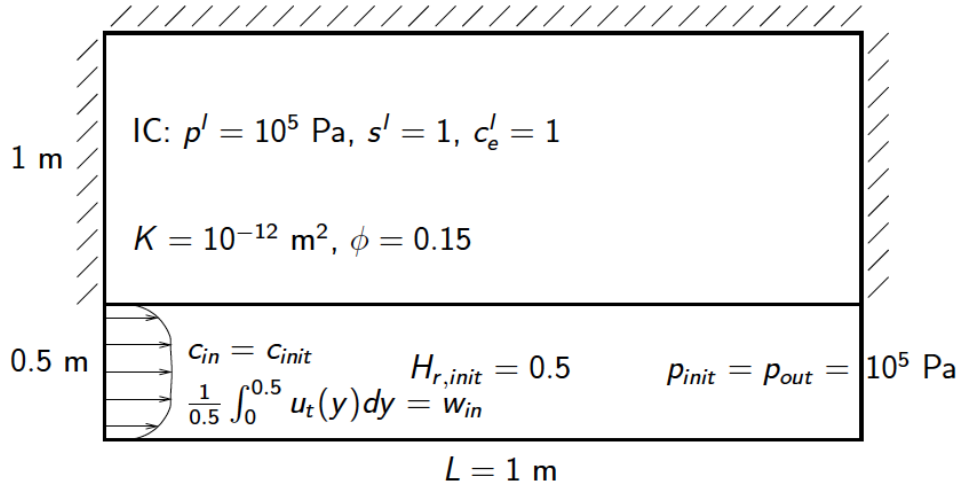


Figure 3.28: Setting of the drying test case.

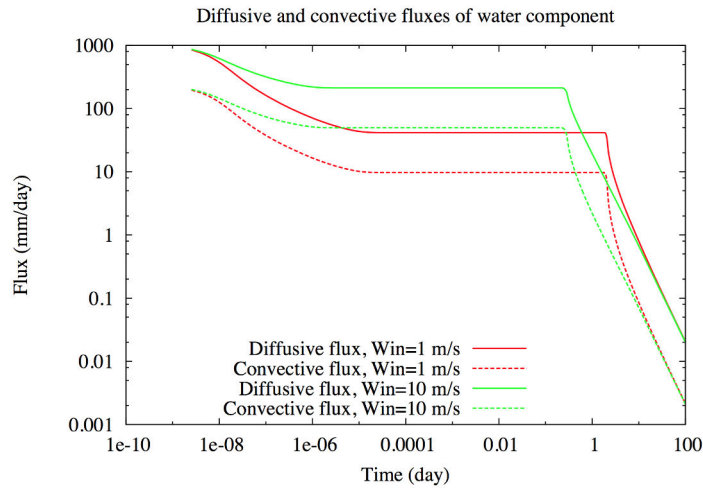


Figure 3.29: Mean diffusive and convective fluxes of water component at the interface as a function of time with the mesh 100×283 .

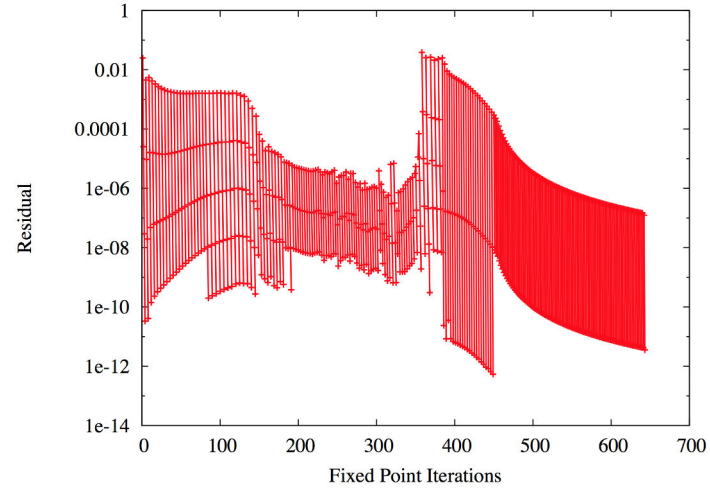


Figure 3.30: Convergence of the residual $\|1 - \sum_{i \in \mathcal{C}} c_i\|_{L^\infty(\Omega^g)}$ of the fixed point iterations for all time steps with $w_{in} = 10 \text{ m.s}^{-1}$ and with the mesh 100×283 .

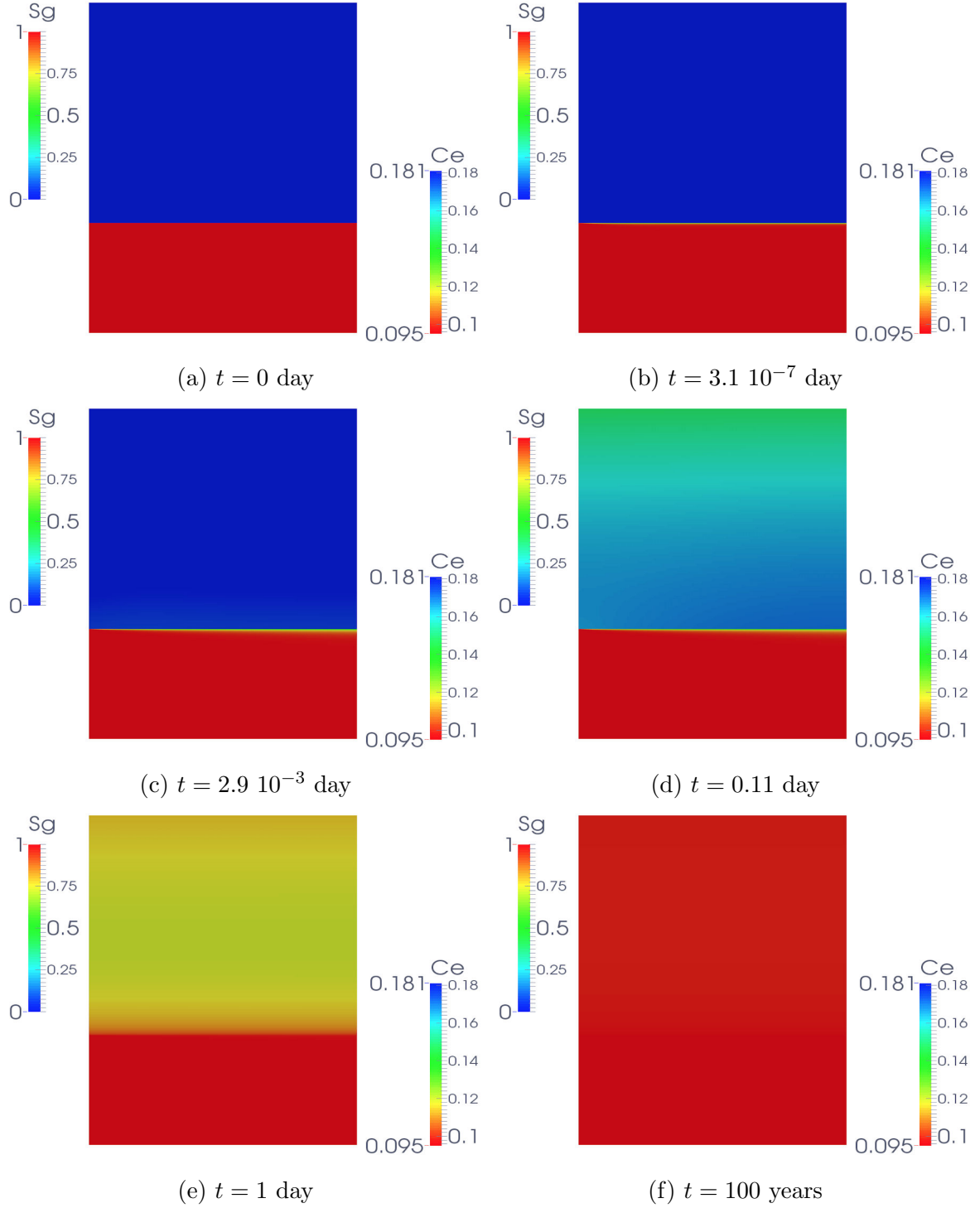


Figure 3.31: Gas saturation in the porous medium and water molar fraction in the gallery with $w_{in} = 10 \text{ m.s}^{-1}$ and the mesh 100×283 at (a) $t = 0$ day, (b) $t = 3.1 \cdot 10^{-7}$ day, (c) $t = 2.9 \cdot 10^{-3}$ day, (d) $t = 0.11$ day, (e) $t = 1$ day, (f) $t = 100$ days.



Figure 3.32: Perturbation \tilde{u} of the x component of the gas velocity at the first stage of the drying process obtained with $w_{in} = 10 \text{ m.s}^{-1}$ and with the mesh 100×283 .

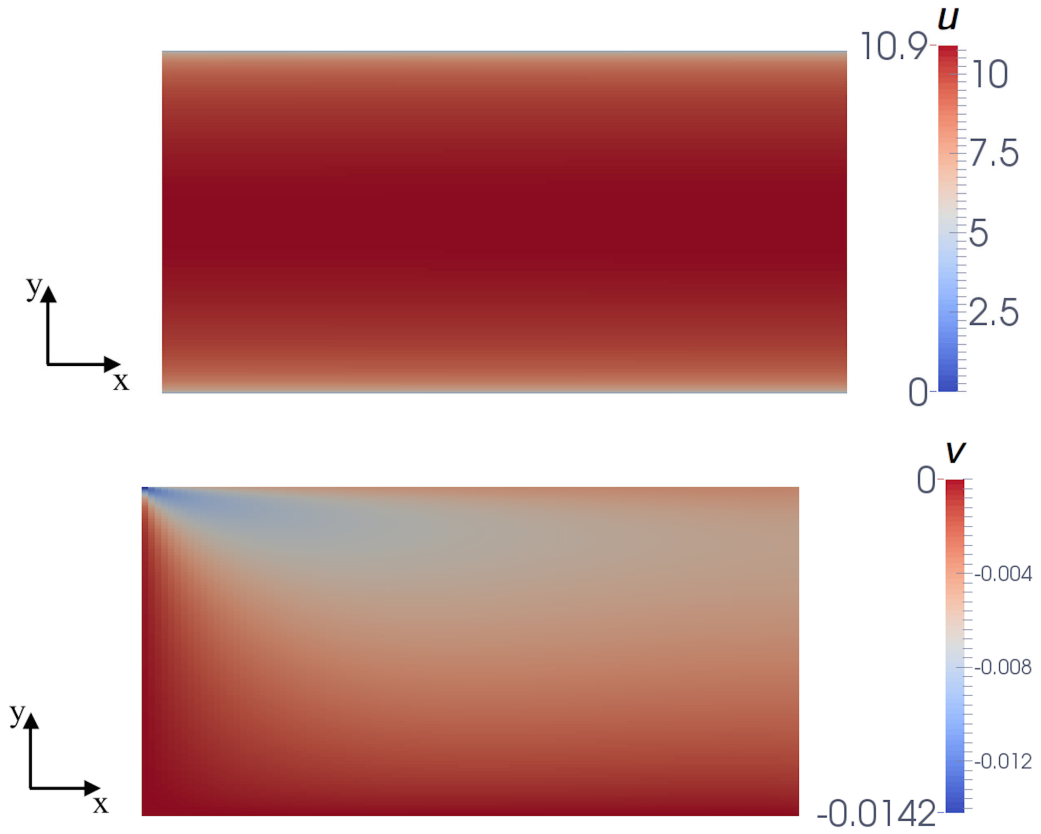


Figure 3.33: Gas velocities u (above) and $v = \tilde{v}$ (below) at the first stage of the drying process obtained with $w_{in} = 10 \text{ m.s}^{-1}$ and with the mesh 100×283 .

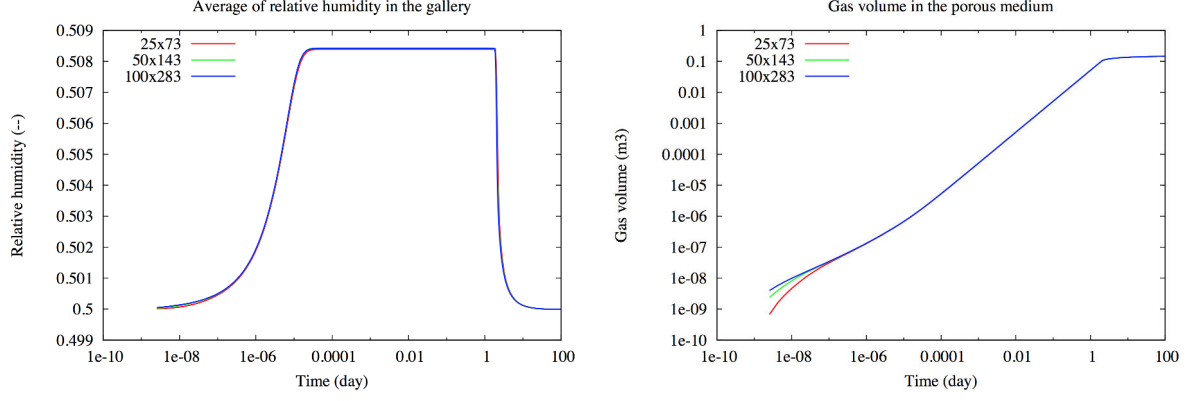


Figure 3.34: For each mesh and for $w_{in} = 1 \text{ m.s}^{-1}$: average of the relative humidity in the gallery (left) and gas volume in the porous medium (right) as a function of time.

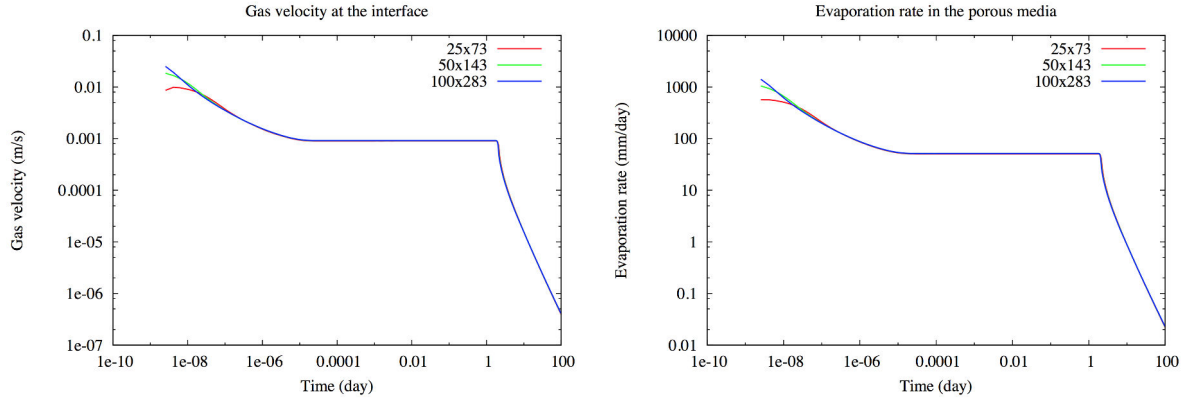


Figure 3.35: For each mesh and for $w_{in} = 1 \text{ m.s}^{-1}$: average of the gas velocity at the interface (left), evaporation rate at the interface (right) as a function of time.

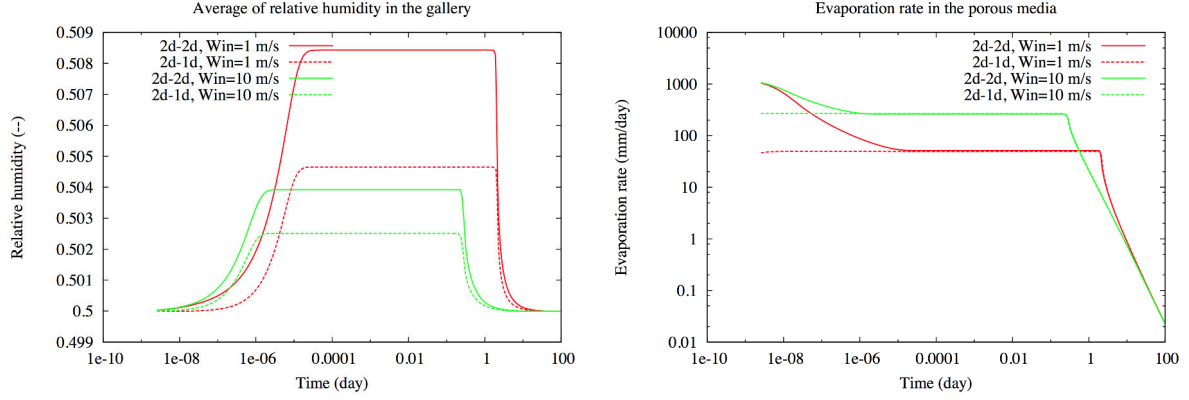


Figure 3.36: Comparison of the solutions obtained by the 2d-2d and 2d-1d models with the mesh 50×143 : average of the relative humidity in the gallery (left), evaporation rate at the interface (right) as a function of time.

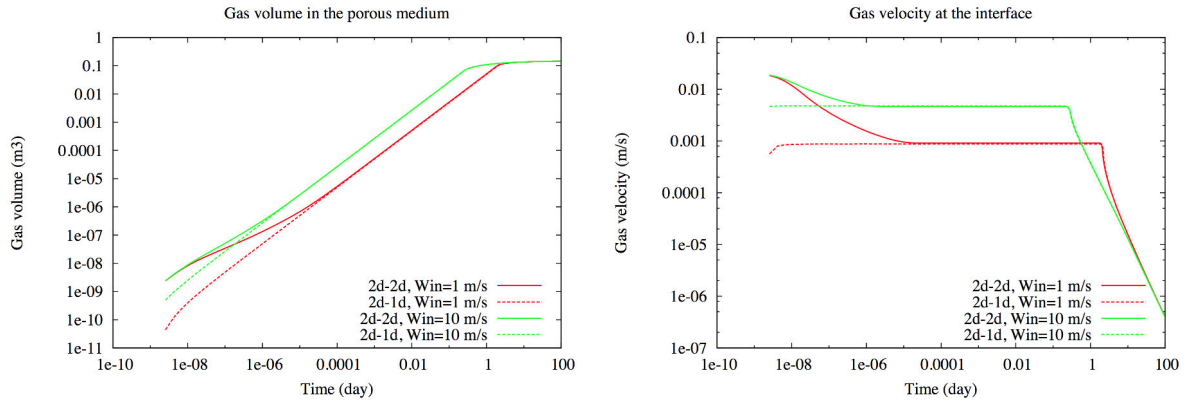


Figure 3.37: Comparison of the solutions obtained by the 2d-2d and 2d-1d models with the mesh 50×143 : gas volume in porous medium (left), average of the gas velocity at the interface (right) as a function of time.

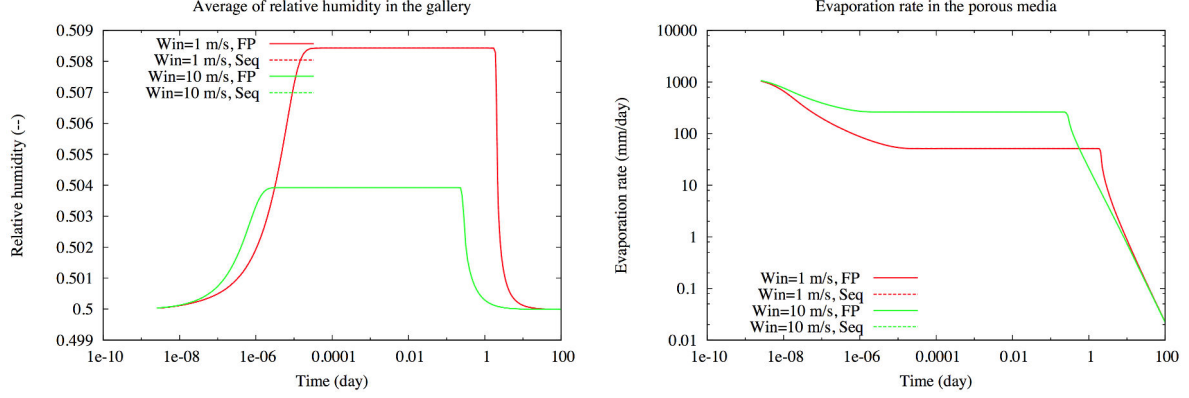


Figure 3.38: Comparison of the solutions obtained by the fixed-point (FP) and sequential (Seq) algorithms with the mesh 50×143 : average of the relative humidity in the gallery (left), evaporation rate at the interface (right) as a function of time.

We present in Tables 3.9 , 3.10 the numerical behavior of the simulations with different choices of w_{in} and for the three meshes:

(i) $w_{in} = 1 \text{ m.s}^{-1}$

<i>meshes</i>	$N_{\Delta t}$	N_{Chop}	N_{Newton}	N_{Pt}	N_{NVS}	CPU(s)	α_{CPU}
25×73	215	2	1879	625	1265	38.00	
50×143	218	3	2767	675	1390	334.00	1.59
100×283	233	7	4458	752	1562	4251.28	1.85

Table 3.9: For each mesh: number $N_{\Delta t}$ of successful time steps, number N_{Chop} of time step chops, number N_{Newton} of Newton iterations, number N_{Pt} of fixed point iterations, number N_{NVS} of quasi-newton iterations, CPU time in seconds, and scaling of CPU time (α_{CPU}) by $CPU \sim \text{cells}^{\alpha_{CPU}}$.

(ii) $w_{in} = 10 \text{ m.s}^{-1}$

<i>meshes</i>	$N_{\Delta t}$	N_{Chop}	N_{Newton}	N_{Pt}	N_{NVS}	CPU(s)	α_{CPU}
25×73	208	0	1446	551	1017	30.47	
50×143	212	1	2233	593	1104	271.19	1.60
100×283	223	4	3561	643	1183	3485.42	1.86

Table 3.10: For each mesh: number $N_{\Delta t}$ of successful time steps, number N_{Chop} of time step chops, number N_{Newton} of Newton iterations, number N_{Pt} of fixed point iterations, number N_{NVS} of quasi-newton iterations, CPU time in seconds, and scaling of CPU time (α_{CPU}) by $CPU \sim \text{cells}^{\alpha_{CPU}}$.

3.5 Conclusions

In this Chapter, a fixed point algorithm has been introduced to solve the problem coupling the liquid gas Darcy flow in the porous medium and the free gas flow in the gallery. This algorithm preserves the strong coupling between the water molar fraction in the gallery and the liquid pressure and flux at the interface, while it relaxes the weak coupling between the porous medium and the velocity and pressure in the gallery. A good convergence of this fixed point algorithm has been observed on Andra and drying test cases in a simple 2D geometrical setting. This algorithm has the advantage compared with fully coupled approaches [6, 41, 48] to lead to the non linear solutions of simpler sub-systems, and to allow large time steps at the scale of the porous medium as opposed to sequential algorithms [26, 24].

This coupled model is compared with the reduced model of Chapter 2 using an approximation of the gas molar fraction boundary layer thickness based on a low frequency diagonal approximation of a Steklov Poincaré operator. The comparisons performed on the 2D test cases show a very good match of the evaporation rate and of the porous medium gas volume. It also exhibits a good match of the relative humidity in the gallery especially, as expected, for high ratios between the length and the diameter of the gallery.

Conclusions et perspectives

Bilan des résultats obtenus

Une étude comparative en 1D et 3D de trois formulations du modèle gaz liquide compositionnel en milieu poreux a été menée au chapitre 1 au terme de laquelle la formulation en pressions des phases et fugacités a été retenue. Sur les cas tests Andra à effets capillaires dominants cette formulation s'avère à la fois performante et la plus simple à mettre en oeuvre du fait de l'absence d'inégalités dans les lois de fermetures et d'un jeu d'inconnues unique indépendant des phases en présence. En revanche la formulation en variables naturelles et la formulation en variables pressions, saturations et fugacités sont clairement plus robustes que la formulation en pressions des phases et fugacités dans les régimes à pression capillaire non dominante. Ce travail a donné lieu à la publication [47].

Un modèle réduit couplant l'écoulement gaz liquide compositionnel 3D dans le milieu poreux avec un modèle 1D de type "No Pressure Wave" dans la galerie de ventilation a été proposé au chapitre 1 sur la base du modèle développé dans [49, 6]. Cette réduction de dimension suppose l'écoulement dans la galerie essentiellement unidirectionnel comme c'est le cas en régime de convection forcée pour une longueur de galerie grande devant son diamètre. Ce modèle réduit tient compte de la diffusion des concentrations dans une couche limite à l'interface poreux galerie par l'introduction d'une concentration de paroi à l'interface et d'un terme de diffusion entre la concentration moyenne dans la galerie et la concentration à la paroi. Le modèle a été discrétisé par le schéma VAG (Vertex Approximate Gradient) de type Control Volume Finite Element. Ce schéma est adapté aux maillages polyédriques et aux milieux anisotropes et évite naturellement le mélange des milieux galerie et poreux dans les volumes de contrôle à l'interface. Les résultats numériques obtenus donnent un ordre de grandeur sur le flux de liquide à l'interface poreux galerie conforme aux mesures dont dispose l'Andra. Une extension du modèle 3D-1D et de sa discrétisation est proposée dans le cas de réseaux de fractures dans le milieu poreux modélisés comme des surfaces de co-dimension 1. Ce travail a donné lieu à deux publications dans des actes de conférences internationales [15], [17] et à une publication soumise à M2AN [16].

L'étude du modèle réduit 3D poreux - 1D libre précédent nous a permis de bien identifier le couplage fortement non linéaire entre la fraction molaire d'eau convectée dans

la galerie de ventilation et la pression et le flux de liquide à l'interface poreux galerie. Ce couplage est lié à l'équilibre thermodynamique liquide gaz à l'interface. Un algorithme de point fixe est développé au chapitre 3 préservant ce couplage fort et relaxant le couplage de la vitesse et de la pression dans la galerie avec les inconnues du milieu poreux et les compositions du gaz dans la galerie. Il consiste à résoudre à la première étape du point fixe les équations du modèle poreux couplées avec les équations de traceur sur les compositions à vitesse et pression fixées dans la galerie. Le flux total à l'interface calculé lors de cette première étape sert ensuite à résoudre les équations de Navier Stokes pour déterminer la vitesse et la pression dans la galerie.

Le comportement numérique de cet algorithme a été étudié dans le cas d'un modèle 2D-2D utilisant dans la galerie un modèle RANS avec viscosité et diffusion turbulentes obtenues par un modèle de turbulence algébrique.

Pour simplifier, on a utilisé une discrétisation en espace de type volume fini avec pressions et compositions aux mailles et vitesses normales aux faces. Le maillage est Cartésien (et conforme à l'interface poreux galerie) et les flux sont deux points (schéma TPFA dans le domaine poreux, et MAC sur maillages décalés dans la galerie). Les résultats obtenus montrent une convergence très rapide du point fixe du fait de la faible perturbation de la vitesse du gaz dans la galerie liée au couplage avec l'écoulement en milieu poreux.

Ce modèle 2D-2D a été comparé avec le modèle réduit 2D-1D approximant en 1D l'écoulement dans la galerie. Pour cela, l'épaisseur de couche limite pour la fraction molaire d'eau est approchée par la résolution de l'équation de convection diffusion stationnaire à vitesse fixée. Les résultats montrent que ce modèle réduit 2D-1D donne, par comparaison au modèle 2D-2D, un très bon ordre de grandeur du taux d'évaporation du liquide, de la désaturation du milieu poreux, et de l'humidité relative dans la galerie.

Perspectives

Méthodes de décomposition de domaine. L'algorithme étudié dans la thèse a l'inconvénient d'être très intrusif au sens où il implique la résolution couplée de l'écoulement diphasique dans le milieu poreux et des équations de traceur dans la galerie. Il est important pour la mise en oeuvre pratique de l'algorithme sous la forme de couplage de codes d'étudier des approches permettant de découpler les calculs dans les deux domaines. On pourrait utiliser pour cela une méthodologie de type décomposition de domaine à élaborer dans un premier temps sur le modèle simplifié couplant l'équation de Richards dans le milieu poreux à l'équation du traceur sur la fraction molaire d'eau dans la galerie. Le bon comportement du modèle 2D-1D nous porte à croire qu'un algorithme de type Schwarz optimisé devrait être efficace. Cet algorithme devra ensuite être étendu au cas du couplage avec le modèle diphasique compositionnel.

Extension à des géométries plus complexes. Le schéma TPFA + MAC mis en oeuvre dans la thèse a l'avantage d'être simple et robuste mais il est limité à des maillages Cartésiens. On pourrait étudier en combinaison avec la méthode de décomposition de

domaine précédente des discrétisations dans les domaines poreux et galerie à la fois non coincidentes à l'interface et adaptées à des maillages plus généraux dans chacun des deux domaines.

Extension à des physiques plus complexes. Une autre perspective est d'étendre l'étude des algorithmes de couplage à des modèles plus complexes que celui étudié dans la thèse.

Une première extension physique à considérer est celle du couplage du modèle Darcy diphasique - Navier Stokes avec la conservation de l'énergie à la fois dans le milieu poreux et dans la galerie. Les échanges thermiques jouent en effet un rôle important dans le stockage et ont une forte influence sur les phénomènes d'évaporation étudiés.

Une autre question plus ouverte en terme de modélisation est l'apparition de la phase liquide à l'interface lors de l'arrêt de la ventilation non prise en compte par le modèle actuel. Une façon de traiter partiellement ce problème consiste à remplacer les conditions d'interface par des conditions de type Signorini de façon à laisser passer le trop plein de liquide dans la galerie dans le cas où la phase gaz devient saturée en eau.

Bibliography

- [1] Abadpour, A. and Panfilov, M., *Method of negative saturations for modelling two phase compositional flows with oversaturated zones*, Transport in porous media, **79(2)**, pp. 197-214, 2010.
- [2] Alboin, C., Jaffré, J., Roberts, J. and Serres, C., *Modeling fractures as interfaces for flow and transport in porous media*, Fluid flow and transport in porous media, **295 AMS**, Chen, Ewing, editors, pp. 13-24, 2002.
- [3] Andra document, *Echange de masse et d'énergie entre l'air de ventilation des ouvrages souterrains et les milieux poreux constituant des parois des ouvrages du stockage*.
- [4] Angelini, O., Chavant, C., Chénier, E., Eymard, R. and Granet, S., *Finite volume approximation of a diffusion-dissolution model and application to nuclear waste storage*, Mathematics and Computers in Simulation, **81(10)**, pp. 2001-2017, 2011.
- [5] Aziz, K. and Settari, A., *Petroleum Reservoir Simulation*, Applied Science Publishers, 1979.
- [6] Baber, K., Mosthaf, K., Flemisch, B., Helmig, R. and Müthing, S., *Numerical scheme for coupling two-phase compositional porous-media flow and one-phase compositional free flow*, IMA Journal of Applied Mathematics, **77(6)**, 2012.
- [7] Beavers, G. S. and Joseph, D. D., *Boundary conditions at a naturally permeable wall*, Journal of Fluid Mechanics, 30:197-207, 1967.
- [8] Belgacem, F. B., *The Mortar finite element method with Lagrange multipliers*, Numerische Mathematik, **84**, pp. 173-197, 1999.
- [9] Bird, R. B., Stewart, W. E., and Lightfoot, E. N., *Transport phenomena*, John Wiley and Sons, 2007.
- [10] J. Bonelle and A. Ern, Analysis of compatible discrete operator schemes for elliptic problems on polyhedral meshes, *ESAIM Math. Mod. Numer. Anal.*, **48(2)**, 553–581, 2014.
- [11] Bourgeat, A., Jurak, M. and Smai, F., *Two phase partially miscible flow and transport in porous media; application to gas migration in nuclear waste repository*, Computational Geosciences, **13(1)**, pp. 29-42, 2009.

- [12] Brenner, K., Groza, M., Guichard, C. and Masson, R., *Vertex approximate gradient scheme for hybrid dimensional two-phase darcy flows in fractured porous media*, ESAIM: M2AN **49(2)**, pp. 303-330, 2015. DOI web-page: <http://dx.doi.org/10.1051/m2an/2014034>.
- [13] Brenner, K., Groza, M., Guichard, C., Lebeau, G. and Masson, R., *Gradient discretization of Hybrid Dimensional Darcy Flows in Fractured Porous Media*, preprint <https://hal.archives-ouvertes.fr/hal-00957203>.
- [14] Brenner, K. and Masson, R., *Convergence of a vertex centred discretization of two-phase darcy flows on general meshes*, International Journal of Finite Volume, **june**, 2013
- [15] Brenner, K., Masson, R., Trenty, L. and Zhang, Y., *Coupling of a two phase gas liquid compositional 3D Darcy flow with a 1D compositional free gas flow*, in the proceedings of FVCA VII, Berlin, june 2014.
- [16] Brenner, K., Masson, R., Trenty, L. and Zhang, Y., *Coupling of a two phase gas liquid compositional 3D Darcy flow with a 1D compositional free gas flow*, submitted to M2AN, 2015.
- [17] Brenner, K., Masson, R., Trenty, L. and Zhang, Y., *Coupling of a two phase gas liquid Darcy flow in fractured porous media with a 1D free gas flow*, Proceedings of MAMERN 2015 conference, 1-5 june, Pau.
- [18] Cao, H., *Development of techniques for general purpose simulators*, PhD thesis, University of Stanfords, 2002.
- [19] Chassaing, P., *Turbulence en Mécanique des Fluides, analyse du phénomène en vue de sa modélisation à l'usage de l'ingénieur*, Cépaduès- Editions, 2000.
- [20] Coats, K. H., *An equation of state compositional model*, SPE Reservoir Simulation Symposium Journal, pp. 363-376, 1980.
- [21] Coats, K. H., *Implicit compositional simulation of single-porosity and dual-porosity reservoirs*, SPE Symposium on Reservoir Simulation, 1989.
- [22] Daïan, J. F., *Equilibre et transfert en milieux poreux*, <http://hal.inria.fr/docs/00/96/75/30/PDF/ETMP314.pdf>
- [23] Deimling, K., *Nonlinear Functional Analysis*, Springer, New York, 1980.
- [24] Defraeye, T., *Convective heat and mass transfer at exterior building surfaces*, PhD thesis, Catholic University of Leuven, Leuven, Belgium, 2011.
- [25] Defraeye, T., *Advanced computational modelling of drying processes, a review*, Applied Energy, **131**, pp. 323-344, 2014.

- [26] Defraeye, T., Blocken, B. and Carmeliet, J., *Analysis of convective heat and mass transfer coefficients for convective drying of a porous flat plate by conjugate modelling*, Int. J. of Heat and Mass Transfer, **55**, pp. 112-124, 2012.
- [27] Demmel, J. W., Eisenstat, S. C., Gilbert, J. R., Li, X. S., and Liu, J. W. H., *A supernodal approach to sparse partial pivoting*, SIAM J. Matrix Analysis and Applications, **20(3)**, pp. 720-755, 1999.
- [28] Discacciati, M., Miglio, E. and Quarteroni, A., *Mathematical and numerical models for coupling surface and groundwater flows*, Appl. Num. Math., **43**, 2002.
- [29] Droniou, J., Eymard, R., Gallouët, T. and Herbin, R., *Gradient schemes: a generic framework for the discretisation of linear, nonlinear and nonlocal elliptic and parabolic equations*, Math. Models Methods Appl. Sci. **23(13)**, pp. 2395-2432, 2013.
- [30] Eymard, R., Féron, P., Gallouët, T., Guichard, C. and Herbin, R., *Gradient schemes for the stefan problem*, IJFV - International Journal on Finite Volumes, **june**, 2013.
- [31] Eymard, R., Gallouët, T. and Herbin, R., *Discretisation of heterogeneous and anisotropic diffusion problems on general nonconforming meshes SUSHI: a scheme using stabilisation and hybrid interfaces*, IMA J. Numer. Anal. **30(4)**, pp. 1009-1043, 2010.
- [32] Eymard, R., C. Guichard, C. and Herbin, R., *Small-stencil 3D schemes for diffusive flows in porous media*, ESAIM: Mathematical Modelling and Numerical Analysis, **46**, pp. 265-290, 2010.
- [33] Eymard, R., Herbin, R., Guichard, C. and Masson, R., *Vertex Centred discretization of compositional Multiphase Darcy flows on general meshes*, Comp. Geosciences, **16(4)**, pp. 987-1005, 2012.
- [34] Eymard, R., Henry, G., Herbin, R., Hubert, F., Klöforn, R. and Manzini, G., *Benchmark 3d on discretization schemes for anisotropic diffusion problem on general grids*, Finite Volumes for Complex Applications VI – Problems and Perspectives. Fort, J. and Furst, J. and Halama, J. and Herbin, R. and Hubert, F. editors, Springer Proceedings in Mathematics, **2**, pp. 95–265, 2011.
- [35] Eymard, R., Guichard, C., Herbin, R. and Masson, R., *Gradient schemes for two-phase flow in heterogeneous porous media and Richards equation*, ZAMM - Journal of Applied Mathematics and Mechanics **94** 7,8, pp. 560-585, 2014.
- [36] Eymard, R., Herbin, R., Guichard, C., Masson, R., *Vertex centred discretization of compositional multiphase Darcy flows on general meshes*, Comp. Geosciences, **16**, pp. 987-1005, 2012
- [37] Ern, A., and Mozolevski, I., *Discontinuous Galerkin method for two-component liquid-gas porous media flows*, Computational Geosciences **16(3)**, 2012.

- [38] Gharbia, I. B. and Jaffré, J., *Gas phase appearance and disappearance as a problem with complementarity constraints*, INRIA report, 2011. <http://hal.inria.fr/hal-00641621>.
- [39] Girault, V. and Rivière, B., *DG approximation of coupled Navier-Stokes and Darcy equations by beaver-joseph-saffman interface condition*, SIAM J. Numer. Anal., **47**, 2009.
- [40] Harlow F. and Welch, J., *Numerical calculation of time-dependent viscous incompressible flow of fluid with a free surface*, Physics of Fluids, **8**, pp. 2182-2189, 1965.
- [41] Helmig, R., Flemisch, B., Wolff, M., Ebigbo, A. and Class, H., *Model coupling for multiphase flow in porous media*, Advances in Water Resources, **51**, 2013.
- [42] Huber, R. and Helmig, R., *Node-centered finite volume discretizations for the numerical simulation of multi-phase flow in heterogeneous porous media*, Computational Geosciences, **4**, pp. 141-164, 2000.
- [43] Japhet, C., Nataf, F. and Rogier, F., *The Optimized Order 2 Method. Application to Convection-Diffusion Problems*, Future generation computer systems, **18(1)**, 17-30, 2001
- [44] Kräutle, S., *The semi-smooth Newton method for multicomponent reactive transport with minerals*, Adv. Water Res. **34**, pp. 137-151, 2011.
- [45] Lauser, A., Hager, C., Helmig, R. and Wohlmuth, B., *A new approach for phase transitions in miscible multi-phase flow in porous media*, Advances in Water Resources, **34**, pp. 957-966, 2011.
- [46] Li, X. S., Demmel, J. W., Gilbert, J. R., Grigori, L., Shao, M. and Yamazaki, I., Technical report LBNL-44289, Lawrence Berkeley National Laboratory, SuperLU Users' Guide, September 1999, <http://crd.lbl.gov/xiaoye/SuperLU>.
- [47] Masson, R., Trenty, L. and Zhang, Y., *Formulation of two phase gas liquid compositional Darcy flows with phase transitions*, International Journal of Finite Volume, **11**, 2014.
- [48] Mosthaf, K., *Modeling and Analysis of Coupled Porous-Medium and Free Flow with Application to Evaporation Processes*, PhD Thesis, University of Stuttgart, 2013
- [49] Mosthaf, K., Baber, K., Flemisch, B., Helmig, R., Leijnse, A., Rybak, I. and Wohlmuth, B., *A coupling concept for two-phase compositional porous-medium and single-phase compositional free flow*, Water Resources Research, **47(10)**, 2011
- [50] MoMaS COUPLEX Workshop, July 26-27 2001, CIRM Luminy-Marseille (France), http://www.ljll.math.upmc.fr/cances/gdrmomax/Ex_qualif/Couplex/couplex_Cem-racs2001.html

- [51] Patankar, S., *Numerical heat transfer and fluid flow. Series in Computational Methods in Mechanics and Thermal Sciences, XIII*. Washington - New York - London: Hemisphere Publishing Corporation; New York. McGraw-Hill Book Company, 1980.
- [52] Peaceman, D. W., *Fundamentals of Numerical Reservoir Simulations*, Elsevier, 1977.
- [53] Reichenberger, V., Jakobs, H., Bastian, P. and Helmig, R., *A mixed-dimensional finite volume method for multiphase flow in fractured porous media*, Adv. Water Resources, **29(7)**, pp. 1020-1036, 2006.
- [54] Saad, Y., *Iterative Methods for Sparse Linear Systems*, 2nd edition, SIAM, Philadelphia, PA, 2003
- [55] Saad, Y., <http://www-users.cs.umn.edu/saad/software/>
- [56] Thual, O., *Hydrodynamique de l'environnement*, éditions de l'Ecole polytechnique, 2010.
- [57] Tran, Q. H., Ferre, D., C. Pauchon, C. and Masella, J. P., *Transient Simulation of Two-Phase Flows in Pipes*, Oil & Gas Science and Technology, **53(6)**, pp. 801-811, 1998.
- [58] Wesseling. P., *Principles of Computational Fluid Dynamics*, Springer, 2001.
- [59] Whitson, C. H. and Michelsen, M. L., *The negative flash*, Fluid Phase Equilibria, **53**, pp. 51-71, 1989.